Simulations of Superbubbles in a Shearing, Stratified and Structured Interstellar Medium

Leonard Elias Cornelius Romano

München 2025

Simulations of Superbubbles in a Shearing, Stratified and Structured Interstellar Medium

Leonard Elias Cornelius Romano

Dissertation
an der Fakultät für Physik
der Ludwig–Maximilians–Universität
München

vorgelegt von
Leonard Elias Cornelius Romano
aus München, Deutschland

München, den 16.07.2025

Erstgutachter: Prof. Dr. Andreas Burkert
Zweitgutachter: Prof. Dr. Rolf-Peter Kudritzki
Tag der mündlichen Prüfung: 27.08.2025

Contents

List of Figures

List of Tables

Zusammenfassung

Supernovae (SNe) gehören zu den energetischsten Ereignissen im Universum. Sie injizieren enorme Mengen an Energie und angereichertem Material in das interstellare Medium (ISM). Supernova Überreste (SNRs), die Asche der SN Explosionen, prägen die Multiphasen-Struktur des ISM, den Antrieb von Turbulenz, die Regulierung der Sternentstehung und die Entstehung galaktischer Ausflüsse. Trotz ihrer enormen Bedeutung für das ISM sind viele Aspekte ihrer langfristigen Entwicklung und ihrer Wechselwirkung mit der galaktischen Umgebung, insbesondere in einem strukturierten ISM, noch unklar.

Diese Arbeit ist der detaillierten Untersuchung der Dynamik von SNRs in komplexen Umgebungen gewidmet. Zunächst stelle ich ein ein neues analytisches Modell basierend auf den Dünnschalen- und Sektoren-Näherungen vor, das die Expansion von SNRs in nicht-uniformen, zeitabhängigen Umgebungen beschreibt. Es berücksichtigt Gravitation, differentielle Rotation sowie Kühlung, reproduziert bekannte Grenzfälle und dient als Grundlage für komplexere Szenarien.

Anhand dieses Modells untersuche ich, wie Stratifizierung, Rotation und galaktische Substrukturen die Dynamik von SNRs beeinflussen. Die Ergebnisse zeigen, dass Gravitation die Fähigkeit von SNe, Ausflüsse zu erzeugen, stark einschränkt, sofern keine ausreichende Energieinjektion erfolgt. Galaktische Scherung und Substruktur deformieren große SNRs und führen zu einer asymptotischen Expansionsgeschwindigkeit von vergleichbarer Größenordung zur Geschwindigkeitsdispersion. Diese Erkenntnisse ermöglichen eine physikalisch fundierte Interpretation der Dynamik von SNRs und galaktischer Winde.

Ergänzend führe ich numerische Simulationen isolierter SNRs in einer homogenen Umgebung durch, mit Fokus auf die wenig verstandene Verschmelzungsphase. Ich charakterisiere den Zustand unmittelbar vor und während dieser Phase, der die Entstehung einer stark kühlenden, rücklaufenden Implosionswelle begünstigt. Diese füllt das zuvor evakuierte Innere auf und führt zur Kondensation einer zentralen Wolke. Ich untersuche, ob solche SN-Implosionswolken Sterne bilden können, und bestimme ihre Sternentstehungseffizienz. Diese Ergebnisse schließen die Entwicklungssequenz von SNRs ab und suggerieren einen neuen Entstehungsmechanismus für besonders metallreiche Sterne.

Den Höhepunkt bildet das **SISSI**-Projekt (**S**upernovae **I**n a **S**tratified, **S**hearing **I**nterstellar medium), in dem ich SNRs innerhalb des stratifizierten, gescherten und strukturierten ISM einer simulierten, isolierten Galaxie untersuche. Die Simulationen zeigen, wie stark Dynamik und Geometrie von SNRs vom Zusammenspiel mit der galaktischen Umgebung geprägt sind. Abschließend wende ich diese Ergebnisse auf die Lokale Blase an und ermittle ein signifikant jüngeres Alter als bisher angenommen wurde.

Diese Arbeit vertieft unser Verständnis darüber, wie SNe das ISM strukturieren. Durch die Verbindung analytischer Theorie, numerischer Modellierung und astrophysikalischer Beobachtungen liefert sie einen umfassenden Rahmen zur Interpretation von SNRs in komplexen galaktischen Umgebungen.

Abstract

Supernovae (SNe) are among the most energetic events in the Universe, injecting vast amounts of energy and enriched material into the interstellar medium (ISM). Their ashes, usually referred to as supernova remnants (SNRs) or superbubbles (SBs) in the case SNRs powered by the clustered explosions of many stars, play a central role in shaping the multiphase structure of the ISM, driving turbulence, regulating star formation, and contributing to galactic outflows. Despite their importance, many aspects of their long-term evolution and interaction with their galactic environment remain poorly understood, particularly in the context of a realistic, structured ISM.

In this thesis, I explore the dynamical evolution of SNRs across a range of scales and physical conditions. I begin by developing a novel one-zone blastwave model, based on the thin-shell and sector approximations, that is designed to capture the expansion of SNRs in non-uniform, time-dependent environments, including the effects of gravity, shear induced by differential rotation, and cooling. This model reproduces known analytic limits and serves as a foundation for exploring more complex configurations.

I apply the model to stratified, rotating, and structured galactic environments, quantifying how these factors alter the dynamics of SNRs. The results demonstrate how gravity limits the ability of SNe to drive outflows unless a sufficient level of energy injection is sustained. Galactic shear and substructure deform large-scale bubbles and asymptotically set a characteristic expansion velocity tied to the ambient velocity dispersion. These insights provide a physically motivated framework to interpret and constrain SB growth and outflow conditions in realistic galactic settings.

Complementing the analytic work, I perform a suite of numerical simulations of isolated SNRs in uniform media, focusing on the poorly understood merging phase. I characterize the physical conditions within SNRs shortly before and during the merging phase, which favor the formation of an implosion wave, a rapidly-cooling, reverse shock-wave that refills the previously evacuated interior and leads to the condensation of a central cloud. Based on these results, I propose that such a SN-implosion driven cloud may form stars and predict the associated star-formation efficiency. These results offer closure to the overall story of SN evolution and provide a new attractive pathway for the formation of the most metal-rich stars.

My thesis reaches its climax with the introduction of the **SISSI** (**S**upernovae **I**n a **S**tratified, **S**hearing **I**nterstellar medium) project, in which I simulate the evolution of SNRs embedded within the stratified, shearing, and structured ISM of a simulated, isolated galaxy. SISSI reveals how the dynamics and geometry of SNRs are affected by their complex interplay with a realistic galactic environment. Finally, I apply these findings to the Local Bubble, reevaluating its formation history, with the surprising result that it should be significantly younger than previously believed.

Together, these studies advance our understanding of how SNe structure the ISM. By bridging analytic theory, numerical modeling, and astronomical observations, this work provides a comprehensive framework for the interpretation of SNRs in complex galactic environments.

Chapter 1

Supernova Remnants

The galactic, multi-phase interstellar medium (ISM) is the dynamic stage shaped by the complex interplay of (magnetohydrodynamical) turbulence, stellar feedback, and gravity, where the stories told in this thesis take place. It consists of cold, molecular clouds surrounded by warm, diffuse gas, which are embedded in a hot, tenuous network of bubbles whose expansion is driven by the moody whims of massive stars (e.g. McKee & Ostriker, 1977; Cox & Reynolds, 1987; Cox, 2005). While locally these structures are in an ever changing, chaotic competition of the various driving forces, such as gravitational collapse and fragmentation, turbulence and stellar feedback, the ISM reveals its underlying structure when we average over larger scales, both spatial and temporal (e.g. de Avillez & Breitschwerdt, 2005; Kim et al., 2023a; Rathjen et al., 2025).

In this statistical sense, the ISM has been characterized and various defining properties, such as the volume filling factors of the different gas phases (de Avillez & Breitschwerdt, 2004; Bieri et al., 2023), the pressure contributions of various sources of pressure (e.g. thermal, turbulent, magnetic, cosmic rays Ostriker & Kim, 2022) and the nature of the turbulence (e.g. solenoidal vs. compressive; sonic vs. subsonic Federrath, 2013; Klessen & Glover, 2016) have been determined (Klessen & Glover, 2016), and are being determined in increasing detail (McComas et al., 2015; Saintonge & Catinella, 2022; McCallum et al., 2025).

Many different processes are being discussed which are hypothesized to contribute to the formation of such a medium (e.g. Burkert & Lin, 2000; Behrendt et al., 2015; Walch et al., 2015), but numerical challenges (de Avillez & Breitschwerdt, 2005; Groth et al., 2025), as well as conceptual issues with the interpretation of the analysis (Groth et al., 2025), and most importantly the incredible dimensions of the modeling space (Walch et al., 2015; Kim et al., 2023a) make it challenging to *faithfully* assess which processes dominate the dynamics of the ISM.

Among these driving forces of the ISM, supernovae (SNe), explosions of stars at the end of their lives, play a central role (Walch et al., 2015; Gent et al., 2020). While there is a wide variety of different explosion mechanisms, most notably thermonuclear explosions of white dwarfs (type-Ia, Fe-rich ejecta Blondin, 2024) and core-collapse SNe (type-II, O-rich ejecta Janka, 2025) driven by various dynamical instabilities in the core of massive stars ($\gtrsim 8\,\mathrm{M}_\odot$), the result is similar to someone like me, who is predominantly interested in the immediate effects on the ISM: an essentially instantaneous release of large amounts of energy ($\sim 10^{51}\,\mathrm{erg}$) and mass ($\gtrsim 1\,\mathrm{M}_\odot$), highly enriched with heavy nuclei – a.k.a. *metals* – that is powerful enough to meaningfully perturb the large-scale ISM (Fichtner et al., 2024). Thus in the context of my thesis, SNe are treated as idealized energy and mass sources, abstracted from their stellar origins and considered as discrete, localized events within a galactic setting.

1.1 The Effects of SNe on the ISM

The ashes of these big astrophysical explosions, form a structure, known as a supernova remnant (SNR). The expansion of SNRs can affect the ISM in many important ways, playing an integral role in the physics of star-formation and galaxy evolution (de Avillez & Mac Low, 2002; Walch et al., 2015).

SNe kickstart chemical evolution in the universe by blowing out metals formed in the interior of stars through nuclear fusion (Saitoh, 2017; Goswami et al., 2024; Janka, 2025), and their remnants can redistribute and mix them throughout the ISM and into the halo (Ibrahim & Kobayashi, 2024), on timescales on the order of 100 Myr (de Avillez & Mac Low, 2002). Among these metals, notably are the short-lived radionuclides (SLRs) ^{26}Al and ^{60}Fe (Kretschmer et al., 2013; Parker et al., 2023), which have long been recognized to play an important role for the formation of rocky planets and ultimately for the ORIGINS of life (Urey, 1955) and a still lively debated fraction of these metals ($\lesssim 0.1 - 10\,\%$) can condense to form dust grains (e.g. Nozawa et al., 2007; Zhukovska et al., 2008; Matsuura et al., 2011), which trace the gas distribution (Leike et al., 2020; Edenhofer et al., 2024), and play an integral role in many galactic process (Wolfire et al., 2003; McKee et al., 2015), such as molecular gas cooling (Hollenbach & Salpeter, 1971) and radiative transfer (Mathis et al., 1977), and again, the formation of rocky planets and life as we know it (Ercolano & Clarke, 2010; Birnstiel, 2024). On the other hand, the environment created by SNe is quite hostile to the survival of dust grains and different models of SNRs expanding into dusty media suggest that they may destroy anywhere from $0 - 100\%$ of the dust they encounter during the early expansion phases (e.g. Nozawa et al., 2007; Bianchi & Schneider, 2007; Kirchschlager et al., 2024). It remains to be shown whether SNRs are net dust sources or sinks.

By heating up and disrupting their environment SNRs can act to regulate star-formation on galactic scales, much like a thermostat (Gatto et al., 2017; Kim et al., 2023a). If a region is excessively forming stars, the overabundance of massive stars will lead to many SNe in the near future, which can temporarily prevent star formation in that region. Meanwhile, in a region with previously little star formation, few SNe are expected to explode, allowing for ongoing accumulation of gas, that may eventually collapse and form stars. While it is generally agreed upon that the net effect that SNe have on star-formation is its suppression, under certain circumstances SNe may actually trigger it (Elmegreen & Lada, 1977; Elmegreen, 1998).

The key insight behind the idea of triggered star-formation is that shocks compress gas and denser gas collapses on a shorter timescale (Elmegreen & Lada, 1977). This is particular true in the case of radiative shocks (Hunter et al., 1986), i.e. after shell formation, where the shocked gas can easily be compressed by a factor of 100 or more (Diesing et al., 2024; Diesing & Gupta, 2025). As a result the shells of radiative shocks, which are subject to a wide range of instabilities can fragment, and form particularly dense overdensities, which grow by further instabilities until they eventually reach a critical mass and become gravitationally unstable and collapse. Besides this traditional mechanism, compressed rings and shells can also collapse globally, though on much longer timescales (Elmegreen, 1998). Small droplets of dense gas can also be engulfed by the hot, overpressurized interior of blastwaves and if they manage to survive the hostile, turbulent environment, they are compressed, and – if the pressure in the SNR is high enough – they may even become gravitationally unstable and form stars (Krause et al., 2018). While these processes certainly do not seem to be very efficient on large scales, due to the extremely short free-fall timescales in the compressed gas, locally they might contribute significantly to the budget of newly formed stars. Indeed, many observations of young star-forming regions in the solar neighborhood find evidence for sequential star-formation (Miret-Roig et al., 2022), which exhibits many of the classical features predicted by the classical models for triggered star-formation, such as radial age-gradients (Posch et al., 2023; Ratzenböck et al., 2023; Swiggum et al., 2024). Yet the role of the various different feedback mechanisms, such as stellar winds, ionizing EUV radiation and

especially that of SNe remains to be unambiguously determined.

SNRs structure the ISM, filling it with a network of hot, voluming-filling bubbles (Cox & Smith, 1974), and banish the cold, molecular and warm, atomic gas onto their surfaces. This network of bubbles and clouds interacts in complex ways, driving turbulence on $\sim 100\,\mathrm{pc}$ scales, which cascades down to increasingly smaller scales and provides kinetic, and hypothetically – by means of a turbulent dynamo – magnetic pressure support to the ISM (Ostriker & Kim, 2022; Gent et al., 2023, 2024). Through interactions with the intergalactic magnetic field in a processes known as diffusive shock acceleration, SNRs are hypothesized to accelerate cosmic rays (Cristofari et al., 2021; Diesing et al., 2024; Diesing & Gupta, 2025) and even dust grains (Epstein, 1980; Ellison et al., 1997; Cristofari et al., 2025), converting up to $\sim 10\,\%$ of the injected energy into cosmic ray energy, with the most energetic CRs reaching up to $\sim 1\,\mathrm{TeV}$ (Cristofari et al., 2020).

1.2 The Life of a Supernova Remnant

SNR evolution proceeds through various stages, probing a wide window of different spatial and temporal scales as outlined in Fig. 1.1 and emitting light in a wide frequency range, characteristic of each stage.

1.2.1 Young SNRs – The Free-Expansion Phase

Initially, the ejecta are only loosely coupled to their surrounding gas, allowing them to expand freely at a speed oftentimes exceeding $\gtrsim 1,000\,\mathrm{km\ s^{-1}}$, as determined by the explosion energy and the ejecta mass. During this stage, SNRs can reach sizes of a few parsec. After a few 100 to 1000 years, once the expanding blastwave has swept up its ejecta mass in ambient medium, the pressure in the expanding shell starts to dominate over the adiabatically cooling interior and drives a reverse shock that thermalizes the ejecta (Truelove & McKee, 1999).

Young SNRs such as Cassiopeia A are routinely observed in a wide variety of wavelength bands, from the radio (e.g. Anderson & Rudnick, 1995; Arias et al., 2018) and infrared (e.g. Milisavljevic et al., 2024; De Looze et al., 2024; Rho et al., 2024) at long wavelengths to optical (e.g. Reed et al., 1995; Fesen et al., 2025), all the way up to X-ray (e.g. Grefenstette et al., 2017; Vink et al., 2024; Suzuki et al., 2025; Bamba et al., 2025) and even gamma ray emission (e.g. Saha et al., 2014; Li et al., 2025) at short wavelengths. This wealth of multi-wavelength data and the time variability of these systems on human timescales allows us to study the dynamics of these systems in great detail (Orlando et al., 2025).

1.2.2 The Adiabatic / Sedov-Taylor Phase

Once the ejecta are fully thermalized, the SNR enters the so-called Sedov-Taylor (Taylor, 1950; Sedov, 1959) or adiabatic phase during which the dynamics are determined by the adiabatic expansion of the shock, which is characterized by energy conservation. Most of the radial momentum that is generated during SNR expansion comes from this stage (Kim & Ostriker, 2015). Adiabatic SNRs can reach sizes of several 10s of parsecs before they start to lose their energy to radiative cooling, which starts to dominate after several 1000 to 10s of thousands of years (Cioffi et al., 1988).

Adiabatic SNRs can be observed mostly in the X-ray (e.g. Khabibullin et al., 2023; Reynolds & Borkowski, 2024; Okada et al., 2025), however observations from other bands such as radio (Jing

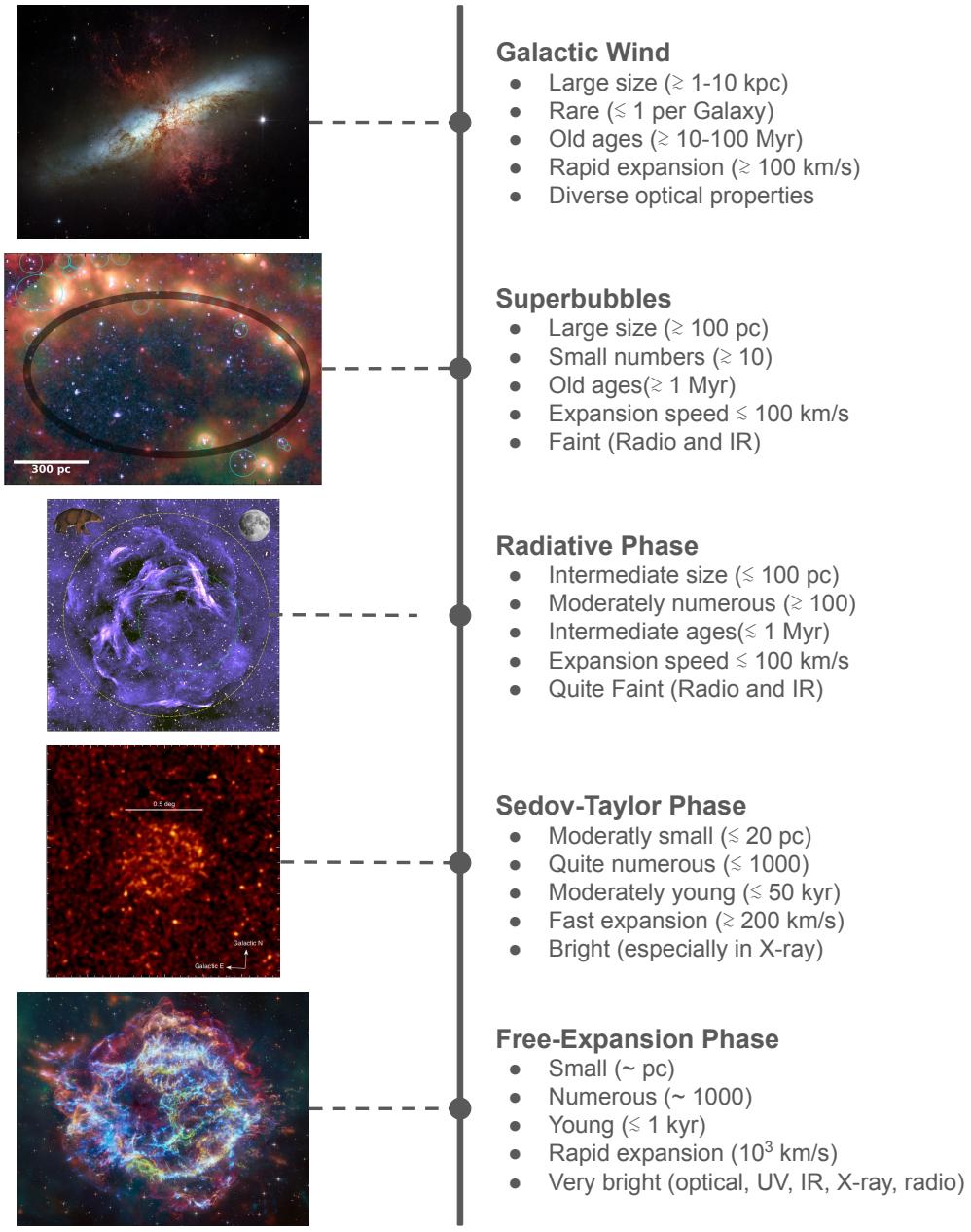

Figure 1.1: Observations of Supernova Remnants on various different scales. From bottom to top (small to large scales): Multi-wavelength image of Cassiopeia A (Schmidt & Arcand, 2024), An X-ray image of G121.1-1.9 (Khabibullin et al., 2023), A radio image (943 MHz) of G278.94+1.35 (Filipović et al., 2024, a.k.a. Diprotodon), Multi-wavelength image of a SB candidate in the NGC 628 (Watkins et al., 2023), and a multi-wavelength image of the galactic outflow in the Cigar Galaxy, M82 (NASA & the Hubble Heritage Team , STScI/AURA).

et al., 2025; Filipović et al., 2025), gamma- and cosmic-rays (Mitchell, 2024), and near infrared (Deng et al., 2023) emission, end even from optical and UV absorption features (Ritchey, 2023) exist. Compared to their younger counterparts, adiabatic SNRs are much fainter and the available data is much sparser. Nonetheless, adiabatic SNRs are an important probe of galactic physics and particularly their potential role in the acceleration of high energy cosmic rays makes them an attractive target for both observational surveys and theoretical investigations.

1.2.3 The Radiative Phases

Once cooling begins to dominate, the high pressure in the interior of the SNR pushes the hot gas in the interior outwards, where it condenses into a thin, dense shell(Chevalier, 1974; Straka, 1974), leaving behind an evacuated low density, low pressure cavity. The pressure-driven evacuation phase is often referred to as the pressure-driven snowplow phase, while the post-evacuation phase is dubbed momentum-driven snowplow phase (Cioffi et al., 1988; Thornton et al., 1998; Fierlinger et al., 2016, e.g.), since the dynamics at this point are dictated by the conserved momentum of the shell.

Due to the rapid radiative cooling and the strong compression of the shell, which greatly enhances emission, the luminosity of radiative SNRs flares up compared to the previous adiabatic phase. Radiative SNRs are commonly observed in radio (e.g. Filipović et al., 2024; Bakış et al., 2025), (sub-) millimeter (e.g. Sofue, 2024; Nonhebel et al., 2024; Shen et al., 2025) (far-) infrared (e.g. Reach et al., 2024), optical (Paylı et al., 2024) and even gamma ray (e.g. Tu et al., 2024; Araya, 2024) emission.

While I have focused here mostly on observations of *Galactic* SNRs of which only about 300 are known with high accuracy (Green, 2025), extragalactic surveys such as PHANGS allow us to discover large numbers of SNRs in nearby galaxies (Li et al., 2024; Zangrandi et al., 2024). Yet, due to the great distance from these objects and the diverse samples, extragalactic SNRs can often be only studied quite superficially and oftentimes it is even hard to tell apart SNRs from bubbles that have formed by other processes, such as HII regions (Winkler et al., 2023; Caldwell et al., 2025).

1.2.4 The Merging Phase

As the blast-wave front, driven by its momentum expands it keeps slowing down eventually reaching the propagation speed of small-scale fluctuations at which point it will start to broaden substantially and *merge* with the ISM. This so-called *merging* usually happens after about a million years of expansion at which point SNRs can reach sizes on the order of 100 pc. While the term merging might suggest, that SNRs fade into the ISM, leaving behind an environment resembling the previously unperturbed ISM, i.e. by fragmentation of the expanding shell and subsequent mixing with the evacuated bubble, prior to my thesis, the details of this process have received surprisingly little attention (however, see Slavin & Cox, 1992).

Since fully-merged SNRs would by definition look identical to the ISM it is very challenging to observe them and to my knowledge, there are no observations of SNRs that are confirmed to have merged with the ISM. However, it is important to keep in mind that the basic setup of an evacuated shell surrounded by a dense, but broadening shell overlaps with the definition of radiative SNRs, so it is quite likely that a fraction of the observed radiative SNRs could be reclassified as *merging*.

1.2.5 Superbubbles – Clusters of SNRs

With merging, the evolution of a *single* SN would be concluded. However, more often than not, stars form in clusters, groups and associations and as a consequence SNe explode in a spatially and temporally correlated way (Leitherer et al., 1999; Ratzenböck et al., 2023; Swiggum et al., 2024). Thus, a fading SNR may be rejuvenated by subsequent SN explosions happening in its vicinity, or even within the bubble itself.

Typical timescales for the time between SNe in a star cluster are on the order of 100 kyr to a few Myr depending on the mass of the cluster, which determines the number of massive stars (Leitherer et al., 1999; Kim et al., 2017). This suggests that in many cases SNRs may indeed coalesce to form larger associations of SNRs, known as superbubbles (SBs), which can grow much larger than individual SNRs and their hot interior is much more long-lived, due to the steady energy injection from the subsequent SNe and their relatively slow expansion, which leads to inefficient adiabatic cooling (Kim & Ostriker, 2015; Gentry et al., 2017; El-Badry et al., 2019).

Extragalactic SBs can be observed through the infrared emission of their shells (e.g. Watkins et al., 2023), while Galactic SBs can be observed in various ways, e.g. through features in optical emission maps (Alsulami et al., 2024), infrared emission maps (Verma et al., 2023), diffuse X-ray emission (Heiles, 1998; Yeung et al., 2024) and through topological analysis of 3D dust-extinction maps (Zucker et al., 2022; O'Neill et al., 2024; Gao et al., 2025).

In extreme cases, SBs can break out of the galactic disk and drive a galactic outflow; a spectacular (Bolatto et al., 2024; Lopez et al., 2025) way for a galaxy to vent its excess energy and simultaneously regulate its star-formation activity (Carr et al., 2023). Galactic outflows can reach over several kpc in size and typically develop over the course of 10s to 100s of Myr (e.g. Jacob et al., 2018; Girichidis et al., 2024).

Stellar-feedback-driven galactic winds are routinely observed in the rest-frame UV (e.g. Heckman et al., 2015; Sugahara et al., 2019; Xu et al., 2022) and optical (e.g. McQuinn et al., 2019; Marasco et al., 2023; Xu et al., 2023b) to trace ionized gas and far-infrared (Romano et al., 2023) to trace the neutral, atomic gas, preferentially in low-mass galaxies ($M_\mathrm{h} \lesssim 10^{12}\,\mathrm{M}_\odot$), since outflows in higher-mass systems are oftentimes attributed to active galactic nuclei (AGN). Recent observations of infrared (Bolatto et al., 2024) and radio (Krieger et al., 2019; Heyer et al., 2025) emission associated with galactic winds, even confirmed the presence of molecular and dusty structures, raising questions about how they could possibly survive in such an inherently hostile environment (e.g. Micelotta et al., 2010; Richie et al., 2024; Richie & Schneider, 2026).

1.3 Are SNRs "solved"?

While this picture captures a wide range of different SNRs over more than six orders of magnitude in spatial scale, the devil lies in the detail and there are many additional complications that were neglected in this broad overview. In the research presented in this thesis, my goal was to address some of these complications, with a strong focus on the role of a realistic galactic environment. Throughout this journey, I learned that the physical effects of the galactic environment are intimately coupled to the *merging* of SNRs with their surroundings. While for sufficiently small and young SNRs the microscopic (compared to the scale of a galaxy) shock physics, outlined above provide a rather accurate description, old and large SNRs and SBs are mesoscopic objects whose dynamics are dictated by the complex interplay of their small-scale shock dynamics and the effects of their larger-scale galactic environment.

The remainder of this thesis is dedicated to a thorough investigation of the question how SNRs

and SBs evolve in a complex galactic environment. In Chapter 2, I present an analytical one-zone model that aims to describe the dynamics of SNRs and SBs in complex environments. In Chapter 3, I apply this model to SBs in a vertically stratified medium, to study the conditions under which a galactic wind may form and investigate the role of cosmic rays. In Chapter 4, I present the results of numerical simulations of SNRs in a uniform stationary medium to characterize the merging phase under such idealized conditions. In Chapter 5, I utilize the findings of the previous chapter to make predictions for the star-formation from clouds that might form from merging SNRs. In Chapter 6, I present a suite of numerical simulations of SNRs and SBs exploding in the ISM of a simulated, isolated galaxy and characterize, how the galactic environment might affect various aspects of their dynamics and geometry. In Chapter 7 I apply some of these findings to the Local Bubble, our local SB, to derive new constraints on its formation history. Finally, in Chapter 8 I summarize my findings and conclude by pointing out possible future directions.

Chapter 2

Modelling the Expansion of Supernova Remnants

> Software used in this chapter:
> Julia v1.10.0 (Bezanson et al., 2017), Matplotlib v3.5.1 (Hunter, 2007), and Healpix v2.3.0 (Tomasi & Li, 2021)

An extended, more detailed version of this work is to be submitted to Astronomy & Astrophysics after the submission of this thesis. As recommended by the members of the thesis committee, I have revised and extended this chapter after my defense. The published version is the final version completed on Jan. 27 2026. The derivation and conceptualization of the model presented in this chapter, as well as the derivation of the results and plots were original work done by myself. My supervisors Andi and Manuel were involved by asking the right questions that guided me in the right direction.

The environment in which supernovae (SNe) explode is far from stationary and uniform. Observations of Galactic SN remnants (SNRs) exhibit many complex features that are usually associated with interactions with their complex, structured surroundings in the circumstellar (e.g. Kobashi et al., 2024; De Looze et al., 2024) or interstellar medium (e.g. Arias et al., 2018; Deng et al., 2023; Paylı et al., 2024). Moreover, extragalactic observations suggest that large scale flows and gravity may also affect the dynamics of SNRs (Watkins et al., 2023).

While significant efforts have been made trying to reproduce these features in the case of specific SNRs such as G1.9+0.3 (Zhang et al., 2023), G332.5-5.6 and G290.1-0.8 (Velázquez et al., 2023), Pa 30 (Duffell et al., 2024) and prominently, the Local Bubble (LB) (Breitschwerdt & de Avillez, 2006; Breitschwerdt et al., 2016), theoretical studies investigating the dynamics of SNRs are usually limited to (near) uniform, stationary environments (e.g. Ostriker & McKee, 1988; Truelove & McKee, 1999; El-Badry et al., 2019), with the role of the complex environment usually being an afterthought (though notable exceptions exist, e.g. Laumbach & Probstein, 1969; Haid et al., 2016; Jiménez et al., 2024; Lau & Bonnell, 2025).

These theoretical investigations have painted a coherent picture of SNR evolution, in which SNRs evolve through various distinct evolutionary stages (e.g. Kim & Ostriker, 2015; Oku et al., 2022). Young SNRs start out with a free-expansion phase (Truelove & McKee, 1999), which is concluded once the reverse-shock has thermalized the ejecta and they transition into the adiabatic so-called Sedov-Taylor phase (Taylor, 1950; Sedov, 1959), which eventually ends once radiative cooling

starts to dominate, leading to shell-formation and the onset of various so-called snowplow phases (Cioffi et al., 1988; Kim & Ostriker, 2015; Fierlinger et al., 2016). SNR evolution is concluded by the merging of SNRs with their environment (Slavin & Cox, 1992; Romano et al., 2024a) or the formation of a superbubble (SB) through the coalescence of many clustered SNRs (El-Badry et al., 2019; Oku et al., 2022). While this picture describes the dynamics of SNRs in idealised, uniform environments with great accuracy, it remains unclear how applicable it is to the actually observed case of SNRs exploding in a highly structured medium affected by turbulence, galactic shear and gravitational tides.

The theoretical studies that focused on these effects usually investigated the role of one or few of these effects in isolation. Laumbach & Probstein (1969) and several others (e.g. Kompaneets, 1960; Moellenhoff, 1976; Koo & McKee, 1990) have investigated the effect of vertical stratification. These authors find, that *adiabatic* blastwaves expanding into a medium with finite mass are reaccelerated after atmospheric breakout, reaching an infinite speed within finite time. Energy-conservation considerations show that the leading shock, which is moving increasingly small amounts of mass, indeed does follow this behavior, while the bulk of the mass is limited to an asymptotic finite speed (Koo & McKee, 1990). However, it is important to note, that these considerations generally neglect the effects of radiative cooling and gravity, on timescales where they would most certainly be relevant.

Tenorio-Tagle & Palous (1987) and a number of other authors (e.g. Bisnovatyi-Kogan & Silich, 1995; Palouš et al., 2020; Jiménez et al., 2024) study the role of shear induced by differential rotation. They find that SNRs expanding into differentially rotating media may be stretched out substantially in the direction of the rotation, within a fraction of the orbital timescale. Jiménez et al. (2024) fit such a model to the southeast superbubble in NGC628 and find that deformation by shear indeed serves as a plausible explanation for its elongated geometry.

Haid et al. (2016) estimate the effects of a turbulent ISM on the radial momentum of SNRs, by averaging over many cones with random density, sampled from a density probability density function with a dispersion dictated by the theory of turbulent compression. They find that in moderately turbulent environments, the average momentum is only marginally affected by turbulence.

Lau & Bonnell (2025) develop an analytic model to study the escape of a SN energy through a low-density channel that connects an H II region embedded within a dense molecular cloud with the ambient ISM, by following the energy flux along a streamline. They characterize how the presence of dense substructures and low density channels *on small scales* can affect the efficiency of momentum- and energy injection into the larger-scale ISM and show how this may affect subgrid models that couple the unresolved small-scale energy-input to the resolved larger scales in numerical simulations as well as SN-driven turbulence.

In a recent paper (Romano et al., 2025a) we introduced the SISSI (Supernovae In a Stratified, Shearing ISM) simulations, in which we study the evolution of SNRs in a realistic galactic environment. There we have found that, while the dynamics of young and small SNRs are well described by the simple analytic models based on SNe exploding in a uniform, stationary ISM, once they reach a certain age ($\gtrsim 1\,\mathrm{Myr}$) and size ($\gtrsim 100\,\mathrm{pc}$) SNRs start being affected by all of the external processes mentioned above. Thus, in order to better understand the dynamics of such large and old SNRs, a comprehensive model that takes all of these effects into account is needed.

In this paper we develop a simple analytic model for the dynamics of SNRs in complex environments, taking into account the lessons learned from the SISSI simulations (Romano et al., 2025a). The model aims to lay out the theoretical foundations for the study of SNRs in complex geometries and serve as a simple tool for exploring the effects of previously unexplored phenomena on SNR dynamics, without the need of computationally challenging and expensive numerical simulations. To achieve this goal we aimed to formulate the model in a modular way, that easily allows for the

Table 2.1: Constants in Eq. 2.5 as function of the adiabatic index γ.

	c_0	c_1	c_2
Value	$\frac{\gamma-1}{2(2\gamma-1)}$	$\frac{3}{2}(\gamma+1)^2$	$3+\frac{4\gamma}{\gamma+1}$
Value ($\gamma = 5/3$)	1/7	32/3	11/2

inclusion of new phenomena.

The remainder of this paper is organized as follows. In Sec. 2.1 we describe our model and evaluate how well it reproduces a number of well established results in Sec. 2.2. In Sec. 2.3 we apply the model to a number of complex settings, in order to investigate their individual effects on SNR evolution. We close in Sec. 2.4 by discussing how these individual effects might conspire to affect the dynamics of SNRs in a realistic galactic setting. In the Appendix we provide some additional background to some aspects of our model.

2.1 Blastwave model

We develop a model for the expansion of a blastwave powered by central energy- and mass-injection. The blastwave is expanding into a medium described by arbitrary density-, velocity- and (gravitational) acceleration fields, denoted by $\rho_0(\vec{r},t)$ $\vec{v}_{\rm ext}(\vec{r},t)$ and $\vec{g}(\vec{r},t)$, respectively. Our model solves the blastwave equation of motion (Ostriker & McKee, 1988) using the thin-shell and sector approximations (Laumbach & Probstein, 1969), which follows the one-zone dynamics of a shell-segment per unit angle, i.e. along a single streamline, by assuming that all of the swept-up mass along the streamline is incorporated into an infinitesimally thin shell. Similarly to other models using the thin-shell approximation (e.g. Bisnovatyi-Kogan & Silich, 1995; Palouš et al., 2020; Jiménez et al., 2024) we model the curving of streamlines due to normal accelerations, but instead of requiring to evolve the whole shock-surface simultaneously, we opt for an exclusively local approach.

The expanding shell segment originates from the explosion center $\vec{r}_{\rm expl}$ and is associated with its initial expansion direction $\hat{e} = (\sin\theta\cos\phi, \sin\theta\sin\phi, \cos\theta)$. We use a HEALPIX tesselation of the unit sphere (Górski et al., 2005) to uniformly sample all directions.

The dynamics of the shell-segments traced by their position $\vec{r}_{\rm s}(t)$, expansion velocity $\vec{v}_{\rm s}(t)$, mass $M(t)$ and energy $E(t)$ are described by the following set of equations

$$\dot{M} \equiv \dot{M}_{\rm in} + \dot{M}_{\rm sw} = \dot{M}_{\rm in} + \rho_0 \vec{\Sigma}\cdot\vec{v}_{\rm s} \ , \tag{2.1}$$

$$\frac{\mathrm{d}}{\mathrm{d}t}(M\vec{v}_s) = \Delta P\,\vec{\Sigma} + M\left(\vec{g} - \dot{\vec{v}}_{\rm ext}\right) + \dot{p}_{\rm in}\vec{n} \ , \tag{2.2}$$

$$\dot{E} = \dot{E}_{\rm in} - \dot{E}_{\rm cool} + M\vec{g}\cdot\vec{v}_{\rm s} \ , \tag{2.3}$$

$$\dot{\vec{r}}_{\rm s} = \vec{v}_s + \vec{v}_{\rm ext} \ , \tag{2.4}$$

where $\dot{M}_{\rm in}$, $\dot{E}_{\rm in}$ and $\dot{p}_{\rm in}$ are the central mass-, energy- and momentum-injection rates, $\dot{M}_{\rm sw}$ is the incorporation rate of swept-up mass, $\dot{E}_{\rm cool}$ is the energy dissipation rate due to radiative cooling $\vec{\Sigma} = \mathrm{d}\vec{A}/\mathrm{d}\Omega$ is the (outward-) oriented surface area and $\vec{n} = \vec{\Sigma}/\left\|\vec{\Sigma}\right\|$ is the outward-pointing normal vector of the shell-surface.

We note that in the sector approximation volumetric quantities such as energy, mass and momentum are to be understood *per unit solid-angle*, i.e. $E = \mathrm{d}E/\mathrm{d}\Omega$. For brevity of notation we will omit this distinction, except where it could lead to confusion.

The pressure gradient force $\vec{F}_{\Delta P} = \Delta P \, \vec{\Sigma}$ is evaluated using the formalism of Laumbach & Probstein (1969) which leads to the expression

$$\Delta P = c_0 \left[c_1 \frac{E}{3\delta V} + 3\rho_0 v_\mathrm{s}^2 + (k_\rho - c_2) \frac{M \, v_\mathrm{s}^2}{3\delta V} \right] \ , \tag{2.5}$$

where the constants c_i are listed in Tab. 2.1,

$$k_\rho = -\frac{\mathrm{dlog}\, \rho_0}{\mathrm{dlog}\, r_\mathrm{s}} \ , \tag{2.6}$$

and we made the substitution $r_\mathrm{s}^3 \to 3\,\delta V$ to account for more general geometry. Due to the gauge freedom of δV described below this expression is ill-defined, but since the shock surface is usually spherical in the situations where it is relevant and thus $\delta V \sim r_\mathrm{s}^3/3$ this is only a minor concern. The derivation of Eq. 2.5 is quite tedious and somewhat technical, so we direct the interested reader to the App. A.1 for more details. Radiative blastwaves are usually modeled by setting the adiabatic index $\gamma = 1$, which leads to $\Delta P \propto (\gamma - 1) = 0$, which justifies simply setting $\Delta P = 0$ once radiative cooling becomes dominant.

The central mass-, energy- and momentum-injection rates are linked

$$\dot{p}_\mathrm{in} = \alpha_\mathrm{p} \sqrt{2 \dot{M}_\mathrm{in} \dot{E}_\mathrm{in}} \ , \tag{2.7}$$

where α_p is a boost-factor that accounts for the coupling of the interior of the SNR to the shell. For adiabatic blastwaves, this coupling is explicitly accounted for with the pressure gradient force Eq. 2.5 and we can set $\alpha_\mathrm{p} = 1$, however Lancaster et al. (2024) have shown that radiative, continuously powered blastwaves approach a so-called *rapidly-cooling wind* solution, where the momentum injected into the shell is mediated by the hot interior, leading to slightly boosted momentum-injection with $\alpha_\mathrm{p} \sim 4$.

The energy dissipation rate due to radiative cooling is

$$\dot{E}_\mathrm{cool} = \chi \frac{\Lambda}{\mu^2} \rho_0 M \ , \tag{2.8}$$

where $\chi = (\gamma + 1) \, / \, (\gamma - 1)$ is the shock-compression ratio in the case of a strong shock and $\mu = 1.4 \, m_\mathrm{H}$ is the mean atomic weight. In adiabatic SNRs the post-shock temperature generally exceeds $10^6 \, \mathrm{K}$, so we can approximate the cooling rate as $\Lambda = 10^{-22} \, \Lambda_{6,-22} \, T_{\mathrm{s},\,6}^{-0.7} \, \mathrm{erg \ s^{-1} \, cm^3}$ (Oku et al., 2022), where $T_\mathrm{s} = 10^6 \, T_{\mathrm{s},\,6} \, \mathrm{K} = \tau \mu v_\mathrm{s}^2 / k_\mathrm{B}$ is the post-shock temperature, with $\tau = 2 \, (\gamma - 1) \, (\gamma + 1)^{-2}$.

For our models with cooling, we transition to the radiative stage by switching off cooling and pressure gradient forces and setting $\alpha_\mathrm{p} = 4$ once $\gtrsim 10 \, \%$ of the injected energy have been radiated away.

We note that in contrast to previous work (e.g. Palouš et al., 2020), we do not modify the dynamics once the shock velocity falls below the velocity dispersion of the ambient medium or the internal pressure falls below the ambient pressure, since simulations do not show any signs of modified dynamics past this point (Romano et al., 2024a, 2025a).

The surface area and its direction depend on the instantaneous geometry of the shock-surface, which either requires evolving the whole surface or a local parameterization of it in a neighborhood of each point – here we opt for the latter. The surface area can be computed from the local tangent vectors

$$\vec{\partial}_\theta = \frac{\partial \vec{r}_\mathrm{s}}{\partial \theta} \qquad \vec{\partial}_\phi = \frac{1}{\sin(\theta)} \frac{\partial \vec{r}_\mathrm{s}}{\partial \phi} \ , \tag{2.9}$$

which are known at $t = 0$ and where we divide out the constant $\sin(\theta)$ for regularity near the poles[1]. The surface element can be obtained by taking their vector product

$$\vec{\Sigma}(t) = \vec{\partial}_\theta \times \vec{\partial}_\phi. \tag{2.10}$$

We evolve the tangent vectors by switching the order of differentiation

$$\dot{\vec{\partial}}_i = \partial_i \dot{\vec{r}}_\mathrm{s} = \partial_i \vec{v}_\mathrm{s} + \vec{\nabla}\vec{v}_\mathrm{ext} \cdot \vec{\partial}_i, \tag{2.11}$$

where the external velocity gradient $\vec{\nabla}\vec{v}_\mathrm{ext}$ is known a priori, and $\partial_i \vec{v}_\mathrm{s}$ is evolved along the flow making use of

$$\frac{\mathrm{d}}{\mathrm{d}t}\partial_i \vec{v}_\mathrm{s} = \partial_i \dot{\vec{v}}_\mathrm{s}(\vec{r}_\mathrm{s}, \vec{v}_\mathrm{s}), \tag{2.12}$$

evaluated by approximating the local on-surface acceleration gradient using finite differences. In particular we evaluate the acceleration from eq. 2.2 by shifting the position, velocity and surface are element by the tiny increments

$$\vec{r}_s \to \vec{r}_s \pm \epsilon\vec{\partial}_i \qquad \vec{v}_s \to \vec{v}_s \pm \epsilon\partial_i\vec{v}_\mathrm{s} \qquad \vec{\Sigma} \to \vec{\Sigma} \pm \epsilon \left\|\vec{\Sigma}\right\| \hat{e}_i, \tag{2.13}$$

where $\hat{e}_i = \vec{\partial}_i / \left\|\vec{\partial}_i\right\|$, and we approximated the local curvature radius with the length of the tangential vector for closure. We assume that all other quantities (M, E, etc.) remain unchanged by a small shift along the surface and we choose $\epsilon \sim 10^{-8}$ for it to be sufficiently small but not so small as to be dominated by numerical noise.

Finally, we define[2] the local volume-element as

$$\delta V = \frac{1}{3}(\vec{r}_s - \vec{r}_\mathrm{expl}) \cdot \vec{\Sigma}, \tag{2.14}$$

where we allow the explosion center $\vec{r}_\mathrm{expl}(t)$ to move as a function of time to model cases where it is not stationary, such as a star cluster following a circular orbit in a galactic disk.

2.1.1 Initial Conditions

Our model is general enough to describe a variety of different types of blastwaves, such as SNe, stellar winds and active galactic nuclei, which may require different initial conditions as well as models for their environment. Here we focus on SN-driven SBs, which begin to expand following a central point-explosion that deposits a large amount of energy E_0 and mass M_0 at $t = 0$. Due to the spherical symmetry $\vec{\Sigma} = r_\mathrm{s}^2\,\hat{e}$, where r_s is the shock radius. Regularity of the solution at $r_\mathrm{s} = 0$ requires the terms in $\Delta P\, r_\mathrm{s}^2$ that are $\propto r_\mathrm{s}^{-1}$ to cancel as $r_\mathrm{s} \to 0$, which leads to $(r_\mathrm{s}, v, M, E) = (0, \sqrt{cE_0/M_0}, M_0, E_0)$, where $c = c_1/(c_2 - k_\rho)$.

Despite this cancellation, we avoid numerical problems due to division by zero, by starting our calculation from a slightly advanced state with $r_\mathrm{s} \gtrsim 0$.

2.1.2 Breakdown of the model

While the model is applicable under a wide range of conditions, there are regimes in which it ceases to yield physically meaningful results. Below we summarize common causes of breakdown and their physical interpretation.

[1] This factor only enters in surface-integrals where now $\Delta\Omega = \sin(\theta)\,\Delta\theta\Delta\phi$.

[2] There is some freedom in the definition of the local volume element. For instance, by applying the divergence theorem the dot-product of any function $\vec{F}$ with $\mathrm{div}\,\vec{F} = 1$ with $\vec{\Sigma}$ defines a viable volume-element. The equivalence class of volume-elements corresponds to such functions differing only by a total derivative on the surface.

In models including gravity, the shock expansion may reverse and lead to collapse. In this situation, where $\vec{v}_\mathrm{s} \cdot \vec{\Sigma} < 0$, physically we expect the shock to stop sweeping up mass. To prevent a formal breakdown of the model, we set $\dot{M}_\mathrm{sw} = 0$. If the shock subsequently re-expands, care must be taken to avoid double-counting material that may have been swept up previously.

Provided the surface normal initially points outward, its topological properties ensure that it remains outward-facing unless it undergoes a continuous transition to an inward orientation, which requires passing through a singular point with $\left\|\vec{\Sigma}\right\| = 0$. Using Eq. 2.11, the time evolution of the surface normal is given by

$$\frac{\mathrm{d}}{\mathrm{d}t}\vec{\Sigma} = \left(\vec{\nabla} \cdot \dot{\vec{r}}_\mathrm{s} - \left(\vec{\nabla}\dot{\vec{r}}_\mathrm{s}\right)^\mathrm{T}\right)\vec{\Sigma} \,, \tag{2.15}$$

which shows that converging flows within the tangent plane of the shock can drive $\vec{\Sigma}$ to zero. We interpret this as the crossing of neighboring streamlines. Beyond this point the local description is no longer valid. Physically, such behavior may correspond to strong compression, or even collapse, of swept-up material and it may therefore be of astrophysical interest to identify where this behavior occurs.

Finally, in certain setups – such as an adiabatic shock expanding into a medium of finite mass – the shock velocity can diverge in finite time (Laumbach & Probstein, 1969; Koo & McKee, 1990). The appearance of divergent or otherwise unphysical quantities typically signals the breakdown of one or more underlying assumptions, such as neglected physics (e.g., radiative cooling or gravity) or an idealized environment, and must be evaluated on a case-by-case basis.

2.2 Notable limits

Here, we analytically confirm that our model reproduces the behavior predicted by many previous studies in the appropriate limits. We first take various analytic limits in Sec. 2.2.1 before comparing them to the results of a numerical integration of Eq. 2.2 in Sec. 2.2.2.

2.2.1 Analytic Considerations

Ejecta-dominated phase

Shortly after the central point-explosion, the SNR expands with an almost constant speed until the swept-up mass becomes comparable to the mass of the ejecta (Truelove & McKee, 1999). In our model this behavior is recovered since for small radii $r_\mathrm{s} \ll (M/\rho_0)^{1/3}$ the acceleration is dominated by terms in $\Delta P\, r_\mathrm{s}^2$ that are $\propto r_\mathrm{s}^{-1}$, i.e.

$$\dot{v}_\mathrm{s} \sim \frac{c_0}{r_\mathrm{s}}\left[c_1 \frac{E}{M} + (k_\rho - c_2)\, v_\mathrm{s}^2\right] \,, \tag{2.16}$$

which rapidly drives v_s towards the constant speed $v_\mathrm{ED} = \sqrt{cE/M}$, where $c = c_1/(c_2 - k_\rho)$.

Adiabatic phase

Once $r_\mathrm{s} \gtrsim (M/\rho_0)^{1/3}$ the contribution of the ram-pressure-terms in Eq. 2.2 can no longer be neglected. After a short transitionary period the solution approaches a powerlaw solution resembling the Sedov-Taylor-solution $r_\mathrm{s} = \xi_\mathrm{ST}\left(Et^2/\rho_0\right)^{1/5}$ (Sedov, 1959) for a single explosion, or an

energy-driven wind solution $r_\mathrm{s} = \xi_\mathrm{W} \left(\dot{E} t^3/\rho_0\right)^{1/5}$ (Weaver et al., 1977) for continuous energy injection. We note that for a better comparison with the spherically symmetrical models of Sedov (1959) and Weaver et al. (1977) in these expressions E refers to the total energy deposited over the whole sky, i.e. $E = \int (\mathrm{d}E/\mathrm{d}\Omega)\, \mathrm{d}\Omega$.

By plugging the respective expressions for $r_\mathrm{s}(t)$ into Eq. 2.2 and solving for ξ we can find the asymptotic solution in the respective regime. For the Sedov blastwave ($E = const.$) we find

$$\xi_\mathrm{ST} = \left\{ \frac{25 c_0 c_1}{8\pi \left[1 - 2c_0 \left(3 - (c_2 - k_\rho)/3\right)\right]} \right\}^{1/5} , \tag{2.17}$$

which for $\gamma = 5/3$ and $k_\rho = 0$ differs from the analytical solution only by $\lesssim 2.34\,\%$. For the continuously driven wind we obtain

$$\xi_\mathrm{W} = \left\{ \frac{25 c_0 c_1}{4\pi \left[7 - 9c_0 \left(3 - (c_2 - k_\rho)/3\right)\right]} \right\}^{1/5} , \tag{2.18}$$

which matches the solution found by Weaver et al. (1977) for $\gamma = 5/3$ and $k_\rho = 0$ with $1\,\%$ accuracy.

Radiative phase

In the absence of the pressure-gradient force and any external forces, the combined momentum of the blastwave and the ejecta is conserved as can be seen by integrating the EoM once:

$$\vec{p} = M \vec{v}_s = \vec{p}_\mathrm{sf} + \dot{\vec{p}}_\mathrm{in} t \ , \tag{2.19}$$

where p_sf is the momentum at the beginning of the radiative stage, also known as *shell formation* (see e.g. Kim & Ostriker, 2015; Oku et al., 2022; Romano et al., 2024a).

For a single explosion ($\dot{\vec{p}}_\mathrm{in} = 0$) the solution approaches the well-known momentum-conserving snowplow solution (Cioffi et al., 1988)

$$r_\mathrm{s} \rightarrow \left(\frac{3 p_\mathrm{sf}\, t}{\pi \rho_0} \right)^{1/4} , \tag{2.20}$$

while for continuously driven superbubbles ($\dot{\vec{p}}_\mathrm{in} > 0$) the solution approaches that of a momentum-driven wind (Oku et al., 2022; Lancaster et al., 2024)

$$r_\mathrm{s} \rightarrow \left(\frac{3 \dot{p}_\mathrm{in}\, t^2}{2\pi \rho_0} \right)^{1/4} . \tag{2.21}$$

As for the adiabatic case, these results are stated in terms of the total momentum (injection-rate) over the whole sky, for a better comparison with the literature.

Radiative SNRs are said to merge with the ISM once they have slowed down to the velocity dispersion of the ISM. The merging phase hosts rich phenomenology, such as SNR implosion (Slavin & Cox, 1992; Romano et al., 2024a), which requires a combined treatment of the bubble and the shell and is therefore outside of the model presented here. The merging timescale is

$$t_\mathrm{merge} = \left(\frac{3\, p_\mathrm{sf}}{256 \pi \rho_0 \sigma^4} \right)^{1/3} , \tag{2.22}$$

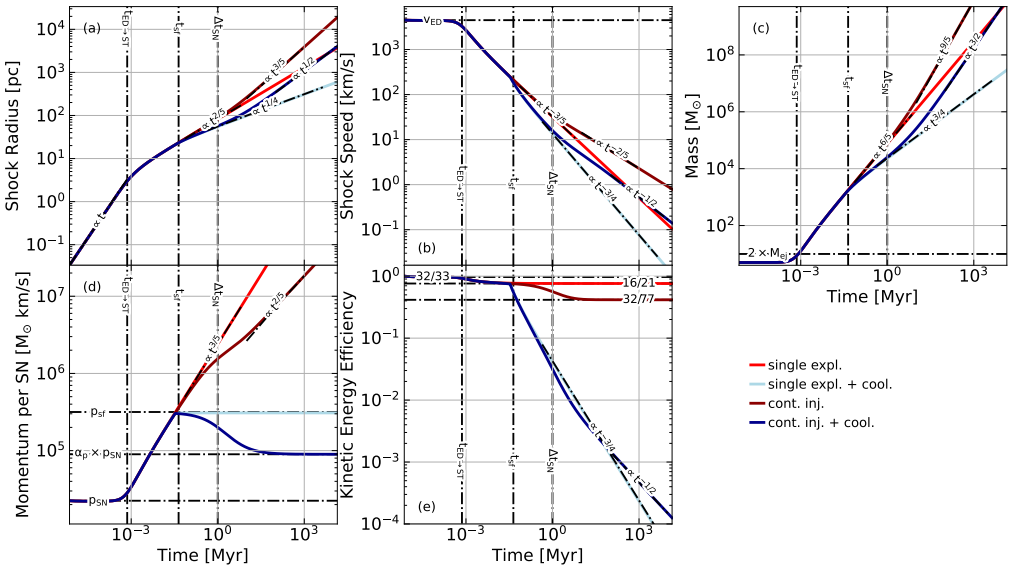

Figure 2.1: Time evolution of shock radius (a), shock speed (b), swept-up mass (c), momentum per SN (d), and energy efficiency (e) in the case of expansion into a stationary, uniform ambient medium for four different explosion models.

for a single explosion and

$$t_{\rm merge} = \left(\frac{3\,\dot{p}_{\rm in}}{32\pi\rho_0\sigma^4} \right)^{1/2} , \tag{2.23}$$

for a continuously driven SB. For a single SN in solar neighborhood conditions, this timescale is $\gtrsim 1\,$Myr (Romano et al., 2024a).

The thin-shell approximation is a one-zone representation of SNR evolution and therefore by definition is unsuited for describing the interplay of the cold shell and the hot bubble. In order to describe e.g. the pressure-driven snowplow phase, the emergence of the reverse shock or SN implosion after merging, a multi-zone extension to this model would be required, which explicitly models the coupled dynamics of the bubble-shell system. Such multi-zone calculations are outside the scope of this current work.

2.2.2 Numerical solutions

In order to verify that our model works as intended, we numerically integrate Eqs. 2.1 - 2.4 for a spherically-symmetric blastwave expanding into a stationary, uniform ambient medium. We consider four different cases:

1. A single SN at $t = 0$, without radiative cooling.
2. A single SN at $t = 0$, with radiative cooling.
3. A single SN at $t = 0$, followed by continuous injection of energy and mass at a fixed rate, without radiative cooling.
4. A single SN at $t = 0$, followed by continuous injection of energy and mass at a fixed rate, with radiative cooling ($\alpha_{\rm p} = 4$).

Figure 2.1 shows the temporal evolution of the shock-radius, shock-velocity, swept-up mass, momentum per SN, and the kinetic energy efficiency $f_{\rm kin} = E_{\rm kin}/E_{\rm inj}\,(t)$. We recover all the limiting cases highlighted in Sec. 2.2. Also highlighted are various characteristic timescales, such as the timescale for the transition from the ejecta-dominated to the adiabatic phase $t_{\rm ED\rightarrow ST}$ (Truelove & McKee, 1999) and the shell-formation timescale $t_{\rm sf}$ (Cioffi et al., 1988; Kim & Ostriker, 2015), which match the times at which the dynamics transition in our model quite well. The relatively high kinetic energy efficiencies ($> 0.22 - 0.27$ (Sedov, 1959; Weaver et al., 1977)) in the adiabatic cases are a well-known shortcoming of the thin-shell approximation (e.g. Koo & McKee, 1990).

We note that in many cases, by changing the variable of integration from time to the radius, Eqs. 2.1 - 2.4 admit analytical solutions in terms of special functions. The resulting solutions are so-called *unified* solutions (Truelove & McKee, 1999), which naturally interpolate between the limiting cases.

2.3 Application: SNRs in SISSI

We apply our model to quantify how a realistic galactic environment can affect the properties of SNRs. We particularly focus on ages $\gtrsim 1\,\mathrm{Myr}$, where our numerical simulations have begun to deviate from previous analytical models (Romano et al., 2025a). We consider three different explosion models:

1. A single SN explosion (SN).
2. An SB powered by 1 SN every $\Delta t_{\rm SN} = 1\,\mathrm{Myr}$ (SB).
3. A starburst powered by 1 SN every $\Delta t_{\rm SN} = 100\,\mathrm{yr}$ (StB).

Each SN injects a total energy of $E = 10^{51}\,E_{51}\,\mathrm{erg}$ and a mass of $M_{\rm ej} = M_{\rm ej,\,0}\,\mathrm{M}_\odot$, corresponding to a momentum of $p_{\rm SN} \sim 10^4\,p_4\,\mathrm{M}_\odot\,\mathrm{km\ s^{-1}}$ across the whole sky. For convenience we introduce $\Delta t_6 = \Delta t_{\rm SN}/\mathrm{Myr}$ and $\dot{p}_{\rm in} = 10^4\,\dot{p}_4\,\mathrm{M}_\odot\,\mathrm{km\ s^{-1}\,Myr^{-1}}$. All models include radiative cooling.

For the environmental effects that might affect SNR evolution we consider vertical stratification, galactic rotation and the effect of dense substructures. To obtain an intuition for each, we first consider each effect separately, before discussing their combined effect in concert.

2.3.1 Vertical stratification

Analytic considerations

The case of an adiabatic blastwave expanding into a vertically stratified atmosphere has been studied extensively using very similar methods as ours (e.g. Kompaneets, 1960; Laumbach & Probstein, 1969; Sakashita & Morita, 1977; Koo & McKee, 1990). These studies find that after the shock has reached a height exceeding a few scale heights, it is re-accelerated and approaches an infinite speed in finite time. This seemingly unphysical behavior has been attributed to a separation of the bulk of the swept-up mass from the shock, which is moving decreasing amounts of material, leaving most of the swept-up mass behind. Indeed, Koo & McKee (1990) have shown that a careful treatment of the dynamics of the swept-up mass reveals that it asymptotically approaches a finite speed in line with the expectation from energy-conservation.

While these considerations accurately describe the dynamics of adiabatic blastwaves, most astrophysical blastwaves are expected to cool long before they can be affected by vertical stratification.

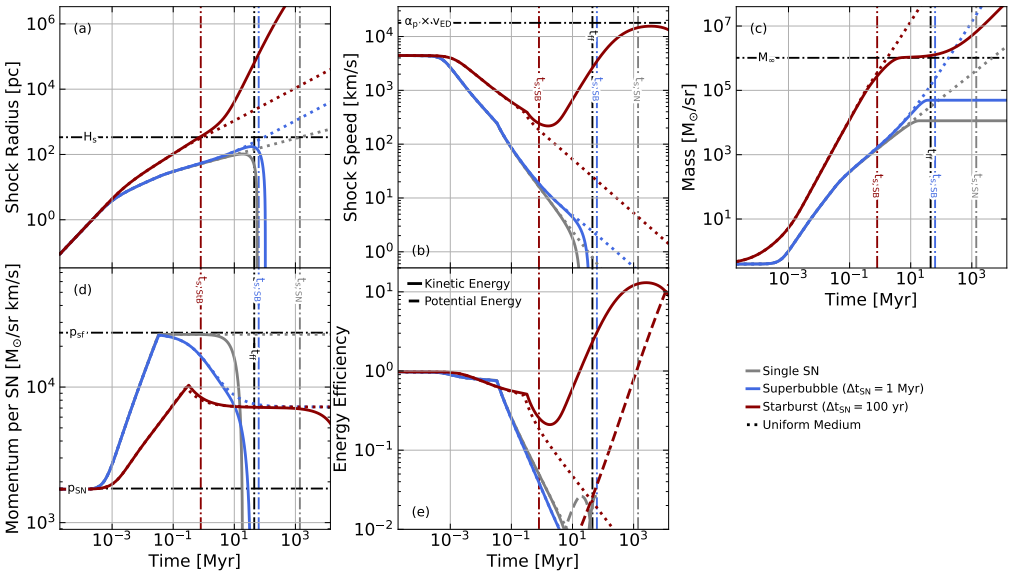

Figure 2.2: Same as Fig. 2.1 for different models in a vertically stratified atmosphere. For comparison, dotted lines corresponding to the same models expanding into a uniform medium are shown. Dash-dotted lines depict various characteristic scales. Both the single SN and the SB stall without breaking out of the galactic disk within about a free-fall timescale, due to the effect of gravity. Only the starburst can resist the gravitational field of the disk and drive a galactic wind.

Moreover, blastwaves breaking out of the galactic disk are subject to the galaxy's gravitational pull, which can keep shocks from leaving the galactic ecosystem (Romano et al., 2025b). However, so far these effects have received only little attention (Bisnovatyi-Kogan & Silich, 1995; Orr et al., 2022; Jiménez et al., 2024).

To address this gap, we consider the vertical expansion of a blastwave from the midplane of an isothermal slab in vertical hydrostatic-equilibrium. The density profile and gravitational acceleration are given by

$$\rho_0(z) = \rho_{\rm mp} \cosh^{-2}\left(\frac{z}{H_{\rm s}}\right) , \tag{2.24}$$

$$g_z(z) = -2\frac{\sigma^2}{H_{\rm s}} \tanh\left(\frac{z}{H_{\rm s}}\right) , \tag{2.25}$$

where

$$H_{\rm s} = \frac{\sigma}{\sqrt{2\pi G \rho_{\rm mp}}} \sim 338\,\sigma_1 n_0^{-0.5}\,{\rm pc} \tag{2.26}$$

is the vertical scale height, $\sigma = 10\,\sigma_1\,{\rm km\ s^{-1}}$ is the velocity disperion of the ISM and $\rho_{\rm mp} = \mu\, n_0\,{\rm cm^{-3}}$ is the midplane gas density.

The mass that is swept up by a blastwave expanding into such a stratified atmosphere asymptotically approaches a finite value

$$\begin{aligned} M_\infty &= \int_0^\infty \rho_0(z)\, z^2 {\rm d}z \\ &= \frac{\pi^2}{12}\rho_{\rm mp} H_{\rm s}^3 \sim 10^6\,\sigma_1^3\, n_0^{-1/2}\,{\rm M}_\odot\ . \end{aligned} \tag{2.27}$$

Effects due to the vertical stratification are expected to become noticeable once the blastwave

radius becomes comparable to the scale height at

$$t_\mathrm{s} \sim 1.4\,\sigma_1^4\,n_0^{-0.87}\,E_{51}^{-0.93}\,\mathrm{Gyr} \quad (\Delta t_\mathrm{SN} \to \infty)\,, \tag{2.28}$$

$$t_\mathrm{s} \sim 294\,\sigma_1^2\,n_0^{-0.5}\,\dot{p}_4^{-0.5}\,\mathrm{Myr} \quad (\Delta t_\mathrm{SN} \ll t_\mathrm{s})\,, \tag{2.29}$$

which already indicates that for SNRs powered by a small number of SNe, vertical stratification rarely plays a big role.

However, gravity becomes relevant much earlier. For $r_\mathrm{s} \ll H_\mathrm{s}$ the gravitational acceleration is $\propto r_\mathrm{s}/H_\mathrm{s}$, while the acceleration due to inertia is $\propto v_s^2/r_\mathrm{s}$, which indicates that the expanding blastwaves will stall without reaching the scale-height within a free-fall timescale

$$t_\mathrm{ff} = \sqrt{\frac{3\pi}{32G\rho}} \sim 44.9\,n_0^{-0.5}\,\mathrm{Myr}\,, \tag{2.30}$$

unless they are powerful enough to break out on a much shorter timescale $t_\mathrm{s} \ll t_\mathrm{ff}$. Yet, even if the shock manages to break out, unless the blastwave is continuously powered by a sufficiently powerful source, it will stall and fall back onto the galactic disk within $\sim t_\mathrm{ff}$ once it has slowed down sufficiently, i.e. $v_\mathrm{s} \lesssim \sigma$.

These considerations imply that shocks can only break out if

$$E_{51} \gg 40\,\sigma_1^{4.3}\,n_0^{-0.4} \quad (\Delta t_\mathrm{SN} \to \infty)\,, \tag{2.31}$$

$$\frac{p_4}{\Delta t_6} \gg 43\,\sigma_1^4 \quad (\Delta t_\mathrm{SN} \ll t_\mathrm{s})\,, \tag{2.32}$$

i.e. if $\gtrsim 40$ SNe explode within $\sim 1\,\mathrm{Myr}$. Moreover, as Romano et al. (2025b) have shown, these shocks cannot escape the gravitational potential of the disk unless the SN-rate exceeds $\sim 1\,\mathrm{SN}$ per $100\,\mathrm{yr}$. Such SNRs that break out, but do not drive outflows might be interpreted as driving fountain flows.

This result has immediate consequences for the interpretation of numerical simulations with insufficient resolution to resolve individual SNe. In such simulations, one might resort to feedback models, that consider the combined effect of many SNe. In these models, if the number of SNe injected per feedback event exceeds these thresholds, the majority of feedback events are expected to break out of the disk, leading to unphysical outflows. We caution simulators that the feedback energy injections should be sufficiently spaced out in time to reduce the impact of such numerical artifacts.

We note that at large distances from the midplane $z \gg 10 - 100\,H_\mathrm{s}$ the isothermal slab model becomes increasingly unrealistic, once the mass-contributions of the circumgalactic medium become important and the gravitational field starts to drop off due to the finite size of the galaxy.

These considerations suggest that for the SNRs in the SISSI simulations (Romano et al., 2025a), vertical stratification might be negligible, since the simulated time span of $t_\mathrm{SISSI} = 10\,\mathrm{Myr}$ is shorter than the free-fall timescale for typical densities of $n_0 \lesssim 10$.

Numerical validation

Figure 2.2 shows the dynamical evolution of the shock radius, the shock speed, the swept-up mass, the momentum per SN and the kinetic- and potential energy efficiencies per unit injected energy for the part of different blastwave models expanding vertically into a stratified medium with finite mass.

The single SN and the SB model do not manage to break out from the midplane, due its strong gravitational pull, which starts to significantly affect the expansion momentum and speed after

$\sim 1/4\, t_{\rm ff}$. The blastwaves stall after $\sim 1/2\, t_{\rm ff}$ and $\sim t_{\rm ff}$, in the SN and the SB cases, respectively, at which point their expansion velocity becomes negative and they begin to fall back onto the disk. These timescales are short enough to potentially influence the dynamics and geometry of SNRs in the SISSI simulations.

The starburst model is powerful enough to overcome the gravitational potential and drive a galactic wind. After breaking out of the disk, the mass encountered by the shock is negligible, while the momentum keeps growing at a constant rate, leading to a constant acceleration. However, after $\sim 200\,$Myr the mass injected at the source, becomes comparable to the swept-up mass, and the gravitational force $\propto M$ begins to grow and overpower the constant force of the central starburst. We note however, that the assumptions of our model cease to be valid on these vast spatial and temporal scales.

The results shown in Fig. 2.2 confirm our analytical considerations and highlight the importance of the effects of radiative cooling and gravity for the dynamics of blastwaves in stratified media. While we have neglected the change in the surface area element in our analytical derivation, we confirm that the deviations from $\left\|\vec{\Sigma}\right\| = r_s^2$ are negligible before the onset of collapse. Moreover, these results support the finding in Romano et al. (2025a) that the minor axis of the simulated blastwaves tends to be aligned with the galactic polar / vertical direction, especially for the SNRs in the densest regions, where the free-fall timescale is more comparable to the simulated 10 Myr.

We note however, that the picture of a uniform galactic midplane in vertical hydrostatic equilibrium is a very simplified picture. Notwithstanding, e.g. low-density channels carved out by turbulence and previous generations of feedback, can create pathways through which weak SBs and even single SNe might be able to break out of the disk and contribute to the galactic fountain flow or galactic winds.

2.3.2 Galactic rotation

Analytic considerations

Observational evidence (Watkins et al., 2023) and theoretical studies (Bisnovatyi-Kogan & Silich, 1995; Jiménez et al., 2024) suggest that large SBs may be subject to galactic shear, which can stretch out their geometry along the rotation direction (Palouš et al., 2020). In the appendix of Romano et al. (2025a) we have presented a simple model for the deformation by galactic shear for the case of a structure of fixed size. According to this model, the volume of the structure is unaffected by the deformation, which becomes significant after $\sim 5-6\,\%$ of an orbit, corresponding to a time of

$$t_{\rm deform} \sim 0.065\, t_{\rm orb} \sim 4\, R_3\, V_{\rm rot,\,2}^{-1}\,{\rm Myr}\ , \tag{2.33}$$

that is similar to the typical timescale on which SNRs evolve. Here, $R = R_3\,$kpc is the galactocentric radius, $V_{\rm rot} = 100\, V_{\rm rot,\,2}\,{\rm km\ s^{-1}}$ is the galactic rotation speed and $t_{\rm orb} = 2\pi R/V_{\rm rot}$ is the orbital timescale.

However, in contrast to the deformation of a structure of fixed size, in the case of SNRs, the expanding motion may couple to the galactic rotation and affect the dynamics in non-trivial ways, that we explore in this section.

The velocity- and gravitational field corresponding to galactic rotation are

$$\vec{v}_{\rm ext} = V_{\rm rot}\hat{\vec{e}}_\varphi\,(\varphi)\ , \tag{2.34}$$

$$\vec{g} = -\frac{V_{\rm rot}^2}{R}\,\hat{\vec{e}}_R\,(\varphi)\ , \tag{2.35}$$

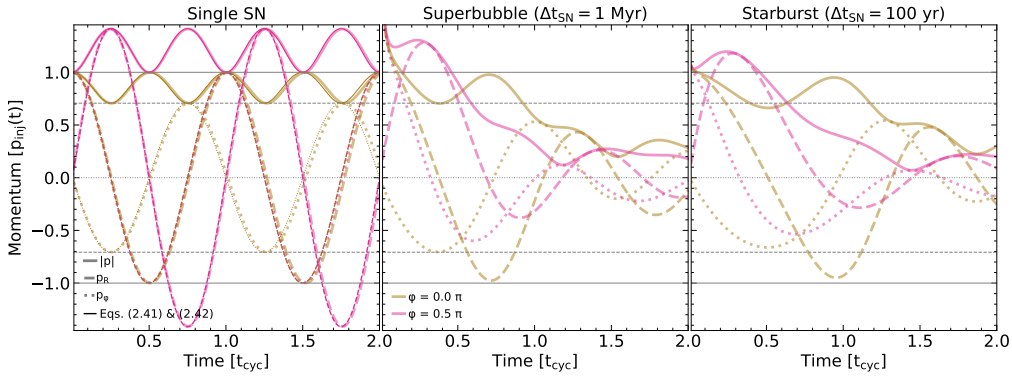

Figure 2.3: Time evolution of the momentum components of blastwaves expanding into a uniform medium subject to galactic rotation. Different panels correspond to the different explosion models. Solid (dashed, dotted) lines correspond to the magnitude (radial-, azimuthal component) of the momentum vector. In the first panel, thin lines depict the expectation the analytical considerations matching well with the numerical results. Horizontal lines correspond to integer multiples of the radial momentum $p_{\rm inj}$ and $p_{\rm inj}/\sqrt{2}$ of a model without shear.

where $\hat{\vec{e}}_\varphi$ and $\hat{\vec{e}}_R$ are the local unit vectors pointing in the (galactic) azimuthal, and radial direction, respectively, and φ is the azimuthal angle.

As the shell expands, its azimuthal angle changes, leading to an implicit time-dependence of $\vec{v}_{\rm ext}$ that enters into the equation-of-motion Eq. 2.2 through

$$\dot{\vec{v}}_{\rm ext} = \frac{{\rm d}\vec{v}_{\rm ext}}{{\rm d}\varphi}\dot{\varphi} = -\frac{V_{\rm rot}\left(V_{\rm rot}+v_{{\rm s},\,\varphi}\right)}{R}\hat{\vec{e}}_R\left(\varphi\right)\ , \tag{2.36}$$

where $v_{{\rm s},\,\varphi}$ is the azimuthal component of the expansion velocity.

Since the timescale for shear to affect the dynamics of an SNR is usually much longer than the shell-formation timescale, here we consider the dynamics of a radiative blastwave under the influence of galactic shear. The equation of motions for the azimuthal and radial momentum components can be written as

$$\dot{v}_{{\rm s},\,\varphi} = -\frac{\dot{M}}{M}v_{{\rm s},\,\varphi} - \frac{V_{\rm rot}}{R}v_{{\rm s},\,R} - \frac{v_{{\rm s},\,\varphi}v_{{\rm s},\,R}}{R} + \frac{\dot{p}_{{\rm in},\,\varphi}}{M}\ , \tag{2.37}$$

$$\dot{v}_{{\rm s},\,R} = -\frac{\dot{M}}{M}v_{{\rm s},\,R} + 2\frac{V_{\rm rot}}{R}v_{{\rm s},\,\varphi} + \frac{v_{{\rm s},\,\varphi}^2}{R} + \frac{\dot{p}_{{\rm in},\,R}}{M}\ , \tag{2.38}$$

where subscripts R and φ correspond to the (galactic) radial and azimuthal components, respectively.

Since the inertial term $\propto \dot{M}/M$ is $\propto v_{\rm s}^2/r_{\rm s}$ it decays faster than the terms $\propto V_{\rm rot}v_{\rm s}/R$ as the expansion slows down. Thus, we expect galactic rotation to become dynamically important when the two terms become comparable, i.e. once $v_{\rm s}/r_{\rm s} \sim V_{\rm rot}/R$ at

$$t_{\rm shear} \sim (8\pi)^{-1}\,t_{\rm orb} \qquad (\Delta t_{\rm SN}\to\infty)\,, \tag{2.39}$$

$$t_{\rm shear} \sim (4\pi)^{-1}\,t_{\rm orb} \qquad (\Delta t_{\rm SN}\ll t_{\rm shear})\,, \tag{2.40}$$

which are both comparable to the deformation timescale of the structure with fixed size.

The acceleration term $\propto v_{\rm s}^2/R$ is always subdominant since $r_{\rm s} \ll R$. Asymptotically, we can discard all terms except the term linear in $v_{\rm s}$. The resulting set of ordinary differential equations

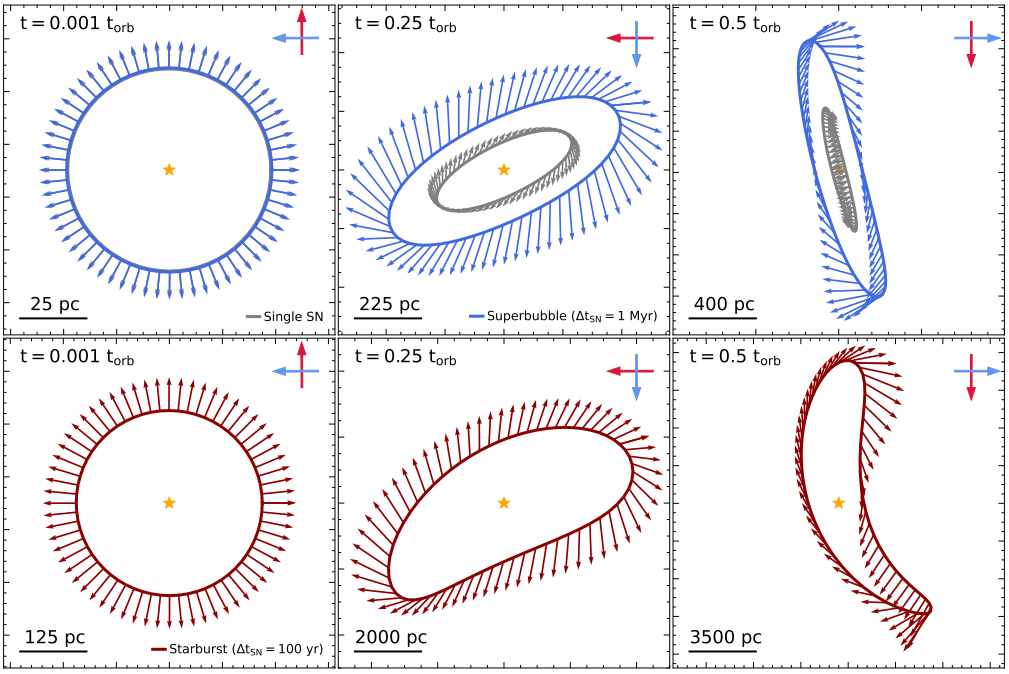

Figure 2.4: Slices through the xy-plane of the shock-surface of different blastwave models expanding in a uniform density medium ($n_0 = 1$) subject to galactic rotation ($R_3 = 8$, $V_{\mathrm{rot},\,2} = 2$). The velocity vectors on the surface are shown as arrows with arbitrary scaling. Top panels show the single SN and SB models; bottom panels show the starburst. Left, center and right panels show slices after 0.1 %, 1/4 and 1/2 of an orbit, respectively. Each panel has a compass pointing towards the galactic center (blue) and the direction of rotation (red). While the SNRs are initially spherically symmetric, after $t_{\mathrm{orb}}/4$ they are significantly stretched out with a pitch angle $\sim 30\,^{\circ}$. The velocity vectors clearly show signs of the epicyclic motion described by Eqs. 2.42 - 2.43. After $\sim t_{\mathrm{orb}}/2$ they cease to be star-shaped making it difficult to measure their geometric properties with our methods.

can be solved approximately, by assuming $R \sim const.$ and dropping the term $\propto v_{\mathrm{s}}^2/R$ and leads to a coupled harmonic oscillation (epicycles) of the momenta, with an oscillation frequency of

$$\kappa = 2\sqrt{2}\pi\, t_{\mathrm{orb}}^{-1}\ . \tag{2.41}$$

Due to the factor of 2 in the radial equation of motion the ratio of the amplitudes of the radial and the azimuthal momentum-oscillations is $p_{\mathrm{s},\,R}^{\mathrm{max}}/p_{\mathrm{s},\,\varphi}^{\mathrm{max}} = \sqrt{2}$.

We can estimate the functional shape of the oscillatory part of the motion by

$$p_{\mathrm{s},R}\,(t,\phi) \approx \sqrt{2}\,p_{\mathrm{s},\varphi}^{\mathrm{max}}\,(t,\phi)\,\cos\left(\kappa t - \phi\right)\ , \tag{2.42}$$

$$p_{\mathrm{s},\varphi}\,(t,\phi) \approx -p_{\mathrm{s},\varphi}^{\mathrm{max}}\,(t,\phi)\,\sin\left(\kappa t - \phi\right)\ , \tag{2.43}$$

where ϕ is the initial angle between the motion and the galactocentric radial direction and we assume, that at the onset of the oscillation, the direction of the motion in the co-rotating frame has hardly changed.

Thus in the case of a single explosion, we expect

$$p_{\mathrm{s},\varphi}^{\mathrm{max}}\,(t,\phi) \approx \frac{p_{\mathrm{sf}}}{\sqrt{1+\cos^2\left(\phi\right)}}\ , \tag{2.44}$$

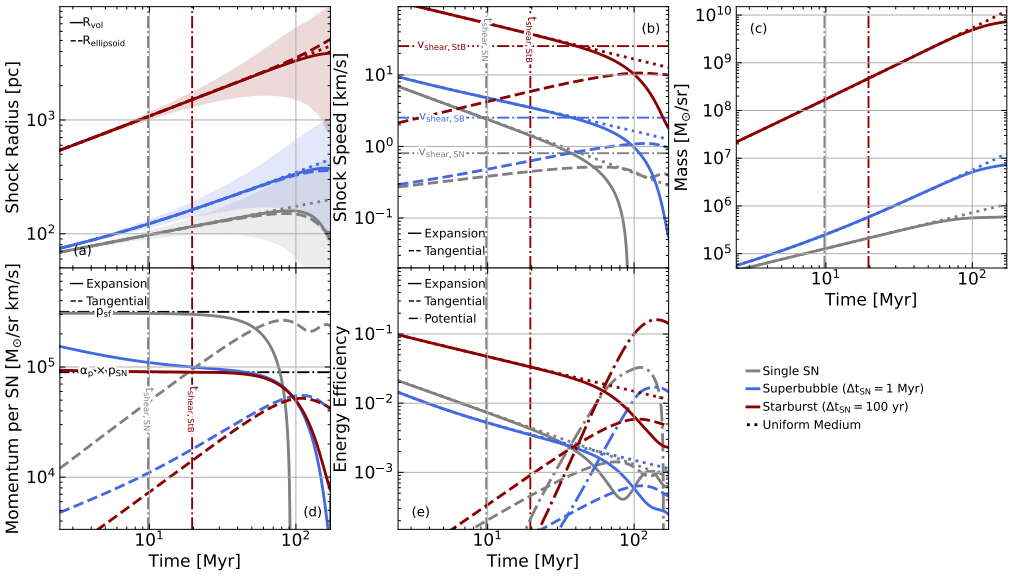

Figure 2.5: Same as Fig. 2.1 for different blastwave models expanding in a uniform density medium ($n_0 = 1$) subject to galactic rotation ($R_3 = 8$, $V_{\mathrm{rot},\,2} = 2$). For comparison, dotted lines corresponding to the same models expanding into a uniform medium without shear are shown. Dash-dotted lines depict various characteristic scales. In all models the net expansion falls below that of the models without shear from $\sim 2\,t_{\kappa,1} \sim 87\,\mathrm{Myr}$, despite the epicyclic boost received in certain directions. Instead, a significant amount of the expansion momentum is converted into tangential motion.

which ensures momentum conservation, in particular $p\,(t=0,\phi) = \sqrt{p_{\mathrm{s},R}^2 + p_{\mathrm{s},\varphi}^2} = p_{\mathrm{sf}}$.

The case of continuous momentum injection is significantly more complicated due to the deformation of the shock-surface. The complex time-dependence in the outward normal vector leads to a non-trivial coupling of the momentum-injection rate. Nonetheless, naïvely one might expect

$$p_{\mathrm{s},\varphi}^{\max}\,(t,\phi) \propto \dot{p}_{\mathrm{in}} t\ . \tag{2.45}$$

For the velocities this implies an oscillation around the expansion speed of an SNR expanding in a medium without shear. However, during the episodes where $\vec{v}_{\mathrm{s}}$ is tangential to the surface or even pointing inwards $\dot{M}_{\mathrm{sw}} \sim 0$ and the oscillation can assume an approximately constant velocity-amplitude for significant fractions of an orbit in the case of a single SN, while in the case of continuous injection the behavior depends on the relative contribution of the injected momentum, in particular the frequency of SN explosion Δt_{SN}.

The first such episode starts after around a quarter of an epicycle after $t_{\kappa,1} \sim \pi/2\kappa \sim t_{\mathrm{orb}}/4\sqrt{2}$. The average speed during this first oscillation oscillates can be approximated by the velocity at $t_{\kappa,1}$, yielding

$$v_{\kappa,1} \sim 4\,R_3^{-3/4}\,V_{\mathrm{rot},\,2}^{3/4}\,E_{51}^{0.23}\,n_0^{-0.28}\,\mathrm{km\ s^{-1}}\ , \tag{2.46}$$

in the case of a single SN and

$$v_{\kappa,1} \sim 4\,R_3^{-1/2}\,V_{\mathrm{rot},\,2}^{1/2}\,\left(\alpha_{\mathrm{p}} p_4/\Delta t_6\right)^{0.25}\,n_0^{-0.25}\,\mathrm{km\ s^{-1}}\ , \tag{2.47}$$

for continuous driving, leading to oscillations amplitudes $\sim 1\,\mathrm{km/s}$ for typical ISM conditions in the solar neighborhood.

In practice, due to the slightly different coupling of radial and azimuthal motions to the galactic shear, different parts of the shock surface will enter this oscillation at a different phase, leading to a phase-gradient. Due to the complex interplay of the shock-surface being deformed by galactic shear and the phase-gradient of the oscillation the velocity amplitude eqs. 2.46 and 2.47 do not, in general, correspond to the average expansion speed of the SNR.

Numerical validation

The dynamical evolution of the blastwave momentum over two epicycles in a uniform-density, shearing medium with a constant galactic rotation speed of 200 km/s at a distance of 8 kpc from the center of rotation is shown in Fig. 2.3. For each blastwave model, we track two representative points on the shock surface: one initially moving radially outward and one moving parallel to the galactic rotation.

For a single supernova, Eqs. 2.42 - 2.43 accurately capture the momentum evolution. The neglected term $\propto v^2/R$ introduces only a small phase shift that accumulates over multiple epicycles. Galactic shear slightly enhances the momentum in initially azimuthal directions, while it slightly reduces the total momentum in initially radial directions. In contrast, models with continuous energy injection only briefly exhibit oscillatory behavior before the momentum decays. After two epicycles, these models retain only $\sim 25\%$ of the injected momentum, indicating that the epicyclic response and the outward-directed injection counteract each other and reduce the overall efficiency of momentum coupling.

We illustrate the SNRs' morphological evolution through slices in the xy-plane shown in Fig. 2.4. All SNRs evolve from an initially spherical shape at $10^{-3}\,t_{\rm orb}$ to increasingly elongated geometries, reaching pitch angles on the order of $\sim 30^\circ$ by $t_{\rm orb}/4$. At this stage, the velocity field clearly exhibits the epicyclic motion predicted in Eqs. 2.42 - 2.43. In the single SN and SB models the geometry is quite similar suggesting that shear-induced epicyclic motion dominates their evolution. By contrast, the starburst develops a more strongly curved geometry. After $\sim t_{\rm orb}/2$ the SNRs cease to be star-shaped, at which point the ellipsoidal approximation used to characterize their geometry no longer applies.

We summarize the evolution of the different blastwave models in Fig. 2.5. Despite transient momentum enhancement in azimuthal directions, we find that galactic rotation suppresses the overall expansion. From $\sim 2\,t_{\kappa,1}$ onward, the remnant size falls below that of an equivalent model without shear, coinciding with a decline–and eventual reversal–of the net expansion speed and radial momentum. At the same time, the tangential momentum grows to values comparable to the initial blastwave momentum, leading to significant tangential motion, comparable to the expansion. This conversion might play an important role for blastwave-driven turbulence generation.

We characterize the blastwaves' geometric response to galactic shear in Figs. 2.6 and 2.7, showing their trajectories in shape phase-space and the time evolution of the pitch angle, respectively. The shape phase-space tracks the minor-to-major (a/c) and intermediate-to-major (b/c) axis ratios, while the pitch angle measures the orientation of the shock surface relative to the galactic rotation vector, with 90° pointing toward the galactic center and -90° toward the anticenter. All blastwaves begin as perfect spheres ($a/c = b/c = 1$). For reference, we show the evolution of a shearing sphere (Appendix D.3) in black.

Across all models, the blastwaves closely follow the shearing-sphere trajectory, confirming that shear largely governs their geometric evolution. More energetic explosions systematically evolve toward larger a/b ratios and retain larger pitch angles, reflecting their stronger resistance to shear-induced deformation. The deformation timescales predicted by Eqs. 2.39 - 2.40, indicated by star symbols, accurately capture the onset of deformation only for the starburst model. For

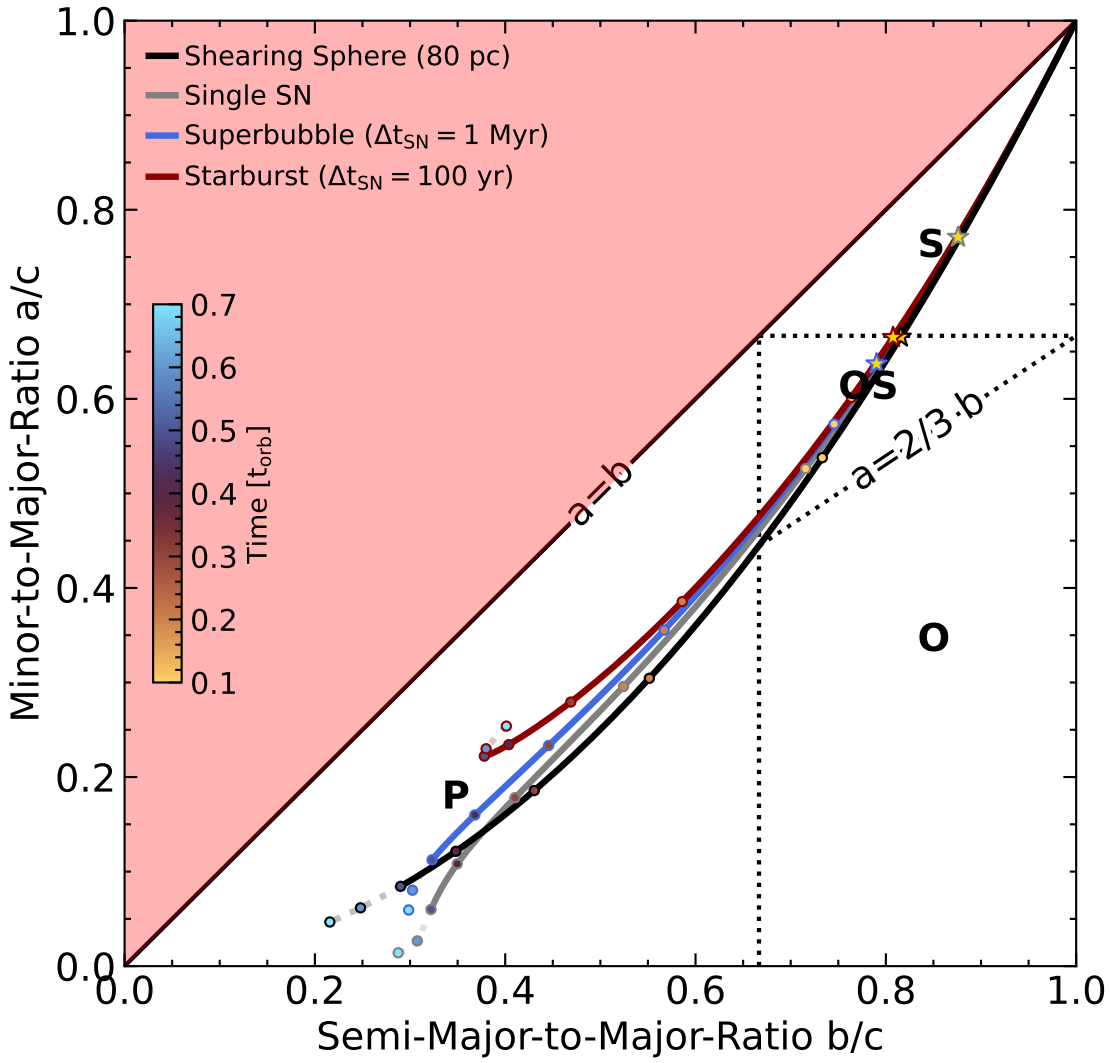

Figure 2.6: Evolutionary tracks in the shape phase-space of the different blastwave models expanding in a uniform density medium ($n_0 = 1$) subject to galactic rotation ($R_3 = 8$, $V_{\mathrm{rot},\,2} = 2$). In different parts of the phase space the SNRs are either spherical (S), oblate spheroids (OS), prolate (P) or oblate (O). The track of a shearing sphere with a constant radius of 80 pc is shown in black. The time at which the blastwaves are expected to cross the $a/c = 2/3$-line is shown as star markers. We also plot circle-markers color-coded with the time to provide a reference how long it takes to reach a given degree of deformation. The blastwaves starts out as perfect spheres and becomes increasingly prolate over time. The blastwave models roughly follow the track of the shearing sphere (no expansion), with a slight tendency of more powerful blastwaves towards larger a/b. After $t_{\mathrm{orb}}/2$ the measured lengths become increasingly unreliable and are thus shown as transparent, dotted lines.

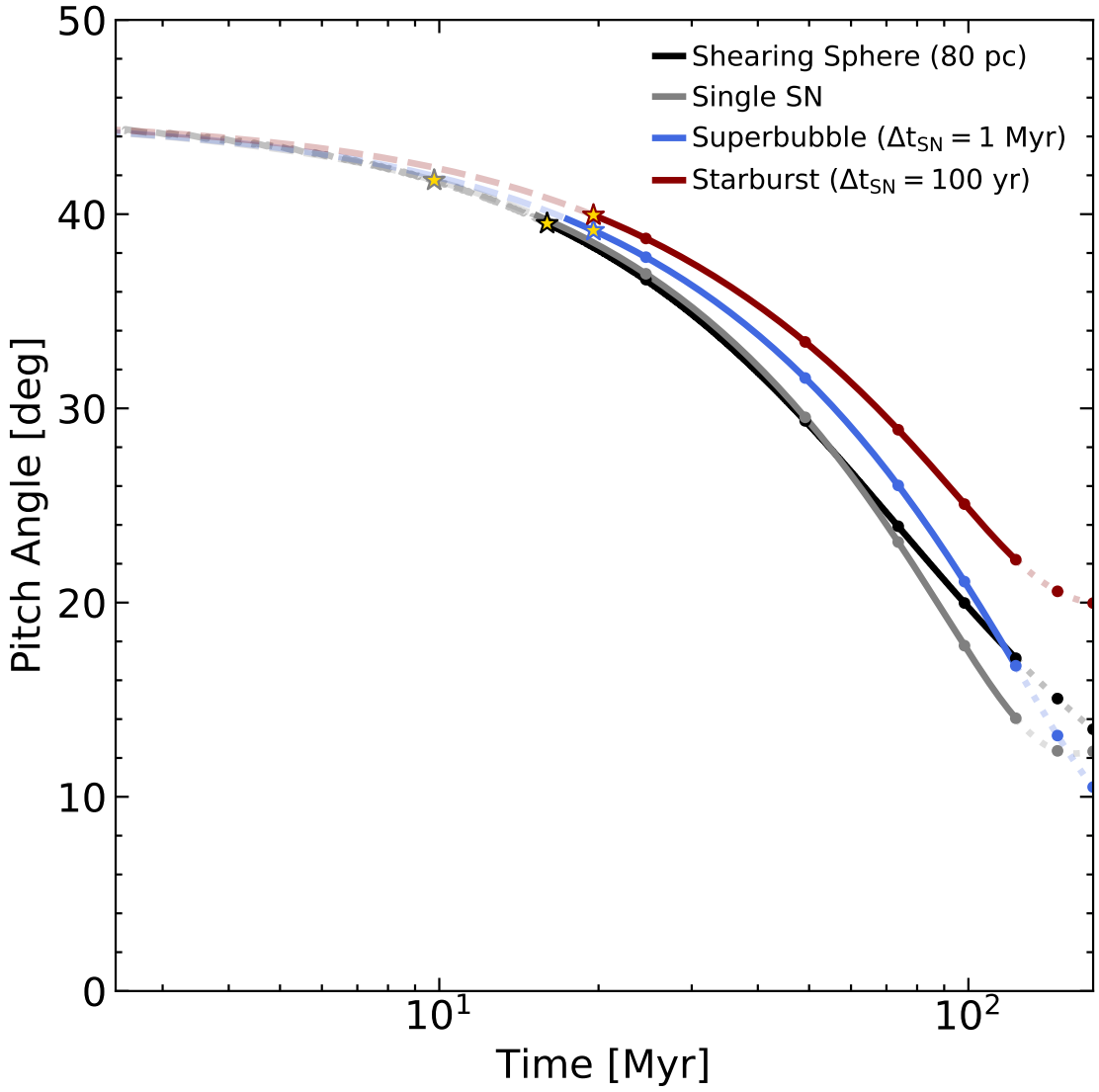

Figure 2.7: Time evolution of the pitch angle of the major axis of the different blastwave models expanding in a uniform density medium ($n_0 = 1$) subject to galactic rotation ($R_3 = 8$, $V_{\mathrm{rot},\,2} = 2$). For reference the pitch-angle of a shearing sphere with a constant radius of 80 pc is shown in black. The time at which the blastwaves are expected to cross the $a/c = 2/3$-line is shown as star markers. During the spherical phase ($a/c > 2/3$) the pitch angle is not very meaningful and is thus shown as transparent dashed lines. After $t_{\mathrm{orb}}/2$ the measured angles become increasingly unreliable and are thus shown as transparent, dotted lines. The pitch angle starts off near 45 ° and decays over time. The blastwaves roughly follow the pitch-angle evolution of the shearing sphere with a tendency towards larger pitch angles for more rapidly expanding models.

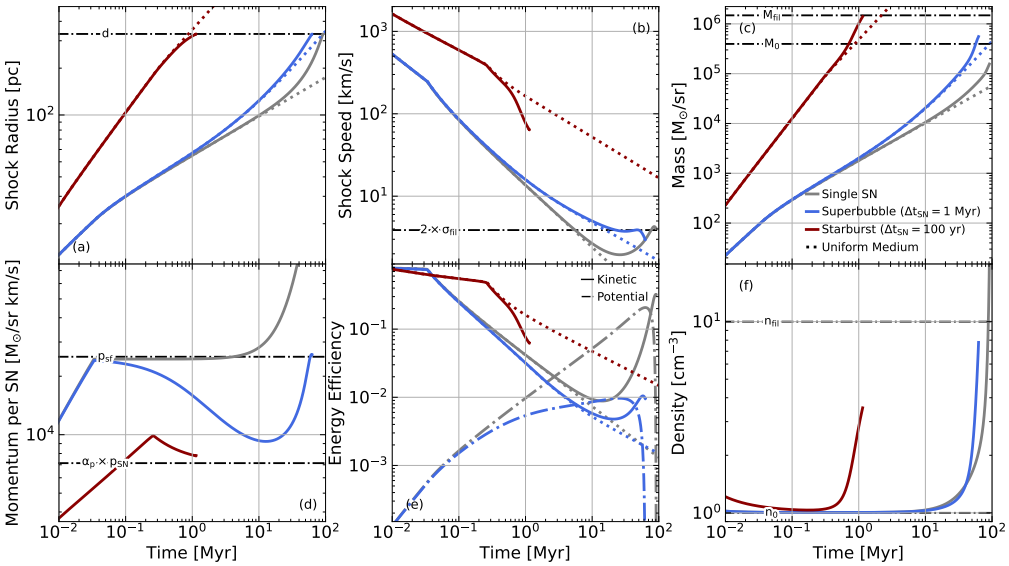

Figure 2.8: Same as Fig. 2.1 for different blastwave models approaching an overdense filament in a background medium ($n_{\mathrm{fil},\,0} = 10$, $T_{\mathrm{fil},\,2} = 6$, $d = 8\,\mathrm{r_{fil}}$, $n_0 = 1$). An additional panel (f) shows the average density to account for the environment's multi-phase nature. For comparison, dotted lines corresponding to the same models expanding into a uniform medium are shown. Dash-dotted lines depict various characteristic scales. Both the single SN and the SB are trapped in the filament's gravitational potential, while the starburst can overrun it. In all cases the average density increases towrds the filament's central density upon approach.

weaker explosions, they either under- or overestimate the deformation time, whereas the shearing-sphere model provides a more reliable reference. This behavior aligns with the expectation that sufficiently slow expansions should approach the shearing-sphere limit. Because Eqs. 2.39 - 2.40 do not depend on explosion parameters, their predictive power for realistic remnants remains limited.

At late times, $t \gtrsim t_{\mathrm{orb}}/2$, deviations from the shearing-sphere behavior become more pronounced. The weaker models fall below the shearing-sphere pitch-angle evolution, likely due to epicyclic contraction, while the shock surfaces themselves cease to be star-shaped. As a result, the ellipsoidal approximation breaks down, rendering both the inferred axis ratios and pitch angles increasingly unreliable, as reflected by the kinks in the shape phase-space trajectories.

2.3.3 Density structures

Analytic considerations

Many SNRs are observed to interact with dense structures in their environment (Hewitt & Yusef-Zadeh, 2009; Mayker Chen et al., 2023; Watkins et al., 2023). Models and simulations have addressed such interactions of SNRs with their immediate surroundings (Haid et al., 2016; Makarenko et al., 2023; Lau & Bonnell, 2025). Yet, models addressing the interaction of large SNRs with galactic scale structures, such as molecular filaments, spiral arms and massive clumps remain scarce.

We expect the sizes and separations of such structures to be on the order of the Jeans- and Toomre-lengths (Jeans, 1902; Toomre, 1964), which are approximately equal in a marginally stable

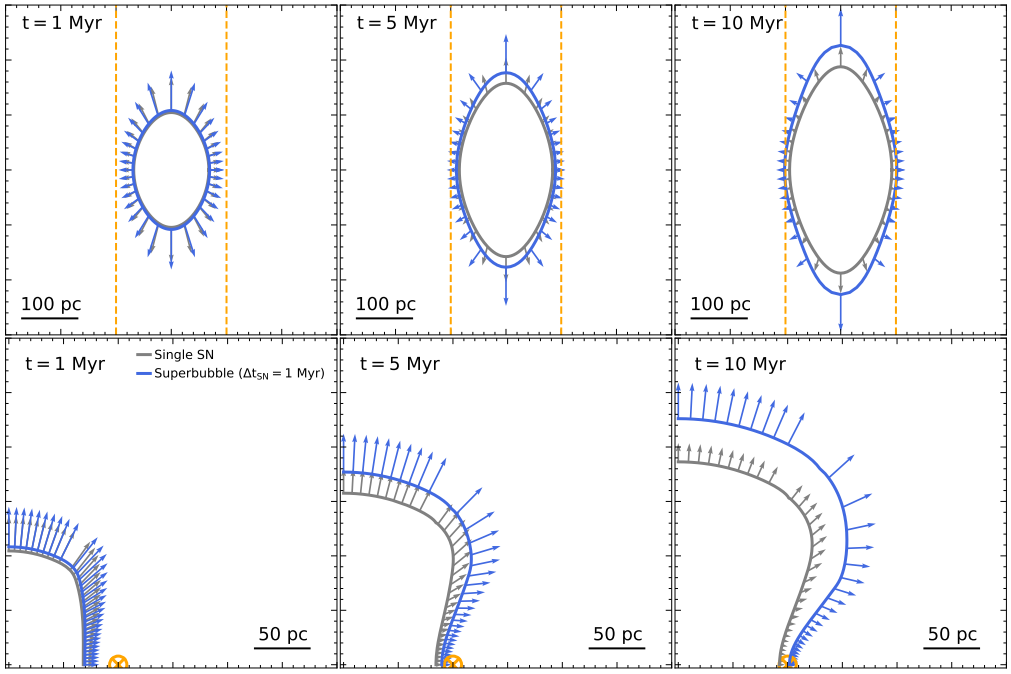

Figure 2.9: Slices through the shock-surface of different blastwave models expanding into the gap ($n_{\mathrm{gap},\,0} = 0.1$) between two filaments ($n_{\mathrm{fil},\,0} = 10$, $T_{\mathrm{fil},\,2} = 2.65$, $d_{\mathrm{fil}} = 200\,\mathrm{pc}$). The velocity vectors on the surface are shown as arrows with arbitrary scaling. Top (bottom) panels show slices through the xy- (yz-) plane. Left, center and right panels show slices after 1, 5 and 10 Myr, respectively. Already at 1 Myr, the SNRs are quite deformed by the geometry of the ISM. The ratio between the SNRs' extent parallel to the filaments and towards them grows in time reaching axis ratios $\sim 1/2$ by 5-10 Myr.

disk (Toomre, 1964),

$$\lambda_{\mathrm{J}} = \left(\frac{15\sigma^2}{4\pi G\rho}\right)^{1/2} \sim 926\,\sigma_1\,n_0^{-1/2}\,\mathrm{pc}\ . \tag{2.48}$$

On scales comparable to λ_{J}, the gravitational acceleration towards such a structure is of order

$$g_{\mathrm{J}} \sim \frac{\sigma^2}{\lambda_{\mathrm{J}}} \sim \frac{\sigma}{t_{\mathrm{ff}}}\ . \tag{2.49}$$

Slowly moving objects, with speeds $v \lesssim \sigma$ – located within about a Jeans-length of the overdensity – experience free-fall onto it, reaching an asymptotic velocity of order σ.

In what follows, we first consider the purely hydrodynamic interaction of a radiative blastwave with an overdensity, neglecting gravity. We then refine these estimates by including gravitational effects where necessary.

We consider a background medium of density n_0 containing an overdensity of the form $\delta, n_0, f(\vec{r})$, where $\delta \gg 1$ sets the overdensity contrast and $f(\vec{r})$ specifies its geometry. We describe the blastwave as momentum-driven, with total momentum

$$\vec{p}(t) \sim \vec{p}_{\mathrm{sf}} + \dot{\vec{p}}_{\mathrm{in}}\,t. \tag{2.50}$$

As the blastwave approaches the overdensity, it sweeps up an excess mass

$$M_\delta \sim \delta\,n_0\,\|\vec{\Sigma}\|\,\lambda_{\mathrm{J},\delta}\ , \tag{2.51}$$

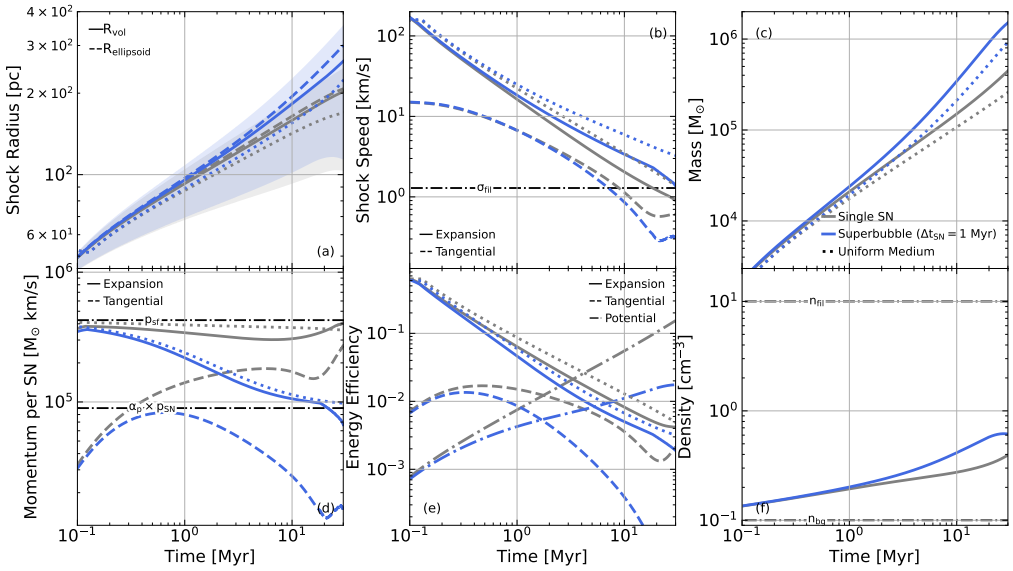

Figure 2.10: Same as Fig. 2.8 for different blastwave models expanding into the gap ($n_{\mathrm{gap},\,0} = 0.1$) between two filaments ($n_{\mathrm{fil},\,0} = 10$, $T_{\mathrm{fil},\,2} = 2.65$, $d_{\mathrm{fil}} = 200\,\mathrm{pc}$). For comparison, dotted lines corresponding to the same models expanding into a uniform medium with an ambient density matching the average density of the corresponding inhomogeneous model at each point in time. Dash-dotted lines depict various characteristic scales. At the same average density, the blastwaves in inhomogeneous media grow larger than those in homogeneous media as indicated both by the radius panel (a) and the mass panel (c).

where $\lambda_{\mathrm{J},\delta}$ denotes the characteristic size of the overdense structure. This contribution dominates over the background for distances

$$d \lesssim \delta\, \lambda_{\mathrm{J},\delta}\ . \tag{2.52}$$

In this regime, the additional mass contributions slow the blastwave in directions facing the overdensity relative to unperturbed directions, with a characteristic velocity ratio

$$\frac{v_\delta}{v_0} \sim \frac{M_0}{M_\delta} \sim \frac{d}{\delta\, \lambda_{\mathrm{J},\delta}}\ . \tag{2.53}$$

We estimate the time required for the overdensity to significantly decelerate the blastwave by comparing this effect to the approach time

$$t_d \sim \beta\, \frac{d}{v_0}\ , \tag{2.54}$$

where $\beta = 1/4$ $(1/2)$ for a single explosion (continuous momentum injection). We estimate the corresponding slowdown timescale to be comparable to the crossing time

$$t_\delta \sim \frac{\lambda_{\mathrm{J},\delta}}{v_\delta} \sim \frac{1}{\delta} \left(\frac{\delta\, \lambda_{\mathrm{J},\delta}}{d} \right)^2 t_d. \tag{2.55}$$

Blastwaves originating far from the overdensity ($d \gtrsim \delta\, \lambda_{\mathrm{J},\delta}$) therefore expand nearly isotropically, while those closer than $\sim \sqrt{\delta}\, \lambda_{\mathrm{J},\delta}$ experience noticeable deformation.

This anisotropic mass loading also biases density estimates inferred from swept-up mass and volume. Averaging over solid angle yields

$$\langle n \rangle \sim \frac{n_0\, \mathrm{d}\Omega_0 + (M_\delta / V_\delta)\ \mathrm{d}\Omega_\delta}{\mathrm{d}\Omega} \sim \frac{\mathrm{d}\Omega_0 + (\delta\, \lambda_{\mathrm{J},\,\delta}/d)\ \mathrm{d}\Omega_\delta}{\mathrm{d}\Omega} n_0\ , \tag{2.56}$$

showing that even a localized interaction with an overdensity can substantially boost the inferred mean density.

The above estimates neglect gravity and therefore break down once the blastwave slows to velocities comparable to the overdensity's velocity dispersion σ_δ, which sets the depth of its gravitational well. In this regime, the gravitational field dominates the dynamics, particularly near the bottom of the potential well, where self-gravity and collapse may become important on timescales of order the overdensity's free-fall time $t_{\mathrm{ff},\delta}$.

A sufficiently strong blastwave can nonetheless overrun the overdensity if its velocity remains larger than the σ_δ. This condition translates into a momentum requirement

$$p_{\mathrm{sf}} + \left(\frac{d}{\lambda_{\mathrm{J},\,\delta}}\right) \dot{p}_{\mathrm{in}}\, t_{\mathrm{ff},\,\delta} \gtrsim \left(\frac{d}{\lambda_{\mathrm{J},\,\delta}}\right)^2 p_\delta \ , \tag{2.57}$$

where

$$p_\delta \sim M_{\mathrm{J},\,\delta}\, \sigma_\delta \sim \delta\, \rho_0\, \lambda_{\mathrm{J},\,\delta}^3\, \sigma_\delta \ , \tag{2.58}$$

is a characteristic momentum scale of the overdensity.

By assuming the usual form Eqs. 2.30 and 2.48 for the free-fall timescale and Jeans length, this condition yields

$$E_{51} \gg 700 \left(\frac{d}{\lambda_{\mathrm{J},\,\delta}}\right)^{2.15} \sigma_{\delta,1}^{4.3}\, n_0^{-0.4}\, \delta_2^{-0.54} \quad (\Delta t_{\mathrm{SN}} \to \infty)\,, \tag{2.59}$$

$$\frac{p_4}{\Delta t_6} \gg 2.4 \times 10^3 \left(\frac{d}{\lambda_{\mathrm{J},\,\delta}}\right) \sigma_{\delta,1}^4 \qquad (\Delta t_{\mathrm{SN}} \ll t_{\mathrm{ff},\,\delta})\,, \tag{2.60}$$

These constraints are quite restrictive for warm structures but indicate that cold (molecular) clouds ($\sigma_{\delta,1} \lesssim 0.1$) are readily overrun by nearby SN feedback.

Conversely, weak radiative blastwaves eventually become gravitationally trapped. In the gravity-dominated regime, where $M \sim M_\delta$ and $g_\delta \sim \sigma_\delta^2/\lambda_{\mathrm{J},\delta}$, the velocity evolves according to

$$\dot{v} \sim \frac{\sigma_\delta^2 - v^2}{\lambda_{\mathrm{J},\,\delta}} + \frac{\dot{\vec{p}}_{\mathrm{in}}}{M_\delta} \ , \tag{2.61}$$

driving the flow toward $v \to \sigma_\delta$ within $\sim t_{\mathrm{ff},\delta}$.

For small SNRs ($r_{\mathrm{SNR}} \lesssim \lambda_{\mathrm{J},\,\delta}$) exploding close to an overdensity $d \lesssim \lambda_{\mathrm{J},\,\delta}$, all parts of the SNR are expanding into approximately the same medium and the gravitational pull is comparable throughout the SNR. In such situations the overdensity can be treated as the background medium. Evidently, Eqs. 2.59 - 2.60 indicate that such a blastwave centered on the overdensity at $d = 0$ would "overrun" it in any case. Nonetheless, it might not be able to escape from its gravitational potential with break-out conditions resembling those of the vertically stratified plane (conditions 2.31 and 2.32). The SNR showcased in Romano et al. (2025a) highlights this scenario of expansion from within a (collapsing) filament and confirms, that the preferred direction of expansion is along the filament, where the gravitational potential is constant, despite the relatively higher density, which slows down the expansion of SNRs. This example also highlights the potential role of ongoing collapse, i.e. the sweeping-up of material with negative radial momentum, which further opposes the expansion out of the overdensity.

Numerical validation

In this section we consider various setups involving isothermal "Ostriker" filaments (Ostriker, 1964), which describe the solutions of the equations of hydrostatic equilibrium for an isothermal

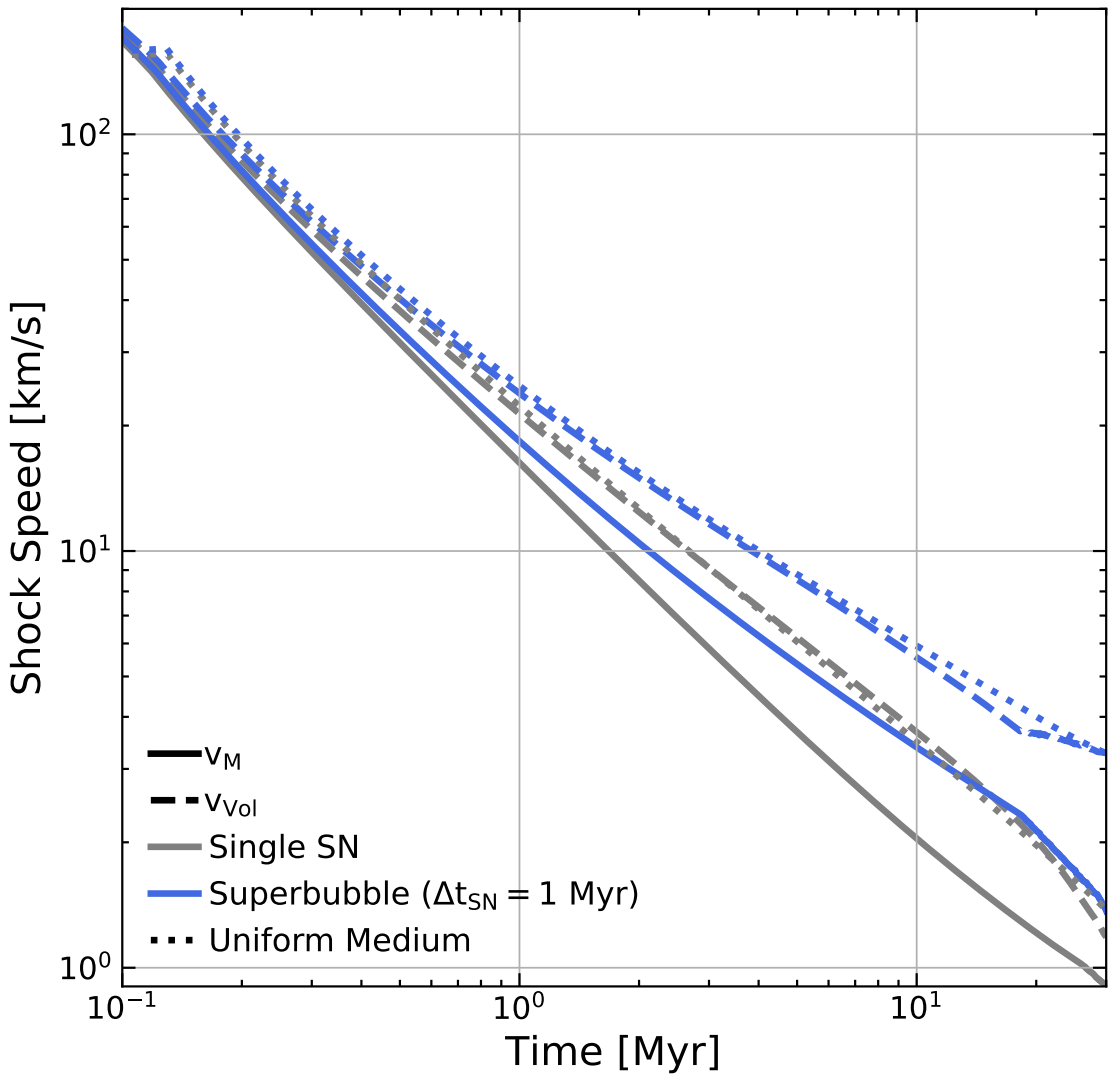

Figure 2.11: Time evolution of the expansion velocity components of blastwaves expanding into the gap ($n_{\mathrm{gap},\,0} = 0.1$) between two filaments ($n_{\mathrm{fil},\,0} = 10$, $T_{\mathrm{fil},\,2} = 2.65$, $d_{\mathrm{fil}} = 200\,\mathrm{pc}$). Solid and dashed lines correspond to the mass-weighted expansion speed and the effective expansion speed obtained by computing the rate of change of the effective radius, respectively For comparison, dotted lines corresponding to the same models expanding into a uniform medium with an ambient density matching the average density of the corresponding inhomogeneous model at each point in time. The mass-weighted expansion speed is strongly suppressed due to the stalled expansion in the directions of the filaments, which contribute significantly to the total mass, but little to the total volume. The effective expansion speed roughly matches that of the uniform medium at the time-dependent average density.

gas in an axisymmetric configuration. The density profile has the form

$$\rho_{\rm fil} = \frac{\rho_{\rm fil,\,0}}{\left(1+(r/r_{\rm fil})^2\right)^2} \ , \tag{2.62}$$

the gravitational potential

$$\Phi_{\rm fil} = 2\,\sigma_{\rm fil}^2 \log\left(1+(r/r_{\rm fil})^2\right) \ , \tag{2.63}$$

and the gravitational acceleration

$$\vec{g}_{\rm fil} = -4\frac{\sigma_{\rm fil}^2}{r_{\rm fil}}\frac{\vec{r}/r_{\rm fil}}{1+(r/r_{\rm fil})^2} \ , \tag{2.64}$$

where $\vec{r}$ is the distance vector from the filament, r its length and

$$r_{\rm fil} = 50\,T_{\rm fil,\,2}^{0.5}\,n_{\rm fil,\,0}^{-0.5}\,{\rm pc} \tag{2.65}$$

is the filaments scale length, depending on its central density $\rho_{\rm fil,\,0} = \mu\,n_{\rm fil,\,0}\,{\rm cm}^{-3}$ and its temperature $T_{\rm fil} = 100\,T_{\rm fil,\,2}\,{\rm K}$. The density profile of the Ostriker filament has a constant density core of size $\sim r_{\rm fil}$ outside of which the density steeply falls off $\propto r^{-4}$. The gravitational acceleration linearly grows outwards, peaking at $\sim r_{\rm fil}$ before it falls off $\propto r^{-1}$.

We test our predictions for blastwaves approaching filaments in Fig. 2.8 which shows the blastwaves' evolution for a filament with a central density and temperature of $n_{\rm fil,\,0} = 10$ and $T_{\rm fil,\,2} = 6$ embedded in a constant density background with density $n_0 = 1$. The explosions occur at a distance of $d = 8\,{\rm r_{fil}} \sim 332\,{\rm pc}$ away from the filament, where its contribution to the density amounts to only $\sim 0.1\,\%$. We stopped the calculation once the blastwave reaches the filament's center.

As expected the starburst overruns the filament. While its speed drops considerably upon reaching the overdensity, it remains well above the escape speed. By contrast, both the SB and the single SN get trapped in the gravitational potential and begin to free-fall approaching the asymptotic free-fall velocity of $\sim 2\,\sigma_{\rm fil}$. Compared to models without a filament, these models reach higher momentum and kinetic energy due to the filament's gravitational acceleration.

In all three models, the average density at the position of the filament exceeds that of the background medium. However, the final density differs between the models. The filament's gravitational field converges neighboring streamlines, leading to a contracting surface area element. While this in turn leads to a slower mass accretion it also shrinks the volume element, ultimately leading to a higher average density. In the case of the single SN the convergence of streamlines is so advanced that the density exceeds the filament's central density.

In order to study the net effect of galactic substructure on the geometry of blastwaves, we next consider blastwaves expanding in the gap between two parallel filaments. The filaments located 200 pc from each other have a central density of $n_{\rm fil,0} = 10$ and a temperature of $T_{\rm fil,2} = 2.65$, chosen such that the density in the gap is $n_0 \sim 0.1$. The filaments are embedded in a uniform background medium with a density of $n_0 = 0.1$. We omit the starburst as it overruns the filaments before 1 Myr.

We illustrate the filaments' effect on the blastwaves' geometry by showing slices through the xy- and yz-planes in Fig. 2.9 after 1, 5 and 10 Myr of expansion. At a background density of $n_0 \sim 0.1$ the blastwaves are expected to reach the filaments after $\sim 1\,{\rm Myr}$ and be significantly deformed after a few Myr. For the single-SN (SB) model, the minor-to-major axis ratio decreases to $\lesssim 2/3$ ($\sim 1/2$) after $5,{\rm Myr}$ and evolves to $\gtrsim 1/2$ (~ 0.45) after $10,{\rm Myr}$. The portions of the shock surface expanding out of the midplane facing either filament are expanding in a low-density medium, but are pulled toward them, while the midplane region is stalled by the steep density

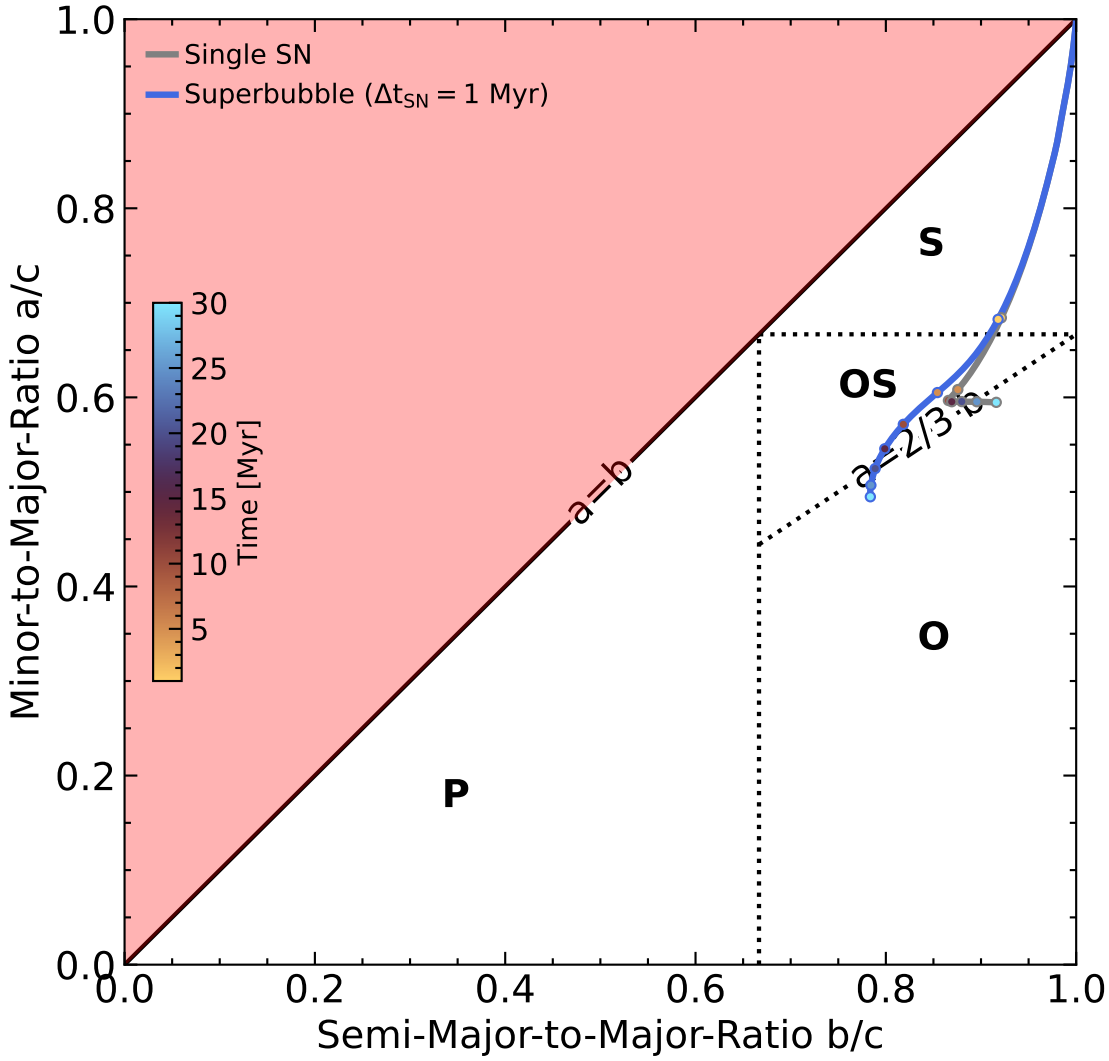

Figure 2.12: Same as Fig. 2.6 for the different blastwave models expanding into the gap ($n_{\mathrm{gap},\,0} = 0.1$) between two filaments ($n_{\mathrm{fil},\,0} = 10$, $T_{\mathrm{fil},\,2} = 2.65$, $d_{\mathrm{fil}} = 200\,\mathrm{pc}$). The blastwaves starts out as perfect spheres and becomes increasingly deformed over time.

gradient. This combination produces an increasingly concave, rectangular morphology, illustrating how filamentary structure can strongly shape the late-time geometry of SNRs and SBs.

We summarize the evolution of the different blastwave models in Fig. 2.10. As expected the presence of the filaments increases the average density encountered by the SNRs. Despite the higher average density, the SNRs grow larger than they would in a uniform medium of the same average density. Curiously however, the mass-weighted expansion speed, obtained by dividing the momentum–which is only slightly affected by the presence of the filaments–by the mass is lower than the expansion speed in a uniform density medium. Moreover, the free-fall-driven acceleration that we found for the regions approaching the filaments in Fig. 2.8 is washed out, when considering the entire SNR. The presence of the filaments drives tangential motion, decaying from initially $\sim 10\,\mathrm{km/s}$ down to $\lesssim \sigma_{\mathrm{fil}}$ after $\sim 10\,\mathrm{Myr}$ which significantly contributes to the SNRs' momentum- and energy budget in the case of a single explosion, but is rather negligible for the SB.

In order to make sense of the lower expansion speed despite the larger size, in Fig. 2.11 we compare the mass-weighted expansion speed $v_M = p_{\mathrm{exp}}/M$ to the effective expansion speed, defined as the rate of change of the effective radius $v_{\mathrm{vol}} = \dot{r}_{\mathrm{vol}}$. We find that the effective expansion speed roughly matches the expansion speed of a blastwave expanding in a uniform medium with ambient density matching the average density of the blastwave in an inhomogeneous medium. This motivates us to approximate the effective radius as

$$r_{\mathrm{vol}}\left(t\right) \sim \int_0^t v_{\mathrm{hom}}\left(t', \langle \rho\left(t'\right)\rangle\right) \mathrm{d}t' \ , \tag{2.66}$$

as opposed to the usually applied

$$r_{\mathrm{obs}}\left(t\right) \sim \int_0^t v_{\mathrm{hom}}\left(t', \langle \rho\left(t\right)\rangle\right) \mathrm{d}t' \ , \tag{2.67}$$

where the difference lies only in the subtle fact, that the former expression requires information about the history of the average ambient density, while the latter depends only on the current "observable" density ($\langle \rho\left(t'\right)\rangle$ vs. $\langle \rho\left(t\right)\rangle$). Since in our setup the density increases with time and a higher density implies a lower speed, this suggests that the "memory" of a previously encountered lower density medium automatically leads to a larger size compared to a model that expanded throughout with the higher average density at later times. Even for the slight overdensity considered here these effects become substantial after a few Myr, providing a plausible explanation for the systematically larger radii at fixed average density seen by Romano et al. (2025a).

Finally, we characterize the blastwaves' geometric response to the presence of filaments in Fig. 2.12, showing their trajectories in shape phase-space. We find that the blastwaves are significantly deformed within $\gtrsim 1\,\mathrm{Myr}$. Since their expansion is mostly stalled in the direction of the filaments, but largely uninhibited in all other directions the SNRs grow increasingly oblate. Nonetheless, for the first $\gtrsim 10\,\mathrm{Myr}$ they retain an minor-to-semi-major axis ratio $a/b \gtrsim 2/3$. Eventually, due to the increasingly concave geometry, the ellipsoidal description of the geometry breaks down and in the case of the single SN develops a kink in the shape phase-space trajectory, while in the case of the SB it smoothly transitions towards greater values of $b/c \sim 1$.

In the SISSI simulations most SNRs populate regions of even lower a/c and b/c, with the majority of SNRs assuming a prolate geometry. This is likely due to the disky geometry of the gas and notably the presence of a stellar disk, which lead to an additional potential well that can further inhibit vertical expansion and thus preferential expansion in the disk plane. In the turbulent multiphase ISM, the density varies over several orders of magnitude allowing SNRs to rapidly travel through large volumes of low-density gas before being stalled by higher-density structures. If these structures are filamentary and preferentially aligned parallel to each other–as would be expected in a differentially rotating disk–we expect SNRs to become preferentially prolate, aligned parallel to the filaments within a few Myr to 10s of Myr, depending on the typical density contrast.

2.4 Galactic environment in concert

In Sections 2.3.1 - 2.3.3 we have explored–in isolation–the various ways in which ubiquitous galactic scale processes can affect SNR evolution. We have found that these processes usually affect SNRs once they reach a certain size or age, provided that they have slowed down sufficiently for these effects to become dominant.

In a marginally stable disk, many of these characteristic time- and length-scales are linked by the Toomre Q_T-parameter (Toomre, 1964). For instance, in Section 2.3.2 we find that galactic rotation dominates the dynamics after half the epicycle timescale, which in a marginally stable disk is comparable to the free-fall timescale $t_{\rm ff}$, governing the collapse of weak blastwaves failing to drive outflows. Similarly, the typical separation and size of dense structures is similar to the disk scale-height $\lambda_{\rm J} \sim \lambda_{\rm T} \sim H_{\rm s}$ (Jeans, 1902; Toomre, 1964; Ostriker, 1964; Behrendt et al., 2015).

We thus expect a variety of these processes to affect the dynamics of old and large SNRs simultaneously. Explicitly modeling these effects in concert turns out to be quite intractable, as it requires the time-dependent modeling of the density and gravitational field of galactic substructure subject to shear, which quickly becomes nearly as complex as the numerical simulations presented in Romano et al. (2025a).

However, the above discussion allows us to draw some general conclusions about SNRs embedded in complex galactic environments The SNRs appear to be most strongly affected by their environment after reaching a characteristic velocity on the order of the velocity dispersion

$$v_{\rm env} \sim \sigma \ , \tag{2.68}$$

and sizes on the order of $\lambda_{\rm J}$. The time it takes for these mechanisms to take effect reaches from a few Myr for the interaction with overdensities to a few 10s of Myr for galactic rotation and vertical stratification, depending on various factors such as the typical distance between dense substructures, the orbital timescale and the depth of the disk's gravitational potential.

In the vertical direction, stratification can affect the dynamics of SNRs if they are powerful enough to break-out (Eqs. 2.31 and 2.32). However, only the most powerful starbursts are expected to be able to break away from the galactic disk (Romano et al., 2025b) and drive winds, which become prolate and aligned vertically. Instead, most weaker SNRs become increasingly oblate due to the gravitational pull of the galactic disk, within about a free-fall timescale. For sufficiently powerful SBs this may take the form of a brief break-out from the galactic disk, followed by stalling and eventual falling back onto the disk, a process that is also known as fountain flow.

Along with their dynamics, SNRs' geometry is affected by their galactic environment as well. Deformation by galactic shear and substructure tend to be synergetic, since the substructure itself is stretched out by galactic shear, leading to departures from spherical symmetry that align with pre-existing substructure. Large SNRs, which are sandwiched between galactic filaments as well as SNRs within filaments are expected to be parallel to them, with pitch angles matching those of the filaments on the order of $28 - 45°$ (Xie et al., 2024).

While we focused here mainly on the role of the gas, which contributes both to the swept-up mass and the gravitational potential, it is worth noting that the stars' and dark matters' contributions to the gravitational potential cannot be neglected likely leading to more pronounced differences from the dynamics in a uniform density medium possibly on even shorter time-scales. Moreover, we only considered stationary or co-rotating media, however anisotropic or turbulent flow-patterns can further affect SNRs' dynamics and deform their geometry in complicated ways once the SNRs' slow down to reach comparable speeds – for turbulence on the order of the velocity dispersion.

Chapter 3

Starburst-Driven Galactic Outflows

Unveiling the Suppressive Role of Cosmic Ray Halos

> Software used in this chapter:
> Julia v1.10.0 (Bezanson et al., 2017), and Matplotlib v3.5.1 (Hunter, 2007)

This work has been accepted for publication in Astronomy & Astrophysics Letters on August 24 2025 and appeared in Volume 701, September 2025, id. L5 (Romano et al., 2025b). It is a truly collaborative effort that I initiated during my visit in Osaka in November 2024. Ellis Owen, a leading expert on Cosmic Ray physics, was responsible for writing most of the introduction, producing Figs. 3.1 and B.1, and for most of the cosmic ray physics, while I was responsible for the physical setup and the blastwave modeling. I wrote the first draft for most of the discussion, results and conclusions sections, which we later collaboratively restructured and rewrote. Kentaro Nagamine, my host in Osaka and an expert in large scale structure, provided useful comments and suggestions that went into the interpretation and he has been very actively contributing to the revision of the paper.

Galaxies with high star-formation surface densities often host large-scale outflow winds. Such winds have been observed in local starbursts, such as Arp 220, M82, and NGC 253 (e.g., Bolatto et al., 2013; Leroy et al., 2015; Walter et al., 2017; Barcos-Muñoz et al., 2018) and are widespread at high-redshifts, where galaxies are typically more compact and have higher star-formation rates relative to their stellar mass (see, e.g. Sugahara et al., 2019; Nianias et al., 2024; Thompson & Heckman, 2024). Outflow winds play an important role in redistributing energy, momentum, and baryons between the interstellar medium (ISM) and halos of galaxies. This makes them a key feedback component that regulates the evolution of galaxy ecosystems. Yet, despite their importance, a complete picture of the role they play remains unsettled (see Zhang, 2018; Thompson & Heckman, 2024, for reviews).

Detailed multi-wavelength observations of nearby starburst galaxies with outflows have revealed certain common features, including a bi-conical shape aligned along the minor axis of their host galaxy (Veilleux et al., 2005), extensions reaching 10s of kpc into the halo (Veilleux et al., 2005; Zhang, 2018), a terminal "cap" at a few kpc, e.g., at ~ 12 kpc in M82 (see Lehnert et al. 1999; Tsuru et al. 2007), and the presence of entrained magnetic fields (e.g. Jones et al., 2019; Lopez-

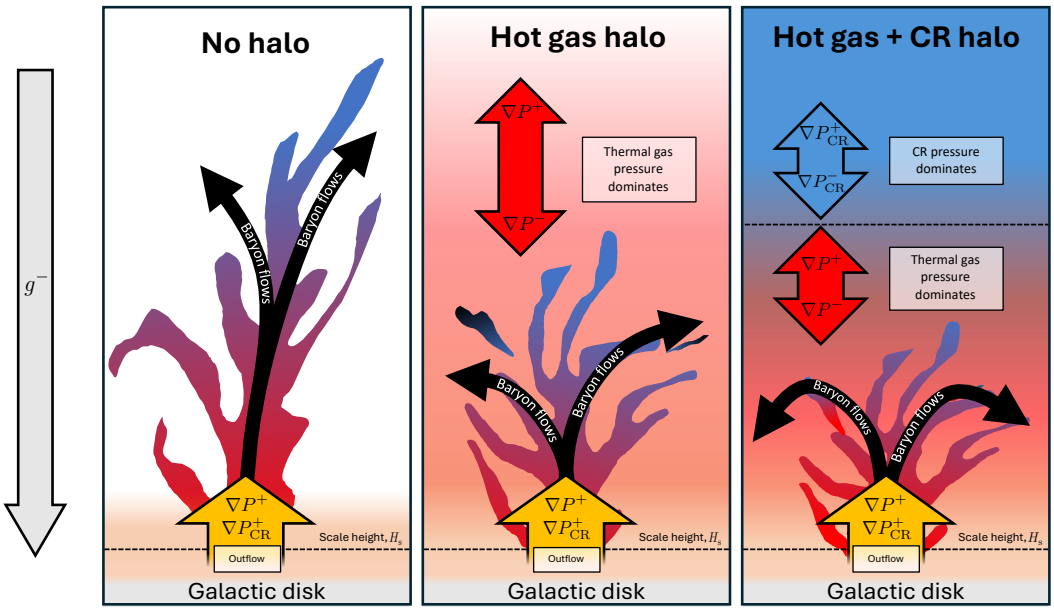

Figure 3.1: Schematic of the structure of a starburst-driven outflow embedded in a galactic halo, propelled by thermal gas pressure and/or non-thermal CR pressure. The scale height of the warm ISM is indicated. All galaxies are embedded in a gravitational potential, g, which opposes the outflow. Superscripts + and - on quantities indicate whether each term contributes to or opposes the outflow, respectively. **Left**: In the absence of a substantial gas halo, outflowing gas is unconfined, allowing it to escape beyond the galaxy ecosystem against the galaxy's gravitational potential. **Center**: As the galaxy builds up its stellar mass, feedback processes form a hot gas halo that suppresses the outflow, promoting baryonic recycling and enriching the CGM (see Ferrara et al., 2005; Shin et al., 2021). **Right**: When CRs are supplied to the halo, they accumulate over time, introducing a non-thermal halo component. Since non-thermal CR pressure gradients operate over larger length scales than thermal pressure gradients, an outflow erupting into the galaxy halo encounters distinct layers where thermally dominated and CR-dominated pressure gradients hinder its development.

Rodriguez et al., 2021) and high-energy CR particles (for an overview, see Irwin et al., 2024).

Despite these apparent similarities, the physical configuration of individual galactic outflows can vary substantially. For instance, flow velocities ranging up to ∼1,000 km s^{-1} have been reported (e.g. Bradshaw et al., 2013; Heckman et al., 2015; Cicone et al., 2016; Cazzoli et al., 2016; Xu et al., 2022; Taylor et al., 2024), while densities and mass-loading factors span over 1.5 orders of magnitude (e.g. Xu et al., 2023a; Heckman et al., 2015). This diversity can be attributed to differences in the energy, matter, and momentum being supplied to an outflow by its host galaxy (Zhang, 2018; Thompson & Heckman, 2024), the underlying driving microphysics (Yu et al., 2020), and environmental factors — particularly the conditions of the surrounding halo.

Hot halo gas exerts inward pressure. This can oppose the development of a galactic outflow by reducing its velocity and limiting its extension compared to systems without a halo (e.g. Shin et al., 2021). By confining metal-enriched outflows and restricting the dispersal of ejecta, halo gas ram pressure has been considered to be instrumental in regulating baryonic recycling flows and enabling the enrichment of galaxies' CGM (Ferrara et al., 2005). In addition to this thermal pressure from the hot gas, galaxy halos may also host a reservoir of CRs. These CRs may originate as a relic population that could be transported by advection, bubbles associated with outflows, or the activity of a central supermassive black hole (see e.g. Owen et al., 2019; Recchia et al., 2021; Shimoda & Inutsuka, 2022).

Halo CRs can modify the structure of the circumgalactic medium (CGM) and alter baryonic flows within galaxy halos (for reviews, see Ruszkowski & Pfrommer, 2023; Owen et al., 2023). Simulations of Milky-Way-mass galaxies suggest that CRs provide additional pressure support to sustain a multi-phase halo gas structure at low temperatures and can propel cool gas out to 100s of kpc (Butsky & Quinn, 2018; Ji et al., 2020). CR-driven winds can even push gas beyond the virial radius (Quataert & Hopkins, 2025). Due to the long CR survival time in halos, these feedback effects can continue to manifest long after the end of the mechanical processes that originally generated the CRs (Quataert & Hopkins, 2025). Halo CRs can also operate alongside hot halo gas to provide an inward non-thermal pressure that counteracts developing outflows. This is illustrated in Fig. 3.1, which compares the suppressive effect of galaxy halos and the implications for baryonic recycling.

In this study, we assess the role of an extended CR halo in modifying the development of galactic winds driven by CR and thermal gas pressure, and derive the criteria for the breakout of an outflow from a galaxy with a CR halo.

3.1 Starburst-driven Outflows in Galaxy Halos

The collective feedback from a central galactic starburst can initiate a blastwave, which may develop into a sustained galactic wind if the starburst activity is continuous. Typically, about one SN explodes per ∼100 $M_\odot$ of star formation, with the exact rate dependent on the choice of the stellar initial mass function (e.g. Leitherer et al., 1999). We can therefore link the supernova event rate $\mathcal{R}_{\rm SN} = \mathcal{R}_{-3}\,{\rm kyr}^{-1}$ to the SFR of a galaxy by $\mathcal{R}_{\rm SF} \sim 100\,M_\odot\,\mathcal{R}_{\rm SN}$. Observationally, star formation activity is typically quantified using the SFR surface density, $\Sigma_{\rm SFR}$. This can be related to $\mathcal{R}_{\rm SF}$ by considering that most star formation contributing to the blastwave occurs within a cylindrical region with a radius comparable to the disk scale height, $\sim H_{\rm s}$, of a galaxy (defined by eq. B.2), i.e. $\Sigma_{\rm SFR} = \mathcal{R}_{\rm SF} \,/\, \left(\pi H_{\rm s}^2\right) = \Sigma_{\rm SFR,\,0}\,M_\odot\,{\rm yr}^{-1}\,{\rm kpc}^{-2}$.

The injection rates of mass ($\dot{M}_{\rm SB} = M_{\rm ej}\mathcal{R}_{\rm SN}$, for $M_{\rm ej} = M_{\rm ej,\,0}\,M_\odot$ as the typical supernova ejecta mass) and energy ($\dot{E}_{\rm SB} = E_{\rm SN}\mathcal{R}_{\rm SN}$, for $E_{\rm SN} = 10^{51}\,E_{51}\,{\rm erg}$ as the typical mechanical energy supplied by a supernova) supplied to an expanding blastwave from a galactic starburst can be

linked to the SFR through the mass- and energy-loading factors $\eta_{\rm m} \equiv \dot{M}_{\rm SB}/\mathcal{R}_{\rm SF} = 0.01 M_{\rm ej,\,0}$ and $\eta_{\rm e} \equiv \varepsilon_{\rm w}\dot{E}_{\rm SB}/\left(E_{\rm SN}\mathcal{R}_{\rm SN}\right) = \varepsilon_{\rm w}$, respectively, where ε_w is a thermalization efficiency factor accounting for energy dissipation in the system (see e.g. Thompson et al., 2016; Kim et al., 2017; Steinwandel et al., 2024). For convenience, we introduce the scaling parameters $\eta_{\rm m,\,-2} = \eta_{\rm m}/0.01$, $\eta_{\rm e,\,-2} = \eta_{\rm e}/0.01$ and $\varepsilon_{\rm w,\,-2} = \varepsilon_{\rm w}/0.01$. The supply of CRs to the wind is parametrized by $f_{\rm CR}$, representing the CR energy fraction at the galactic mid-plane. In our model, these parameters are treated as constants, remaining fixed throughout the evolution of the outflow, and the flow is considered to be driven by the combination of central thermal and kinetic energy-injection, and CR pressure gradients.

3.1.1 CR halos and their effects on outflows

Several observational studies have suggested the presence of extended CR reservoirs in galactic halos. These include a γ-ray halo around M31 reaching to 100s of kpc, which likely traces an interacting population of hadronic CRs (Recchia et al., 2021), γ-ray emission originating from halo clouds at kpc heights around the Milky Way (Tibaldo et al., 2015), and kpc-scale synchrotron emission from edge-on galaxies (e.g. Mulcahy et al., 2018; Mora-Partiarroyo et al., 2019). It has also been proposed that diffuse X-ray emission from the halos of Milky Way, M31, and lower-mass galaxies could originate from inverse Compton scattering, driven by a leptonic CR population (Hopkins et al., 2025).

The formation of CR halos is a consequence of CR production during galaxy evolution. The long energy loss times of hadronic CRs in these environments (see Appendix B.1.1) ensure that most of the CR energy density supplied to a galaxy halo during its development can survive to the present day. Galaxies with significant historical stellar mass buildup are expected to host rich CR halos, even if their current star formation activity is low. Observations in γ-rays tentatively support this distinction, with CR halos primarily identified around massive late-type galaxies, while lower-mass galaxies show no indications of hosting such structures (Pshirkov & Nizamov, 2024).

To assess whether a CR halo can influence a developing outflow, the CR pressure contributions from both the halo and the outflow can be compared at a given altitude, z (see Appendix B.1; eqs. B.3 and B.7). For CRs to drive an outflow, the outward CR pressure must exceed the inward pressure from the halo CRs. When external and internal CR pressures become comparable, the driving effect of CR pressure gradients diminishes.

As illustrated in Fig. 3.1, the presence of a CR halo is expected to frustrate slow outflows if its scale height significantly exceeds the altitude where external and internal CR pressures are equal, $z_{\rm CR}$. In units of the disk scale height, $H_{\rm s}$, this CR pressure equilibrium height is given by:

$$z_{\rm CR} \sim 1.5\,\varepsilon_{\rm w,\,-2}^{1/2}\,E_{51}^{1/2}\,\mathcal{R}_{-3}^{1/2}\sigma_1^{-2}v_{\infty,2}^{-1/2}\,H_{\rm s}\ , \tag{3.1}$$

where $\sigma = 10\,\sigma_1$ km/s is the gas velocity dispersion, and $v_{\infty,2}$ is the rescaled terminal flow velocity defined as $v_\infty = 100\,v_{\infty,2}$ km/s at large distances from the galactic plane. Equation 3.1 indicates that $z_{\rm CR}$ is typically located at low altitudes for most galaxies. This suggests that CR-driven outflows are easily suppressed by the presence of an extended CR halo, if the halo has a scale-height $\gg H_s$. Galactic winds in systems with a well-developed CR halo are therefore expected to experience suppression, with their driving primarily dependent on thermal and kinetic energy-injection rather than CR pressure.

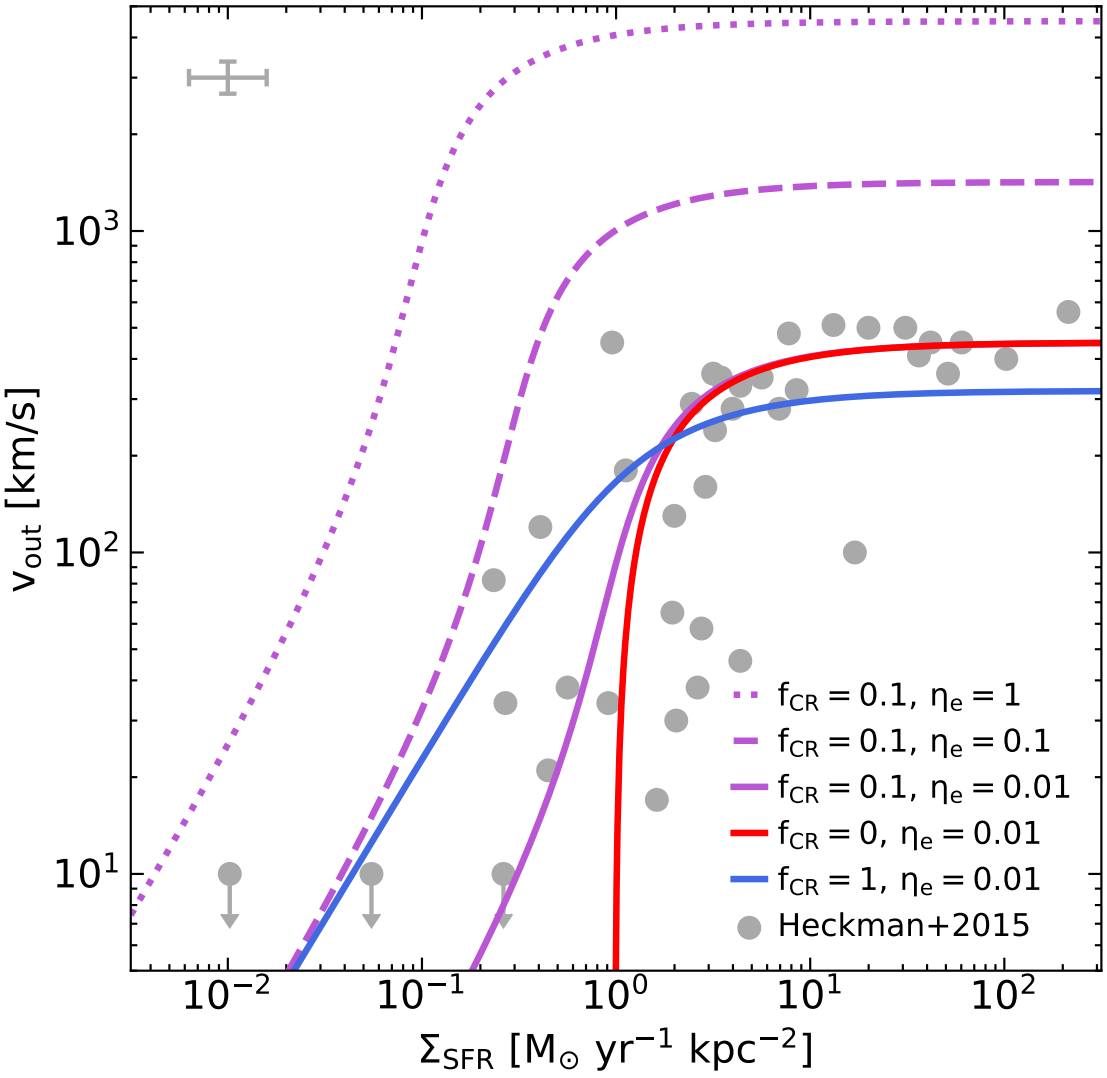

Figure 3.2: Terminal outflow velocities as a function of star formation rate surface density for different choices of CR energy fractions, $f_{\rm CR}$, and energy loading factors, $\eta_{\rm e}$. The model predictions are compared with data from Heckman et al. (2015), which show measured outflow velocities for a sample of nearby starburst galaxies with stellar masses in the range $\log_{10}(M_*/{\rm M}_\odot) \in [7.1 - 10.9]$. Typical uncertainties are indicated in the top-left corner. The model with $\eta_{\rm e} \sim 0.01$ and $f_{\rm CR} \sim 0.1$ provides a good match with the observed data. Models with higher energy loading values ($\eta_{\rm e}$) generally predict outflow velocities in excess of the observations. The transition from slow outflows in weak starbursts to fast outflows in strong starbursts is best captured by models with $f_{\rm CR} > 0$.

3.1.2 Outflow breakout criterion and terminal velocity

For an outflow to break out from a galaxy, a minimum critical SFR surface density can be defined in the absence of a CR halo (see Appendix B.1.2). This is given by:

$$\Sigma_{\rm SFR,\,c} \gtrsim 2.14\, n_0\, \sigma_1^2\, \eta_{\rm e,\,-2}^{-1/2}\, \eta_{\rm m,\,-2}^{-1/2} \quad {\rm M_\odot\,yr^{-1}\,kpc^{-2}}, \tag{3.2}$$

where $n_{\rm H,\,mp} = n_0\,{\rm cm^{-3}}$ is introduced as the mid-plane gas number density. In a strong star-starburst (i.e. when $\Sigma_{\rm SFR} \gg \Sigma_{\rm SFR,\,c}$), the maximum flow speed that can develop tends towards an asymptotic limit (see eq. B.10).

CR-driven outflows can always be launched without a specific breakout criterion. However, in weak star formation scenarios (i.e. $\Sigma_{\rm SFR} \ll \Sigma_{\rm SFR,\,c}$), only very slow flow velocities can be achieved:

$$v_\infty^{\rm weak} \rightarrow 237\, f_{\rm CR} \eta_{\rm e,\,-2}\, \Sigma_{\rm SFR,\,0}\, \sigma_1^{-2}\; n_0^{-1} \;\; {\rm km\;s^{-1}}\;. \tag{3.3}$$

In this regime, the CR pressure equilibrium height reduces to:

$$z_{\rm CR}^{\rm weak} \rightarrow 1.85 f_{\rm CR}^{-1/2}\, H_{\rm s} \tag{3.4}$$

which decreases as the CR supply to the system increases. This indicates that a CR halo strongly suppresses weak outflows that rely on CR driving (c.f. the right panel of Fig. 3.1).

In the strong starburst limit (when $\Sigma_{\rm SFR} \gg \Sigma_{\rm SFR,\,c}$), much faster terminal velocities are expected:

$$v_\infty^{\rm strong} \rightarrow 10^3\, \eta_{\rm e,\,-2}^{1/2}\, \eta_{\rm m,\,-2}^{-1/2}\, \frac{\sqrt{1+f_{\rm CR}} + \sqrt{1-f_{\rm CR}}}{2} \;\; {\rm km\;s^{-1}}. \tag{3.5}$$

The CR pressure equilibrium height in this regime is then

$$z_{\rm CR}^{\rm strong} \rightarrow 0.47\, \varepsilon_{\rm w,\,-2}^{1/4}\, E_{51}^{1/4}\, M_{\rm ej,\,0}^{1/4}\, \mathcal{R}_{-3}^{1/2} \sigma_1^{-2}\, H_{\rm s}\;. \tag{3.6}$$

Although the inward halo CR pressure overtakes the outward flow-driving CR pressure near the disk scale height, the independence of $z_{\rm CR}^{\rm strong}$ from $f_{\rm CR}$ suggests that outflows in this regime are momentum-dominated. Such outflows are unlikely to be significantly influenced by the presence of a CR halo, with thermal gas pressure likely playing a more critical role in regulating flow dynamics (see the central panel of Fig. 3.1).

The terminal velocities predicted by our model allow for comparison with observations. Figure 3.2 shows terminal outflow velocities as a function of SFR surface density for a fiducial model with (dimensionless) parameters $n_0 = 1$, $\sigma_1 = 1$, $\eta_{\rm m,\,-2} = 5$, and varying values of $f_{\rm CR}$ and $\eta_{\rm e,\,-2}$ as indicated in the legend. These calculations assume that all galaxies in the sample share a similar dynamical equilibrium pressure, $P_{\rm DE} \sim \rho_{\rm mp}\sigma^2 \sim G\Sigma^2$ (Ostriker & Kim, 2022) for $\rho_{\rm mp}$ as the galactic mid-plane gas volume density and Σ as the corresponding surface density that sets $\Sigma_{\rm SFR,\,c}$. For comparison, observed outflow velocities for a sample of nearby starburst galaxies with stellar masses in the range $\log_{10}(M_*/{\rm M_\odot}) \in [7.1 - 10.9]$ are also shown (Heckman et al., 2015). Our model captures the general trend of observed flow velocities with parameter choices of $\varepsilon_{\rm w,-2} \sim \eta_{\rm e,-2} \sim 1$ and $\eta_{\rm m,\,-2} \sim M_{\rm ej,\,0} \sim 5$. These choices align well with the energy and mass loading factors reported in numerical simulations of galactic outflows at altitudes of a few kpc (e.g. Kim & Ostriker, 2018; Rathjen et al., 2021; Steinwandel et al., 2024; Kjellgren et al., 2025).

3.2 Discussion and Implications

The structure of galactic winds has been extensively studied through theoretical approaches (e.g. Chevalier & Clegg, 1985; Fielding & Bryan, 2022; Modak et al., 2023), detailed numerical simulations (e.g. Kim & Ostriker, 2018; Vasiliev et al., 2023; Kjellgren et al., 2025) and observational

studies (e.g. Krieger et al., 2019; Xu et al., 2023b; Bolatto et al., 2024). These studies have shown that galactic winds are ubiquitous, particularly among star-forming galaxies, and that galaxies with high SFRs tend to drive faster and hotter winds. However, not all galaxies show clear signatures of outflows. Some systems show that gas launched from the ISM is recycled within a galaxy ecosystem rather than expelled (Marasco et al., 2023). While the qualitative framework for wind launching is well established (see Thompson & Heckman, 2024, for a review), few studies quantify outflow launching conditions (e.g. Heckman et al., 2015; Orr et al., 2022).

Heckman et al. (2015) examined outflow speeds of galactic winds in a sample of nearby starbursts, and reported a sharp drop in flow velocities when the central SFR surface density fell below a critical threshold of $\Sigma_{\mathrm{SFR,\,c}} \sim 1\,M_{\odot}\,\mathrm{yr}^{-1}\,\mathrm{kpc}^{-2}$. Our model shows that this critical SFR surface density arises due to the depth of the gravitational potential, which can only be overcome by sufficiently strong starbursts. The predicted value aligns with observations when considering typical dynamical equilibrium pressures set by the weight of the ISM, together with wind-loading parameters that are consistent with recent numerical studies of galactic winds in dwarf (Steinwandel et al., 2024) and spiral galaxies in the local Universe (Kjellgren et al., 2025). However, we note that other studies find significantly higher mass and energy loading, depending on the methodology used (e.g. Muratov et al., 2015; Smith et al., 2024).

Orr et al. (2022) investigated the feedback from star formation in a marginally Toomre-stable disk. They proposed that a young star cluster could launch an outflow if the starburst-driven shock reaches the disk scale height before its speed drops below the ISM's velocity dispersion. By assuming the formation of one star cluster per orbital timescale, they derived an expression for the critical SFR surface density, which is in rough agreement with the threshold found observationally by Heckman et al. (2015). However, their study does not account for the effects of gravity, which would alter the wind-launching criterion.

Most numerical simulations of starburst-driven galactic winds show that the inclusion of CRs improves their ability to drive warm outflows with high mass-loading factors (e.g. Girichidis et al., 2016; Rathjen et al., 2021; Chan et al., 2022; Armillotta et al., 2024). This is in agreement with our results, which indicate that outflow speed in the CR-dominated regime is independent of the mass-loading factor, and suggest that CR-driven winds can sustain substantial mass-loading before being significantly slowed. However, current numerical models do not typically include a pre-existing CR halo in their initial conditions. Instead, they only model the accumulation of CRs within a galaxy ecosystem over time, usually as a consequence of stellar feedback. The widespread findings of substantial feedback impacts from CR-driven outflows in the literature may reflect this limitation — a situation that would have certain parallels with earlier numerical studies that lacked CGM thermal pressure, leading to unrealistically strong outflows in simulations of isolated galaxies (Shin et al., 2021).

At high redshift, several studies have reported high outflow velocities up to 1,000 km s^{-1} (Sugahara et al., 2019; Xu et al., 2022). In general, higher outflow speeds require higher energy loading factors and lower mass loading factors. Observations suggest that high-redshift galaxies tend to be compact and turbulent (Genzel et al., 2023), with high gas fractions and surface densities (e.g. Genzel et al., 2011), as well as low metallicities (Maiolino et al., 2008). Since the critical SFR surface density scales with the dynamical equilibrium pressure as $\dot{\Sigma}_{\mathrm{SFR,\,c}} \propto P_{\mathrm{DE}} \propto \Sigma^2$, thermally-driven outflows become ineffective in a highly turbulent, high surface-density environment. On the other hand, lower metallicities result in longer cooling times, leading to higher momentum-loading (Oku et al., 2022). If mass-loading factors in high-redshift galaxies are comparable to those in low-redshift galaxies, then lower metallicities could explain the high observed outflow velocities in high-redshift galaxies, provided that the increased ISM weight does not suppress outflows.

Curiously, the critical SFR surface density exhibits a stronger dependence on gas surface density than on the SFR surface density itself, which follows $\dot{\Sigma}_{\mathrm{SFR}} \propto \Sigma^{1.4}$ (Kennicutt, 1989). This suggests

that, counterintuitively, fast thermally-powered galactic outflows are expected to be more common at low surface densities, such as in dwarf galaxies, while being suppressed in extreme star-forming environments - including massive clumps in high-redshift galaxies (Genzel et al., 2011) and the proposed feedback-free starburst galaxies at $z \sim 10$ (Finkelstein et al., 2023; Dekel et al., 2023). At high redshifts, CR-driven slow outflows may be more prevalent in these systems, as there would not have been sufficient time for them to establish a CR halo capable of suppressing outflows. Indeed, highly mass-loaded outflows are essential for regulating star formation and explaining observed metallicity trends at high redshift (Toyouchi et al., 2025), which could naturally be accounted for by CR-driven outflows.

3.3 Conclusions

In this study, we constructed a galactic outflow model driven by a continuous central feedback source, including the effects of CR pressure in the outflow and surrounding galaxy halo. We applied this model to a starburst galaxy to assess how the presence of a CR halo may influence outflow development. We found:

1. In the absence of CRs, galactic outflows are only launched if the SFR surface density exceeds a critical threshold proportional to the dynamic equilibrium pressure. At high SFR surface densities, these momentum-driven outflows approach the ejecta speed, reaching up to 1,000s of km s^{-1}.
2. CRs can always drive slow outflows. We identified two different regimes: slow, CR-dominated outflows at SFR surface densities below the critical threshold, and fast, momentum-driven outflows at high SFR surface densities.
3. In the presence of an extended CR halo, CRs become ineffective in sustaining outflows beyond the galactic scale height, leading to the suppression of CR-driven winds.

While our simplified approach is subject to substantial limitations (see Appendix B.2), it provides useful insights into the qualitative behavior of starburst-driven outflows and the influence of a CR halo. However, more detailed studies - including numerical simulations with CR halos as an initial condition - are needed to properly explore the physical impacts of CRs on the dynamical processes within galaxy halos.

Chapter 4

Cloud Formation by Supernova Implosion

> Software used in this chapter:
> Julia v1.6.5 (Bezanson et al., 2017), Matplotlib v3.5.1 (Hunter, 2007), Mera v1.4.0 (Behrendt, 2023a), Paraview v5.11.1 (Henderson, 2007), and Ramses v19.10 (Teyssier, 2002)

This work has been published in the Astrophysical Journal, Volume 965, Issue 2, April 2024, id. 168, pp. 15 (Romano et al., 2024a). The set-up, implementation and the execution of the simulations presented in this chapter as well as the analysis were done by me. Some of the RAMSES-patches, particular those related to radiative cooling were implemented by Manuel. Andi pointed out, that the implosion was interesting physics, which I initially dismissed as a numerical artifact. However, afterwards the interpretation was done by myself, guided by useful questions and comments by my collaborators Andi and Manuel. The manuscript was written by myself, but I received many useful comments from Andi, Manuel and the anonymous referee.

It has long been recognized that supernovae (SNe) play an important role in maintaining the balance and structure of the interstellar medium (ISM). Even though there is only about one supernova per 100 $M_\odot$ of formed stars, due to their enormous energy output, these destructive events can have an enormous impact on their surroundings.

Many aspects of galaxy formation and evolution, like star formation and the modeling of galactic outflows (e.g. Fielding et al., 2017; Orr et al., 2022), are tightly linked to the evolution of supernova remnants (SNRs). SNe are believed to maintain the hot phase (e.g. de Avillez & Breitschwerdt, 2004; Bieri et al., 2023), drive turbulence and outflows (e.g. Rosen & Bregman, 1995; Krumholz et al., 2018; Fielding et al., 2018; Oku et al., 2022), regulate the star formation rate in disk galaxies (e.g. Shetty & Ostriker, 2012; Shimizu et al., 2019; Herrington et al., 2023) and enrich their surroundings with heavy elements and dust (e.g. Kozasa et al., 1989; Bianchi & Schneider, 2007; Nozawa et al., 2007).

Of particular interest is the concept of positive SN feedback or *triggered star formation*, where a strong shock wave compresses the gas, leading to further collapse, fragmentation and eventually the formation of new stars. This processes has been predicted in numerous theoretical works (e.g. Dwarkadas et al., 2017; Krause et al., 2018; Herrington et al., 2023) and has recently been confirmed with observations from the *Gaia* mission (e.g. Zucker et al., 2022; Miret-Roig et al.,

2022; Ratzenböck et al., 2023).

SNR evolution in a uniform medium has been studied at great length using analytical models (e.g. Woltjer, 1972; Gaffet, 1978; Ostriker & McKee, 1988), and numerical simulations in one (e.g. Chevalier, 1974; Cioffi et al., 1988; Fierlinger et al., 2016), two (e.g. Blondin et al., 1998; Ntormousi et al., 2011; Meyer et al., 2023) and three dimensions (e.g. Kim & Ostriker, 2015; Makarenko et al., 2023), which have lead to a comprehensive picture comprised of a series of different stages, characterized by different deceleration parameters $q = -\mathrm{d}^2R/\mathrm{d}t^2$ and conserved quantities. In the first stage, known as the *free expansion* phase the SNR expands with constant velocity until the reverse shock has fully thermalized the ejecta (Truelove & McKee, 1999). In the next so-called Sedov-Taylor (ST) phase (Sedov, 1959; Taylor, 1950), the SNR expands adiabatically as cooling losses are still negligible and thus energy is conserved. The ST phase ends, when radiative cooling losses become important and a thin, cold shell forms at the shock front. After the shell has formed, the SNR keeps expanding in what is known as the pressure-driven snowplow (PDS) phase (Cox & Anderson, 1982; Ostriker & McKee, 1988). During the PDS, the hot bubble is rapidly evacuated as hot material is pushed into the shell (Gaffet, 1983; Cioffi et al., 1988; Kim & Ostriker, 2015). Once the bubble pressure has dropped below that of the shell, the PDS ends and transitions into a momentum conserving snowplow (MCS) phase (Cioffi et al., 1988; Thornton et al., 1998). It has been claimed that the SNR evolution ends, when the shock velocity becomes comparable to the typical velocity dispersion of the ambient medium (Cioffi et al., 1988; Draine, 2011; Faucher-Giguère et al., 2013; Krumholz et al., 2018) and the shock merges with the ISM. However, the details of the merging have only received little attention and it remains unclear how the evacuated bubble carved out by the blast wave is refilled.

In order to address this gap, in this work, we utilize three-dimensional, hydrodynamical simulations with cooling to study the late radiative stage of SNR evolution and the onset of fade out. We thus provide a more complete picture for the later stages of SNR evolution. We show that as the SNR shell pressure approaches the ISM pressure, the SNR implodes, filling the central cavity. This implosion leads to the formation of a dense compact, cloud in its center, which has the potential to form new stars and thus provides a novel pathway for triggered star formation.

The remainder of this paper is organized as follows. In section 4.1 we describe the numerical scheme and the setup of our simulation suite. In section 4.2 we present the results of our numerical simulations. We discuss the limitations and implications of our results in section 4.3. Finally, we summarize our findings and conclude in section 4.4. In the appendix we present a number of tests, related to the question of numerical convergence and the adopted treatment for radiative cooling.

4.1 Methods

4.1.1 Numerical Methods

We utilize the adaptive mesh refinement (AMR) code RAMSES (Teyssier, 2002) to simulate the hydrodynamic evolution of blast waves in a uniform density medium, including radiative cooling. RAMSES is solving the system of hydrodynamic equations utilizing a second-order unsplit Godunov method (MUSCL scheme) on a finite volume, cartesian grid. Variables at the cell interfaces are reconstructed from the cell-centered values using the HLLC Riemann solver (Toro et al., 1994) with MinMod total variation diminishing scheme. Cooling is solved for the default *courty* cooling function implemented in RAMSES, which provides a basic treatment of primordial chemistry, metal line cooling and heating due to ultraviolet background (UVB) radiation.

In our fiducial simulation suite we consider a cubic computational domain with a side length of

Table 4.1: Overview of the simulation suite

Model	$N_{\rm SN}$	$n_{\rm H}$ $[{\rm cm}^{-3}]$	$\Delta x_{\rm min}$ [pc]	$\lfloor R_{\rm sf} / \Delta x_{\rm min} \rfloor$ [a]	Comment
N1_n-1_L11	1	0.1	0.5	118	
N1_n0_L11	1	1	0.5	45	
N1_n0_L11_HC	1	1	0.5	45	L = 256 pc, $\Delta x_{\rm max} = 2\,{\rm pc}$, $t_{\rm end} = 1.5\,{\rm Myr}$
N1_n1_L11	1	10	0.5	17	
N1_n1_L11_HC	1	10	0.5	17	L = 64 pc, $\Delta x_{\rm max} = 0.5\,{\rm pc}$, $t_{\rm end} = 1.5\,{\rm Myr}$
N1_n2_L12	1	100	0.25	13	
N1_n2_L13	1	100	0.125	26	
N1_n2_L13_noAMR	1	100	0.125	26	L = 128 pc, $\Delta x_{\rm max} = 0.125\,{\rm pc}$
N1_n2_L13_HC	1	100	0.125	26	L = 64 pc, $\Delta x_{\rm max} = 0.5\,{\rm pc}$, $t_{\rm end} = 1.5\,{\rm Myr}$
N1_n2_L14	1	100	0.0625	52	
N5_n-1_L11	5	0.1	0.5	189	
N5_n0_L11	5	1	0.5	72	
N5_n1_L11	5	10	0.5	27	
N5_n2_L11	5	100	0.5	10	
N14_n-1_L11	14	0.1	0.5	255	
N14_n0_L11	14	1	0.5	97	
N14_n1_L11	14	10	0.5	36	
N14_n2_L11	14	100	0.5	14	
N1_n1_L11_Dust	1	10	0.5	17	Dust only cooling model of Ploeckinger & Schaye (2020).
N1_n1_L11_PS20	1	10	0.5	17	Fiducial cooling model of Ploeckinger & Schaye (2020).

[a] Equation 4.3

$L = 1024\,{\rm pc}$ and periodic boundaries, which we refine with $l_{\rm min} = 7$ to $l_{\rm max} = 11$ refinement levels, corresponding to a spatial resolution of $\Delta x_{\rm max} = 8\,{\rm pc}$ and $\Delta x_{\rm min} = 0.5\,{\rm pc}$, respectively. However, we ensure that the resolution criterion of Kim & Ostriker (2015) is fulfilled and accordingly increase the resolution in runs, where the expected radius at shell formation would not be resolved with at least 10 grid cells.

Initially, the simulation domain is filled with uniform density gas with $\log n_{\rm H} \left[{\rm cm}^{-3}\right] \in \{-1, 0, 1, 2\}$ at solar metallicity and an initial temperature set to be close to cooling equilibrium. In the domain center, we initialize the explosive ejecta uniformly within a spherical region of radius $R_{\rm inj} \sim 5\,\Delta x_{\rm min}$. We inject $E_{\rm SN} = 10^{51}\,{\rm erg}$ and $M_{\rm ej} = 5\,{\rm M}_\odot$ per SN, corresponding to an initial ejecta temperature of $T_{\rm SN} \sim 10^9\,K$. We ensure that the injection region is maximally refined, by statically refining the central $R_{\rm ref} = 50\,\Delta x_{\rm min}$ with the maximum resolution.

In order to ensure that the shock and the bubble are maximally refined, while only as little as possible of the surrounding medium is refined, we advect a passive scalar variable $Z_{\rm ej}$ with the injected mass and maximally refine all cells where $Z_{\rm ej} > 10^{-15}$. The criterion might fail, if numerical errors in the advection of pristine cells trigger the criterion or if cells just behind the shock are not polluted enough to trigger refinement. However, we have checked that both of these cases do not occur frequently enough to cause any serious problems. In the Appendix C.1 we discuss the role of the AMR in more detail.

Besides different densities we also consider different explosion strengths, mimicking the feedback from a single stellar population with $N_{\rm SN} \in \{1, 5, 14\}$ massive stars exploding all at once, by simply injecting $N_{\rm SN}$ times as much mass and energy. We thus label a model with $N_{\rm SN} = x$, $\log n_{\rm H} = y$ and $l_{\rm max} = z$ as Nx_ny_Lz. While this simplistic approach can capture some aspects of clustered feedback, it is worth noting that studies that take into account the time delay between explosions find some qualitative differences, such as an increased momentum per SN (Walch & Naab, 2015; Gentry et al., 2019) and a longer lived hot bubble (Kim et al., 2017).

All models are run until $t = 14\,{\rm Myr}$ at which point the largest bubbles are reaching the domain limits. We reran some of the models in a smaller domain for a shorter time span, but with a much higher frequency of snapshots. For these models we add the suffix _HC to the name and the part of the name referring to the resolution refers to the *equivalent* refinement level for the fiducial

domain, i.e. L11 refers to $\Delta x_{\rm min} = 0.5\,{\rm pc}$ in both the fiducial and the HC runs.

In appendix C.3 we will discuss the effect that different cooling functions could have on our results. To this end, we rerun a few of the models with different cooling tables taken from Ploeckinger & Schaye (2020) and label the models with suffices corresponding to the respective alternate cooling model.

Finally, in section C.2 we are discussing the results obtained for the N1_n2 model at different resolutions.

A list of all the different models and their properties is given in table 4.1.

4.1.2 Data Analysis

In order to quantify the global evolution of the gas, we distinguish between bubble and shell gas and further within these components, differentiate between gas which is moving radially outward ($v_r > 0$) and inward ($v_r < 0$). We distinguish between the SNR and the ISM using the passive scalar, i.e. gas with $Z_{\rm ej} > 10^{-10}$ is considered part of the SNR. The bubble is defined as SNR gas that is either hot ($T > 2 \times 10^4\,{\rm K}$) or diffuse ($n_{\rm H} < 10^{-2}\,{\rm cm}^{-3}$), while the shell is all SNR gas that is not part of the bubble. A summary of the classification is given in Figure 4.1.

Kim & Ostriker (2015) use a similar criterion for the bubble gas, considering only the temperature of the gas. The addition of the density criterion only becomes important at late times, when the bubble has cooled below $10^4\,K$ at which point the temperature criterion alone would fail to differentiate between the bubble and the shell.

The partition of the SNR into a bubble and shell, allows us to measure the shell formation timescale $t_{\rm sf}$, which denotes the time when the cold shell at the shock front forms. We follow Kim & Ostriker (2015), who define the numerically measured shell formation timescale $t_{\rm sf}^{\rm n}$ as the time at which the mass of the hot bubble reaches its maximum.

4.2 Results

In this section we describe a mechanism for the formation of a cloud through the implosion of a radiative SNR. In section 4.2.1 we give a brief overview of the physical mechanism. We provide a detailed description of our simulation results for a single SN in a high density ISM in section 4.2.3. In section 4.2.4 we extend our analysis to the whole simulation suite and investigate the dependence of the relevant timescales on the explosion parameters in section 4.2.4. We describe the properties of the implosion clouds in section 4.2.5. Finally, in section 4.2.2 we describe a model for the launching of the implosion.

4.2.1 Schematic Overview

Figure 4.2 gives a schematic description of the evolution of the SNR after shell formation, which is separated into four stages.

In the first stage, shortly after shell formation the interior of the SNR is still hot and overpressurized relative to the isothermal shell, which is kept at about $T \sim 10^4\,{\rm K}$. During this stage the rarefied bubble material tries to expand and as a result is pressed into the shell. This phase corresponds

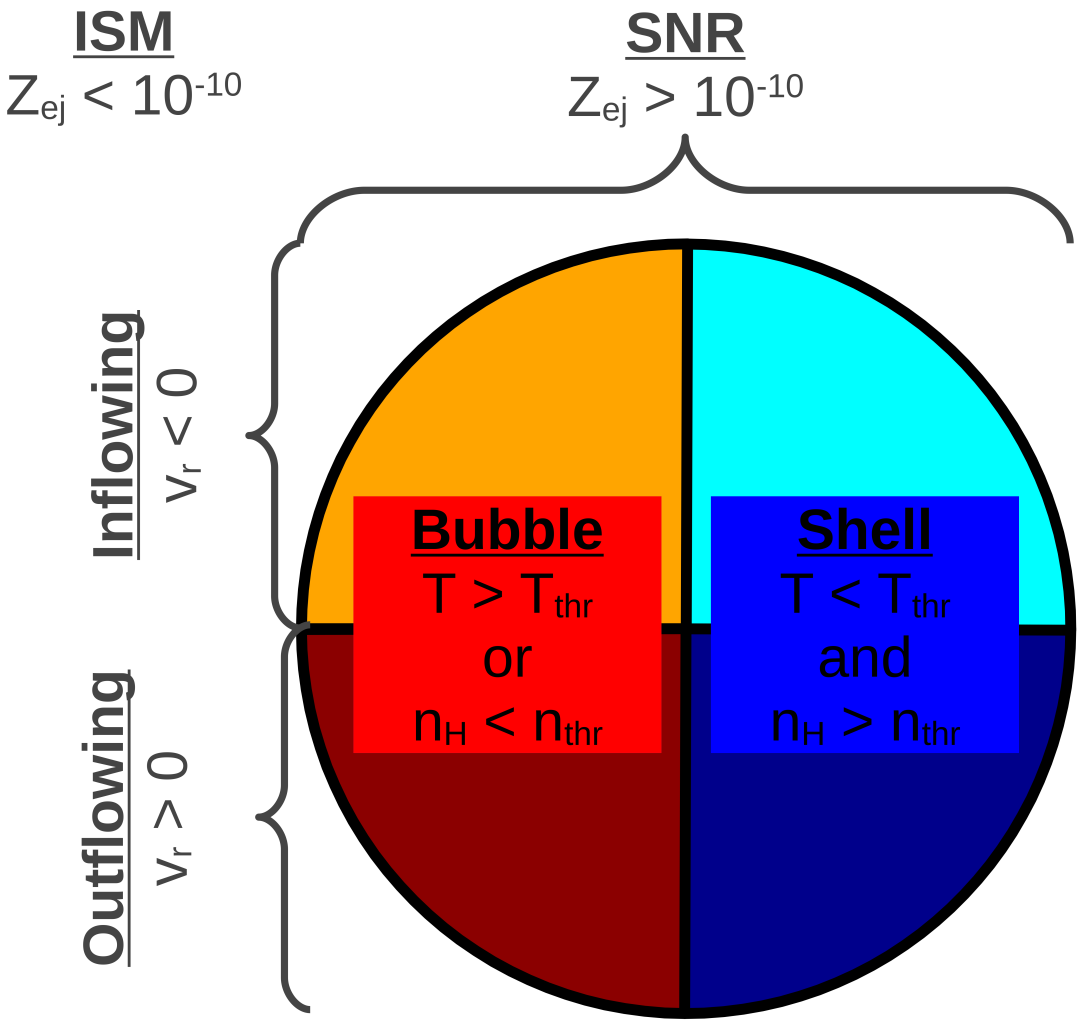

Figure 4.1: Schematic overview of the different gas components, described in section 4.1.2. The classification differentiates between the ISM (gray) and the SNR (color), consisting of a bubble (shades of red) and a shell (shades of blue), which itself might be out- or inflowing. To reduce the amount of colored area the background color of this figure was modified with respect to the original in the journal article.

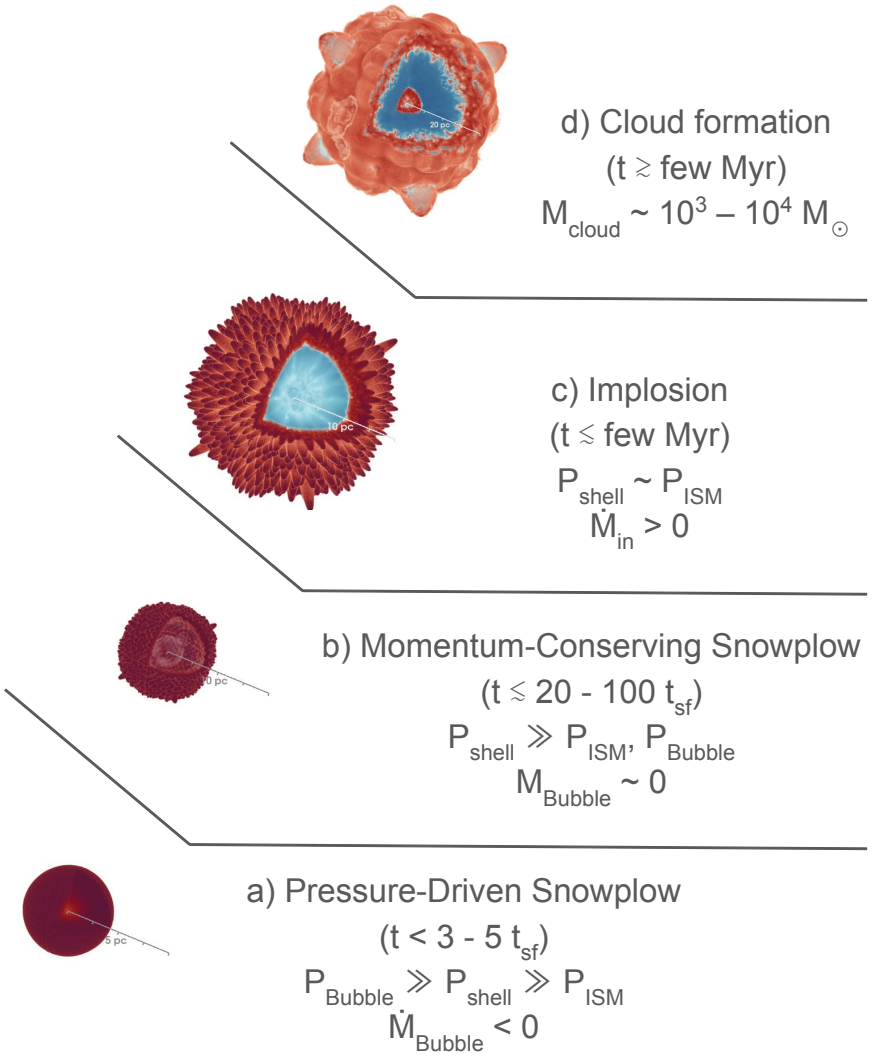

Figure 4.2: Schematic overview of our proposed cloud formation mechanism. We show volume renderings of the radial mass flux in the model N1_n2_L14, during different phases of SNR late stage evolution. The physical scale differs between the frames. Opacity alpha is scaled with the logarithm of the density and is set to zero for densities in the range $n_{\mathrm{H}} \in (95, 105)\,\mathrm{cm}^{-3}$ in order to remove the foreground. The octant facing the observer has been made transparent. To reduce the amount of colored area the background color of this figure was modified with respect to the original in the journal article.

to the modified PDS phase described by Cioffi et al. (1988) and Kim & Ostriker (2015). After about $3-5$ shell formation timescales the bubble has been evacuated and its pressure has dropped below that of the shell.

At this point, the expansion of the SNR is entirely inertia driven, corresponding to the MCS. The mass of the evacuated bubble is negligibly small and its density is many orders of magnitude below the ambient density. The shell which is now overpressurized relative to both the ISM and the bubble, begins to broaden, leading to a gradual reduction in the shell pressure and an accelerated weakening of the shock. Meanwhile, the shell begins to get deformed and fragmented due to thin-shell overstability and nonlinear thin-shell instability (Vishniac, 1983; Blondin et al., 1998).

Once the shell pressure reaches pressure equilibrium with the ISM a reflected version of the outgoing shock wave is launched driving cooling material from the shell back into the center, refilling the warm, evacuated cavity. We refer to this reflected wave as *Implosion* or *Backflow*. The implosion is very similar to the so-called "negative phase" in the context of terrestrial blast waves (see e.g. Glasstone & Dolan, 1977) and appears to be a purely hydrodynamic realization of the hydromagnetic Rayleigh-Taylor instability (RTI) described by Breitschwerdt et al. (2000).

After a few Myr, the backflow reaches the center of the SNR and collides with the backflowing gas from all directions. The colliding gas piles up in the center and is reflected, forming a slowly expanding cloud. The cloud keeps accreting material from the backflowing gas reaching a mass of $10^3 - 10^4\,\mathrm{M}_\odot$ within $\sim 10\,\mathrm{Myr}$. As the cloud is directly formed from the SN ejecta, it is highly chemically enriched.

4.2.2 Model for the Launching of the Backflow

In the previous subsection we have given an overview of the different phases of the radiative stage. Here we describe a model for estimating the relevant timescales.

Right after shell formation, we assume that the bubble is following the modified PDS described by Kim & Ostriker (2015). In their description the thermal energy of the bubble evolves as

$$E_{\mathrm{th,\ PDS}} = 0.8\, E_{\mathrm{th,\ ST}} \left(\frac{R_{\mathrm{sf}}}{R}\right)^2 \frac{t_{\mathrm{sf}}}{t}, \tag{4.1}$$

where t_{sf} and R_{sf} are given by (Kim & Ostriker, 2015)

$$t_{\mathrm{sf}} \sim 0.044\, E_{51}^{0.22}\, n_0^{-0.55}\,\mathrm{Myr}, \tag{4.2}$$

$$R_{\mathrm{sf}} \sim 22.6\, E_{51}^{0.29}\, n_0^{-0.42}\,\mathrm{pc}, \tag{4.3}$$

$E_{\mathrm{th,\ ST}} = 0.72\, E_{\mathrm{SN}}$ and

$$R = R_{\mathrm{sf}} \left(\frac{t}{t_{\mathrm{sf}}}\right)^{2/7}. \tag{4.4}$$

Here $E_{51} = E_{\mathrm{SN}} / \left(10^{51}\,\mathrm{erg}\right)$. The average bubble pressure is then given by

$$P_{\mathrm{Bubble,\ PDS}} = (\gamma - 1)\, \frac{E_{\mathrm{th,\ PDS}}}{4\pi/3 R^3}. \tag{4.5}$$

Meanwhile, the temperature of the shell remains roughly constant at $T_{\mathrm{shell}} \sim 10^4\,K$ and the compression ratio of the shell is $\chi \sim 10$, leading to a shell pressure of $P_{\mathrm{shell,\ PDS}} \sim 10^5\, n_0\, k_{\mathrm{B}}\,\mathrm{K\,cm^{-3}}$. The PDS phase ends, when the pressure in the shell and bubble is equal, at

$$t_{\mathrm{PDS}} \sim 3.4\, E_{51}^{0.05}\, n_0^{0.11} t_{\mathrm{sf}} \sim 0.15\, E_{51}^{0.27}\, n_0^{-0.44}\,\mathrm{Myr}. \tag{4.6}$$

The radius of the SNR at this time is

$$R_{\mathrm{PDS}} \sim 32.1\, E_{51}^{0.3}\, n_0^{-0.39}\,\mathrm{pc}. \tag{4.7}$$

After the PDS phase has ended, the momentum of the shell remains constant and the MCS phase begins. During this phase the radius of the SNR evolves $\propto t^{1/4}$ and correspondingly the shock velocity evolves $\propto t^{-3/4}$. If one assumes a constant compression ratio and that the temperature of the shell is proportional to the square of the velocity, as one would expect for a strong shock, one finds for the pressure during the MCS phase

$$P_{\mathrm{Shell,\ MCS}} = P_{\mathrm{shell,\ PDS}} \left(\frac{t}{t_{\mathrm{PDS}}} \right)^{-3/2}. \tag{4.8}$$

The SNR implodes, when the pressure of the shell approaches the pressure of the ISM. In the standard RAMSES cooling prescription at solar metallicity, which assumes collisional ionization equilibrium the pressure on the cooling-equilibrium curve for a given density is approximately (see e.g. Figure 17 of Kim et al. (2023b))

$$P_{\mathrm{ISM,\ eq}} \sim 6 \times 10^3\, n_0^{1/2}\, k_{\mathrm{B}}\,\mathrm{K\,cm^{-3}}. \tag{4.9}$$

Thus, the launching timescale can be inferred as

$$t_{\mathrm{launch}} \sim 0.98\, E_{51}^{0.27}\, n_0^{-0.11}\,\mathrm{Myr}, \tag{4.10}$$

and the radius of the SNR at this time is

$$R_{\mathrm{launch}} \sim 51.3\, E_{51}^{0.3}\, n_0^{-0.27}\,\mathrm{pc}. \tag{4.11}$$

Finally, cloud formation happens once the imploding shell has reached the center. The cloud formation timescale is thus the combination of the launching and the crossing timescale

$$t_{\mathrm{cf}} \sim t_{\mathrm{launch}} + \frac{R_{\mathrm{launch}}}{V_{\mathrm{in}}}, \tag{4.12}$$

where V_{in} is a characteristic inflow velocity. The results in section 4.2.4 indicate that this velocity is independent of the explosion energy, but depends on the ambient density in a complicated way.

4.2.3 Single Supernova in a High Density Medium

In this subsection we describe the time evolution of the SNR formed by a single SN in a stationary, uniform, high density medium in cooling equilibrium.

We first give a qualitative overview of our ultra high resolution model N1_n2_L14 with a maximum grid resolution of $\Delta x = 0.0625\,\mathrm{pc}$. In Figure 4.3 the density (top panels) and radial mass flux (bottom panels) is shown in slices through the xy-plane at four different points in time corresponding to the four different stages of SNR evolution after shell formation. In order to provide a quantitative reference, radial profiles of various physical quantities at the same points in time are shown in Figure 4.4.

During the first stage, right after shell formation, the shell reaches a maximum compression ratio of $\chi \sim 10$. Its width is comparable to the resolution limit $\Delta R \sim \Delta x = 0.0625\,\mathrm{pc}$. The pressure of the hot interior is about an order of magnitude higher than that of the rapidly cooling shell, and as a result bubble material is condensing onto the shell.

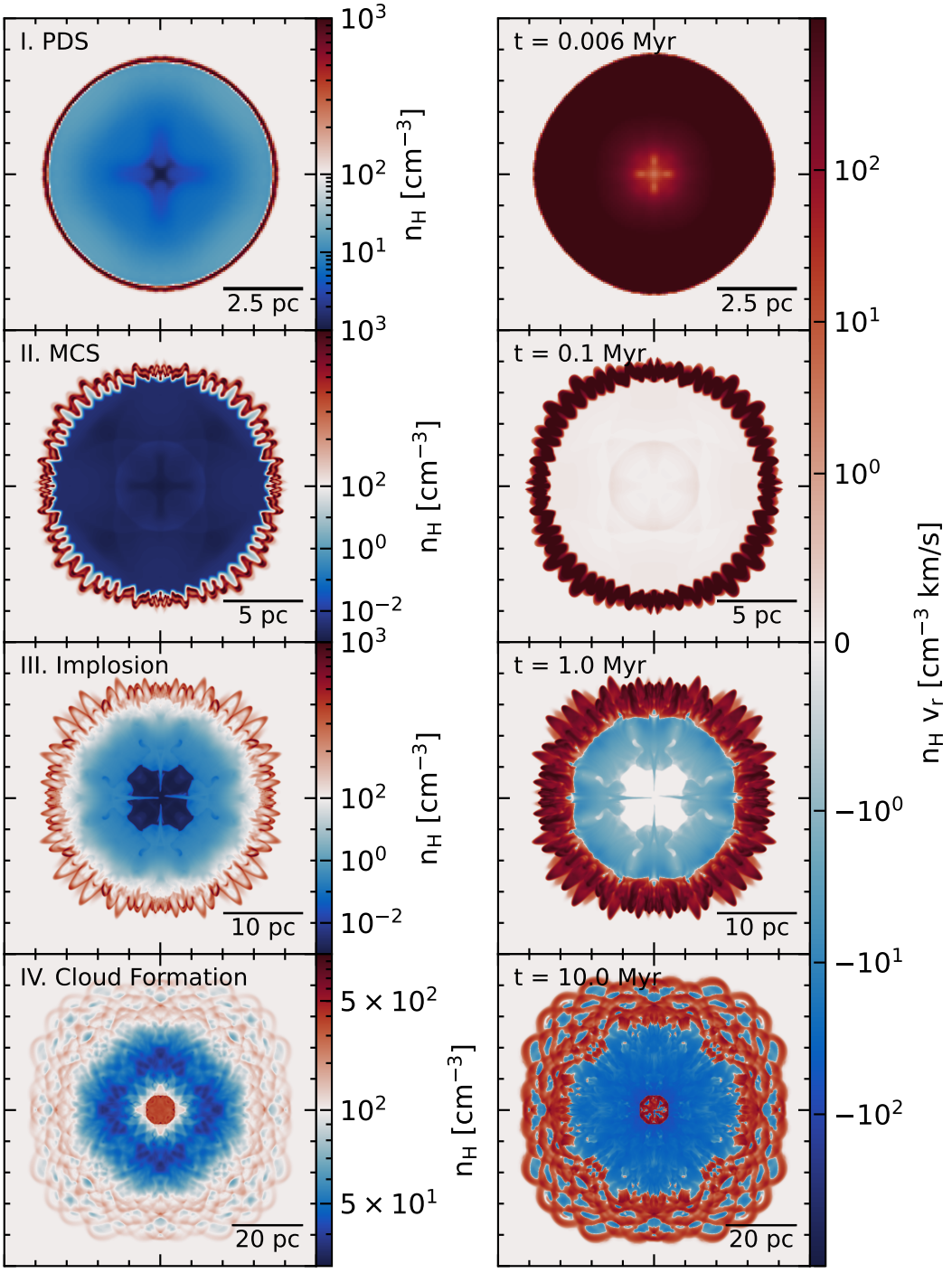

Figure 4.3: Slices through the XY-plane of the model N1_n2_L14. The left and right columns display density and radial mass flux at different stages during the radiative phase of SNR evolution, respectively. The panels from top to bottom correspond to t = 0.006, 0.1, 1 and 10 Myr. Each panel showing density has a different color scale due to the large changes in dynamic range. The color scale for the density slices is logarithmic and asymmetrically centered around the ambient density $n_{\mathrm{H,\,ISM}} = 100\,\mathrm{cm}^{-3}$. The color scale for the radial mass flux is the same in all panels.

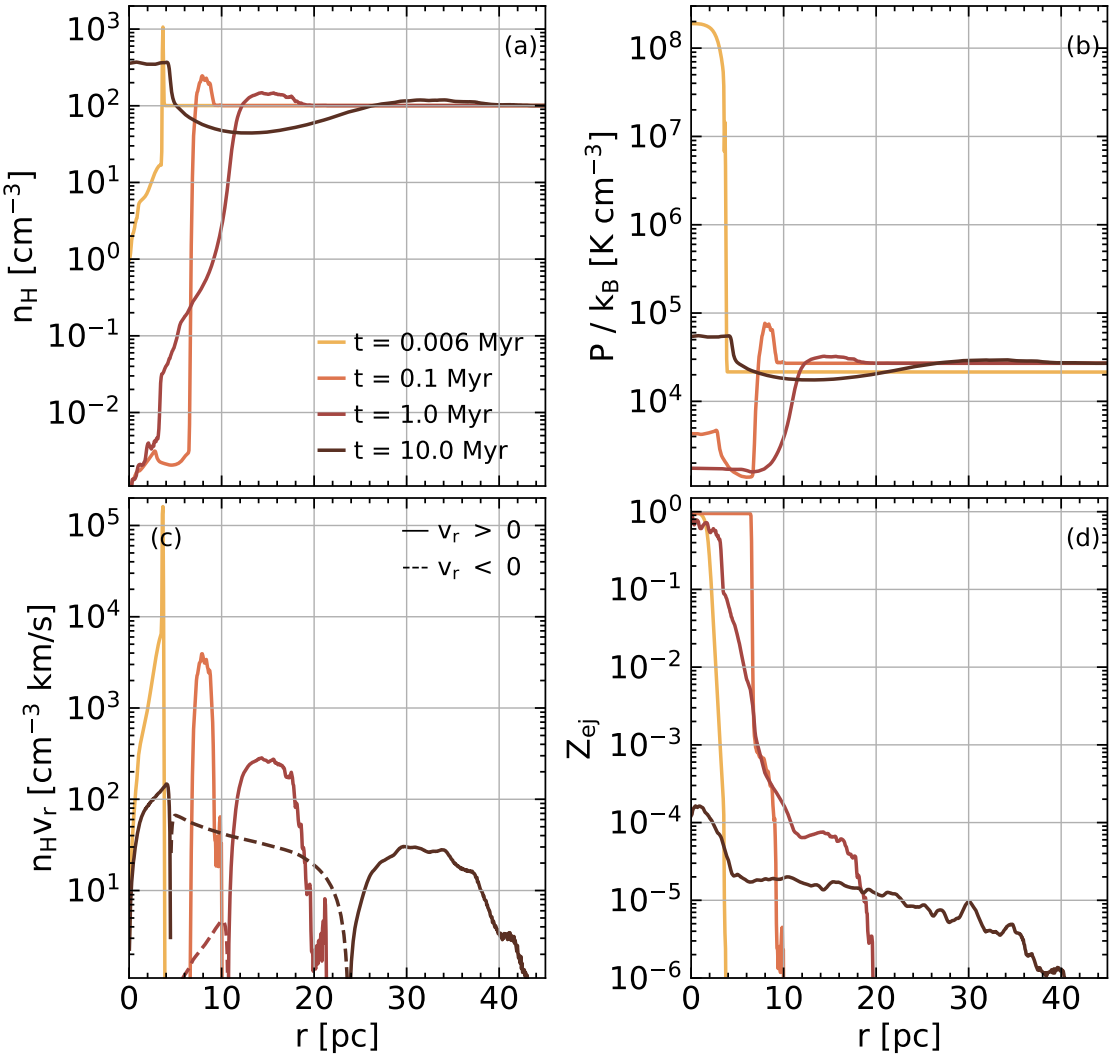

Figure 4.4: Radial profiles of (a) number density, (b) pressure, (c) mass flux, and (d) enrichment of model N1_n2_L14. The differently shaded curves correspond to t = 0.006, 0.1, 1 and 10 Myr, respectively. In panel (c) solid (dashed) lines correspond to outward (inward) mass flux.

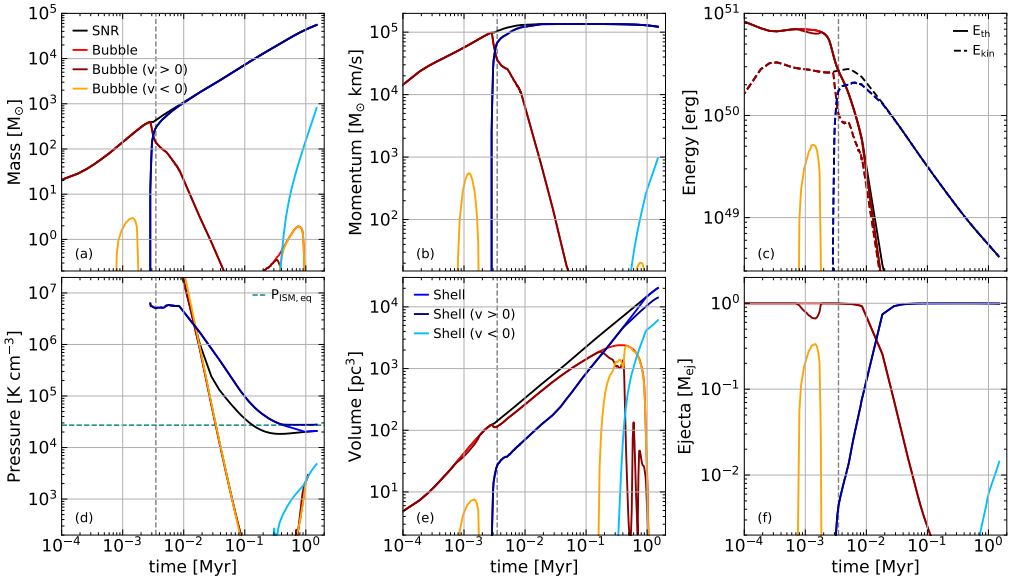

Figure 4.5: Time evolution of various quantities for model N1_n2_L13: (a) mass, (b) momentum, (c) energy, (d) pressure, (e) volume, (f) ejecta. Differently colored lines correspond to different gas components as described in Figure 4.1. The vertical dashed line marks the theoretical estimate of the shell formation time (Equation 4.2). In panel (c) the thermal (solid) and kinetic (dashed) energy is shown. The horizontal green dashed line in panel (d) marks the equilibrium pressure of the ISM. The bubble pressure is initially very high ($\gtrsim 10^9\,\mathrm{K\,cm^{-3}}$) and thus outside of the axis limits.

After 0.1 Myr, the bubble has been mostly evacuated ($n_{\mathrm{H,\ Bubble}}/n_{\mathrm{H,\ ISM}} < 10^{-4}$) and the shell has thickened considerably ($\Delta R \sim 3\,\mathrm{pc}$), leading to an overall reduction in the compression ratio ($\chi \sim 2.5$) of the shell. The pressure in the bubble has dropped significantly to about 10 % of the ISM pressure, while the pressure of the shell is still overpressurized with respect to the ISM. During this stage the mass flux is concentrated within the shell, with only little outward mass flux from inside the bubble. The shell is subject to thin-shell overstability and nonlinear thin-shell instability (Vishniac, 1983, 1994; Blondin et al., 1998), resulting in ripples on the shell's surface.

We note that we do *not* explicitly seed perturbations that would drive these instabilities. Instead, they arise from grid scale perturbations due to the mapping of the sphere onto a Cartesian grid and numerical instabilities such as the *carbuncle instability* (see e.g. appendix C of Stone et al., 2008). We refer the interested reader to appendix C.2, where we discuss in more detail the dependence of these artifacts on the resolution and how they might affect our results.

After 1 Myr the flow just behind the shell has reversed and is now flowing inward, starting to slowly fill up and cool the bubble with material from the backside of the shell. Meanwhile, the pressure of the shell has dropped to a level comparable to the ISM pressure. The shell continues to broaden ($\Delta R \sim 7\,\mathrm{pc}$) and the compression ratio ($\chi \sim 1.5$) continues to drop, approaching unity. During these first three stages, most of the mass of the bubble gas is composed of ejecta material.

Finally, after 10 Myr the inward flow has reached the center and is compressed into a compact, dense, expanding cloud with a constant density of about 3 times the ISM density and a size of about 5 pc. The mass fraction of the ejecta in the cloud is up to an order of magnitude larger than in the rest of the SNR. The outer radius of the cloud is bounded by more inflowing material, which is slightly underdense relative to the ISM. Meanwhile, the shell has broadened to about $\Delta R \sim 20\,\mathrm{pc}$ and the compression ratio is only slightly above unity. The shell instabilities have

lead to complex substructure within the shell. The shell is composed of many $\sim$ pc size *blisters*, which are bounded by outflowing, overdense shells and filled with inflowing, underdense gas.

In order to describe the launching mechanism of the implosion in more detail, in Figure 4.5 we show the time evolution of various globally computed quantities for the model N1_n2_L13_HC with a maximum grid resolution of $\Delta x = 0.125\,\mathrm{pc}$. Here we use the L13 model, because due to storage limitations it was not feasible to run an L14 model with high output cadence. The different panels show the time evolution of mass, momentum, kinetic & thermal energy, pressure, volume and ejecta mass, calculated for the different gas components described in Figure 4.1.

Extensive quantities are computed by summing up the contributions from each cell belonging to the respective gas components. The volume averaged pressure of each gas component i is calculated as

$$p_i = (\gamma - 1)\,\frac{E_{\mathrm{th},i}}{V_i}, \tag{4.13}$$

where $\gamma = 5/3$ is the adiabatic index, $E_{\mathrm{th},i}$ is the thermal energy and V_i is the volume.

After an initial relaxation period the solution approaches the energy-conserving ST phase, during which the entire SNR is hot and $\sim 70\,\%$ of the energy is thermal, in agreement with analytical calculations (Taylor, 1950; Sedov, 1959).

Shortly before shell formation, after $t \sim 10^{-3}\,\mathrm{Myr}$, a reverse pulse emerges, is reflected in the center and merges with the shock again.

At shell formation $t_{\mathrm{sf}} \sim 3{\times}10^{-3}\,\mathrm{Myr}$ the bubble mass reaches a maximum and the shell mass begins to increase. Similarly the momentum of the bubble gas reaches a maximum as the momentum of the shell starts to increase. The total thermal energy begins to drop steeply, while the kinetic energy remains constant. The thermal energy is dominated by the bubble while the shell carries negligible amounts of thermal energy. On the contrary the kinetic energy of the bubble drops rapidly and is taken over by that of the shell. The pressure of the shell after its formation is initially roughly constant and much lower than that of the bubble, which however drops rapidly. The volume of the SNR is dominated by the hot bubble, which after shell formation initially decreases until it reaches a fixed volume filling factor of about $\sim 2/3$, with a corresponding volume filling factor of the shell of about $\sim 1/3$. Most of the ejecta stay within the bubble and only slowly get incorporated into the shell. This behavior is in line with the modified version of the PDS phase described in 1D by Cioffi et al. (1988) and in 3D by Kim & Ostriker (2015).

After about $10^{-2}\,\mathrm{Myr}$ most of the SNRs mass, momentum and kinetic energy is carried by the still entirely outward moving shell. Until this point the momentum has still been increasing, but at this point the increase stops, marking the beginning of MCS phase. The kinetic energy starts to decrease as $t \propto t^{-0.75}$, consistent with the analytical expectation. The pressure of the shell begins to decrease due to the effect of radiative cooling, while the pressure of the bubble keeps decreasing rapidly. About $10\,\%$ of the ejecta are now in the shell.

After $2 \times 10^{-2}\,\mathrm{Myr}$ the pressure of the bubble falls below that of the shell. At this point the volume filling factor of the bubble begins to decrease and that of the shell correspondingly has to increase, corresponding to a relative broadening of the shell. At this point the majority of the ejecta mass is in the shell.

The backflow emerges after $t_{\mathrm{launch}} \sim 0.3\,\mathrm{Myr}$ at the same time as the pressure of the shell approaches the ambient pressure. This inward flow is quite different from the series of reflected sound waves described by Cioffi et al. (1988). While the sound waves are associated with the bubble and carry negligible amounts of mass, the implosion is associated with the shell and carries relatively large amounts of mass, which are growing. The pressure of the outward moving shell levels off at the ISM pressure, while that of the inward moving component increases. The emergence of the

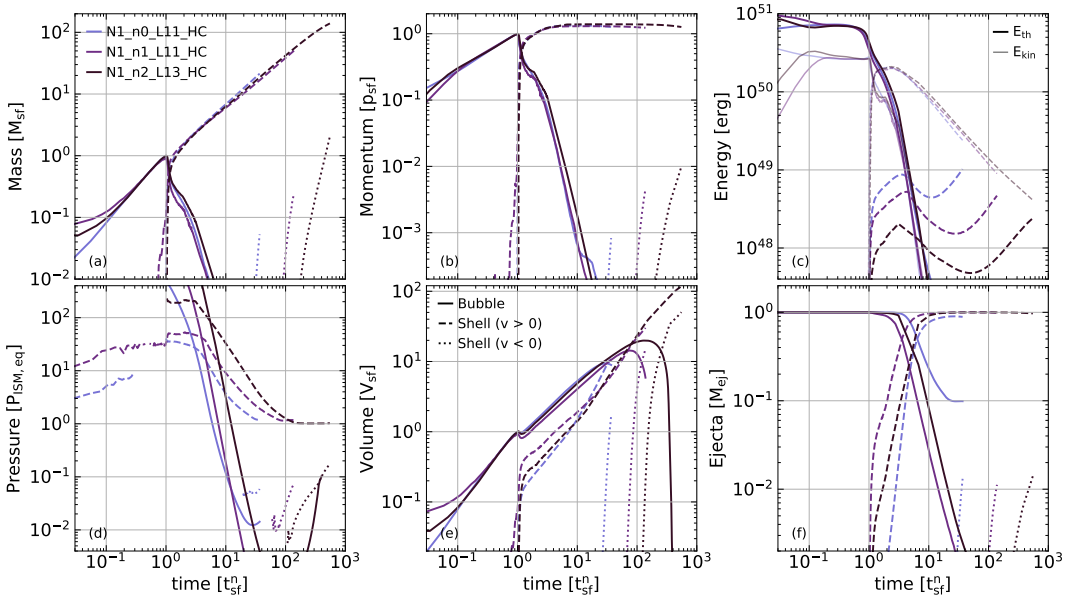

Figure 4.6: Rescaled version of Figure 4.5 for various models in media with different density. Solid, dashed and dotted lines correspond to the hot bubble, outflowing, and inflowing shell, respectively. The time is normalized by $t_{\rm sf}^{\rm n}$ (see text). Quantities with subscript 'sf' correspond to the value of the whole SNR at $t = t_{\rm sf}^{\rm n}$. In panel (c) the thermal and kinetic energy are plotted with an opacity alpha of 1 and 0.5, respectively.

backflow leads to a slight decrease in total radial momentum.

After 1.5 Myr, about 1 % of the shell mass is moving inward, carrying about 1 % of the ejecta back to the center. At this point, the bubble has disappeared entirely.

4.2.4 Universality of the Mechanism

In Figure 4.6 we show a rescaled version of Figure 4.5 for the models N1_n0_L11_HC, N1_n1_L11_HC and N1_n2_L11_HC. Time is measured in units of the shell formation timescale $t_{\rm sf}^{\rm n}$. Mass, momentum and volume are normalized to their value at $t_{\rm sf}^{\rm n}$ and pressure is normalized to the ISM value in cooling equilibrium.

As expected from the self-similarity during the ST phase (Sedov, 1959), all models exhibit a very similar time evolution before shell formation. In the models N1_n0_L11_HC and N1_n1_L11_HC there is already some small amount of cold gas during this phase. This is due to the method used to extract SNR gas, which might include a negligible number of unshocked cells.

After shell formation, the time evolution in all models is qualitatively the same as for N1_n2_L13_HC, though timescales in units of the shell formation timescale may differ. In the models N1_n0_L11_HC and N1_n1_L11_HC the pressure of the outward moving shell starts to decrease after the bubble pressure falls below it after 3 – 4 $t_{\rm sf}^{\rm n}$, while in N1_n2_L13_HC it already starts to decrease already slightly before that.

We interpret this difference as follows: The pressure can either decrease by radiative cooling or adiabatic expansion. When the pressure of the bubble drops below the shell pressure before radiative cooling becomes important, the shell will cool adiabatically. On the other hand, if the

cooling timescale is shorter than the timescale to reach pressure equilibrium between the shell and the bubble, the shell will start to cool radiatively before the bubble pressure has dropped. In both cases the shell pressure will start to decrease, albeit with a slightly different scaling. It is therefore no surprise that in the run with a higher density and therefore a shorter cooling timescale, the pressure starts to drop slightly earlier.

In all models, once the pressure of the shell approaches that of the ISM, a steadily growing backflow is launched.

Timescales

Having established the universal emergence of backflows, once the shell pressure approaches that of the ambient medium, we may investigate next, how the timescales for launching the backflow t_{launch} and subsequently forming a central overdensity t_{cf} depend on the explosion parameters.

We define the launching timescale as the earliest time, when the inflowing shell mass exceeds $0.1\,M_{\odot}$. We choose this threshold, because especially in the runs, where the shell is resolved with many cells, instability of the shell itself can lead to eddies within the shell, which lead to a small amount of inflowing shell gas that is not associated to the implosion. The cloud formation timescale is defined as the earliest time after launching, when the density in the innermost radial bin exceeds the ambient density.

Due to the limited temporal resolution of the snapshots, the events actually occur somewhere between the first snapshot when the above conditions are met and the previous snapshot. We therefore report the arithmetic mean of the two time points and indicate the time interval between the two snapshots with error bars.

In Figure 4.7 the timescales are shown as functions of the ambient density (left panels) and the explosion energy (right panels). The markers are colored by the respective other variable.

We find launching timescales between a few hundred kyr and few Myr. There is a negative trend with density and a positive trend with energy. The scaling and normalization are in rough agreement with Equation 4.10, with factor of ~ 2 differences.

At high densities differences might arise, because in the derivation of Equation 4.10 we have neglected the role of radiative cooling below $T \sim 10^4\,\mathrm{K}$ for the shell gas (see also discussion of Figure 4.6), which would lead to a shallower scaling of t_{PDS} (Eq. 4.6) with density, which in turn manifests as a steeper scaling of t_{launch}.

At the low density end, the differences might arise, because here $P_{\mathrm{shell,\ PDS}}$ is already quite similar to $P_{\mathrm{ISM,\ eq}}$ and therefore the assumed scaling might not apply since the shock is already quite weak at t_{PDS}.

The cloud formation timescale is on the order of several Myr to over 10 Myr for our simulations with the highest explosion energies and lowest densities. At $n_{\mathrm{H}} = 0.1\,\mathrm{cm}^{-3}$ no overdense clouds have formed by the end of our simulations. There is no clear trend with density. The cloud formation timescale becomes shorter for SNRs in higher density environments, though for high explosion energies the timescale appears to level off and it even slightly increases for the highest densities. The timescale generally increases with energy, roughly scaling like $t_{\mathrm{cf}} \propto E_{51}^{0.3}$.

The scaling with the explosion energy appears to be the same as the scaling of the radius of the SNR at launching $R_{\mathrm{launch}}\,(E_{51}, n_{\mathrm{H}})$, as predicted by Equation 4.11. Equation 4.12 then implies that the implosion velocity V_{in} is independent of explosion energy and depends only on density.

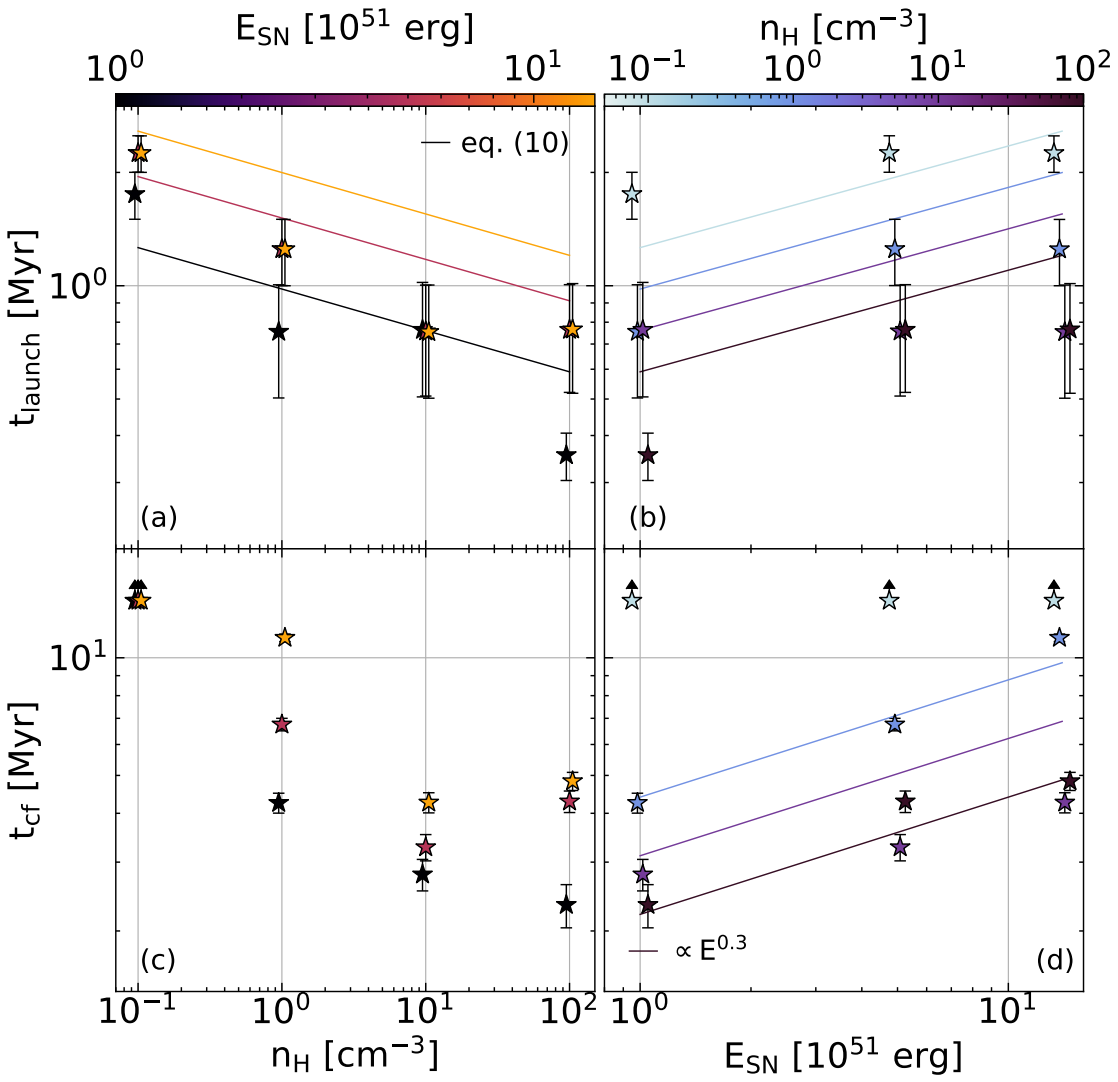

Figure 4.7: Launching timescale (top panels, a & b) and cloud formation timescale (bottom panels, c & d) as a function of explosion parameters. Left panels (a & c) show the timescales as a function of ISM density and right panels (b & d) as a function of explosion energy. Solid lines correspond to the model described in section 4.2.2. Data points are colored by the respective other explosion parameter. We added a small displacement ($\leq 5\,\%$) to the x-values in order to reduce the overlap of the markers.

4.2.5 Cloud Properties

In the previous section we have shown that for a wide range of explosion parameters, the SNRs implode and form a cloud in their center. Here we summarize the properties and evolution of these clouds and discuss how they depend on the explosion parameters.

To this end, we utilize radial profiles of density, kinetic and thermal energy density to compute the size, mass and virial parameter of the clouds. We note that our simulations are strictly without self-gravity. The timescale for self-gravity to have a qualitative effect on the evolution of the SNR is much longer than the simulation time. Nonetheless, it might have an effect on the evolution of the dense cloud, and in order to estimate the importance of self-gravity for the cloud and predict whether or not it might become self-gravitating and eventually form stars it is useful to look at the virial parameter.

We define the size of the cloud as the radius of the interface between the innermost radial bin, where the density falls below the ambient density. The cloud mass is defined as the integral of the density profile up to that radius and the virial parameter is defined as the ratio of the sum of kinetic and thermal energy and the modulus of the potential energy of the cloud. The kinetic and thermal energy are computed by integrating over the respective radial profiles and the potential energy is defined as

$$|E_{\rm pot}| = \frac{3}{5}\frac{GM_{\rm cloud}^2}{R_{\rm cloud}}. \tag{4.14}$$

Here we assume that the density profile within the cloud is flat and that all motion within the cloud is opposing the gravitational pull. Both of these assumptions approximately hold true (see e.g. Figure 4.4).

In Figure 4.8 we present the time evolution of the cloud's size, mass and virial parameter for the different models.

In panel a) the cloud radius is shown as a function of time. The cloud grows to a size of several to few tens of parsecs within 10 Myr. In lower density environments clouds grow larger, with little dependence on the explosion energy.

Panel b) shows the cloud's mass as a function of time. At the end of the simulation, the mass of the central cloud has reached a value of several thousand to about 2×10^4 solar masses, with only a small dependence on the density of the ambient medium. Clouds in high density environments become somewhat more massive. There is only little dependence on the explosion energy.

Panel c) shows the cloud's virial parameter as a function of time. The initial virial parameter scales with the ambient density roughly as

$$\alpha_{\rm vir,0} \sim 10^4\, n_0^{-1}, \tag{4.15}$$

where $n_0 = n_{\rm H}/{\rm cm}^{-3}$, and decreases steadily approaching and dropping below $\alpha_{vir} \sim 1$ for the high density runs, suggesting that indeed the clouds would become self-gravitating. There is little variation due to the explosion energy.

The masses and radii of the clouds formed by SN implosion are comparable to the values used in the initial conditions for the clouds in the STARFORGE (Grudić et al., 2022; Grudic et al., 2023; Farias et al., 2024) simulation suite, which studies the star formation from the collapse of a single giant molecular cloud. This suggests, that the thus formed clouds might indeed trigger another generation of star formation.

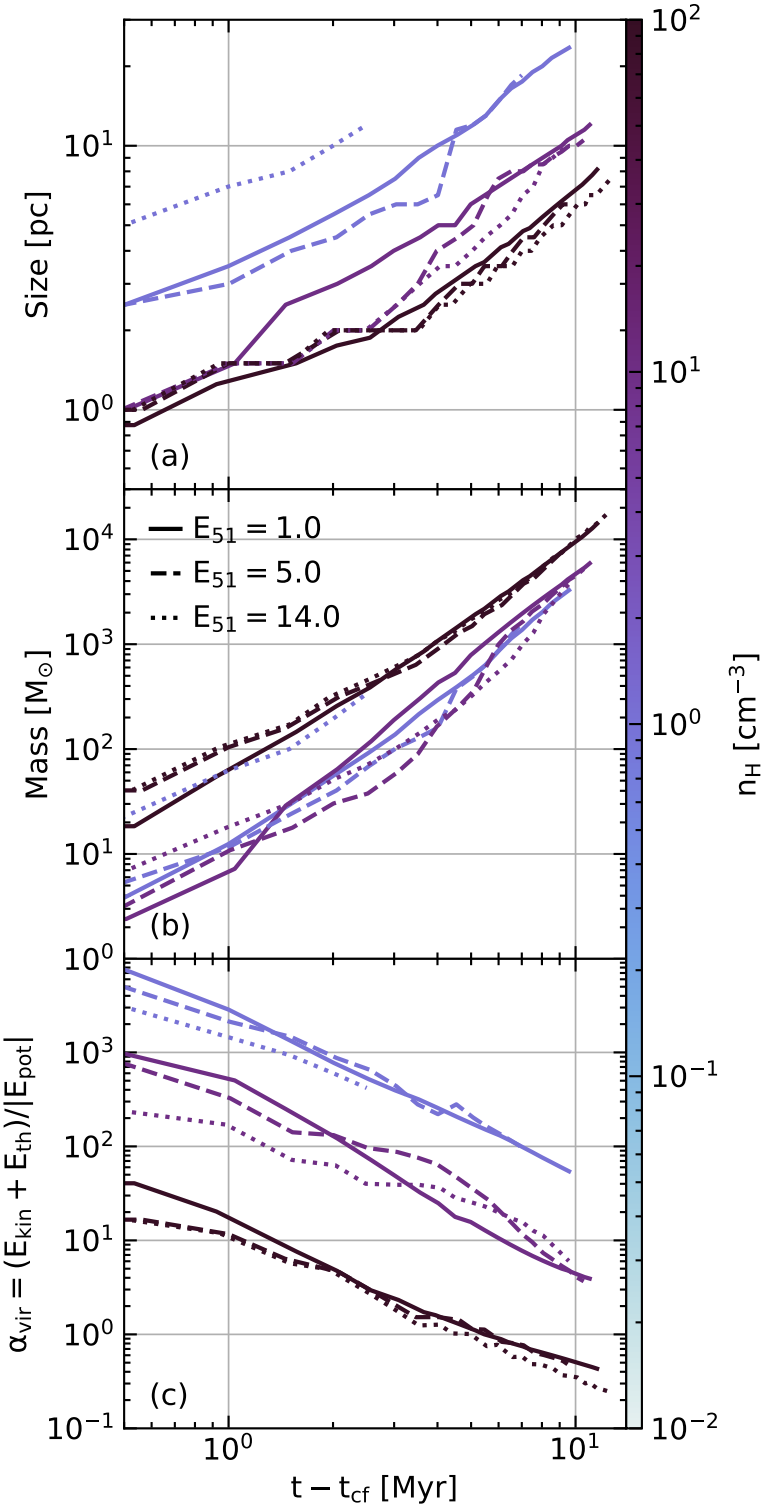

Figure 4.8: Time evolution of the central cloud's radius (a), mass(b) and virial parameter (c) for the different models. Solid, dashed and dotted lines correspond to an explosion energy of $E_{51} = 1.0$, $E_{51} = 5.0$ and $E_{51} = 14.0$, respectively. Lines are colored by the ISM density.

4.3 Discussion

In the previous section we have described a new mechanism by which a cloud can form inside a radiative SNR due to its implosion as the shell pressure approaches that of the ISM. In the following, we will discuss some of the limitations of our model, the role of some of our model ingredients and the implications of our findings in the context of galaxy evolution.

4.3.1 Limitations

In this work, we have shown the existence of SN implosions and subsequent cloud formation in the center of the SNR, using a suite of hydrodynamic simulations of SN explosions in a uniform and stationary medium. Of course, a uniform and stationary ISM is a great simplification of the complexity of a realistic ISM.

In a more realistic model for the ISM, like the kind of turbulent, stratified box used in state-of-the-art ISM simulations (see e.g. Walch et al., 2015; Kim & Ostriker, 2017), the existence of backflows as described in our work is a priori not guaranteed. Continuous or sufficiently frequent energy injection can keep the SNR overpressurized and prevent an implosion (Kim et al., 2017). Indeed, stellar populations are expected to explode SNe in regular intervals before they run out of fuel (see e.g. Leitherer et al., 1999). However, in the cases of runaway stars or populations hosting a sufficiently small number of massive stars this limitation does not apply and even in the case of stellar populations that remain active for a long time, eventually the bubbles are going to evacuate and cool off enough to make an implosion feasible.

Besides the importance of continuous driving, the role of the ambient medium cannot be ignored. In a more realistic description of the ISM, the ambient medium is highly structured due to the combined effect of turbulence, shear and stratification. SNe exploding in such an environment will follow the geometry of the ISM (Makarenko et al., 2023), as the shock wave can only slowly penetrate into dense structures, but will quickly fill out the volume filling low density medium, leading to highly amorphous SNR shapes (Kim & Ostriker, 2015; Lancaster et al., 2021). In such a configuration, the SNR will reach pressure equilibrium at different times in different directions, leading to a displacement and deformation of the clouds formed in this way. If the momentum carried by the backflowing gas from different directions is not equal and opposite, the cloud would further end up with a net momentum leading to a drift. Similar asymmetries can follow from the interaction of the SNR with neighboring shocks, e.g. due to neighboring superbubbles (Breitschwerdt et al., 2000) or small-scale turbulence, which can locally contribute to the pressure opposing the shock expansion. In Appendix C.4 we show, that asymmetries in the ambient pressure can indeed trigger an implosion locally.

Besides the limitations due to the environment, more complete physics might also qualitatively modify our conclusions.

As mentioned in section 4.2.5 the virial parameter of the clouds drops below unity a few Myr after their formation. While it seems plausible that self-gravity is too weak to have an important effect on the implosion mechanism and the crossing of the inflowing gas, once the cloud has formed, it might collapse and fragment due to its self-gravity.

Kim & Ostriker (2015) have demonstrated that magnetic fields play only a subdominant role in SNR evolution. On the contrary, Gentry et al. (2019) show that magnetic fields suppress the growth of instabilities at the bubble-shell interface, which reduces mixing and delays radiative cooling in the case of multiple consecutive SNe. However, it is important to note that Kim & Ostriker (2015) used a mesh code, while Gentry et al. (2019) used a Lagrangian method. While both

methods achieve comparable resolution in the shell, the mass resolution in the bubble is several orders of magnitude higher in mesh codes, which are thus likely less affected by spurious cooling of bubble gas. Nonetheless, contributions to the pressure from a magnetic field and cosmic rays can potentially alter the timescales for implosion and cloud formation or even prevent these processes, if they can maintain a high enough bubble pressure. Indeed, in the case of the hydromagnetic RTI Breitschwerdt et al. (2000) have shown, that the magnetic field has a stabilizing effect, that implies a characteristic length scale at which the instability can act. In this case the backflowing gas fragments into blobs of size similar to the fastest growing wavelength.

Sharma et al. (2014) conducted 1D spherically symmetric simulations of SNe. They note that most of the heat losses occur in the unresolved layer between the bubble and the shell. The physical width of this layer is much too small to resolve, even with their 1D method, but they show that nonetheless the cooling losses are converged, even for moderate resolution.

Similarly, as discussed by Fierlinger et al. (2016), while the length scale associated with thermal conduction is much too small to be resolvable with current techniques, its effect is negligible. However, recent results by El-Badry et al. (2019) in the context of continuously driven superbubbles suggest that heat conduction does in fact play an important role for the transport of energy and mass across the bubble-shell interface. However, it is worth nothing that El-Badry et al. (2019) artificially enhanced the conduction rate to model turbulent mixing due to 3D instabilities, which makes a direct comparison difficult. Lancaster et al. (2021) simulate the expansion of a continuously driven wind bubble in a turbulent medium confirming that turbulence indeed enhances the mixing across the bubble-shell interface leading to catastrophic cooling losses in ideal hydrodynamics. Yet, the importance of these effects remains unclear in a picture where magnetic fields suppress the growth of the instabilities responsible for the mixing. Further studies of individual SNe with resolved heat conduction, magnetic fields and turbulence are required in order to settle this ongoing debate.

4.3.2 Role of the cooling model

In section 4.2.2 we have presented a model for the launching of the backflow. There are two ingredients of our model that are sensitive to assumed cooling physics. First, we have assumed that the temperature of the shell right after shell formation remains stable at 10^4 K, as the time it takes to cool beyond this temperature is much longer than the dynamical timescale. Second, we assume that the ISM is in cooling equilibrium, when we equate the shell pressure with the ISM pressure. Both of these assumptions invoke the assumed cooling physics, which may affect the resulting timescales and cloud properties.

Kim et al. (2023b) compare their detailed radiative transfer model to a range of commonly used cooling functions (see their Figure 17). They find that in these functions the equilibrium pressure at a given density may differ by up to three orders of magnitude between the models. In the Ramses cooling model utilized in this work the equilibrium pressure is indeed relatively high. As a consequence the SNR is expected to implode 100 times earlier with our cooling model, than e.g. with the model by Ploeckinger & Schaye (2020), which has an exceptionally low equilibrium pressure. Further complications like thermal instability and non-equilibrium effects (Katsuragawa et al., 2022), might also qualitatively alter our conclusions.

For a more detailed discussion, we refer the interested reader to appendix C.3, where we compare the results of simulations with different cooling models. The comparison indicates, that indeed a lower ambient pressure will delay the implosion and that the details of the cooling physics, may have a slight effect on the details of cloud formation, even at a comparable ambient pressure.

4.3.3 SN Implosion in the Literature

Despite the fact that the evolution of SNRs in a uniform medium has been studied in great detail for more than 40 years, to our knowledge there has been no mention of SN implosion. Here we discuss the various reasons for why this process might have remained unnoticed for so long.

Many authors (e.g. Chevalier, 1974; Straka, 1974; Thornton et al., 1998; Kim & Ostriker, 2015) only focus on the transition to the radiative phase and would therefore not advance their simulations far enough to reach the implosion stage.

Cioffi et al. (1988) set the pressure of the ambient medium to an artificially low value in order to maintain a strong shock, which in turn delays the implosion.

Fierlinger et al. (2016) use one-dimensional hydrodynamic simulations to study the energy input from SNe in a uniform and stationary media with a range of densities and an initial temperature of 1000 K. They advance their models until the shock velocity approaches the sound speed of the ISM and thus in principle should have been able to see an implosion. However, the internal structure of the SNRs was out of their scope and thus they did not report any backflow.

Gent et al. (2020) utilize three-dimensional hydrodynamic simulations of radiative SNRs to validate the PENCIL code. Even though they advance their models until the shock becomes sonic, as they mostly focus on benchmarking their code with previous work, they do not report any backflow.

Breitschwerdt et al. (2000) use linear perturbation theory to describe a type of hydromagnetic RTI that, in the limit of vanishing magnetic field, is very similar in nature to the SN implosion described here. They show, that the interaction of two SNRs can lead to an inward flow of clouds originating from the interaction region. Our results, which appear to correspond to the same kind of instability, seem to confirm the linear prediction of Breitschwerdt et al. (2000).

To our knowledge there are no instances of SN implosions reported in observations. This might however simply attest to the fact, that radiative SNRs, in particular those close to merging with the ISM, are very dim and thus are often difficult to observe (Green, 2019; Koo et al., 2020; Zhou et al., 2023). Moreover, the fact that the morphology of imploding SNRs differs qualitatively from traditional SNRs might have lead to a misclassification of imploding SNRs as something other than a SNR.

4.3.4 Implications for Galaxy Evolution

We have shown that under quite general conditions, old SNRs will implode and form a compact, massive, and potentially self-gravitating cloud in its center. Such a cloud could collapse and fragment under its own self-gravity to form stars, suggesting a novel mode of positive feedback.

Furthermore, given that such clouds would be highly enriched with the SN ejecta, and therefore with short-lived radionuclides (SLRs) like ^{26}Al, this provides an attractive pathway to the formation of planetary systems, where the heating due to SLRs plays an important role (Urey, 1955). Indeed, it has been concluded by Forbes et al. (2021) that the enrichment with SLRs would have to occur prior to core formation, a condition that at face value is readily fulfilled by our proposed mechanism. However, further studies are necessary to investigate to what extent mixing due to small-scale turbulence might further dilute the imploding gas.

Besides the importance for star and planet formation we make a clear prediction for the lifetime of hot cavities in the ISM, which are filled shortly after the implosion is launched. This number is an important parameter in models for the multiphase structure of the ISM (McKee & Ostriker, 1977; Wolfire et al., 2003; Draine, 2011), which are used to estimate a wide variety of ISM properties.

4.4 Concluding Remarks

We have performed 3D hydrodynamic simulations of SNRs in a uniform, stationary medium with non-negligible thermal pressure in order to study their evolution after shell formation. Our simulations reveal that radiative SNRs implode after the shell reaches pressure equilibrium with the ISM. The implosion leads to the formation of a compact, massive cloud that might soon become self-gravitating and that is highly enriched with SN ejecta. As we discuss, this novel mechanism of cloud formation provides attractive initial conditions for star and planet formation and might have some important implications for the theory of the ISM.

While the idealized setup is useful for understanding the underlying physical mechanism, understanding the role of SN implosion and subsequent cloud formation in a more realistic setup deserves further investigation.

We conclude that the dispersal and merging of SNRs with the ISM offers a wealth of hidden complexities, which deserve further study as they can help understand the physics of the ISM.

Chapter 5

Star Formation by Supernova Implosion

> Software used in this chapter:
> Julia v1.6.5 (Bezanson et al., 2017), and Matplotlib v3.5.1 (Hunter, 2007)

This work has been published in the Astrophysical Journal Letters, Volume 971, Number 2, August 2024, L44 (Romano et al., 2024b). After we submitted the paper presented in the previous chapter, Andi requested, I come up with a way to estimate the star-formation rate from the implosion clouds. During February 2024, I suffered from pneumonia, and was gone from work for about a month. During this time, in fever-delirium the solution to the problem came to me in a dream. After I got back to work I worked out the details of the model in no time and after receiving useful feedback from Andi and Manuel as well as many people at the MIAPbP ADONIS workshop held from March 25 – April 19 2014, we finalized the paper in no time.

Star formation is easy. Giant Molecular Clouds (GMCs) with masses $\sim 10^4 - 10^7\,\mathrm{M}_\odot$ (Williams & McKee, 1997; Miville-Deschênes et al., 2017) fragment, producing gravitationally unstable cores that collapse (e.g. Jeans, 1902; McKee & Ostriker, 2007; Rosen et al., 2020) and form stars. Yet, a closer look reveals that our understanding of the processes linking these stages of star formation and even the formation of the GMCs themselves is far from being predictive (see e.g. Lada et al., 2013; Chevance et al., 2020). Indeed, the processes underlying star formation remain to be one of the biggest puzzles in the current framework of galaxy formation and evolution.

One of these processes, which could explain the formation of star-forming GMCs is so-called *triggered star-formation*(Elmegreen, 1998, 2011). The underlying idea being that shocks, e.g. due to Supernovae (SNe) or other feedback processes, could compress the ambient gas and drive it towards gravitational instability (GI).

Observational evidence suggests that stars form spatially and temporally correlated (Gaczkowski et al., 2015, 2017; Krause et al., 2018; Zucker et al., 2022; Ratzenböck et al., 2023; Verma et al., 2023), pointing towards triggered star-formation scenarios. Meanwhile, many of the proposed triggers have been confirmed in numerical simulations (Dobbs et al., 2022; Herrington et al., 2023; Horie et al., 2024).

Recently, Romano et al. (2024a) have found that besides the classical triggering by shock-compression, SNe will eventually implode due to the pressure of the interstellar medium (ISM) and form a dense,

highly chemically enriched cloud in their center, which might collapse and form stars. In this letter, we leverage their results to give an estimate of the amount of star formation that can be expected from this process.

5.1 Methods

A common way to quantify the star-formation efficiency is the so-called *star-formation efficiency per free-fall time* $\epsilon_{\rm ff}$. It is defined as the ratio of the star-formation timescale and the free-fall timescale (see e.g. Schinnerer & Leroy, 2024, for a review):

$$\epsilon_{\rm ff} = \frac{t_{\rm ff}}{t_{\rm sf}} \,. \tag{5.1}$$

The average free-fall timescale in the ISM prior to the explosion

$$t_{\rm ff} = \sqrt{\frac{3\pi}{32 G \rho}} \sim 44.9 \, n_0^{-0.5} \, {\rm Myr} \,, \tag{5.2}$$

where n_0 is in units of ${\rm cm}^{-3}$. $t_{\rm ff}$ depends only on the density $\rho = \mu \, m_{\rm H} \, n_0$ of the ambient medium, where $\mu = 1.4$ is the mean atomic weight and $m_{\rm H}$ is the mass of a hydrogen atom. On the other hand, the star-formation timescale

$$t_{\rm sf} = \left(\frac{1}{\rho} \left. \frac{{\rm d}\rho}{{\rm d}t} \right|_{\rm sf} \right)^{-1} \,, \tag{5.3}$$

depends on the details of the processes that convert gas into stars.

Here we derive an expression for the timescale of SN-implosion-triggered star-formation. We consider two cases. In both cases a central stellar population drives a shock which will implode due to the pressure of the ISM, leading to the formation of a central cloud (Romano et al., 2024a). Once the cloud becomes gravitationally unstable it collapses and forms new stars. In the first, *cyclic* case, we consider the long term average of stellar populations that can produce enough massive stars to keep maintaining a continuous cycle. In the second, *single-burst* case we consider a stellar population or a single star driving a single iteration of SN-implosion-triggered star-formation, which may then either continue on indefinitely as in the cyclic case, or cease due to the lack of newly formed massive stars. The main difference between the two scenarios is that in the former, the number of SN explosions per cycle is fixed by the expected stellar mass that is formed by each cycle, while in the latter it is kept as a free parameter. A schematic overview of such a cycle is shown in Figure 5.1.

We utilize the results of recent simulations by Romano et al. (2024a). Their results include timescales for various stages of SN Remnant (SNR) evolution and cloud formation as well as information about various cloud properties as a function of time after its formation (see e.g. their figures 7 and 8).

Besides these results, we need to make the following simplifying assumptions:

1. Stellar populations follow the *canonical Initial Mass Function* (IMF) $\xi_{\rm star}\,(m)$ from Kroupa & Jerabkova (2021).
2. Implosion-triggered star-formation can only be sustained if it leads to the formation of at least one massive ($m_\star > 8\,{\rm M}_\odot$) star, which can trigger another SN implosion.
3. The ambient medium is initially at rest, with a uniform density of $n_{\rm H} = n_0$ and returns to this state by the end of each cycle.

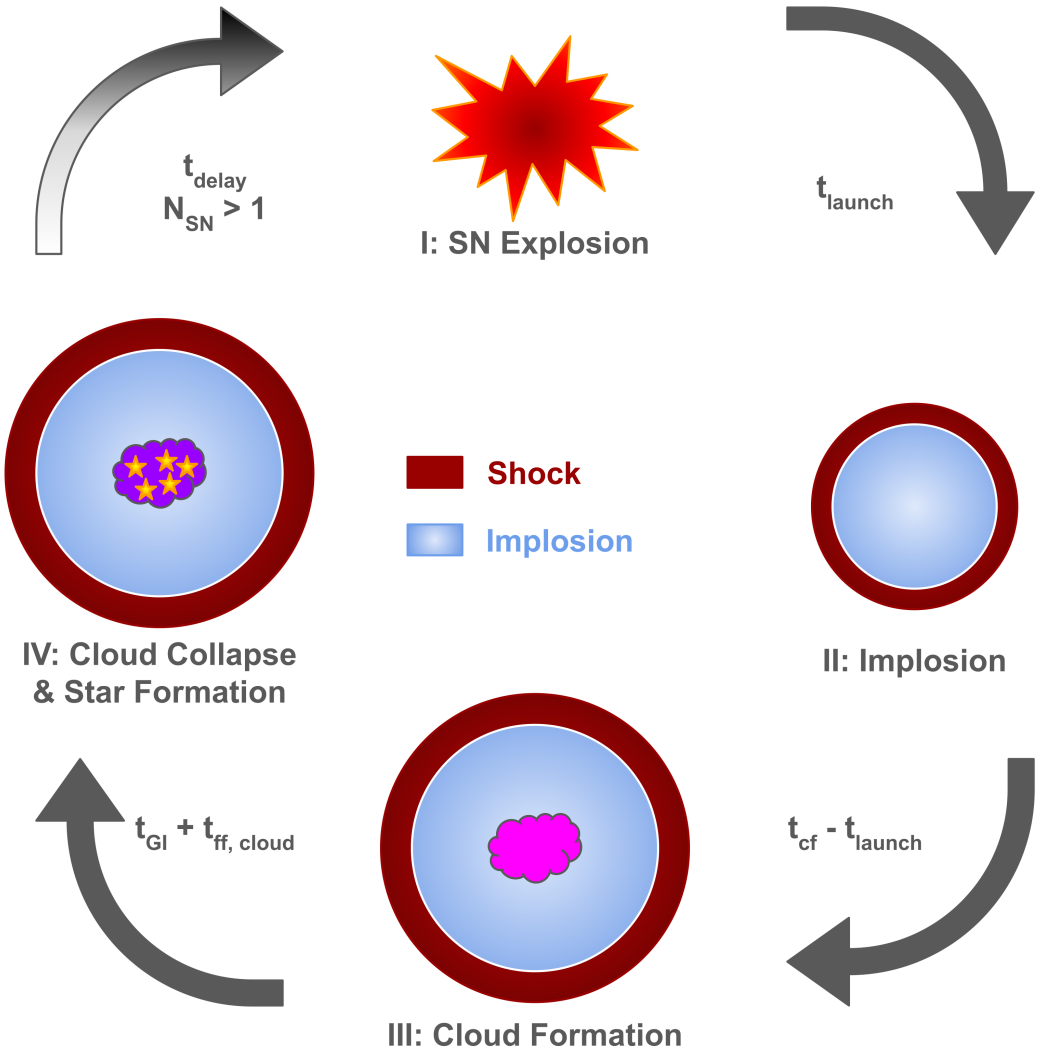

Figure 5.1: A schematic overview of SN-implosion-triggered star-formation. In this process, an explosion from a central source drives a shock (I), which eventually implodes (II) and leads to the formation of a central cloud (III). The central cloud grows and eventually becomes gravitationally unstable, leading to star formation (IV). Depending on whether there are newly-formed, massive stars, this cycle can repeat. The arrows connecting the different stages are decorated with the corresponding transition timescales defined in equations 5.5, 5.7, 5.10 and 5.12. The cloud formation time $t_{\rm cf}$ is measured from the time of the explosion so the time between implosion and cloud formation is $t_{\rm cf} - t_{\rm launch}$.

4. We neglect the role of early feedback (i.e. stellar winds and ionizing stellar radiation) and assume that all stars in the stellar population explode simultaneously in a common location, injecting a total energy of $E_{\rm SN} = 10^{51}$ erg per SN into the ambient medium.

5. We neglect all other sources of star formation and stellar feedback.

The star-formation-rate per unit volume for this process can be written as

$$\left.\frac{\mathrm{d}\rho}{\mathrm{d}t}\right|_{\rm sf} = \frac{M_{\star,\,\rm formed}}{t_{\rm cycle} V_{\rm exp}}\,, \tag{5.4}$$

where the stellar mass formed per cycle $M_{\star,\,\rm formed} = \epsilon_\star\, M_{\rm cloud}$ is parameterized as a fraction $\epsilon_\star$ of the mass of the central cloud prior to collapse, $V_{\rm exp} = 4\pi/3\, R_{\rm exp}^3$ is the volume traced by the shock during its expansion, and

$$t_{\rm cycle} = t_{\rm delay} + t_{\rm cf} + t_{\rm GI} + t_{\rm ff,\,cloud}\,, \tag{5.5}$$

is the time it takes to complete one cycle.

The fraction of cloud mass that is converted into stars $\epsilon_\star$ has been constrained both from observations (Lee et al., 2016; Chevance et al., 2020) and simulations (Grudić et al., 2022; Farias et al., 2024). It shows large variation with a typical value of $\epsilon_\star \sim 10\,\%$. Due to its large uncertainties, we treat this number as a model parameter, with a fiducial value of $\epsilon_\star^{\rm fid} = 10\,\%$.

In summary the resulting free-fall efficiency, associated with SN-implosion-triggered star-formation can be compactly written as

$$\epsilon_{\rm ff} = \epsilon_\star \frac{M_{\rm cloud}}{M_{\rm exp}} \frac{t_{\rm ff}}{t_{\rm cycle}} \tag{5.6}$$

where $M_{\rm exp} = \mu m_{\rm H} n_0 V_{\rm exp}$ is the total mass swept up by the SNR during it's expansion, and $t_{\rm ff}$, $t_{\rm cycle}$ and $M_{\rm cloud}$ are given by eqs. 5.2, 5.5 and 5.11, respectively.

There is some delay before the massive stars in a newly formed population explode. This time delay has been computed by Saitoh (2017) under the single stellar population approximation and is typically in the range of $t_{\rm delay} \sim 2.2 - 4.6\,$Myr. We treat this timescale as a model parameter with a fiducial value of $t_{\rm delay}^{\rm fid} \sim 3\,$Myr. However, we note that for stellar populations with exclusively long-lived massive stars, the time delay can be over an order of magnitude longer.

For $n_0 \gtrsim 1$ the cloud-formation timescale (Romano et al., 2024a)

$$t_{\rm cf} \sim 4\, n_0^{-0.15}\, N_{\rm SN}^{0.3}\,\mathrm{Myr}\,, \tag{5.7}$$

where $N_{\rm SN}$ is the number of SNe exploding simultaneously.

After its formation the central cloud evolves and its mass grows roughly like

$$M_{\rm cloud} \sim 20 \left(\frac{t}{1\,\mathrm{Myr}}\right)^{2.6} \mathrm{M}_\odot\,, \tag{5.8}$$

and its virial parameter drops

$$\alpha_{\rm vir} \sim 6000\, n_0^{-1} \left(\frac{t}{1\,\mathrm{Myr}}\right)^{-1.75} \mathrm{M}_\odot\,. \tag{5.9}$$

The cloud collapses when it becomes gravitationally unstable, i.e. $\alpha_{\rm vir}\,(t_{\rm GI}) \sim 1$, which leads to

$$t_{\rm GI} \sim 144\, n_0^{-0.57}\,\mathrm{Myr}\,, \tag{5.10}$$

$$M_{\rm cloud}\,(t_{\rm GI}) \sim 8 \times 10^6\, n_0^{-1.49}\,\mathrm{M}_\odot\,. \tag{5.11}$$

After the onset of collapse, the cloud is expected to collapse on a free-fall timescale, which depends on the density of the cloud at $t_{\rm GI}$.

We find that the overdensity of the cloud relative to the ambient medium does not follow a simple pattern, but its overall magnitude oscillates in time, with typical values in the range of $\chi \sim 2-4$ and no clear correlation with the simulation parameters. We thus treat the overdensity as a model parameter with a fiducial value of $\chi^{\rm fid} = 3$, which is justified by our results in section 5.2 that show that the value of χ only has a marginal effect on the star-formation efficiency. The collapse timescale of the cloud is thus

$$t_{\rm ff,\,cloud} = \chi^{-0.5}\, t_{\rm ff} \sim 44.9\, \chi^{-0.5}\, n_0^{-0.5}\, {\rm Myr}\,. \tag{5.12}$$

In the meantime the blastwave expansion has affected a spherical region of radius $R_{\rm exp}$. Assuming that the blastwave expands as a momentum-conserving snowplow, i.e. $R \propto t^{1/4}$, we estimate the size of the affected region as

$$R_{\rm exp} \sim R_{\rm launch} \left(\frac{t_{\rm cf} + t_{\rm GI} + t_{\rm ff,\,cloud}}{t_{\rm launch}} \right)^{1/4}\,, \tag{5.13}$$

where $R_{\rm launch} \sim 51.3\, n_0^{-0.27}\, N_{\rm SN}^{0.3}\,{\rm pc}$ and $t_{\rm launch} \sim 0.98\, n_0^{-0.11}\, N_{\rm SN}^{0.27}\,{\rm Myr}$ (Romano et al., 2024a).

The scaling of the cloud mass eq. 5.11 implies that above a certain density $n_{\rm max}$, the cloud mass becomes so low that it becomes unlikely to form massive stars, which could trigger the next cycle of star formation.

By normalizing the IMF to the stellar mass formed from the collapsing cloud, we find that the number of massive stars is

$$N_{\rm SN} = \int_{8\,{\rm M}_\odot}^{\infty} \xi_{\rm star}\,(m)\,{\rm d}m \sim 1.08\,\frac{\epsilon_\star M_{\rm cloud}}{100\,{\rm M}_\odot}\,, \tag{5.14}$$

which in combination with eq. 5.11 implies that the maximum density at which one can expect the formation of at least one massive star is

$$n_{\rm max} \sim 1070\,\epsilon_\star^{0.67}\,{\rm cm}^{-3}\,. \tag{5.15}$$

A further constraint can be imposed by considering that the dynamics may be dramatically altered due to vertical stratification if the shock breaks out of the galactic ISM before the implosion is launched (see e.g. Koo & McKee, 1990). Indeed, for the lowest density considered here the SNR would have expanded to a radius of $R_{\rm launch} \sim 780\,{\rm pc}$ before imploding and thus if located in an ISM resembling the solar neighborhood with a scale height of 150 pc (McKee et al., 2015) would have broken out before it could have imploded.

For an isothermal, single-component disk in vertical hydrostatic equilibrium the vertical density profile is $\propto {\rm sech}^2\,(z/z_0)$ with scale height (Behrendt et al., 2015)

$$z_0 = \frac{\sigma}{\sqrt{2\pi G \rho_{\rm mp}}} \sim 338\,\sigma_{10} n_0^{-0.5}\,{\rm pc}\,, \tag{5.16}$$

with velocity dispersion $\sigma = 10\,\sigma_{10}\,{\rm km/s}$ and midplane density $\rho_{\rm mp}$. By assuming that the SNe explode in the midplane and requiring that the implosion should be launched before shock breakout, one obtains the constraint

$$n_{\rm H} < 3.6 \times 10^3\,\sigma_{10}^{4.35} N_{\rm SN}^{-1.3}\,{\rm cm}^{-3}\,. \tag{5.17}$$

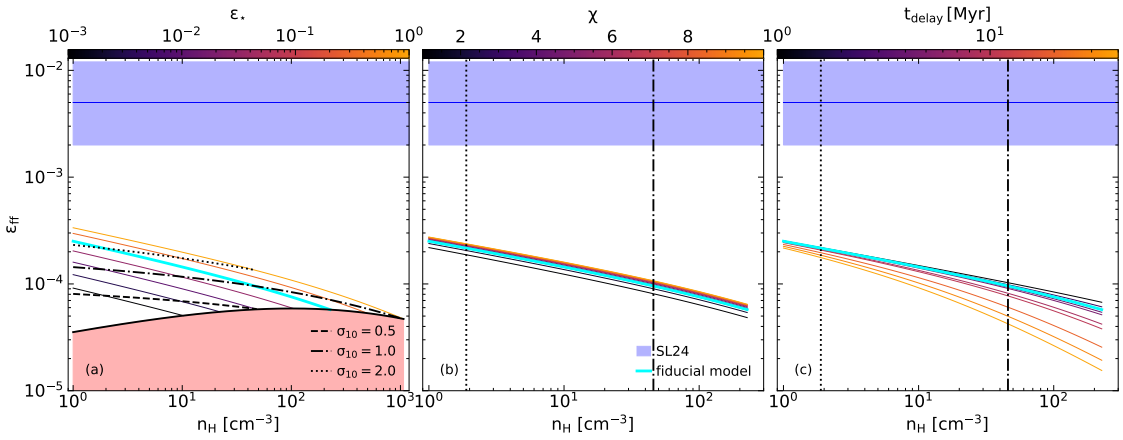

Figure 5.2: Star-formation efficiency per free-fall time as a function of density for various models in the cyclic scenario. In panels (a), (b) and (c) the star-formation efficiency $\epsilon_\star$, cloud overdensity χ and stellar-population lifetime $t_{\rm delay}$ are respectively varied, while the remaining two parameters are kept at their respective fiducial values of $\left(\epsilon_\star^{\rm fid}, \chi^{\rm fid}, t_{\rm delay}^{\rm fid}\right) = (0.1, 3, 3\,{\rm Myr})$. Below the solid black line in panel (a) not enough stars are formed to reliably maintain cyclic star-formation (eq. 5.15). The dashed, dot-dashed and dotted black lines correspond to the lower limit for the density below which shock break-out is expected to affect the dynamics for various values of the ISM velocity dispersion σ_{10} (eq. 5.18). The blue line and shaded area correspond to the value of $\epsilon_{\rm ff}$ and its uncertainty derived from observations on scales of $\sim 100\,{\rm pc}$ (Schinnerer & Leroy, 2024).

For the cyclic case $N_{\rm SN}$ is given by eq. 5.14 and thus this translates into a lower limit for the density

$$n_{\rm min} = 1.1 \times 10^3\, \sigma_{10}^{-4.6} \epsilon_\star^{1.38}\, {\rm cm}^3 \ , \tag{5.18}$$

while in the single burst case eq. 5.17 provides an upper limit for the density, due to the different scaling with density of $R_{\rm launch}$ and z_0.

In summary the density in the cyclic case is constrained to be in the range

$$\max\left(1.1 \times 10^3\, \sigma_{10}^{-4.6} \epsilon_\star^{1.38}, 1\right) < n_0 < 1070\, \epsilon_\star^{0.67} \ , \tag{5.19}$$

and for a single burst

$$1 < n_0 < 3.6 \times 10^3\, \sigma_{10}^{4.35} N_{\rm SN}^{-1.3} \ . \tag{5.20}$$

Comparing the upper and lower limits for the density, we find that the cyclic case requires

$$\epsilon_\star < 0.93 \sigma_{10}^{6.5} \ , \tag{5.21}$$

and a single burst only triggers star formation if

$$N_{\rm SN} < 550 \sigma_{10}^{3.35} \ . \tag{5.22}$$

Both requirements are readily fulfilled for typical values of the parameters.

5.2 Results

In the previous section we have described a model to estimate the star-formation efficiency per free-fall time $\epsilon_{\rm ff}$ for SN-implosion-triggered star-formation. Here we explore how our model compares to observational estimates of $\epsilon_{\rm ff}$ and its dependency on the model parameters.

5.2.1 Cyclic Star-Formation

In the cyclic scenario, the number of SNe per cycle is determined by eqs. 5.14 and 5.11. In the limit of $t_{\rm GI}/t_{\rm cycle} \sim 1$, we thus find

$$\epsilon_{\rm ff} \propto \epsilon_\star^{0.3}\, n_0^{-0.22}\,. \tag{5.23}$$

In Figure 5.2 we show how $\epsilon_{\rm ff}$ varies with respect to the model parameters $\epsilon_\star$, χ and $t_{\rm delay}$ and compare it to the most recent observational estimate of $\epsilon_{\rm ff}$ as reported by Schinnerer & Leroy (2024).

Panel (a) shows the variation of $\epsilon_{\rm ff}$ with respect to $\epsilon_\star$. The range of densities where cyclic star-formation can be maintained becomes increasingly narrow as $\epsilon_\star$ is reduced, as expected from eq. 5.15. In media with $\sigma < 45\,\mathrm{km/s}$ and thus sufficiently small scale-height, shock break-out constrains the range of densities where our model for cyclic star-formation can be applied. Furthermore, it becomes clear that for fixed density, $\epsilon_{\rm ff}$ scales as expected from eq. 5.23, since $t_{\rm cf} \ll t_{\rm GI} + t_{\rm ff,\,cloud}$ for $n_0 \geq 1$.

Panel (b) shows the variation of $\epsilon_{\rm ff}$ with respect to χ. Higher χ generally implies higher $\epsilon_{\rm ff}$, with a diminishing effect as $\chi \gtrsim 4$. The effect diminishes because $t_{\rm GI} \sim 3\,t_{\rm ff}$ and both timescales scale similarly with density. Thus, reducing $t_{\rm ff,\,cloud} \propto t_{\rm ff}$ will reduce the importance of $t_{\rm ff,\,cloud}$ relative to the much longer $t_{\rm GI}$, but hardly affect $\epsilon_{\rm ff}$.

Panel (c) shows the variation of $\epsilon_{\rm ff}$ with respect to $t_{\rm delay}$. For $t_{\rm delay} \ll 10\,\mathrm{Myr}$ only a slight reduction in $\epsilon_{\rm ff}$ is noticeable at high ambient densities. For longer delay times, comparable to $t_{\rm ff}$, the effect is stronger. Since the details of cloud formation are independent of $t_{\rm delay}$ and only $t_{\rm cycle}$ depends on it affine-linearly, $\epsilon_{\rm ff} \propto t_{\rm delay}^{-1}$ in the limit where $t_{\rm delay} \gg t_{\rm exp}$, i.e. high densities or high $t_{\rm delay}$. However, we do not expect this limit to play a big role, as extremely high values of $t_{\rm delay} \gtrsim 40\,\mathrm{Myr}$ are unexpected and even at the maximum density eq. 5.15 $t_{\rm delay} < t_{\rm exp}$ indicating that the role of $t_{\rm delay}$ is almost negligible for SN-implosion-triggered star-formation.

The range of values of $\epsilon_{\rm ff}$ obtained with the fiducial set of parameters is about two orders of magnitude below that derived from observations $\epsilon_{\rm ff}^{\rm obs} = 0.5^{+0.7}_{-0.3}\,\%$ with a relatively weak scaling with density $\epsilon_{\rm ff} \propto n_0^{-0.22}$. The fact that we cannot explain $\epsilon_{\rm ff} \sim 0.5\,\%$ is however not a problem and rather a feature as we expect several other processes such as classical triggered star-formation (see e.g. Elmegreen, 1998) or spontaneous gravitational collapse (Kennicutt, 1989; McKee & Ostriker, 2007) to contribute to the star formation as well.

Given that the mass of the central cloud is significantly smaller than the total swept up mass, it is not surprising that the contribution to the star formation is minor. However, it should be noted, that the stars formed in the implosion cloud are expected to be more chemically enriched than the bulk of the stars formed by other processes (Romano et al., 2024a). Moreover, we note that the process is self-regulated, i.e. the cloud makes up a larger fraction of the swept up mass for fewer SNe, which motivates us to study the single-burst scenario, which we explore below.

5.2.2 Single-Burst Star-Formation

In the single-burst scenario, we consider $\epsilon_{\rm ff}$ for a single iteration of SN-implosion-triggered star-formation. Such an iteration could be triggered by the collective feedback of an entire stellar population or the explosion of a single star, which includes both type-Ia and type-II SNe. It is thus reasonable to measure $t_{\rm cycle}$ from the time of the explosion, as the delay time bears no meaning in this case, i.e. setting $t_{\rm delay} = 0$.

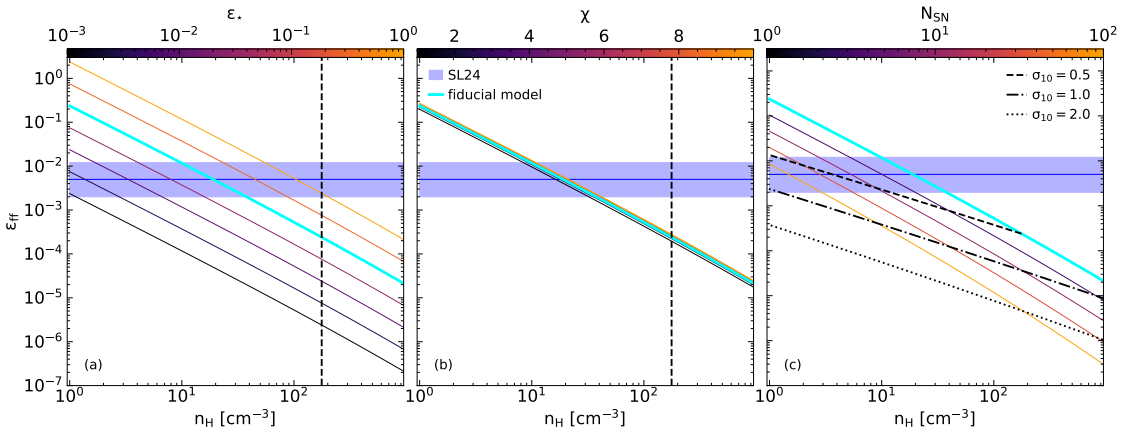

Figure 5.3: Same as Figure 5.2, but in the case of the single-burst scenario. Panel (c) shows the dependency of $\epsilon_{\rm ff}$ with respect to $N_{\rm SN}$, with a fiducial value of $N_{\rm SN}^{\rm fid} = 1$. Here the dashed, dot-dashed and dotted black lines correspond to the upper limit of the density above which shock break-out is expected to affect the dynamics for various values of the ISM velocity dispersion σ_{10} (eq. 5.17).

As opposed to the cyclic case, in the single-burst scenario $N_{\rm SN}$ is not determined by eq. 5.14, but instead is treated as a free parameter. This implies, that now in the limit of $t_{\rm cycle} \sim t_{\rm GI}$,

$$\epsilon_{\rm ff} \propto \epsilon_\star \, N_{\rm SN}^{-0.7} \, n_0^{-1.26} \, . \tag{5.24}$$

These scalings are reflected by panels (a) and (c) in Figure 5.3. Panel (b) shows, that as for the cyclic case, the effect of χ is small, since $t_{\rm cycle}$ is dominated by $t_{\rm GI}$.

Due to the strong scaling with density, the range of values of $\epsilon_{\rm ff}$ obtained with the fiducial set of parameters spans four orders of magnitude. At low densities, star formation is very efficient with $\epsilon_{\rm ff} \sim 10\,\%$ exceeding the observational mean by over an order of magnitude, while at higher densities it becomes increasingly inefficient.

The fact that $\epsilon_{\rm ff}$ can significantly exceed the global average derived from observations does, however, not cause any conceptual problems, as the single-burst case should only occur occasionally. Thus, while the single-burst scenario might contribute to the scatter, it is not expected to dominate the global average.

5.3 Discussion

In the previous section we have shown the efficiency of SN-implosion-triggered star-formation in two different scenarios. Here, we discuss some of the limitations of our model, and the implications of our findings in the broader context of galaxy evolution.

5.3.1 Limitations

The model considered in this letter is a detailed analysis of the implications of the results of Romano et al. (2024a). As such, the limitations applying to their results also apply to this model.

Neglecting the turbulent nature of the ISM likely affects both the timescales involved as well as the

properties of the central cloud. Similarly, as discussed by Romano et al. (2024a) including more complete physics models for processes, such as magnetic fields, cosmic rays, and heat conduction, could qualitatively modify the cloud-formation process. Finally, the inclusion of early stellar feedback and realistic time delays between SNe can further delay the implosion and thus cloud formation (see e.g. Fichtner et al., 2024), leading to a lower star-formation efficiency.

A model is only as good as its assumptions. It is thus worthwhile to consider the role of our model assumptions.

For sufficiently massive clouds, assuming an IMF seems to be justified by the observed statistics of stellar populations (Kroupa & Jerabkova, 2021). However, for clouds with small masses, the IMF is not well sampled in the high-mass end and the number of massive stars that are formed per cycle will be dominated by stochasticity (see e.g. Grudic et al., 2023). Nonetheless, since our cyclic model considers a long-term average, populations with $N_{\rm SN} > 1$ should – over a larger number of iterations – sample the high-mass end of the IMF well enough to justify our treatment. We have checked eq. 5.14 for different shapes of the IMF commonly used in the literature (e.g. the list of IMFs in Saitoh, 2017) and have found only minor differences; The result that there is about 1 SN per $100\,M_\odot$ of newly formed stars is on strong footing.

Clearly it is unreasonable to expect the ambient medium to return *exactly* to its initial state of a uniform medium with constant density at rest. Nonetheless, in the context of the simulations of Romano et al. (2024a) it is revealed that after cloud formation the density in the region between the shock and the cloud indeed approaches the initial density of the ISM as the cavity is refilled with backflowing material from the ever broadening front of the blastwave, while the remaining kinetic energy is dissipated through small-scale shocks, leaving a nearly static, and slightly turbulent medium.

Likewise, we expect the density in the cloud to be locally enhanced after its collapse. However, as long as the SNR can break out of the cloud before shell formation the dynamics are not expected to be strongly influenced. Furthermore, in a more complete picture early feedback might counteract this density enhancement and with more realistic delays between the SNe the central mass distribution is expected to have only a small effect compared to the potentially large time delay before the last SN of the population explodes.

In a more realistic galactic environment, however, these considerations are confounded by several factors. The complex interplay of neighboring shocks, gravitational torques, shear, and stratification effects is expected to lead to significant inhomogeneities in the density and velocity distribution.

We expect the analysis of the single-burst case to be less affected, since the ISM in the immediate vicinity of the SNR is not expected to change dramatically during one cycle.

On the other hand, in the cyclic case, we consider the long-term average, which means that necessarily all of these effects will have enough time to affect the dynamics. As long as these effects do not prevent cloud formation or disrupt the central clouds before they can collapse, we expect the effect to be small. Nonetheless, in order to be certain a more thorough analysis is required.

We expect that the effects of vertical stratification can be neglected if the SNR is contained within a scale height of the galactic ISM. By assuming vertical hydrostatic equilibrium in an isothermal, single-component disk we find that this constrains the range of densities for which our model can be applied. These constraints however scale very strongly with the velocity dispersion and are likely negligible at high redshift, where the velocity dispersion often exceeds 100 km/s (Krumholz & Burkhart, 2016).

Moreover, in the regime where the effective turbulent pressure dominates the ambient pressure, we expect the implosion to be launched even earlier due to the increased ambient pressure, reducing the importance of the stratification constraint. On the other hand, in this turbulent regime we expect larger density fluctuations and more overall anisotropy which would affect our conclusions in a way that is out of the scope of the simple model presented in this work.

Finally, we have neglected the role of other sources of star formation and feedback. While theoretical considerations suggest that individual SN shocks are an unlikely candidate for triggered star-formation (Elmegreen, 2011), we anyway consider the potential contribution, given the uncertainty of the subject.

Classical, triggered star-formation has been estimated to be delayed by about a free-fall timescale (Elmegreen, 1998). For low ambient densities, we thus do not expect it to strongly affect the mass budget for cloud- and subsequent star-formation by SN implosion, while at sufficiently high densities, the onset of triggered star-formation might be before the onset of cloud formation and thus reduce the mass budget for cloud formation.

On the other hand, we expect feedback from massive stars formed by classical, triggered star-formation to interfere with the process in several ways. Feedback that is sourced sufficiently far away from the explosion center might heat the ambient medium and increase its pressure, leading to an earlier implosion and thus accelerate the star-formation process. However, if the source of the feedback is too close, it might disrupt the cloud before it can form stars and delay or even prevent further star formation, leading to a reduction of the free-fall efficiency.

5.3.2 Implications for Galaxy Evolution

We have shown that SN-implosion-triggered star-formation can contribute $\lesssim 5\,\%$ of the globally averaged star formation. While this might not seem like a large contribution, it should be noted that a bulk fraction ($\gtrsim 10\,\%$) of the highly enriched SN ejecta are expected to be locked up in the central, star-forming cloud. Indeed, if would be problematic if ϵ_{ff} were much higher, as this would potentially indicate that our model predicts too much metal-rich star-formation, the implications for which we are discussing in the following.

The increment in metallicity per cycle can be expressed in terms of the fraction of ejecta material locked up in the cloud $M_{\mathrm{ej,\,cl}}/M_{\mathrm{cl}}$, the metallicity of the ejecta Z_{ej} and the metallicity of the ambient medium Z_0:

$$\delta Z = \frac{M_{\mathrm{ej,\,cl}}}{M_{\mathrm{cl}}} \left(Z_{\mathrm{ej}} - Z_0\right) \,. \tag{5.25}$$

The simulations of Romano et al. (2024a) suggest that $\gtrsim 10 - 50\,\%$ of the ejecta end up in the cloud before it collapses. Indeed, in the absence of numerical diffusion, for a spherically symmetric explosion, one expects $100\,\%$ of the ejecta to be locked up in the central cloud, since radial shells cannot cross in ideal hydrodynamics.

Shimizu et al. (2019) have computed the yields from various feedback processes for a Chabrier IMF with mass range 0.1 to 120 $\mathrm{M}_\odot$ (Chabrier, 2003) using CELIB (Saitoh, 2017). They find that for metallicities $Z \gtrsim 10^{-6}$, stellar populations eject $\sim 10\,\%$ of their mass in type-II SNe, with $Z_{\mathrm{ej}} \sim 15 - 20\,\%$. In the more uncertain case of primordial metallicity the stellar populations eject $\lesssim 90\,\%$ of their mass in type-II SNe, with $Z_{\mathrm{ej}} \sim 33\,\%$. While their IMF differs slightly from the one we have adopted here, we expect the results to only change slightly.

Combining these results and relating the mass of the stellar population to the cloud mass through $\epsilon_\star$ we find that for sufficiently high metallicity $\delta Z \gtrsim 10^{-3}\,\epsilon_\star$ and for primordial metallicity $\delta Z \gtrsim$

$3 \times 10^{-2}\,\epsilon_\star$.

A single cycle takes about $t_{\rm cycle} \lesssim 10^7 - 10^8$ yr, so over the lifetime of the universe there could have been $\lesssim 100 - 1000$ cycles, during most of which the metallicity would have been non-primordial. Neglecting physical dilution effects (but implictly accounting for numerical dilution, which may account for a similar degree of dilution), we thus expect a maximum enrichment of $\Delta Z_{\rm max} = N_{\rm cycle} \times \delta Z \sim (0.1 - 1)\ \epsilon_\star$, slightly higher than the metallicities of the most metal-rich stars that have been observed (see e.g. Do et al., 2015; Sextl et al., 2024; Rix et al., 2024).

We note that while the enrichment per generation might seem small, it still represents a massive enhancement compared to the expected enrichment one would obtain if the ejecta were instead fully mixed. Typically $M_{\rm cl}/M_{\rm exp} \sim 10^{-2} - 10^{-3}$, so without confining the ejecta into the central cloud, it would take $10^4 - 10^5$ cycles to reach solar level metallicities and beyond. Of course, since globally star-formation is ~ 100 times more efficient this difference can be overcome and on average solar level metallicities are commonly reached by today.

As the chemical enrichment in this scenario is primarily due to type-II SNe, we expect an elevated level of α-elements in the resulting stellar populations.

However, we note that we have neglected other enrichment mechanisms such as type-Ia SNe and stellar winds from asymptotic giant branch and massive stars (Kobulnicky, 1999; Saitoh, 2017), which would lead to even higher metallicities and less extreme α-abundances. On the other hand, dynamical effect such as turbulence and galactic shear could counteract the local self-enrichment by mixing the enriched gas with lower metallicity, ambient gas and limiting the maximum number of cycles during which the system remains coherent. A detailed study of these limitations is out of the scope of our simple model.

In summary, implosion triggered star formation can *locally* accelerate chemical evolution. If left alone, the thus formed stellar populations can reach super-solar metallicities long before it would be possible for populations that are formed in clouds that were mainly enriched by *external* sources. Ultimately, the maximum metallicities and the number of highly enriched stars that can be reached through implosion triggered star formation depend on the timespan during which the system can coherently undergo this process.

5.4 Concluding Remarks

We have analyzed the efficiency of SN-implosion-triggered star-formation and its contribution to the global star formation. Our analysis reveals that if maintained, star-formation from SN implosion is quite inefficient, contributing only about $\lesssim 5\,\%$ of the observed star-formation efficiency per free-fall time $\epsilon_{\rm ff}$. Nonetheless, because of the projected high metal enrichment of the thus formed stars, we expect this process to contribute significantly to the formation of metal-rich stars.

While our idealized model is useful for obtaining a rough estimate of the contribution from SN-implosion-triggered star-formation, more detailed models are required to explore the role of the galactic environment and external sources of feedback.

We conclude that SN-implosion-triggered star-formation offers a compelling, well-motivated pathway to the formation of metal-rich stars.

Chapter 6

SISSI: Supernovae in a stratified, shearing interstellar medium

I. The geometry of supernova remnants

> Software used in this chapter:
> Julia v1.10.0 (Bezanson et al., 2017), Matplotlib v3.5.1 (Hunter, 2007), Mera v1.4.4 (Behrendt, 2023b), Ramses v19.10 (Teyssier, 2002), and Healpix v2.3.0 (Tomasi & Li, 2021)

This work has been accepted for publication in Astronomy & Astrophysics on August 6 2025 and appeared in Volume 702, October 2025, id. A12 (Romano et al., 2025a). The work builds heavily on ongoing work by my collaborator Manuel, who provided the setup of the isolated galaxy and the cooling and ISM models. Manuel provided useful guidance throughout the whole project. I worked out the details turning the idea into a finished paper, presented in this work, by implementing the various zoom-in refinement models, the resolution-scaling of the star-formation model and the modifications to the SN-injection model, running and analyzing the simulations, and creating all the figures and results presented in this chapter.

Advances in observational techniques over the last decades have made it possible to study the three-dimensional (3D) geometry of structures in the nearby galactic interstellar medium (hereafter ISM, e.g. Arenou et al., 1992; Lallement et al., 2019; Edenhofer et al., 2024). Of particular interest is the Local Bubble (hereafter LB Cox & Reynolds, 1987; Linsky & Redfield, 2021), a diffuse, X-ray emitting cavity, with a diameter of several hundred parsec, which curiously we are observing right from the center (Zucker et al., 2022; Yeung et al., 2024). The LB is believed to be a superbubble (SB) evacuated due to the collective feedback from massive stars, such as ionizing radiation (Linsky & Redfield, 2021), stellar winds (Heiles, 1998) and supernovae (hereafter SNe Breitschwerdt & de Avillez, 2006; Wallner et al., 2021).

The geometry of SBs and supernova remnants (SNRs) provides a valuable tool for understanding phenomena such as galactic outflows, chemical enrichment and star-formation, with both observations and theory. Moreover, while the LB is to date the only SB whose 3D geometry has been studied in great detail, novel techniques and a wealth of data will enable the study of many more Galactic SBs (Leike et al., 2020; Edenhofer et al., 2024). Despite the lack of 3D information, extragalactic observations also provide hints to the geometry of SBs (Watkins et al., 2023; Jiménez

et al., 2024). In order to be able to interpret this wealth of data, predictions from numerical simulations and analytical models for the geometry of SNRs and SBs are required.

Over the last five decades, the evolution of spherical SBs expanding into a uniform ISM has been studied in great detail (e.g. Chevalier, 1974; Cioffi et al., 1988; Truelove & McKee, 1999). While these efforts have provided useful intuition for the different processes dominating the dynamics of expanding SBs and shaped the theoretical methods used to describe their evolution (Kim & Ostriker, 2015; Romano et al., 2024a), they lack the complexity needed to explore the physical processes governing the departure from spherical symmetry.

The processes that might deform SNRs are manifold. It has been recognized early on that blast-waves expanding into a vertically stratified atmosphere are stretched out along the density gradient (Kompaneets, 1960; Laumbach & Probstein, 1969). SNRs have been found to preferentially expand into low density channels, following the density structure of the ambient ISM, shaped by gravity and turbulence (Kim & Ostriker, 2015; Ohlin et al., 2019; Makarenko et al., 2023; Lau & Bonnell, 2025). Moreover, galactic shear might stretch out a SB along the direction of rotation (Tenorio-Tagle & Palous, 1987; Bisnovatyi-Kogan & Silich, 1995).

Observations of starburst galaxies reveal that many galaxies host galactic outflows (Xu et al., 2022), suggesting that vertical stratification plays an important role in shaping the geometry of SBs, provided they are powered by a sufficiently strong source. Studies of SBs in nearby star-forming galaxies report ellipsoidal geometries, aligned with the galactic rotation (Watkins et al., 2023), suggesting that galactic shear might be at play. However, from the same observations it becomes clear that density structures, such as low density channels and high-density filaments align themselves in the same way (Xie et al., 2024), making it difficult to disentangle the role of shear and density structure in shaping the geometry of SNRs.

While these studies, have shown the effectiveness of these various physical processes in deforming SNRs in isolation, there is only little work, addressing how they affect the geometry in concert (e.g. Jiménez et al., 2024, who however neglect radiative cooling). Indeed, most studies investigating the effect of stellar feedback in turbulent, stratified, and occasionally shearing media, focus on the collective effect stellar feedback has on the average properties of the multi-phase ISM and galactic outflows (e.g. de Avillez & Breitschwerdt, 2005; Walch et al., 2015; Fielding et al., 2018; Kim & Ostriker, 2017). However, a clear picture of how the different processes affecting SNR geometry compete remains unavailable.

In this paper, we present the SISSI (Supernovae In a Stratified, Shearing ISM) simulation suite, which aims to address this gap and enable a more comprehensive study of the phenomenology of SNRs. The SISSI project, which aims to evolve well resolved SNRs in a realistic, but controlled environment, will enhance our theoretical understanding of the complex interaction of SNRs with their environment and provide future observational studies with new tools for disentangling the complex physics of SNRs in the galactic ISM.

The remainder of this paper is organized as follows. In Sects. 6.1 and 6.2 we describe the numerical and analysis methods and give a description of the SISSI simulation suite. In Sects. 6.3 and 6.4 we give an overview of the time evolution of our simulated sample of SNRs as well as an analysis of the geometry. We discuss our results in Sec. 6.5. Finally, we summarize our findings and conclude in Sec. 6.6. In the Appendix we present the properties of the ISM of our simulated galaxy, and provide some additional background to some of models and data used in our analysis.

6.1 Numerical methods

We model the evolution of SNRs embedded in an isolated disk galaxy, using the adaptive mesh refinement (AMR) code RAMSES (Teyssier, 2002), which solves the system of hydrodynamic equations on a finite volume, cartesian grid using a second-order unsplit Godunov method (MUSCL scheme). The code reconstructs variables at the cell interfaces from the cell-centered values utilizing the HLLC Riemann solver with MinMod total variation diminishing scheme (Toro et al., 1994). RAMSES employs a conjugate gradient method and cloud-in-cell interpolation of particle contributions to solve the Poisson equation.

We relate the gas pressure and internal energy using an adiabatic index of $\gamma = 5/3$. We implement radiative cooling and heating based on the HEIKOU integration scheme (M. Behrendt et al. 2025, in prep.), which is based on the exact integration scheme (Townsend, 2009; Zhu et al., 2017), utilizing the UVB_dust1_CR0_G0_shield0 cooling table from Ploeckinger & Schaye (2020) at solar metallicity. We model star-formation by allowing gas with densities $n_{\mathrm{H}} > 100\,\mathrm{cm}^{-3}$ and temperatures $T < 150\,\mathrm{K}$ to form star particles with $m_\star = 10^3\,\mathrm{M}_\odot$ at a rate given by a local Schmidt-law (see e.g. Katz, 1992; Springel & Hernquist, 2003; Shimizu et al., 2019; Oku et al., 2022), with $\epsilon_{\mathrm{ff}} = 1\,\%$.

The simulation is separated into two stages. In the first stage, we relax an isolated disk galaxy into a quasi-steady state where gravitational collapse and cooling are balanced by stellar-feedback-driven turbulence and heating. In the second stage, we turn off the feedback and zoom into the ISM in various locations where we inject energy and mass to model the evolution of SNRs in a self-consistently generated galactic ISM.

6.1.1 Setup: Isolated disk galaxy

The SISSI galaxy is part of the AVALON galaxy formation and evolution project (M. Behrendt et al. 2025, in prep.), which utilizes the GALAXY COMPOSER package (M. Behrendt et al. 2025, in prep.) to generate the initial conditions of an isolated Milky-Way-like galaxy with galaxy parameters taken from Bland-Hawthorn & Gerhard (2016). The simulation domain is a cubical box with side length $L = 48\,\mathrm{kpc}$ and outflow boundaries, subdivided into a coarse grid of 256 cubic cells, corresponding to a maximum cell size of $\Delta x_{\mathrm{max}} = 187.5\,\mathrm{pc}$. Cells are refined up to an effective resolution of 2^{12} ($l_{\mathrm{max,\,ISM}} = 12$) or $\Delta x_{\mathrm{min,\,ISM}} \approx 11.7\,\mathrm{pc}$ if they are larger than $N_{\mathrm{Jeans}} = 8$ local Jeans lengths or if they contain a mass exceeding 20 (star) particle masses, which ensures that star-forming cells are Jeans-unstable. We model the influence of the stellar disk, bulge and dark matter halo as a static, axisymmetric background-potential. The gas is initially set up as a combination of a warm, isothermal disk in vertical hydrostatic equilibrium and a hot, diffuse uniform background.

During the initial relaxation stage, we model stellar feedback by injecting a thermal energy of $2 \times 10^{52}\,\mathrm{erg}$ and a mass of $200\,\mathrm{M}_\odot$ into a single cell hosting a star particle 8 Myr after its formation. We avoid overcooling by flagging cells affected by stellar feedback with a passive scalar that disables cooling for the first $\sim 500\,\mathrm{kyr}$ after the feedback event.

We evolve the isolated disk galaxy for $\lesssim 500\,\mathrm{Myr}$ until it has settled into a quasi-steady state where gravitational collapse and cooling are balanced by feedback-driven heating and turbulence. We show a projection of the surface density of the ISM after the initial relaxation in Fig. 6.1. Shown here is only a small cut-out of the simulation domain focusing on the galactic ISM. While the large box size is required to ensure a realistic galactic eco-system (galactic outflows and large-scale fountain-flows) and reduce numerical effects due to the domain boundaries, for this study the details of the circumgalactic medium can be ignored, as our focus lies mainly on the central

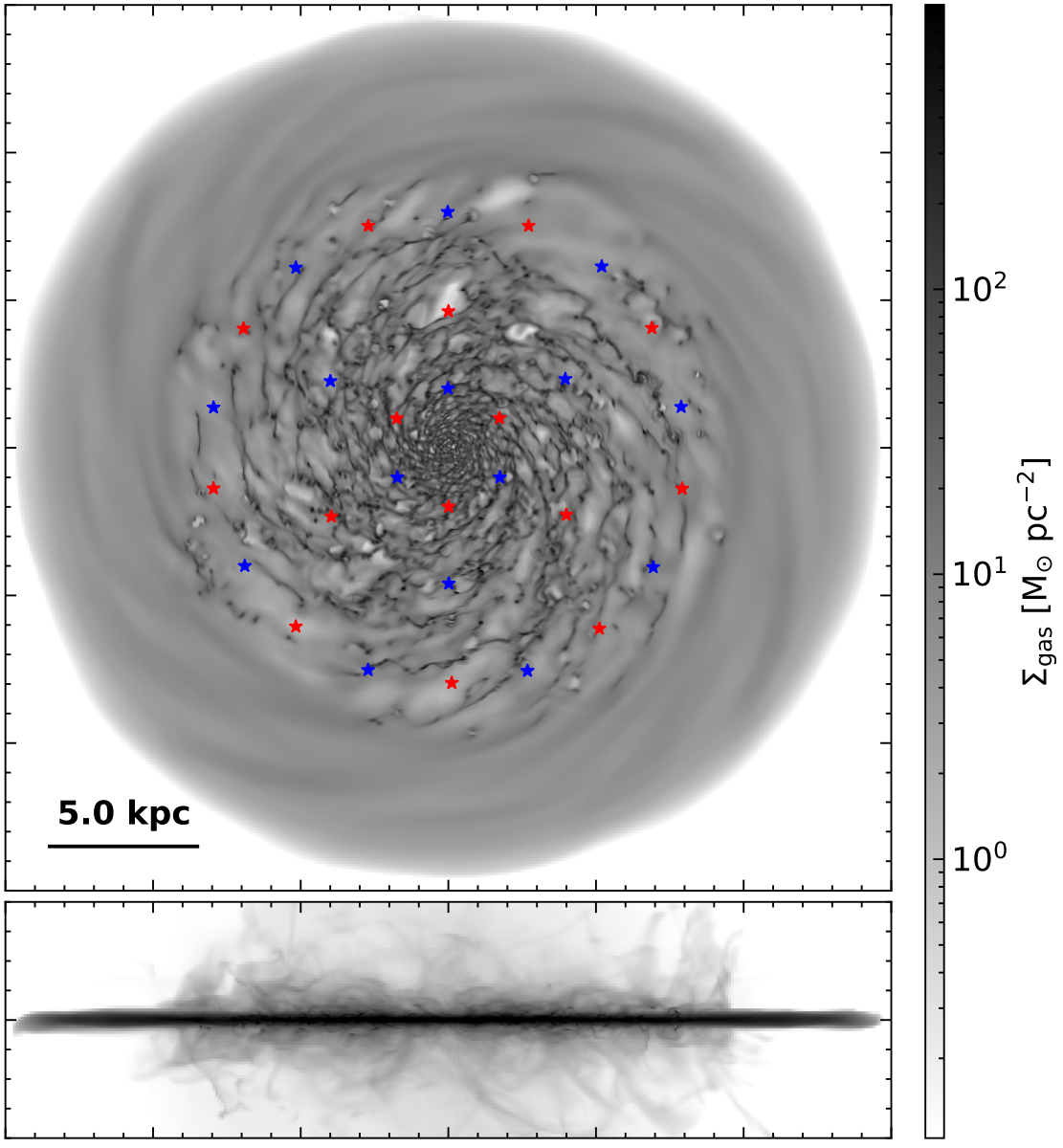

Figure 6.1: Face-on (top) and edge-on (bottom) projection of the simulated galaxy at $t = 0$. We mark the explosion sites of the SNRs with star markers. Different marker colors correspond to the different passive scalars associated with the SN ejecta. The ISM in the inner $\sim 10\,\mathrm{kpc}$ is highly structured with filamentary outflows that reach several kpc above the midplane, while the ISM in the outskirts is rather smooth without any prominent vertical features.

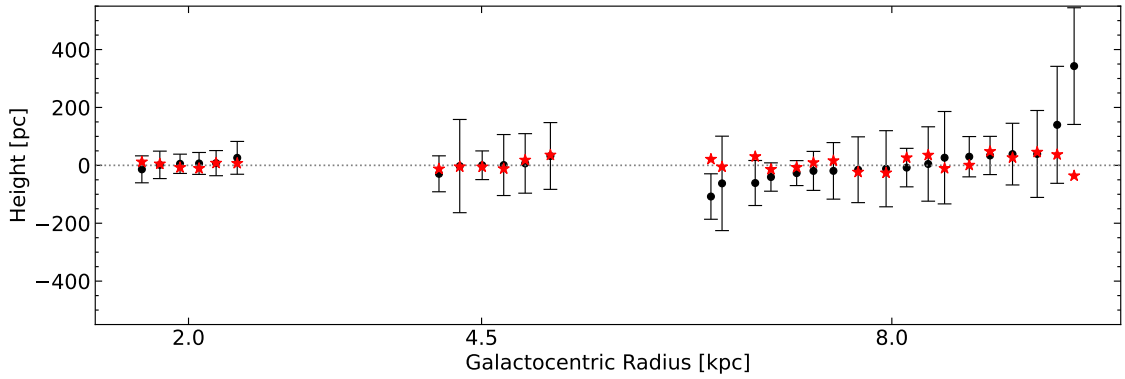

Figure 6.2: Initial vertical height of the explosion sites, grouped by galactocentric radius (star markers). Black dots denote the local galactic midplane; error bars the vertical scale height defined in the App. D.1. Radial coordinates, corresponding to $R = 2$, 4.5 and 8 kpc, were shifted for visibility. Even though the explosion sites were chosen to be close to $z = 0$, due to the warping of the disk, some of the SNRs are located outside the midplane.

$\sim 8\,\mathrm{kpc}$.

6.1.2 Zoom-in: Treatment of supernova remnants

We flag 30 star particles at three galactocentric radii $R \in \{2, 4.5, 8\}$ kpc and $z \sim 0$, spaced equidistantly in polar direction as *SNR* particles (see markers in Figs. 6.1 and 6.2). An overview of the local ISM properties in the selected regions is given in the App. D.1.

We refine all cells within $r_{\mathrm{zoom},l} = N_{\mathrm{zoom}}\Delta x_l$ of an SNR particle up to a maximum zoom-in resolution of $l_{\mathrm{max}} = 18$, corresponding to $\Delta x_{\mathrm{min}} \approx 0.18\,\mathrm{pc}$, where $N_{\mathrm{zoom}} = 15$. We further relax the system for $\lesssim 50\,\mathrm{kyr}$ to avoid numerical artifacts due to the sudden refinement. Unless specified otherwise, we measure time from the time of the snapshot at the end of this final relaxation step ($t = 0$).

Starting from $t = 0$, each SNR particle injects N_{SN} SNe per injection. SN injections may happen every Δt_{SN}. Models differ only by the choice of N_{SN} and Δt_{SN}.

Per SN, each SNR particle distributes $E_{\mathrm{SN}} = 10^{51}\,\mathrm{erg}$ of thermal energy and $M_{\mathrm{ej}} = 5\,\mathrm{M}_\odot$ of ejecta mass evenly within a sphere of radius $R_{\mathrm{inj}} = 5\Delta x_{\mathrm{min}} \approx 0.92\,\mathrm{pc}$ centered at the SNR particle's position. In addition each SNR particle injects one of two passive scalars $Z_{\mathrm{ej,\,i}}$, corresponding to red and blue markers in Fig. 6.1, used to label the mass fraction of SN ejecta and distinguish between the ejecta of neighboring SNRs. We note that our method of injecting the SN energy in a purely thermal fashion can lead to numerical artifacts that can affect the early expansion period (private communication). However, in Romano et al. (2024a) we have demonstrated that the later evolution from the ST phase onward is correctly reproduced, in agreement with the results of Walch & Naab (2015), who find that different injection methods reproduce the ST phase equally well, provided short enough time steps are used.

We refine polluted cells with $Z_{\mathrm{ej,\,i}} > 10^{-15}$ to at least $l_{\mathrm{min,\,zoom}}$ and even further up to at most $l_{\mathrm{max,\,zoom}}$ if

$$\Delta x > 0.1\,R_{\mathrm{sf}}^{\mathrm{KO15}}\,(n_{\mathrm{H}}) = 2.3\,\left(\frac{n_{\mathrm{H}}}{\mathrm{cm}^{-3}}\right)^{-0.42}\,\mathrm{pc}, \tag{6.1}$$

which roughly resembles the convergence criterion proposed by Kim & Ostriker (2015). We show an

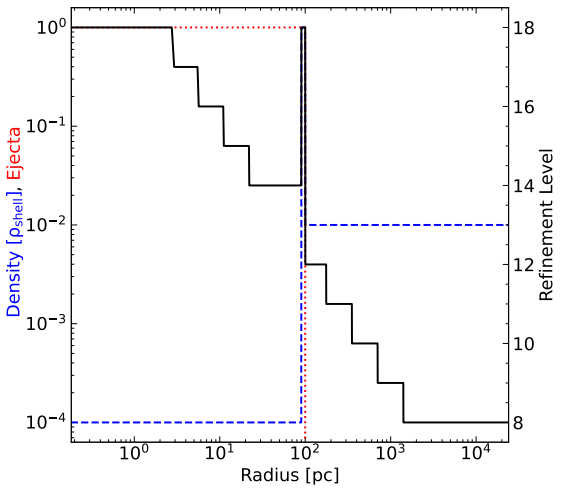

Figure 6.3: Refinement map produced with the refinement method outlined in Sec. 6.1.2 for the idealized situation of a diffuse bubble with a dense shell, designed to roughly resemble an SNR after shell formation. The solid-black, dashed-blue and dotted-green lines show the radial profiles of the refinement level, gas density and ejecta fraction (scalar tracer field), respectively. The resolution is decreasing radially outward, levels off at $l_{\mathrm{min,\ zoom}} = 14$ and increases again to $l_{\mathrm{max,\ zoom}} = 18$ inside the shell.

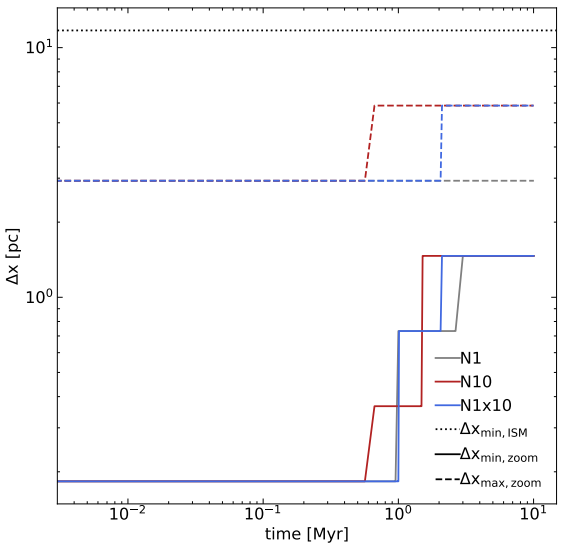

Figure 6.4: The resolution in the zoom-in region as a function of time. Gray, red and blue lines correspond to the three different runs, while different linestyles correspond to different refinement parameters. The resolution was decreased between restarts of the simulation when the memory requirements became too large. The maximum resolution in the refinement regions around the central SNR particles was left untouched.

idealized refinement map in Fig. 6.3. We initially set the zoom-in resolutions to $l_{\mathrm{min,\ zoom}} = 14$ and $l_{\mathrm{max,\ zoom}} = 18$, corresponding to $\Delta x_{\mathrm{max,\ zoom}} \approx 2.9\,\mathrm{pc}$ and $\Delta x_{\mathrm{min,\ zoom}} \approx 0.18\,\mathrm{pc}$, respectively, and reduce the resolution as the SNRs grow in order keep the numerical cost at a manageable level as shown in Fig. 6.4. With this refinement prescription, we are thus able to resolve the momentum generation during the Sedov-Taylor phase and the transition to the radiative phase for a single SN up to densities of $n_{\mathrm{H,\ max}} \sim 430\,(\Delta x/\Delta x_{\mathrm{min,\ zoom}})^{-2.4}\ \mathrm{cm}^{-3}$ (see e.g. Kim & Ostriker, 2015; Romano et al., 2024a).

With our implementation of star-formation, the mass of star particles formed at higher resolution needs to be adjusted in order to ensure that stars are forming if and only if cells are Jeans-unstable and fully refined. This condition is satisfied by scaling $m_{\star,l} \propto \Delta x_l$.

6.1.3 Simulation suite: An overview

Our simulation suite consists of *four* different runs: A baseline simulation without SNe (N0) and three simulations with SNe labeled N1, N10 and N1x10, corresponding to $(N_{\mathrm{SN}},\ \Delta t_{\mathrm{SN}}) = (1,\ \infty)$, $(10,\ \infty)$ and $(1,\ 1\ \mathrm{Myr})$, respectively. In particular, the models N1 and N10 feature a single explosion event at $t = 0$, while only in N1x10 there are subsequent explosion events every $\Delta t_{\mathrm{N1x10}} = 1\,\mathrm{Myr}$.

In N0 no zoom-in is applied. In order to estimate the effect the refinement might have, we have run a 5th simulation labeled N0_zoom without SNe, but with $N_{\mathrm{zoom}} = 85$.

6.2 Analysis

6.2.1 Classification of ISM components

In order to be able to meaningfully analyze the SNRs' properties we need to reliably differentiate between SNRs and the unperturbed ISM. Moreover, we classify different components of the SNRs, similarly to the approach of Romano et al. (2024a) for a single SNR in a uniform ISM.

We adopt the same method of using the passive scalars to flag cells belonging to an SNR. Neighboring SNRs inject different passive scalars, which enables us to resolve ambiguities if the SNRs approach or even overlap. Naïvely, each SNR corresponds to the set of cells polluted with the respective scalar that are closest to its center (e.g. the corresponding SNR particle). However, in practice since some SNRs get significantly larger than others, we find that this simple prescription would lead to a large number of cells being grouped incorrectly once the SNRs become too large. We avoid this problem by creating a weighted Voronoi-tesselation in face-on projection with cells centered at the position of the SNR particles and assigning weights, such that all polluted cells belonging to an SNR lie within the corresponding cell. We assign these weights by visual inspection.

As opposed to the case studied in Romano et al. (2024a), here, the ISM into which the SNRs are expanding is undergoing constant change. Thus, in order to study how the properties of the SNRs depend on the that of the ISM, we need to find an appropriate definition of the *local ISM*. Here, we define the local ISM as the contents of the smallest rectangular box, containing the entire SNR at all times. The *unperturbed, local ISM*, then corresponds to the contents of the local ISM without the SNRs, which necessarily shrinks as the SNRs grow. This leads to the slight bias, that once a region is swept up by the SNR, it ceases to contribute to the description of the unperturbed ISM. Nonetheless, the instantaneous state of the immediate surroundings of the SNRs describes the

unperturbed ISM much more accurately than its state at a single point in time (i.e. at $t = 0$ or at the time of observation). We note that while in this study, we do not make use of this definition, future analyses using the SISSI simulations will (L. Romano et al., in prep).

We further classify different components of the unperturbed ISM and the SNRs.

For the SNRs we follow the classification of Romano et al. (2024a). We distinguish between radially inflowing and outflowing shell and bubble components. The *bubble* corresponds to polluted, hot ($T > 2 \times 10^4\,\mathrm{K}$) or diffuse ($n_\mathrm{H} < 10^{-2}\,\mathrm{cm}^{-3}$) gas, while the *shell* corresponds to cold and dense, polluted gas. We decide whether the gas is in- or outflowing by measuring the radial velocity, measured from the center of mass of the SNR in the co-rotating, center-of-mass frame of each SNR.

For the unperturbed ISM we distinguish between *cold* ($T < 7 \times 10^3\,\mathrm{K}$), *warm* ($7 \times 10^3\,\mathrm{K} < T < 10^5\,\mathrm{K}$) and *hot* ($10^5\,\mathrm{K} < T$) gas phases, which are expected to coexist co-spatially in a turbulent medium with inhomogeneities driven by SN explosions and differential cooling (see e.g. McKee & Ostriker, 1977; Cox, 2005). The choice of $7 \times 10^3\,\mathrm{K}$ for the threshold between warm and cold gas, slightly less than the commonly used $\sim 10^4\,\mathrm{K}$, arises from the adopted cooling function, which produces persistent gas at this temperature as is shown in the App. D.1.

We also classify the stars within the ISM boxes based on whether they are *old*, i.e. formed before $t = 0$ or *young*. For the *young* stars we further distinguish between stars that are formed from *polluted* or *pristine* gas.

6.2.2 Definition of polluted cells

We define a cell to be polluted if its passive scalar concentration exceeds some threshold value $Z_{\mathrm{ej,\,thr}}$. The choice of this threshold value is arbitrary and can systematically bias our results. If we choose a value of $Z_{\mathrm{ej,\,thr}}$ that is too low, we risk including gas that is only (slightly) polluted due to numerical noise, but that physically is not associated with the SNRs. On the other hand if we choose a value that is too high, we risk missing parts of the SNRs.

In practice it seems impossible to entirely prevent both effects from happening, so we aim for a compromise and state our results in terms of range of plausible values based on a slightly high and a slightly low threshold value. We first perform our analysis for a slightly low value $Z_{\mathrm{thr,\,low}} = 10^{-12}$, comparable to the value used in Romano et al. (2024a). After defining the local ISM boxes, based on the SNRs defined by the choice of $Z_{\mathrm{thr,\,low}}$, we define $Z^i_{\mathrm{thr,\,high}}(t)$ for each SNR and snapshot, by requiring that the total ejecta mass of cells with $Z_{\mathrm{ej,\,i}} > Z^i_{\mathrm{thr,\,high}}(t)$ just exceeds 99.99 per cent of the total gas-phase ejecta-mass in the ISM box.

6.2.3 SNR geometry

We study the dynamical evolution of the SNRs' geometry, by analyzing how their shape tensors evolve over time. We define the shape tensor as

$$S_{ij} = V_\mathrm{SNR}^{-1} \int_\mathrm{SNR} \left(\|\mathbf{x}\|^2 \delta_{ij} - x_i x_j \right) \mathrm{d}^3\mathbf{x} \,, \tag{6.2}$$

which is the volume weighted inertia tensor, assuming a constant density of unity. By assuming an approximately ellipsoidal shape, we can define the three ellipsoidal radii, defined as

$$r_i = \sqrt{2.5\left(\mathrm{tr}\,(S) - 2S_i\right)} \,, \tag{6.3}$$

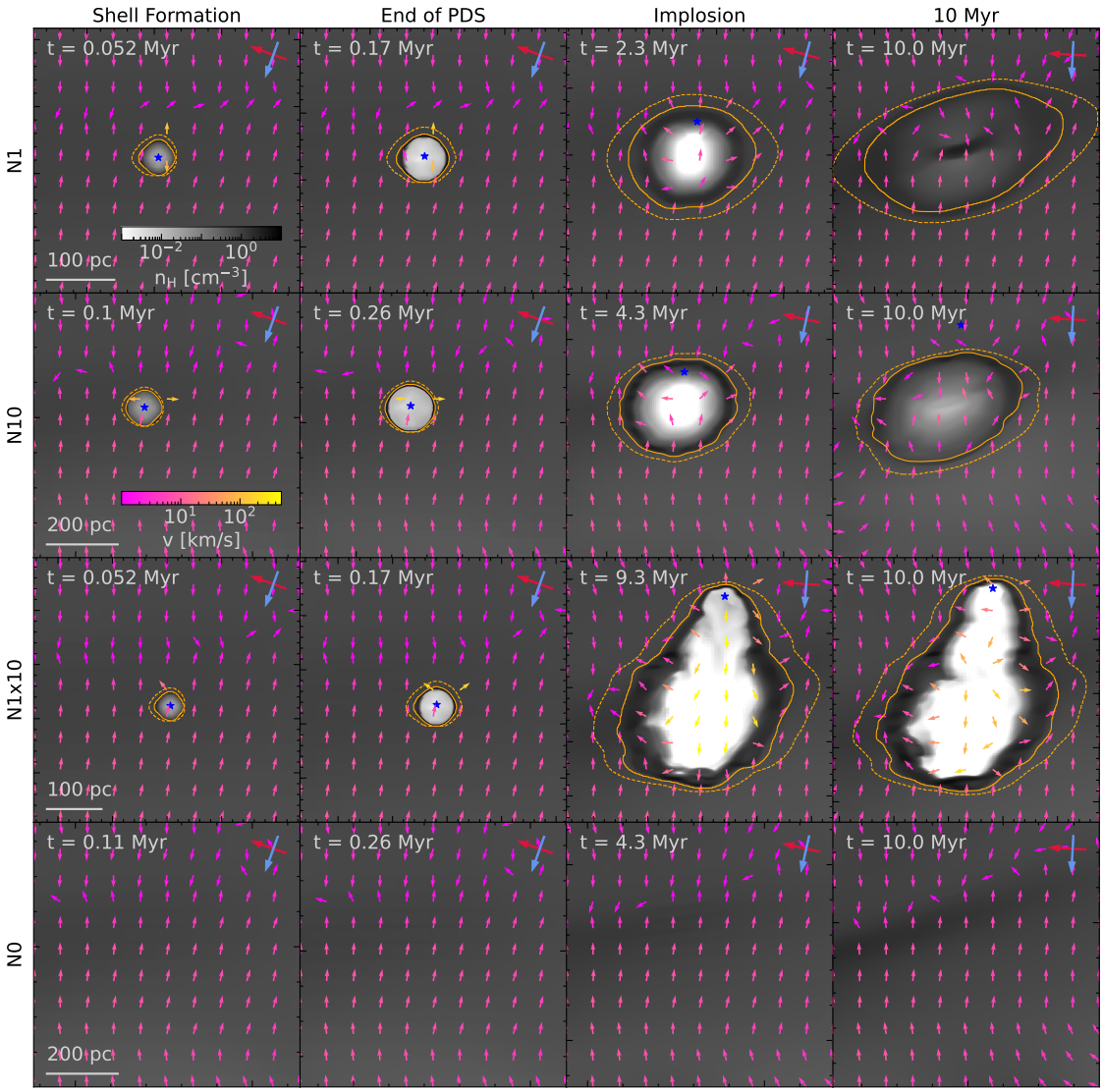

Figure 6.5: Density-slices through the central plane of the SNR #22 at various points in time for each model. Arrows are depicting the velocity field in the co-rotating center-of-mass frame of the local ISM. The various timescales correspond to different points in time for the different models. Red and blue arrows in the top-right corner of each panel indicate the directions of the galactic rotation and the galactic center, respectively. The dashed orange contour corresponds to the surface where $Z_{\rm ej} = Z_{\rm thr,\ low}$, while the solid contour corresponds to $Z_{\rm ej} = Z_{\rm thr,\ high}$. Since the various timescales are undefined for the model no_expl, we are using the same times as model N10. The SNe explode into a fairly homogeneous ISM, with a slowly collapsing, slight overdensity right where the SNe explode. At similar evolutionary stages the SNR is about twice as large in N10 compared to N1, with very similar geometry; Spheroidal with a slight elongation in the direction of rotation. On the other hand the geometry in the model N1x10 qualitatively differs from the other models, with an elongated cavity normal to the rotational direction, due to the elliptical orbit ($v_{\rm R} \sim 20\,{\rm km/s}$) of the explosion site. Only in the model N1, after 10 Myr a dense cloud, aligned with the SNR is forming in the center as predicted by Romano et al. (2024a).

where S_i are the eigenvalues of S_{ij} and $\mathrm{tr}\,(S)$ the trace. We refer to the smallest, intermediate and largest eigenvalue as the minor a, semi-major b and major c axis, respectively. We define the effective size of an SNR as the geometric mean of the three eigenvalues

$$r_{\mathrm{eff}} = (abc)^{1/3} \quad . \tag{6.4}$$

To determine the alignment of the SNRs within the galaxy, we measure their pitch angle α and polar direction $\cos(\theta)$ for both the major and minor axes. The pitch angle is defined relative to the direction of galactic rotation, with $\alpha = 90°$ and $\alpha = -90°$ corresponding to the galactic center and anti-center, respectively. The magnitude of the polar direction is 0 (1) for directions parallel (perpendicular) to the galactic plane.

6.3 Time evolution of SNRs

6.3.1 Showcase: Supernovae in relatively uniform medium

The case of stellar feedback in an ambient medium with solar metallicity and an ambient density of $n_{\mathrm{H}} \sim 1\,\mathrm{cm}^{-3}$ has been widely studied (e.g. Kim & Ostriker, 2015; Fierlinger et al., 2016; Oku et al., 2022; Romano et al., 2024a). In this section we showcase the results of SNR #22, which happens to explode in a relatively uniform medium with an ambient density close to $1\,\mathrm{cm}^{-3}$ and compare its time evolution to that found in previous studies.

In Fig. 6.5 we show slices of the density field through the center of SNR #22 parallel to the xy-plane at various characteristic times for the different models. In each panel, the outline of the SNR is shown by orange lines, depicting contours of constant Z_{ej}, corresponding to $Z_{\mathrm{thr,\,low}}$ (dashed line) and $Z_{\mathrm{thr,\,high}}$ (solid line).

As can be seen in the bottom row, corresponding to the N0 model, the density field is indeed rather uniform, but some collapse into a filamentary structure over several Myr is visible.

At shell formation (first column) the SNRs are spherical with a slightly underdense central region and a thin, overdense shell. The time of shell formation and the SNRs' sizes are in agreement with previous work (e.g. Kim & Ostriker, 2015).

After shell formation, SNRs enter the so-called pressure-driven snowplow (PDS) phase, which ends once the pressure in the cavity drops below that of the shell (second column). At this time, the SNRs are spherical, with an increasingly underdense central region and a thin, overdense shell. The time at which the PDS phase ends and the SNRs' sizes are in agreement with previous estimates (Romano et al., 2024a).

Romano et al. (2024a) have shown that SNRs implode as they merge with their ambient medium. In their simulations, a SNR in an ambient medium with $n_{\mathrm{H}} \sim 1\,\mathrm{cm}^{-3}$, such as the one considered here, began to implode after $\sim 1\,\mathrm{Myr}$. In the third column we show the SNRs right after the onset of implosion. By this time the SNRs are slightly elongated, parallel to the collapsing filament, which is at a slight angle to the direction of galactic rotation. In all cases, the implosion occurs significantly later than our expectation based on previous work. In the model N1x10, the implosion seems to be coincident with the explosion happening at $t \sim 9\,\mathrm{Myr}$ and is no longer visible by $t = 10\,\mathrm{Myr}$. We rule out this "implosion" as a false positive and caution that with our definition of the implosion timescale we cannot distinguish between brief moments of radially "inflowing" ejecta in N1x10 due to a displacement of the explosion sites and sustained inflows of cold gas from the shell.

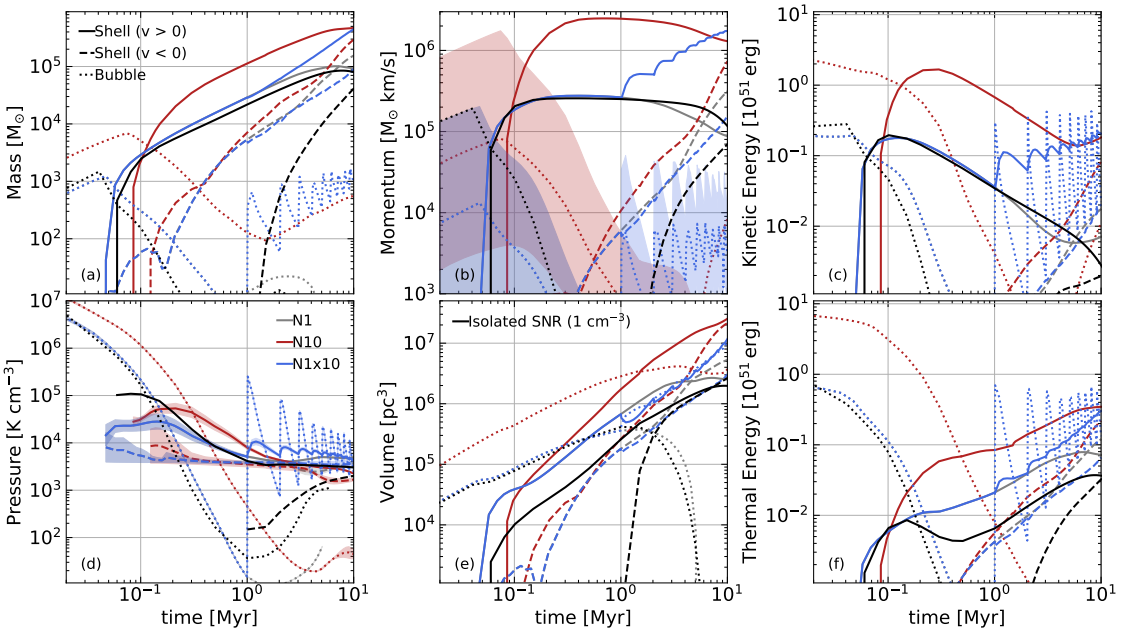

Figure 6.6: Various properties (Mass, momentum, kinetic and thermal energy, pressure and volume) of the SNR #22 as a function of time for the various models using the classification introduced in Sec. 6.2.1. Shaded regions correspond to the margin of uncertainty introduced by the choice of $Z_{\mathrm{ej,\,thr}}$, while the lines correspond to the geometric average of the values obtained with high and low values of $Z_{\mathrm{ej,\,thr}}$. For comparison we show the time evolution of an isolated SNR at a similar ambient density ($n_{\mathrm{H}} = 1\,\mathrm{cm}^{-3}$) taken from Romano et al. (2024a). As expected, the models N1 and N10 exhibit similar behavior and the model N1 also agrees quantitatively quite well with the isolated SNR. In the model N1x10, the SNR initially follows the model N1 and then after the onset of the consecutive SNe diverges reaching a comparable mass, momentum and size as the model N10 after 10 Myr. However, the fraction of thermal energy in the bubble is higher in N1x10 compared to N10, indicating more efficient hot phase generation. Difference due to the choice of $Z_{\mathrm{ej,\,thr}}$ are largest before shell formation and are most pronounced in the mass and momentum of the bubble, indicating that ejecta are initially lagging behind the shock, but catch up once a cold shell forms.

After 10 Myr (fourth column), the SNRs in models N1 and N10 have been stretched out considerably in the direction of the collapsing filament. The implosion in N1 has reached the center and condensed into a growing, filamentary implosion cloud, as predicted by Romano et al. (2024a,b), which is stabilized by the rapid radiative dissipation of the energy carried by the implosion shocks colliding in a central region. In N10 the center of the SNR is still underdense indicating that the implosion has not yet reached the center. Meanwhile, in N1x10 the SNR is stretched out predominantly in radial direction following the wake of the explosion center, which happens to be drifting radially outward. The interior of the superbubble remains strongly underdense.

One can see, that the volume traced by the dashed line corresponding to $Z_{\mathrm{thr,\,low}}$ tends to be slightly larger than the SNRs, particularly along the directions aligned with the Cartesian grid at early times, and at late times the direction of galactic rotation.

In Fig. 6.6 we show various global properties of the SNRs as a function of time and compare them to those of a single SN exploding into a uniform medium with an ambient density of $n_{\mathrm{H}} = 1\,\mathrm{cm}^{-3}$ taken from Romano et al. (2024a). We note that they used a different cooling function, leading to a slightly lower equilibrium pressure (see panel (d)).

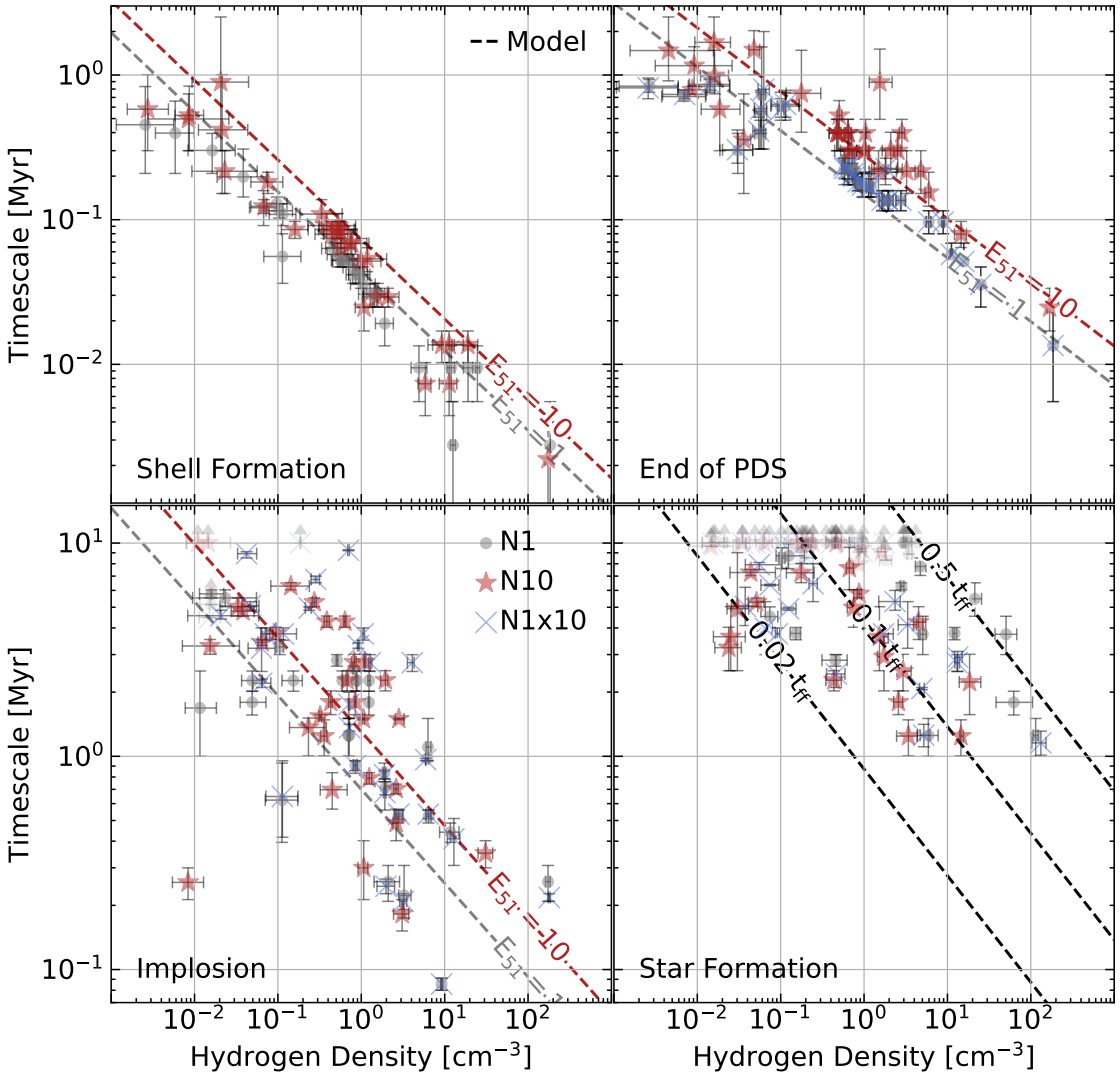

Figure 6.7: Various timescales as a function of ambient density for our simulated sample of SNRs. Uncertainties arise due to the finite spacing of the snapshots and due to the choice of $Z_{\mathrm{ej,\,thr}}$. The timescales of shell formation, the end of the PDS phase and SNR implosion agree well with the predictions from models based on simulations of isolated SNRs (Kim & Ostriker, 2015; Romano et al., 2024a). The timescale measuring the onset of star formation within the SNRs is within a factor of five of 10 per cent of the free-fall timescale of the star-forming SNRs.

All quantities are defined in essentially the same way as in Romano et al. (2024a), i.e. extensive quantities are computed by summing up the contributions from all cells belonging to the respective gas phases and the pressure is calculated as a volume weighted average. However, due to the differential movement of the ambient medium, differences might arise in the momentum and kinetic energy due to the choice of inertial system, which we here have chosen to be the center-of-mass system after subtracting the galactic rotation, azimuthally averaged in linearly spaced, radial bins with spacing $\Delta R \approx 47\,\mathrm{pc}$.

In the model N1, all quantities except the pressure and the thermal energy agree with the isolated SNR for the first $\sim$ 2Myr within uncertainties. At late times the radial momentum and kinetic energy drop more rapidly. The kinetic energy, eventually recovers and levels off at $\sim 1\,\%$ of the injected explosion energy. However, these small differences might well be explained by the choice of the inertial system.

Model N10 appears to be a rescaled version of N1, in line with the idea, that SNRs undergo a series of self-similar evolutionary stages.

After 1 Myr, model N1x10 starts to diverge from N1. The amount of swept up mass, the total radial momentum, and kinetic as well as thermal energy of the SB grow to be quite similar to those of N10, at $t = 10\,\mathrm{Myr}$; though with large temporal variations in the distribution between the bubble and the shell. This indicates that these quantities are mostly sensitive to the total amount of injected energy, regardless of the exact interval between injections, in stark contrast to the geometry and mass distribution within the SNR, as shown in Fig. 6.5. Nonetheless, in model N1x10 the SNR is retaining more radial momentum, and sustaining a higher pressure, indicating that the subsequent radiative losses are determined by the multi-phase structure of the ISM at the injection site.

6.3.2 The full SISSI sample

We have shown, that SNR #22 adheres well to the expectations from isolated SNRs in uniform ambient media. However, this might just have been a special case that cannot be applied to the whole sample. Thus, in this section we evaluate to what extent our full sample of SNRs follows the expectations from previous work.

In Fig. 6.7 we show various characteristic timescales as a function of ambient density, defined here as the ratio of the swept-up mass and the volume covered by each SNR at each point in time, for the different models and compare them with analytical results from previous work, described in the App. D.2, shown as red and gray lines in the different panels.

We find that the shell-formation timescale of the simulated SNRs matches the theoretical estimate Eq. D.3, in line with the expectation that SNRs are hardly affected by the galactic environment during the early adiabatic expansion phase. The same holds true for the timescale for the end of the PDS (Eq. D.6), with some exceptions at very low densities.

Differences to the purely analytic picture become more apparent when comparing the timescale of implosion Eq. D.8, where we assume $\sigma_1 = 0.8$ corresponding to an ambient pressure of $P_\mathrm{ISM} \sim 10^4\,k_\mathrm{B}\,\mathrm{K\,cm^{-3}}$, matching the pressure of the isobaric phase of the ISM (Fig. D.1). Here we define t_launch slightly differently from Romano et al. (2024a), who defined t_launch as the time of the first snapshot when at least $0.1\,\mathrm{M_\odot}$ are in the form of backflowing shell gas. In SISSI, this condition would be met at almost all times, due to the uncertainties in the selection of the SNR gas and the turbulent motion of the background medium. We thus restrict the criterion to the ejecta, and define t_launch as the earliest time when the backflowing part of the shell contains at least $2\,\%$ of the ejecta, tagged by the respective scalar tracer. We find, that while the bulk of SNRs is not

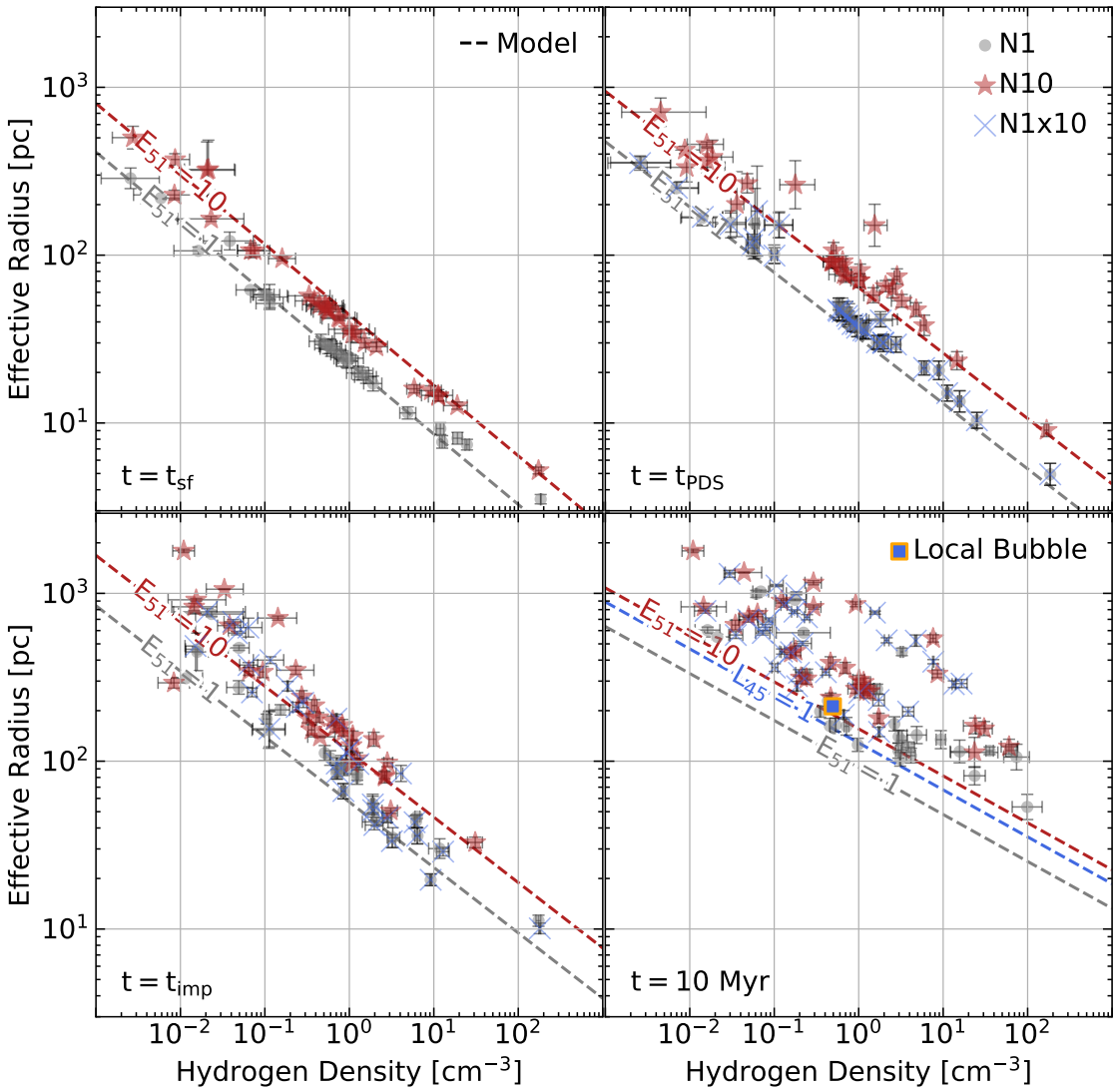

Figure 6.8: SNR size at various characteristic points in time as a function of ambient density for our simulated sample of SNRs. Uncertainties arise due to the finite spacing of the snapshots and due to the choice of $Z_{\mathrm{ej,\,thr}}$. An orange and blue square depicts the effective radius of the LB derived from the 3D dust maps of Edenhofer et al. (2024) in the panel corresponding to $t = 10\,\mathrm{Myr}$. Error bars are smaller than the marker and thus not shown. The radii at shell formation, the end of the PDS phase and at SNR implosion agree well with the predictions from models based on simulations of isolated SNRs (Kim & Ostriker, 2015; Romano et al., 2024a) for sufficiently large ambient densities. At low densities the sizes tend to exceed the model predictions. After 10 Myr the SNRs are about twice the expected size.

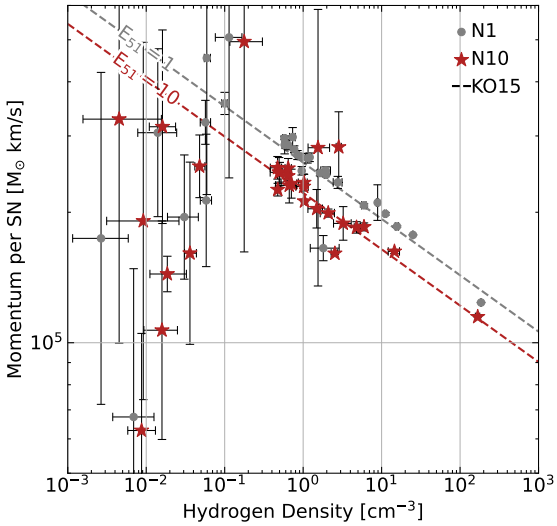

Figure 6.9: Outward, radial momentum per SN at the end of the PDS phase as a function of ambient density. Uncertainties arise due to the finite spacing of the snapshots and due to the choice of $Z_{\rm ej,\,thr}$. At sufficiently high density $n_{\rm H} \gtrsim 0.1\,{\rm cm}^{-3}$ the momentum input matches well the the prediction of simulations of isolated SNRs (Kim & Ostriker, 2015; Romano et al., 2024a). On the other hand, at lower densities the momentum per SN is often lower than expected, with large error bars.

too far from the analytical model, there is considerable scatter and a number of extreme outliers. Moreover, as we note in the discussion of Fig. 6.5, the interpretation of SNR implosion in the context of model N1x10 is somewhat unclear, as the interior pressure of the SBs tends to remain high.

We also show the time after which stars start to form from material polluted by SNe. There is no star-formation from polluted gas for the first 1 Myr, but within about a factor of 5 of $0.1\,t_{\rm ff}$ stars begin to form within the SNRs, where

$$t_{\rm ff} = \sqrt{\frac{3\pi}{32 G \rho}} \sim 44.9\,n_0^{-0.5}\,{\rm Myr}\,, \tag{6.5}$$

is the free-fall timescale. Importantly, in many cases this star formation does not appear to be triggered within the SNRs, but rather is the continued star-formation in pre-existing star-forming regions, that are swept up and enriched by the SNRs. A more detailed analysis of the potential triggering of star-formation in SISSI is out of the scope of this work and will be the focus of future publications (L. Romano et al. 2025, in prep.).

In Fig. 6.8 we show the effective size, as defined in Sec. 6.2.3, as a function of ambient density for the different models at various characteristic points in time. Red, gray and blue lines depict the expected sizes, building on the theoretical models described in the App. D.2. In the panel corresponding to the last snapshot at 10 Myr, the orange and blue square corresponds to the effective size of the LB derived from the data products of Edenhofer et al. (2024) as described in a companion paper (L. Romano et al. 2025).

We find, that overall SNR sizes are in line with theoretical expectations during the stages of SNR evolution before merging with the ISM, i.e. before $t = t_{\rm launch}$, but start growing larger than expected at later times. SNRs in low density environments $n_{\rm H} \lesssim 0.1\,{\rm cm}^{-3}$ start to diverge from the theoretical expectation by $t_{\rm imp} \gtrsim 1\,{\rm Myr}$.

After 10 Myr all SNRs are about twice the expected size, indicating the need for better models of old SNRs in a shearing, stratified ISM. Interestingly, the LB is on the smaller end of the sizes for simulated SNRs in similar density media, even though it is expected to be older, i.e. $t_{\rm LB} \sim 14\,{\rm Myr}$ (Zucker et al., 2022; Breitschwerdt & de Avillez, 2006). We further discuss this point and its implications in a companion paper (L. Romano et al. 2025).

In Fig. 6.9 we show the momentum input per SN at the end of the PDS stage and compare it to the theoretically expected value, assuming a momentum enhancement after shell-formation of $\sim 20\,\%$, slightly lower than the $\sim 50\,\%$ reported by Kim & Ostriker (2015). The momentum input in the denser regions $n_{\rm H} \gtrsim 0.1\,{\rm cm}^{-3}$ roughly follows the theoretical expectation, with little scatter. In contrast to lower density regions, where the momentum per SN drops off with large scatter. This behavior is likely due to the large size ($\gtrsim 100\,{\rm pc}$) of these SNRs, leading to more frequent energy dissipation due to interactions with high density structures.

6.4 Geometry of simulated SNRs

In the previous section we have shown that while young SNRs are well described by the theory based on models in a uniform, stationary medium, the models start to fail, on longer timescales $\gtrsim 1\,{\rm Myr}$. In order to obtain some clues as to what may be causing these differences, here we study their geometry, which reveals a preferential alignment that may point us towards the governing physical processes.

6.4.1 The shape phase-space

In Fig. 6.10, we show the trajectories of the SNR #22 for the different explosion models in the shape phase space, defined by the minor-to-major and semi-major-to-major axis ratio. By definition, at $t = 0$ the SNR starts as a perfect sphere ($a/c = b/c = 1$) and by deformation through various processes may evolve to become increasingly prolate ($b/c < 2/3$) or oblate ($a/c \to 0$ and $b/c > 2/3$). In purple, we also show the trajectory of a shearing sphere as described in the App. D.3. The sphere of radius $r_0 = 100\,{\rm pc}$ is initially located at a galactocentric radius of $R_0 = 8\,{\rm kpc}$ and is rotating at a constant rotation velocity, matching that measured in the simulation.

In the models N1 and N10, the trajectory in the shape phase-space is smooth, with almost constant minor-to-semi-major axis-ratio $a/b > 2/3$ and ever decreasing a/c, i.e. the SNRs are becoming increasingly prolate. In model N1, a/b is slightly larger than in N10, i.e. the SNR is slightly more prolate. The simulated SNRs are significantly more deformed than the shearing sphere, which after 10 Myr is still quite spherical ($a/c \sim 0.75$, $b/c \sim 0.85$).

The trajectory in the model N1x10 has a kink, corresponding to the onset of further explosions, which deform the SNR in chaotic ways, ultimately leading to a more spherical shape. The final shape is similar to that of the shearing sphere.

In Fig. 6.11 we show the locations of our sample of SNRs in the shape phase-space at various characteristic points in time. Markers are colored by the ambient density. In the panel corresponding to the last snapshot at 10 Myr, we compare the shape of the LB derived from the data products of Edenhofer et al. (2024), shown as an orange and blue square, to our simulated sample.

The three panels corresponding to shell-formation, the end of the PDS phase and the onset of the implosion reveal that most SNRs remain close to spherical throughout the main stages of SNR evolution, with $a/b \gtrsim 2/3$ and $b/c \gtrsim 2/3$. In contrast, SNRs in very low density ambient media $n_{\rm H} \lesssim 10^{-2}\,{\rm cm}^{-3}$ already begin to deviate from spherical symmetry before shell formation, likely

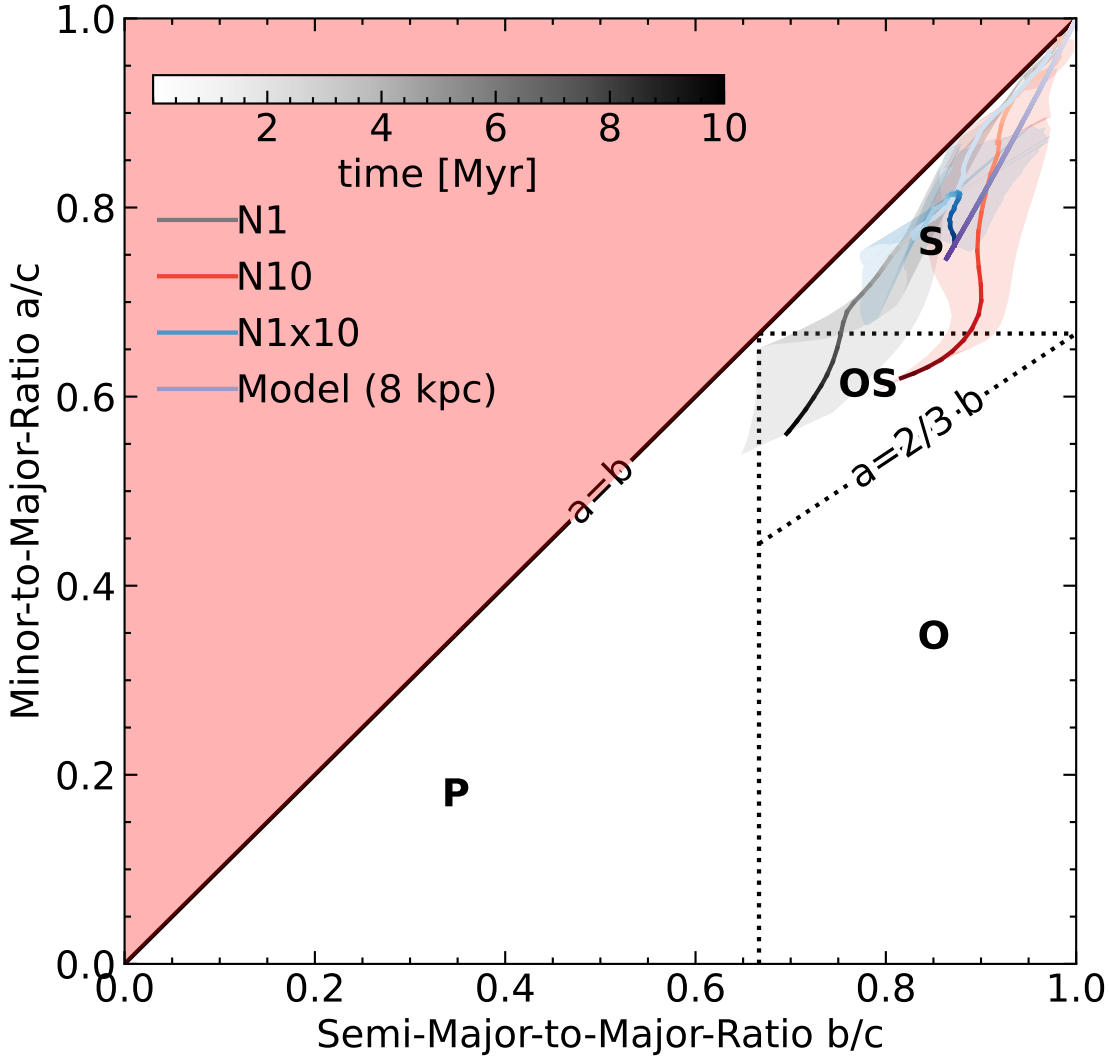

Figure 6.10: Evolutionary tracks of the SNR #22 in the shape phase-space for the various explosion models. Uncertainties due to the choice of $Z_{\mathrm{ej,\ thr}}$ are shown as shaded regions. In different parts of the phase space the SNRs are either spherical (S), oblate spheroids (OS), prolate (P) or oblate (O). The SNR starts out as a perfect sphere and becomes increasingly prolate over time. The ratio of the two minor axes remains close to one and never falls below 2/3. In the model N10 the SNR remains spherical for longer compared to N1. Similarly the consecutive SN explosions in the model N1x10 restore spherical symmetry.

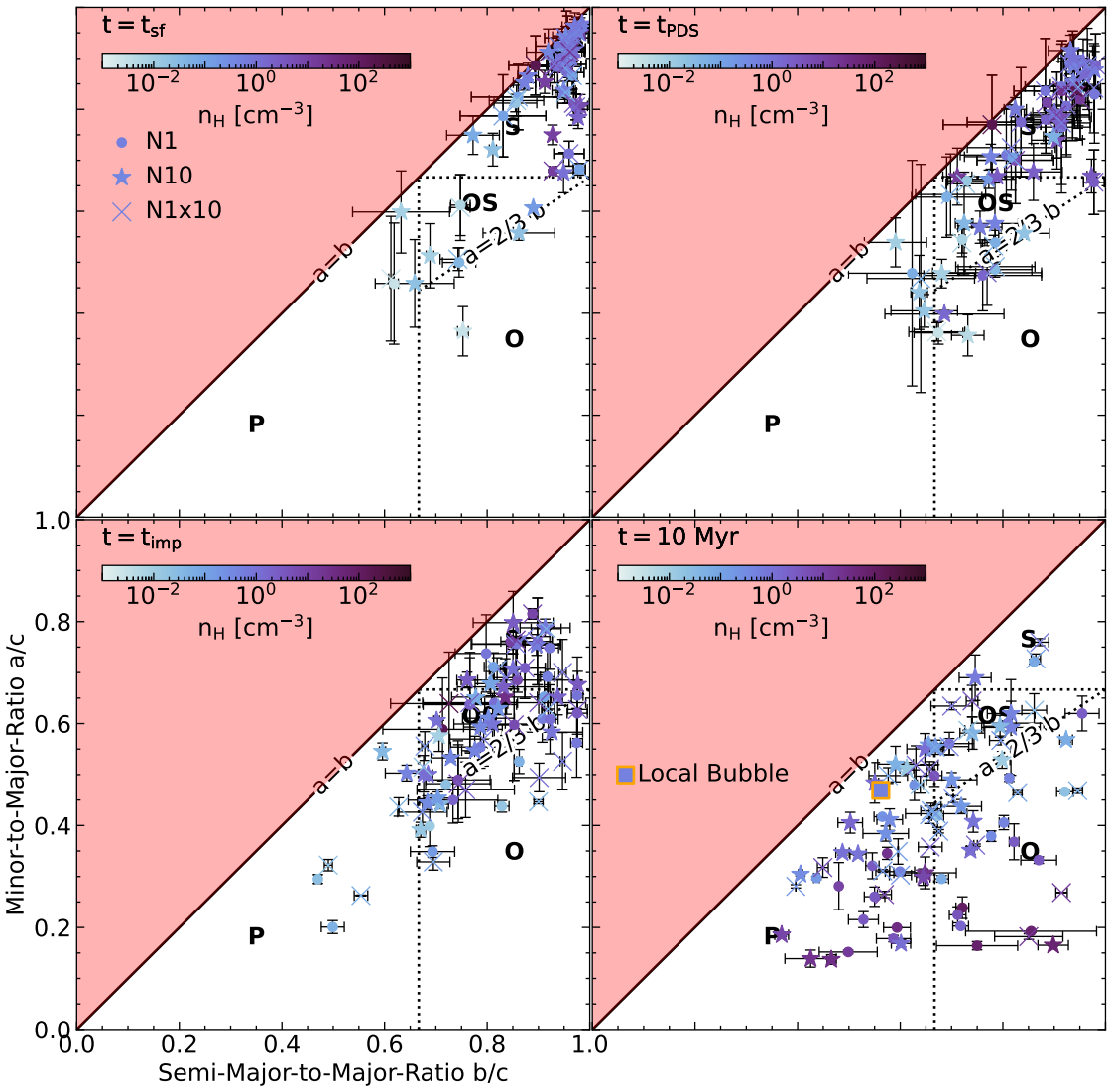

Figure 6.11: Distribution of SNR shapes at various characteristic points in time for the different explosion models. Uncertainties due to the choice of $Z_{\mathrm{ej,\ thr}}$ are represented by error bars. Different regions are labeled as in Fig. 6.10. An orange and blue square depicts the shape of the LB derived from the 3D dust maps of Edenhofer et al. (2024) in the panel corresponding to $t = 10\,\mathrm{Myr}$. Error bars are smaller than the marker and thus not shown. At shell formation the SNRs tend to be spherical, with SNRs in lower-density environments being somewhat less spherical. At the end of the PDS stage and the onset of the implosion, most SNRs are still spherical or oblate spheroids with $a/b \gtrsim 0.5 - 0.67$. However, some of the lower-density SNRs are already quite asymmetric falling into the prolate and oblate category. The SNRs in the N10 model tend to be somewhat more spherical. At 10 Myr, the majority of SNRs are asymmetric. In dense environments SNRs tend to be quite asymmetric with low $a/c \sim 0.2$. The model N1 tends to have lower $a/b \sim 0.5$ compared to the other explosion models which tend to have $a/b \gtrsim 2/3$.

due to their older age and larger size at the the same evolutionary stage, indicating that they are likely tracing a more anisotropic environment than their high-density counterparts.

After 10 Myr the trend is reversed. The SNRs with the highest ambient densities are deformed the most, exhibiting highly anisotropic shapes $a/c \sim 0.2$ with a wide range of geometries $1/3 \lesssim b/c \lesssim 1$. Only 4 SNRs remain spherical, with most SNRs being slightly prolate and some oblates. The LB has a usual shape for an SNR with its ambient density, being slightly prolate with $a/b \sim 0.8$ and $a/c \sim 0.5$.

6.4.2 Alignment of SNRs within the galaxy

In the previous subsection we have shown that the simulated SNRs evolve towards increasingly anisotropic geometries, suggesting that they may expand more in certain directions than others. In order to check, whether there are any preferential directions, in Fig. 6.12 we show the time-span weighted distribution of the pitch angles and the magnitude of the polar directions as defined in Sec. 6.2.3 of the minor axis (oblates, orange) and major axis (prolates, purple). We also show the alignment of the minor- and major-axes of the LB derived from the data products of Edenhofer et al. (2024), shown as an orange and a purple square, respectively. The $1\,\sigma$-confidence intervals are shown as shaded regions in the one-dimensional histograms.

We find that for most of the time, the minor axis of the oblate SNRs is pointing perpendicular to the disk plane, with a broad distribution of negative pitch angles, centered around $\alpha_{\mathrm{oblate}} \sim -60°$. In contrast, in the case of prolate SNRs, the polar direction of the major axis is broadly distributed, with most of the weight lying below $|\cos(\theta)| \lesssim 0.5$, corresponding to the directions within the galactic plane. The distribution of pitch angles has three peaks around $\alpha_{\mathrm{major}} \sim 15°$, $25°$ and $50°$, in line with the expectations for structures deformed by shear (App. D.3, see also the alignment of underdense substructure in Fig. 6.1).

While the LB is slightly prolate, its minor axis points in a direction in agreement with that of oblate SNRs. On the other hand, its major axis is pointing slightly towards the galactic outskirts and is slightly more perpendicular than the bulk of our sample of SNRs.

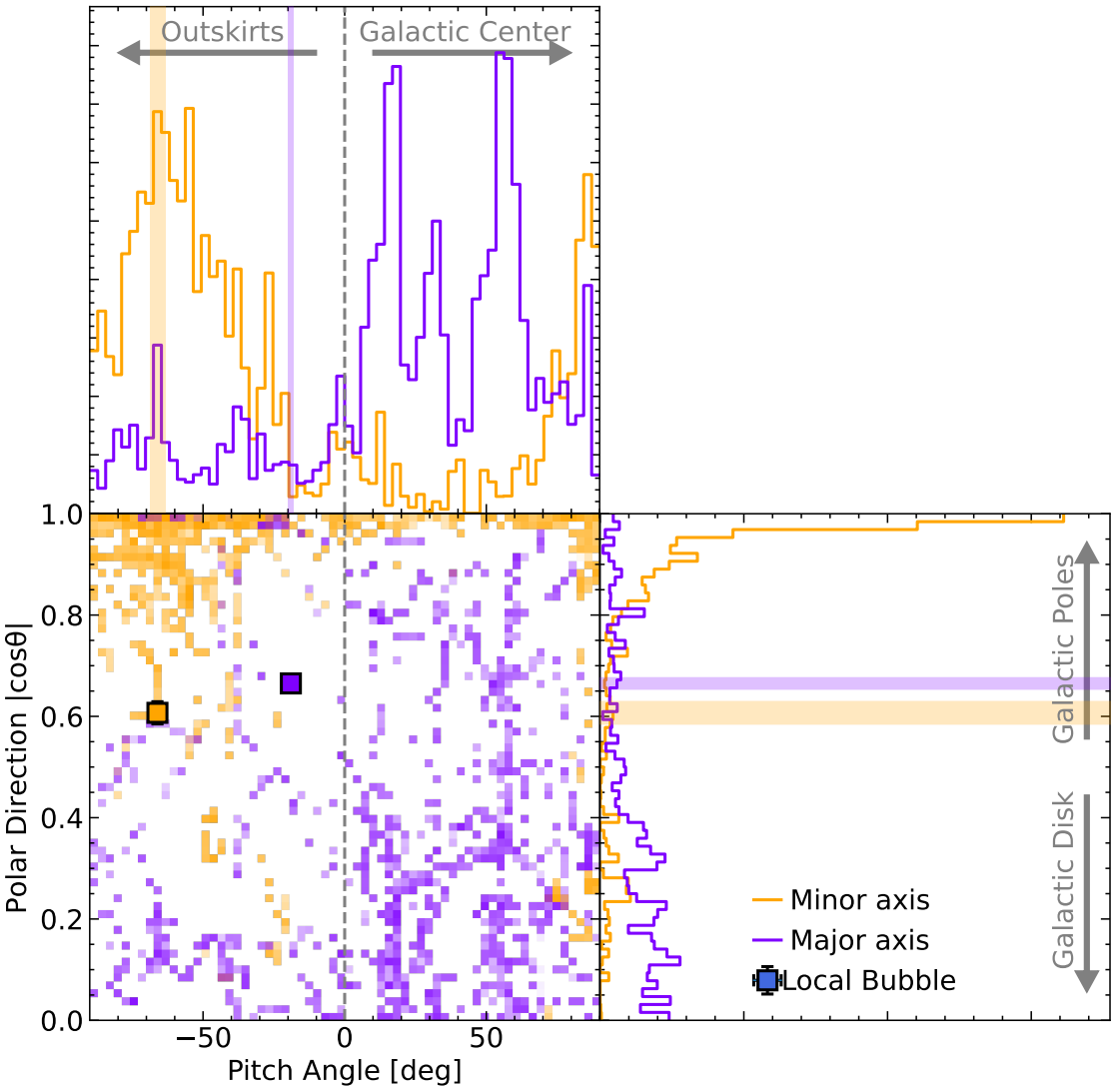

Figure 6.12: Time-span-weighted-histograms showing the distribution of SNR directions for asymmetric SNRs. Distributions of oblate (prolate) SNRs are colored orange (violet). For oblate (prolate) SNRs we show the direction of the minor (major) axis. We show the polar direction normal to the disk plane and the pitch angle relative to the direction of galactic rotation. We do not differentiate between directions above or below the disk. Positive pitch angles point between the galactic center and negative angles point towards the galactic outskirts. Orange and purple squares depict the directions of the minor and major axes of the LB, respectively, derived from the 3D dust maps of Edenhofer et al. (2024). The $1\,\sigma$-ranges for the LB are also indicated as shaded areas in the one-dimensional histograms. Oblate SNRs tend to point vertically out of the disk and towards the galactic outskirts with a typical pitch angle of $\alpha_{\mathrm{minor}} \lesssim -50\,\mathrm{deg}$. On the other hand, prolate SNRs tend to lie within the disk plane $|\cos(\theta)| \lesssim 0.5$ pointing slightly towards the galactic center $\alpha_{\mathrm{major}} \sim 10 - 60\,\mathrm{deg}$.

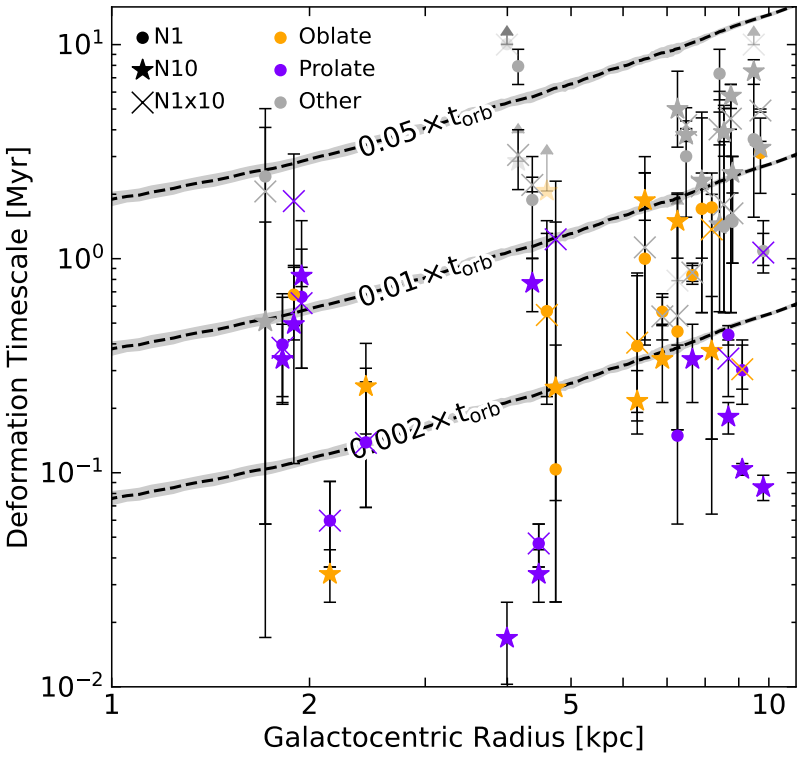

Figure 6.13: Deformation timescale as a function of galactocentric radius. Uncertainties arise due to the finite spacing of the snapshots and due to the choice of $Z_{\mathrm{ej,\,thr}}$. For visibility, markers are slightly shifted around their respective radii $R_{\mathrm{gal}} = 2$, 4.5 and 8 kpc, with the same shift used for the same SNR, but different explosion model. Typical deformation timescales are on the order of a few percent of the orbital timescale at each radius, slightly shorter than what is expected from deformation by galactic shear alone.

6.4.3 Deformation timescale

In the previous subsections we have found, that our sample of simulated SNRs evolving into the shearing, stratified ISM of the SISSI galaxy grow increasingly anisotropic, assuming a geometry that aligns with the sheared structure of the galaxy. The time it takes for an initially spherically symmetric structure such as SNR to become deformed hints at the processes governing the deformation. To this end, we define the deformation timescale as the time at which the minor-to-major ratio drops below $a/c = 2/3$.

The shearing-sphere model (App. D.3) indicates that shear can deform a spherical structure within a few percent of an orbital timescale. To test, whether shear alone is enough to explain the deformation of the SNRs we show the deformation timescale as a function of galactocentric radius in Fig. 6.13. Markers are colored based on the shape classification of the SNRs.

The majority of the SNRs is deformed within $\lesssim 1\,\%$ of the orbital timescale, with several SNRs being deformed much before even a thousandth of an orbit. More spherical SNRs, i.e. SNRs that are classified neither as prolate or oblate, tend to have longer deformation timescales, more plausibly explicable by shear alone. There are relatively more oblate SNRs at larger galactocentric radius. Overall, the deformation of the SNRs is too rapid to be explained by shear alone.

Another likely relevant source of deformation are preexisting density anisotropies in the ambient

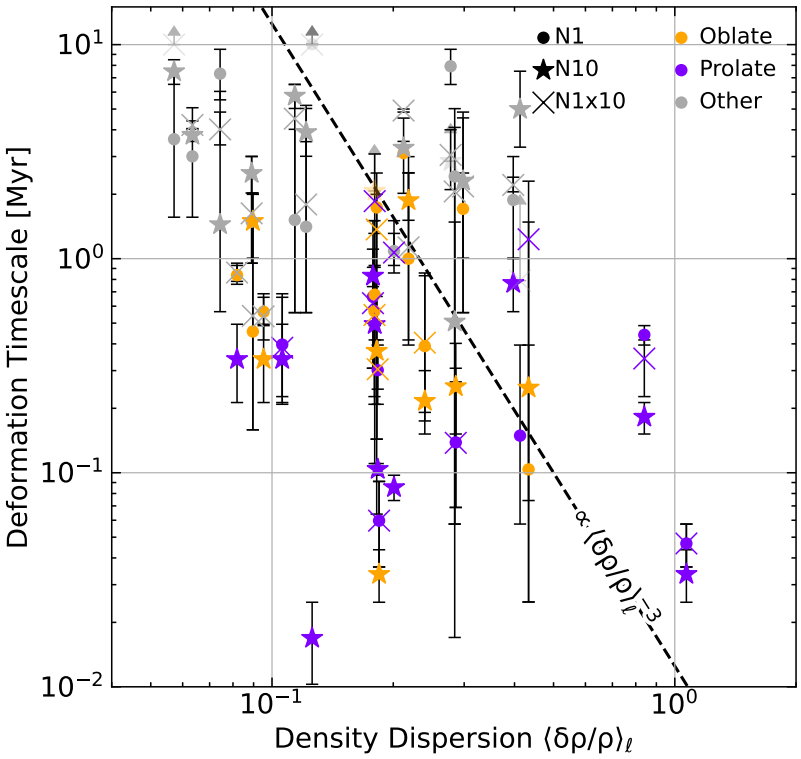

Figure 6.14: Deformation timescale as a function of density dispersion. Uncertainties arise due to the finite spacing of the snapshots and due to the choice of $Z_{\mathrm{ej,\ thr}}$. The deformation timescale is roughly $\propto (\delta\rho/\rho)^{-3}$ with significant scatter, qualitatively in line with the expectation that SNRs are deformed earlier in more anisotropic media.

ISM, which imprint onto the geometry of the SNRs as they expand into them (Makarenko et al., 2023). We quantify the degree of spatial variation in the density field, by measuring its relative variation at $t = 0$ across spatial scales, by averaging over nested ISM patches of side-lengths $\ell = 0.2$, 0.5, 1, 1.5 and 2 kpc, corresponding to the scatter in Fig. D.2.

In Fig. 6.14 we show the deformation timescale as a function of the thus defined density dispersion. We find a steep decline in the deformation timescale with increasing density dispersion $\propto (\delta\rho/\rho)^{-3}$, in qualitative agreement with the expectation that indeed anisotropies in the density distribution might be dictating the geometry of SNRs in a turbulent ISM. Since the dense structures in the ISM themselves are subject to differential rotation, they can be stretched out considerably by galactic shear over timescales that are much longer than the age of the SNR and thus imprint a relatively larger degree of anisotropy than the expansion of an SNR subject to shear alone.

6.5 Discussion

In the previous sections we have described the evolution of the geometry of SNRs expanding into an ISM structured by the complex interplay of gravity, galactic rotation and turbulence. In the following, we will discuss some of the limitations of our simulations, how our results compare to observations of SNRs as well as implications of our findings to the study of galaxy evolution and the structure of the ISM.

6.5.1 Limitations

The SISSI simulation suite aims to simulate the evolution of SNRs in a realistic galactic environment. Of course, simulating a realistic galactic ISM is challenging and the numerical prescriptions and sub-grid physics involved can greatly influence the phase structure and the morphology of the galaxy as a whole. A discussion of the quality of the simulated ISM of the SISSI galaxy, which is part of the AVALON simulation suite, focusing on the modeling of various aspects of galaxy evolution related to the structure of the ISM is out of the scope of this work, and will be presented elsewhere (M. Behrendt et al. 2025, in prep.).

Highly resolved simulations of SNRs, alongside an entire galaxy are computationally challenging and the computational resources to resolve large patches of the ISM with our maximum zoom-in resolution, are out of reach for currently available computing hardware. Therefore, we had to resort to the refinement strategy outlined in Sec. 6.1.2, which may itself introduce numerical artifacts. In the case of a uniform medium and without gravity, Romano et al. (2024a) have shown that our method of a co-evolving refinement region does not greatly affect the evolution of SNRs. However, we do find some differences in the star-formation activity and the partition of energy between the models N0 and N0_zoom, suggesting that the properties of the background ISM might differ substantially, based on the resolution. We account for this fact, by relaxing the initial conditions for 50 kyr, however it remains unclear, whether there is an optimal relaxation duration, given that the differences between the high- and low-resolution ISM do not seem to reach an asymptotic state and instead may be attributed to chaos, due to unresolved gravitational collapse coupled to stochastic star-formation.

More detailed modelling of physical processes, such as cosmic rays, magnetic fields, thermal conductivity, non-equilibrium radiation chemistry as well as more detailed stellar models, that include sources of early stellar feedback can influence the dynamics as well as the geometry of SNRs (e.g. Gentry et al., 2019; Makarenko et al., 2023; Diesing et al., 2024; Guo et al., 2025). In the present work we opted for a lightweight physics model, to lower the computational cost, allowing for higher resolution. However, future efforts involving more detailed physics models may certainly be worthwhile.

6.5.2 Observations of SNR geometry

As SNRs evolve, so do the wavelengths of light in which they can be observed. Young SNRs are usually observed in the optical, infrared and X-ray (e.g. Fesen et al., 2023; Kobashi et al., 2024; De Looze et al., 2024) and their geometry is dictated by the explosion mechanism as well as their immediate surroundings. These SNRs are usually fairly close to spherical symmetry, justifying our spherically symmetric injection of energy and ejecta mass.

Once SNRs enter the ST phase, they are extremely hot and bright in X-rays with diffuse X-ray emission coming from their center (Khabibullin et al., 2023; Reynolds & Borkowski, 2024). In this evolutionary stage, most SNRs are very close to spherically symmetric, though interactions with nearby clouds can lead to asymmetric features (Chi et al., 2024) in agreement with our sample of simulated SNRs, where the majority of SNRs remain close to spherically symmetric, with the exception of those exploding in low-density conditions, which are likely affected by interactions with clouds and low-density channels.

Galactic SNRs are usually only observed until shortly after they enter the radiative stage, as they quickly become too faint to be observed. Observed radiative SNRs, tend to be quite spherically symmetric (Payı et al., 2024), with few exceptions due to interactions with nearby density structures (Arias et al., 2024), in agreement with our simulations, which indicate that most SNRs

remain spherically symmetric between shell-formation and the end of the PDS phase.

Older SNRs are usually too faint to be observed directly. However, once they become large enough, they may be indirectly observed by looking for large cavities in the dust distribution. Such large cavities are routinely observed both in the Galaxy (Pelgrims et al., 2020; Zucker et al., 2022; Li et al., 2022; Verma et al., 2023) as well as in nearby galaxies (Watkins et al., 2023; Sánchez-Cruces & Rosado, 2023; Li et al., 2024). At first glance, observed SBs exhibit a wide variety of shapes and orientations, however due to the scarcity of detailed analyses of their shapes and orientation with respect to galactic structure, it is difficult to say to what degree, the observed sample agrees or disagrees with our simulated sample.

Fortunately, due to the recent 3D dust map made available by Edenhofer et al. (2024), we are in a position to study the geometry of the LB, a SB believed to be excavated by the SN explosions of $\sim \mathcal{O}(10)$ massive stars within the last $\sim \mathcal{O}(10)$ Myr (Breitschwerdt & de Avillez, 2006; Wallner et al., 2021; Zucker et al., 2022). We find that, while the orientation of the LB is slightly unusual for an SB its age, its shape fits right into the range of shapes that we report for our sample of simulated SNRs after 10 Myr. Moreover, we find that its effective size of $R_{\rm eff} \sim 212.3 \pm 1.0$pc is on the lower end of sizes obtained after 10 Myr. In a companion paper focusing on this aspect (L. Romano et al. 2025) we further discuss the implications, in particularly regarding current age estimates of the LB.

6.5.3 Implications and future directions

Our numerical simulations show, that the geometry of evolved SNRs is changed due to the complex interplay of the expanding shell and a variety of environmental factors. Since different processes affect the geometry of the SNR on different timescales, it might be possible to disentangle their contributions and deepen our understanding of the underlying physical processes shaping the internal structure of galaxies.

By leveraging novel analysis techniques (Edenhofer et al., 2024), and increasingly detailed observations (Gaia Collaboration et al., 2023) it will soon be possible to study the geometry of an ever growing sample of galactic SNRs. Already, the data products of Edenhofer et al. (2024) can be used to study the neighboring known SBs, such as the Per-Tau SB (Bialy et al., 2021) and GSH 238+00+09 (Heiles, 1998), which could provide additional hints to the assembly of structures in the solar neighborhood.

While we have focused on SNR geometry in this work, there are many more aspects of SNR phenomenology that can be addressed by the SISSI simulations. In future studies we aim to investigate the role of SNRs in driving interstellar turbulence, their coupling to and potential driving of galactic outflows as well as triggered star-formation.

6.6 Concluding Remarks

We have introduced the SISSI simulation suite, featuring 3D hydrodynamic zoom-in simulations of SNRs embedded in the realistic, self-consistently generated ISM of an isolated, Milky-Way-like galaxy, in order to deepen our understanding of various aspects of SNR physics. In this work, we focus on the geometry of the SNRs and show how it can be used as a useful observational diagnostic for understanding the various environmental effects, affecting the evolution of the system. Here we summarize our most important findings:

1. The dynamics of young SNRs ($\lesssim 1\,\mathrm{Myr}$) are well described by standard analytical models. However, these models become less accurate for SNRs exploding in low-density ($\lesssim 0.1\,\mathrm{cm}^{-3}$) environments, likely due to the large size of the SNRs, which increases the likelihood of interactions with both high- and low-density structures, such as clouds and channels.

2. SNRs tend to be deformed greatly on a timescale shorter than a few times the orbital timescale, with SNRs in environments with larger density fluctuations being deformed earlier, as they tend to follow the geometry of dense structures, which are deformed by shear and aligned with the galactic rotation.

3. The deformation of SNRs has preferred directions. The minor axis of oblate SNRs tends to be aligned with the galactic poles, with a slight tilt towards the galactic outskirts, suggesting that the vertical expansion of these SNRs is stalled by the graviational pull of the galactic disk. The polar angle of the major directions is broadly distributed, slightly favoring directions in the galactic plane, with pitch angles peaked between $\sim 20°$ and $\sim 50°$ slightly pointing towards the galactic center, in agreement with the expectation from alignment due to galactic shear.

4. The LB has a typical geometry for a SB of its age and size, however it appears slightly small compared to the size of the SNRs in the SISSI sample at 10 Myr. This suggests, that previous estimates of the age, based on idealized, one-dimensional models of SB expansion might need to be revised. The LB might be just old – and large – enough to be affected by its galactic environment, which makes it a unique laboratory to study the expansion of SBs at the interface between local ISM physics and galactic dynamics.

We conclude that SNR geometry offers a novel observational tool for understanding the complex physics of galaxies and their impact on galactic substructure, leveraging the full potential of recent high quality observations.

Chapter 7

SISSI: Supernovae in a stratified, shearing interstellar medium

II. Star formation near the Sun is quenched by expansion of the Local Bubble

> Software used in this chapter:
> Julia v1.10.0 (Bezanson et al., 2017), Matplotlib v3.5.1 (Hunter, 2007), Healpix v2.3.0 (Tomasi & Li, 2021), and Galpy v.1.10.2 (Bovy, 2015)

A slightly revised version of this chapter is to be submitted to Astronomy & Astrophysics Letters after the submission of this thesis (Romano & Burkert, 2025, Accepted for publication on Jan. 1st 2026). This work builds heavily on the results from the previous chapter, but is very closely related to Andi's initial proposal that initiated this project. As with the previous chapter, I worked out the details turning the proposal into a finished paper, presented in this work, by analyzing and combining the diverse data sets and interpreting guided by physical intuition obtained from the cumulative work presented in the previous chapters. Throughout the processes of writing this paper Manuel and Andi provided useful comments, pointing out potential shortcomings and flaws in the reasoning that I incrementally addressed. Unfortunately there was not yet sufficient time for me to receive all of these comments, which is the reason why this work has not yet been submitted.

Recent advances in observational methods allow us to map out the structure in the nearby galactic interstellar medium (ISM) in three spatial dimensions (3D) (3D, e.g. Arenou et al., 1992; Lallement et al., 2019; Edenhofer et al., 2024). One of the most prominent structures, mapped by these techniques is the Local Bubble (hereafter LB Cox & Reynolds, 1987; Linsky & Redfield, 2021), a large cavity, several hundred parsec across, centered around the solar system (Zucker et al., 2022), which has been linked to diffuse soft X-ray emission (e.g. Snowden et al., 2000; Yeung et al., 2024). Superbubbles (SB) such as the LB are believed to be carved out by the various feedback channels of massive stars, such as stellar winds (Tenorio-Tagle et al., 1990), ionizing radiation (Linsky & Redfield, 2021) and supernovae (hereafter SNe Tenorio-Tagle et al., 1990; Breitschwerdt & de Avillez, 2006; Wallner et al., 2021).

Over the past few decades, many studies have tried to constrain the origin of the LB. Studies using

Table 7.1: Properties of the Local Bubble

Property	This work	Zucker et al. (2022)	O'Neill et al. (2024)	Unit
Effective Radius	212.3 ± 1.0	165 ± 6	170^{a}	pc
Mass	6.24 ± 0.07	$14^{+6.5}_{-6.2}$	6.0 ± 0.7^{b}	$10^5\,M_\odot$
Hydrogen number density	0.494 ± 0.006	$2.71^{+1.57}_{-1,02}$	0.61^{c}	cm^{-3}
Momentum	$(2.96 \pm 0.05)^{d} \times (\mathrm{Myr}\,/\,t_{\mathrm{age}})$	$1.0^{+0.4}_{-0.4}$	–	$10^7\,M_\odot\,km\,s^{-1}$
Minor-to-major-ratio	0.469 ± 0.007	–	–	–
Semi-major-to-major-ratio	0.562 ± 0.011	–	–	–
Pitch angle (major axis)	-19.0 ± 1.0	–	–	°
Polar direction (major axis)	0.665 ± 0.011	–	–	–
Pitch angle (minor axis)	-66.1 ± 2.7	–	–	°
Polar direction (minor axis)	0.607 ± 0.022	–	–	–

$^{(a)}$ Median peak distance $^{(b)}$ Mass enclosed within shell $^{(c)}$ Median peak density $^{(d)}$ Bias corrected (see App. E.1.4)

astrometry, tracing back the positions of nearby star-clusters suggest that $\sim 10-20$ SNe originating from the Scorpius-Centaurus OB association (Sco-Cen) might have contributed to the expansion of the LB $\sim 10\,\mathrm{Myr}$ ago (Maíz-Apellániz, 2001; Zucker et al., 2022). Numerical simulations of SNe expanding into a turbulent, stratified ISM, confirm that ~ 20 SNe exploding sequentially throughout the last $\sim 14\,\mathrm{Myr}$ could explain, the observed size of the LB, the observed column densities of O VI in the interior as well as the deposition of sedimentary ^{60}Fe (Breitschwerdt & de Avillez, 2006; Breitschwerdt et al., 2016). Fossil records show that the incorporation rate of ^{60}Fe and ^{244}Pu on earth has peaked $\lesssim 4\,\mathrm{Myr}$ and $\lesssim 7\,\mathrm{Myr}$ ago (Wallner et al., 2016, 2021). Combining this with the work of Zucker et al. (2022), who find that the solar system would have entered into the LB $\sim 5\,\mathrm{Myr}$ ago, suggests that at least the more recent peak might coincide with SNe associated with the LB (see also Breitschwerdt et al., 2016).

In (Romano et al., 2025a), we introduce the SISSI (Supernovae In a Stratified, Shearing ISM) zoom-in simulation project, focusing on the properties of highly-resolved, simulated supernova-remnants (SNRs) expanding into the self-consistently generated ISM of an isolated, Milky-Way-like disk-galaxy. There, we find that SNRs in a realistic environment, expand faster than previously expected at later times $t \gtrsim 1\,\mathrm{Myr}$, due to galactic shear, the gravitational influence of nearby substructures and the presence of low-density channels. A comparison of our simulated sample of SNRs at $t = 10\,\mathrm{Myr}$ with the LB, suggested that it would be too small for a SB of its age, powered by SNe exploding at the rate suggested by previous studies.

In this work, we follow up on this curiosity, by presenting a new analysis of the LB, derived from the 3D dust maps of Edenhofer et al. (2024) using a method similar to that of O'Neill et al. (2024). As opposed to Zucker et al. (2022), who assume that the stellar kinematics trace the dynamics of the gas through triggered star-formation, we directly estimate the size, momentum and ambient density of the LB from the 3D dust maps of Edenhofer et al. (2024) and by utilizing the dynamical evolution of the SNRs in the SISSI simulation we constrain its age and the number of SNe powering its evolution.

7.1 Geometry of the Local Bubble

We recover the properties of the LB by applying a similar analysis as O'Neill et al. (2024), based on the 3D dust maps of Edenhofer et al. (2024), to obtain estimates for the LB's geometry, through the means of the shape tensor, defined in Romano et al. (2025a) (See also App. E.1.6 for the definition). Some steps of our analysis require the original data products of Edenhofer et al. (2024), so we opted for an independent analysis, instead of directly using the data products of O'Neill et al. (2024).

We follow the same basic steps of smoothing, peak finding and finally an analysis of the mass distribution enclosed by the peaks, used by O'Neill et al. (2024), with only minor differences. In contrast to O'Neill et al. (2024) we directly work with the logarithmically spaced grid of the 12 sample dust maps rather than sampling the 3D dust maps on a linearly spaced grid of the mean of the sample maps. Moreover, we weight the smoothing kernel to explicitly account for the non-uniform volume-elements $\mathrm{d}V \propto r^2\,\mathrm{d}r$ (App. E.1.1) and we linearly extrapolate the density field beyond the grid boundaries to better capture the profile-shape in their vicinity (App. E.1.2). In the App. E.1.3 we show that our results largely agree with those of O'Neill et al. (2024), demonstrating the robustness of the method.

Our peak identification and conversion between differential extinction and hydrogen number density are identical to O'Neill et al. (2024).

We apply the definition from Romano et al. (2025a) to compute the shape tensor from the coordinates of the shell-surface.

We obtain the average density of the LB, by dividing the total mass, obtained by performing a volume integral of the density from $r = 0$ to the outer edge of the shell, defined as the first point past the peak with half the peak's prominence, by the volume, including the mass contained within the central $\sim 69\,\mathrm{pc}$, for which we assume a constant hydrogen number density along each line-of-sight, proportional to the integrated extinction at $\sim 69\,\mathrm{pc}$, to account for the missing differential extinction in this region of the dust map.

We also estimate the momentum as a function of age, by assuming a rapidly-cooling wind expansion, i.e. $R \propto t^{1/2}$ (Oku et al., 2022; Lancaster et al., 2024) as well as homologous expansion $v \propto r$, which leads to

$$p_{\mathrm{LB}}\left(t_{\mathrm{age}}\right) = \int_{\mathrm{LB}} v\,\mathrm{d}M \approx \frac{1}{2\,t_{\mathrm{age}}} \int\int_{0}^{R_{\mathrm{out}}(\Omega)} \mu n_{\mathrm{H}}\left(r,\Omega\right) r^3 \mathrm{d}r\,\mathrm{d}\Omega\ , \tag{7.1}$$

where radial integrals are performed by summing contributions from all radial bins of the unsmoothed profile within the outer shell radius of the LB along a line-of-sight, the angular integrals are performed by summing all such contributions for all HEALPIX lines-of-sight, which have constant $\mathrm{d}\Omega \approx 1.6 \times 10^{-5}\,\mathrm{rad}^2$ and we substitute $v \approx r/\left(2t_{\mathrm{age}}\right)$ for the velocity, where t_{age} is the age of the LB. In the App. E.1.4 we show that Eq. 7.1 tends to overestimate the momentum by a factor of ~ 2. We correct for this, by dividing the momentum by said factor.

Eq. 7.1 describes the momentum as a function of time for a fixed (observed) size R, consistent with the expansion of a SB given a constant momentum injection rate $\dot{p}_{\mathrm{SN}}$, such that the momentum $p_{\mathrm{LB}} \propto R^4/t \propto \dot{p}_{\mathrm{SN}}\,t$.

The thus obtained properties of the LB are summarized in Tab. 7.1. For comparison, we also show the values obtained by Zucker et al. (2022) and O'Neill et al. (2024) where available. Overall our results are similar to the more recent investigation of O'Neill et al. (2024), however we also calculated the momentum, which we can use to estimate the age of the LB.

7.2 The age of the LB

The properties of a SB are determined by the strength of its energy source, the density of the environment and its age. Previous studies suggest that the radial momentum imparted per SN onto an expanding radiative shell only depends weakly on the density and is independent of the age of the SB (Walch & Naab, 2015; Oku et al., 2022), i.e. by knowing the momentum, we can precisely determine the number of SNe responsible for the expansion of the SB. In Romano et al.

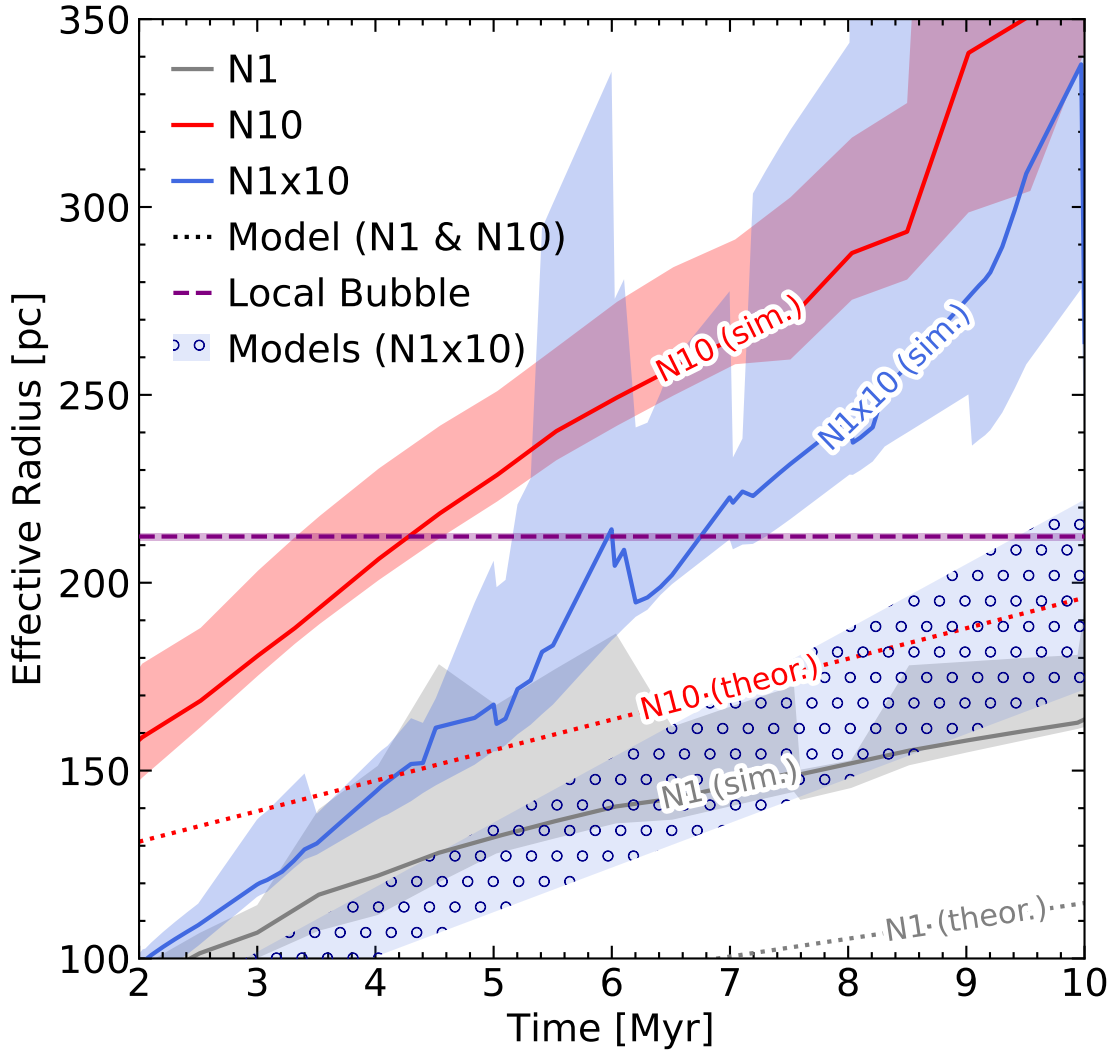

Figure 7.1: Time evolution of effective size of the simulated sample of SNRs of the SISSI sample between 2 and 10 Myr, for SNRs with ambient densities within 0.3 dex of the LB (Tab. 7.1). Gray, red and blue lines correspond to different explosion models. Solid lines correspond to the median size of the simulated bubbles, with shaded areas corresponding to the range between the 30th and 70th percentiles. Dotted lines and the hatched blue contour correspond to theoretical models based on radiative blastwaves in uniform media (App. E.2). For model N10, the size of the LB corresponds to an age of $\sim 4.5\,\mathrm{Myr}$, while for N1x10 it corresponds to $\sim 6 - 7\,\mathrm{Myr}$.

Table 7.2: Expansion parameters of the LB.

Property	This work	Zucker et al. (2022)	Unit
Age	$\sim 3.5 - 5.5$	$14.39^{+0.78}_{-0.74}$	Myr
Number of SNe	$\sim 19 - 30$	15^{+11}_{-7}	–
Time between SNe	$\sim 0.1 - 0.3$	$1.06^{+0.63}_{-0.39}$	Myr
Star cluster mass	$\sim 1.4 - 3.4$	~ 0.4	$10^4\,\mathrm{M}_\odot$
Star-Formation Efficiency	$\sim 2 - 5$	~ 0.3	%
Expansion speed	$\sim 38 - 59$	$6.7^{+0.5}_{-0.4}$	$\mathrm{km\ s^{-1}}$

(2025a) we have found that the momentum imparted per SN is approximately

$$\hat{p}_{\mathrm{SN}} \sim 2.6 \times 10^5\, n_0^{-0.13}\, \mathrm{M}_\odot\,\mathrm{km\ s^{-1}}\ , \tag{7.2}$$

where $n_{\mathrm{H}} = n_0\,\mathrm{cm^{-3}}$ is the ambient number density of hydrogen.

For the LB, using the newly derived density estimate in Tab. 7.1 this corresponds to a momentum input per SN of $\hat{p}_{\mathrm{SN,\,LB}} \sim (2.854 \pm 0.005) \times 10^5\,\mathrm{M}_\odot\,\mathrm{km\ s^{-1}}$. Using the age-dependent momentum estimate, we can relate the number of SNe to its age

$$N_{\mathrm{SN,\,LB}}\,(t_{\mathrm{age}}) = p_{\mathrm{LB}}/\hat{p}_{\mathrm{SN,\,LB}} \sim (104 \pm 2) \times (t_{\mathrm{age}}/\mathrm{Myr})^{-1}\ . \tag{7.3}$$

We validate the applicability of this estimate in App. E.1.5.

In contrast to the momentum, the size of a SB depends only weakly on the energy input, and in turn depends most strongly on its age. In Fig. 7.1 we show the time evolution of the effective size of our simulated sample of SNRs, introduced in Romano et al. (2025a), for SNRs with ambient densities within 0.3 dex of that of the LB. It can be seen that the SB evolving in a realistic galactic environment (solid lines) grow significantly faster, than what would be expected from blastwave models in uniform environments (see App. E.2 El-Badry et al., 2019; Oku et al., 2022). The size of the SB driven by subsequent SNe (N1x10) closely matches that of the SNR of a single SN (N1) for $t \lesssim 3\,\mathrm{Myr}$, while it approaches that of the SNR of 10 SNe exploding all at once (N10) after $\sim 10\,\mathrm{Myr}$. For the models with multiple SNe, the size of the LB is reached after $\sim 4.5\,\mathrm{Myr}$ (N10) and after $6 - 7\,\mathrm{Myr}$ (N1x10).

At the age at which the simulated SNRs (N1x10) reach the size of the LB, 15-17 SNe are required to explain the momentum of the LB (Eq. 7.3), in contrast to the 6-7 SNe that exploded in the simulation. A SB powered by such a high number of SNe would have reached the same size earlier (e.g. N10), significantly younger than previous age estimates (Maíz-Apellániz, 2001; Breitschwerdt & de Avillez, 2006; Zucker et al., 2022). While our simulations do not match an explosion scenario that can explain both the momentum and size of the LB, we can extrapolate, using theoretical considerations, to find a reasonable estimate.

Previous models of radiative blastwaves in uniform ambient media (El-Badry et al., 2019; Oku et al., 2022; Lancaster et al., 2024) suggest that the effective size is roughly $\propto \dot{N}_{\mathrm{SN}}^{0.15-0.25}$. A blastwave powered by more frequent SNe, would thus only lead to a mild increase in the size, and would be largely consistent with an age $\lesssim 6\,\mathrm{Myr}$. In Fig. 7.2 we show that for $R \propto \dot{N}_{\mathrm{SN}}^{\alpha}$ with $\alpha \lesssim 0.225$ the size matches that of the LB for $t_{\mathrm{age}} \sim 3.5 - 5.5\,\mathrm{Myr}$, while for $\alpha > 0.225$, there are no solutions that can simultaneously explain the size and the momentum of the LB. A more detailed evaluation is out of the scope of this work and will be subject to future investigation (L. Romano et al., in prep.).

By invoking standard assumptions about the stellar initial mass function, the average time between

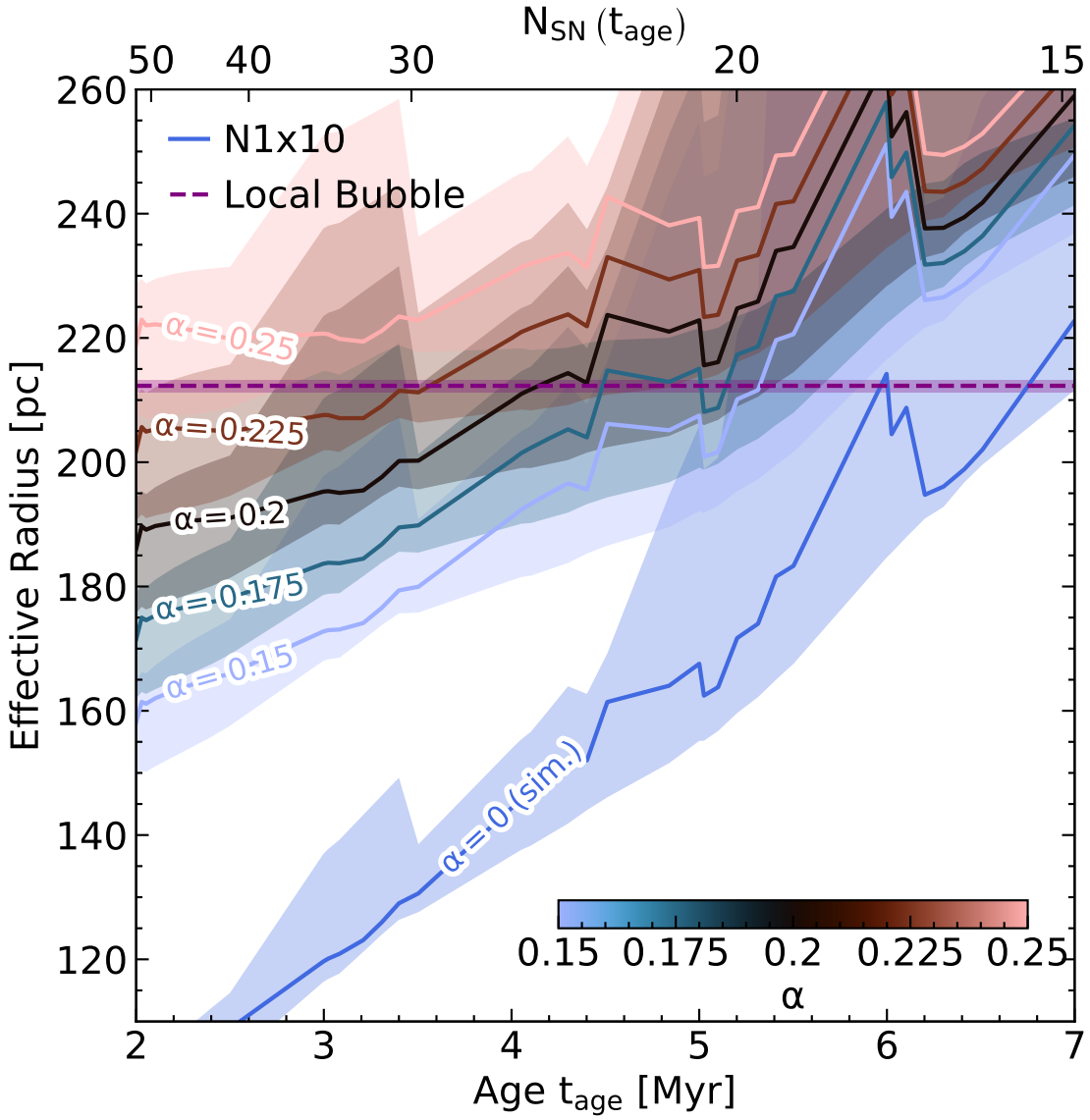

Figure 7.2: Effective size as a function of age or number of SNe, respectively, extrapolated from the model N1x10 and the mean of the momentum constraint Eq. 7.3 for various values of α; namely, $R_\alpha = R_{\mathrm{N1x10}}\,(t = t_{\mathrm{age}}) \times \left[\dot{N}_{\mathrm{SN,\,LB}}\,(t_{\mathrm{age}})\ /\,1\,\mathrm{Myr}^{-1}\right]^{\alpha}$, where $\dot{N}_{\mathrm{SN,\,LB}} = N_{\mathrm{SN,\,LB}}/t_{\mathrm{age}}$. For $\alpha \lesssim 0.225$, the extrapolated sizes match the LB for ages in the range $3.5 - 5.5\,\mathrm{Myr}$, while for $\alpha \gtrsim 0.225$ the two constraints on the size and momentum cannot be satisfied simultaneously.

SNe in a star cluster can be linked to its mass (Kim et al., 2017)

$$\Delta t_{\rm SN} \sim 0.4 \left(\frac{M_{\rm cl}}{10^4\,{\rm M}_\odot} \right)^{-1} {\rm Myr} \ , \tag{7.4}$$

which for the range of ages found above would correspond to a mass of $M_{\rm cl,\ LB} \sim 1.4{-}3.4 \times 10^4\,{\rm M}_\odot$ for the progenitor cluster of the LB.

We can compare this number to the swept-up mass, and assuming that the swept up mass roughly corresponds to the mass of the birth-cloud of the cluster driving the expansion of the LB, obtain the cloud-scale star-formation efficiency

$$\epsilon_\star = \frac{M_{\rm cl,\ LB}}{M_{\rm sw,\ LB}} \sim 2 - 5\,\% \ , \tag{7.5}$$

in agreement with the range of values found in observational (Lee et al., 2016; Chevance et al., 2020) and numerical studies (Grudić et al., 2022; Farias et al., 2024).

We summarize our results and compare them to those of Zucker et al. (2022) in Tab. 7.2.

The obtained cluster mass is somewhat higher than the stellar mass of Sco-Cen (Krause et al., 2018), which is oftentimes assumed to be progenitor cluster of the LB (Maíz-Apellániz, 2001; Zucker et al., 2022). Similarly, our result that the LB should be younger than previously believed is in slight tension with the older age ($\sim 15 - 17\,{\rm Myr}$) of the stars in Sco-Cen.

An important constraint for the SN origin of the LB comes from the fossil records of sedimentary radionuclides (Wallner et al., 2021; Ertel et al., 2023; Ertel & Fields, 2024). Both the scenario proposed in this work (App. E.3), and that of Zucker et al. (2022) satisfy this constraint. A more detailed analysis of the dynamical incorporation of the dusty, radioactive material may provide additional evidence in favor of either scenario.

According to Swiggum et al. (2024), Sco-Cen is part of a larger family of stars known as the α-Persei family (αPer), which reportedly had an average time between SNe of $\Delta t_{\alpha{\rm Per}} = 0.32^{+0.50}_{-0.23}\,{\rm Myr}$. Moreover, the star-formation history (SFH) of αPer indicates episodic star-formation over the past $\gtrsim 60\,{\rm Myr}$ with peaks every $\gtrsim 12.5\,{\rm Myr}$ and the latest peak within the last $\sim 12.5\,{\rm Myr}$.

Our results are in agreement with the SFH in αPer if we assume that the LB was powered by the latest peak of star-formation rather than the trough associated with the formation of Sco-Cen. In Appendix E.4 we construct a more detailed star-formation and SN-rate history over the past 40 Myr to substantiate this claim.

The high expansion speed $v_{\rm LB} > 30\,{\rm km\ s^{-1}}$ suggests that the LB might be only mildly affected by its Galactic environment, which typically dominates as $v \lesssim \sigma_{\rm turb} \sim 10\,{\rm km\ s^{-1}}$. Thus, models for SBs expanding into a uniform medium (App. E.2) might provide a reasonable age-estimate after all. For the slowly-cooling-wind model used by Zucker et al. (2022) with updated ambient density and the SN rate following Swiggum et al. (2024) we obtain $t_{\rm age}^{\rm SCW} \sim 6.6^{+2.4}_{-2.3}\,{\rm Myr}$, while for a rapidly-cooling-wind model (Oku et al., 2022) we obtain $t_{\rm age}^{\rm RCW} \sim 9^{+5}_{-4}\,{\rm Myr}$.

The LB appears to be at the tipping point between *microscopic* SNRs, whose dynamics are dominated by local shock physics and *mescoscopic* SBs that are strongly affected by galactic-scale processes. More detailed models of such large SBs as well as more precise stellar ages (e.g. Miret-Roig et al., 2022; Ratzenböck et al., 2023; Swiggum et al., 2024) are needed to shed more light on the progenitor cluster and expansion history of the LB.

7.3 Concluding Remarks

We compare the momentum and the effective size of the LB, derived from publicly available, high-quality 3D dust maps to our sample of simulated SNRs expanding into the shearing, stratified ISM of the isolated Milky-Way-like SISSI galaxy.

We find that in order to match both constraints on the radial momentum, and the effective size, the LB would have to be driven by a larger number of SNe and be significantly younger than previously reported. In particular, a rough agreement requires an age of $t_{\mathrm{age,\,LB}} \sim 3.5 - 5.5\,\mathrm{Myr}$ for $N_{\mathrm{SN,\,LB}} \sim 19 - 30$, in agreement with estimates of the average time between SNe in αPer (Swiggum et al., 2024). While our analysis focuses on SNe only, a fraction of the energy could have also been derived from other sources of stellar feedback, such as stellar winds and H II regions. Such a young age puts to question the claim of feedback-induced star-formation in the solar neighborhood (Zucker et al., 2022) and the star-formation history (Fig. E.6) even suggests that the expansion of the LB might have quenched the star-formation in the solar neighborhood.

While our results are in tension with previous estimates, which assumed that the LB was exclusively powered by SNe in Sco-Cen, they are in better agreement with more recent observational data on the star formation in the solar neighborhood. We note, however, that the high frequency of SNe lies outside of the parameter space covered by our simulations, which adds substantial uncertainties to our extrapolations. Better models for old ($t \gtrsim 1\,\mathrm{Myr}$) SBs expanding into a realistic galactic ISM as well as additional observational constraints are required to resolve these uncertainties and obtain a clearer picture for the origin and history of the LB.

Chapter 8

Conclusions and Outlook

8.1 Modelling SNRs in their Natural Habitat

The dynamical evolution of SNRs and SBs has been studied for over 50 years (Chevalier, 1974), taking into account increasing levels of complexity. While observational studies by default are faced with the complexities of the turbulent, multi-phase ISM (Watkins et al., 2023; O'Neill et al., 2024), most theoretical studies aimed at interpreting these observations, have relied on simplifying assumptions, such as a stationary, uniform (Thornton et al., 1998), sometimes even pressure-less (Cioffi et al., 1988) ambient medium, neglected potentially relevant physical processes such as (self-) gravity and are oftentimes limited to short SNR ages (e.g. Tenorio-Tagle et al., 1990; Fierlinger et al., 2016; Kim & Ostriker, 2015). In this work, for the first time, I have studied the detailed evolution of SNRs in a realistic galactic environment using the simulations presented in chapter 6 and developed a simple analytical model, presented in chapter 2, that allows to study the impact of various potentially relevant physical processes without the need of expensive numerical simulations.

8.2 The Local Bubble

I have proceeded to use these simulations to interpret recent observational data of the Local Bubble in chapter 7, providing a new age estimate of the system in slight tension with previous estimates (Maíz-Apellániz, 2001; Zucker et al., 2022), but in agreement with complementary constraints from recent data (Edenhofer et al., 2024; Swiggum et al., 2024). While the tension is rather weak, resolving these inconsistencies is a great opportunity to improve our understanding of the physics of SNRs in a dynamical galactic environment, triggered star formation and the dynamical evolution of the stars and gas in the solar neighborhood.

8.3 Modelling of Superbubbles and Galactic Winds

In Chapter 2 I have developed a versatile semi-analytical model that is designed to follow the dynamical evolution of blastwaves in complex environments. Besides basic shock-physics and radiative cooling, the model can account for external flow fields, gravity and even cosmic rays (See Chapter 3). I have confirmed, that the model reproduces known limits from a number of previous

studies (e.g. Weaver et al., 1977; Koo & McKee, 1990; Truelove & McKee, 1999), and by applying it to more complex environments have demonstrated what kind of behavior is expected in more complex settings, such as a differentially rotating disk and SNe exploding in the vicinity of dense, galactic substructures (Jeans, 1902; Toomre, 1964).

In the paper showcased in Chapter 3, I have applied the model, to provide insights into the physics of galactic outflows, the most extreme manifestation of SNRs. In particular, while there has been a lot of work on the structure and properties of galactic winds (e.g. Chevalier & Clegg, 1985; Fielding & Bryan, 2022), the question of which environments are conducive to the formation of such a wind, driven by star-formation potentially assisted by a cosmic-ray pressure-gradient has received only little attention. In the work presented in the paper, I have collaborated with Dr. Ellis Owen, an expert in cosmic-ray physics to address this gap. I have derived a condition for how much stellar feedback is required in order to drive a galactic outflow – a condition that is mainly determined by the balance of the driving forces (pressure gradients and cosmic rays) and gravity. Moreover, while we have found that in the absence of a cosmic-ray halo surrounding a galaxy, cosmic rays are able to drive arbitrarily mass-loaded, slow galactic winds regardless of the star-formation rate, the presence of a cosmic-ray halo can suppress their formation, rendering cosmic-rays ineffective in such systems. We discuss that such halos are expected to form in massive, old galaxies, such as the Milky Way or its immediate neighbor the Andromeda Galaxy (Recchia et al., 2021).

8.4 Characterization of the Merging-stage

By studying the dynamics of old SNRs at ages much beyond what has been reported in most studies, I inadvertently entered the previously unexplored regime of SNR evolution past the merging stage, which has been neglected due to the expectation that nothing interesting would happen past this point (But see Slavin & Cox, 1992). Yet, much to our surprise, in the study presented in chapter 4, I showed that when the SNR shock merges with the ISM it accelerates a reflected, radiative shock-wave towards its interior, much resembling the *reverse shock* in the free-expansion stage (e.g. Truelove & McKee, 1999); a process which we dubbed *Supernova Implosion*. The implosion wave refills the extremely underpressurized, evacuated interior driving a mixture of swept-up and ejected material into the center of the SNR, where it condenses due to rapid cooling, forming a massive, overdense and highly enriched cloud.

Moreover, in the study presented in Chapter 6, where I used simulations of SNRs expanding into a realistic galactic environment at unprecedented resolution, I discovered that SNRs in the merging phase are strongly affected by galactic physics, such as differential rotation, the interplay of vertical stratification and the vertical gravitational field and galactic substructure. While they may still implode and form central clouds (see Fig. 8.1 for a 3D-rendering of the SNR highlighted in Chapter 6), their dynamics and in particular their geometry is greatly affected, exhibiting signs of stretching due to shear and interactions with galactic substructure, as well as flattening due to gravity and gravity-driven external flows.

8.5 Triggered Star-Formation

In the study presented in chapter 5, I discuss that clouds formed by SN implosion might plausibly form stars, and estimate the star-formation efficiency associated with this processes. While I find that star formation triggered by SN implosion is relatively inefficient, in line with the general expectation that SNe reduce the star-formation rate, I speculate that since the stars produced in this process form from highly enriched gas, the proposed mechanism might provide an attractive

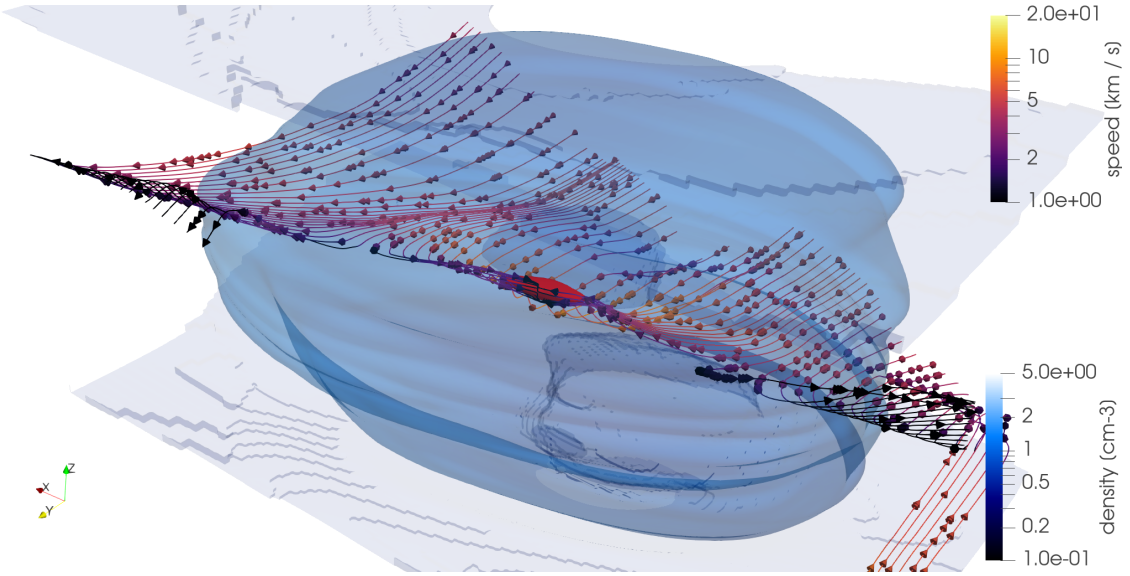

Figure 8.1: 3D rendering of the simulated SB # 22 (Chapter 6) at an age of 10 Myr. The density on the shell (iso-surface of the tracer variable) is shown in shades of blue. The density-iso-surface with a density of $0.5\,\mathrm{cm}^{-3}$, roughly corresponding to the disk-halo-boundary is shown in faint-blue. The central overdensity formed by SN implosion is shown in red. Velocity-streamlines penetrating through the overdensity are also shown, colored by the local flow speed.

pathway to the formation of metal-rich stars.

In this study, I made the simplifying assumption that only core-collapse SNe contribute. However, over the long timescales considered other sources of chemical enrichment such as thermonuclear SNe and the winds of asymptotic giant-branch stars are expected to be relevant as well (Saitoh, 2017). The ejecta of core-collapse SNe are generally considered to be rich in α-elements, such as oxygen or nitrogen (Janka, 2025). By neglecting these other processes the metal-rich stars predicted by this study are generally also highly enriched with α-elements, in stark contrast to the observational result that metal-rich stars tend to have relatively low α-element abundances, more aligned with the other enrichment processes (Nieuwmunster et al., 2023).

Thus, in order to obtain a more robust prediction, a refined calculation, including the effects of thermonuclear SNe and asymptotic giant-branch stars is a crucial next step.

8.6 The SISSI Simulations: A Treasure Trove

There is no doubt that besides the applications of the SISSI project, presented in Chapters 6 and 7, these simulations contain much more than could be presented within their scope and that of this thesis. I designed these simulations to be able to tackle a wealth of questions related to the complex interplay of SNRs with their galactic environment, yet due to the time-limitations of my studies, here, I had to restrict myself to the most accessible of these questions.

Here, I want to give a strictly non-exhaustive list of physical processes that can and hopefully will be thoroughly investigated using the wealth of data provided by this simulation suite:

1. **Triggered star-formation.** SNe are generally expected to clear their environment of po-

tentially star-forming material, providing physical conditions that are unfavorable for further star formation (Tacconi et al., 2020; Freundlich, 2024), yet under certain circumstances they have been proposed to actively trigger star-formation, by compressing gas, pushing it past the tipping point of gravitational (in-)stability (Elmegreen & Lada, 1977; Zucker et al., 2022). Yet, a well-established, in-depth theoretical understanding of this process in the context of SN-driven triggered star-formation remains elusive. In SISSI, I capture the star-formation following the SN explosions and, using the passive tracer variables, I am able to distinguish stars that have formed from pristine or polluted gas. Moreover, using the runs without SNe, I can directly pin-point when the SN-Feedback was preventative and when it has triggered star formation.

2. **SN-driven turbulence.** SNe are expected to drive turbulence in the ISM (e.g. Mac Low & Klessen, 2004; Klessen & Glover, 2016; Krumholz & Burkhart, 2016). Models of SN-driven turbulence usually assume that SNe inject a fixed momentum per formed unit stellar mass (Krumholz & Burkhart, 2016), or assume that a fixed fraction of the injected energy is available to drive turbulence (Fierlinger et al., 2016), yet how and at what stage during SNR evolution exactly this conversion occurs remains unclear. In SISSI I simulate the dynamical evolution of SNRs long past the onset of the merging phase, at which point one might expect at least some degree of turbulence driving to occur. Thanks to the high spatial resolution of the SISSI simulations, and the availability of highly resolved baseline ISM simulations, it is possible to study the residual impact of SN Feedback on the turbulent properties of the ISM and capture SN-induced turbulence driving in the act.

8.7 Future Directions

In recent years, observational surveys have made tremendous progress in advancing our knowledge of interstellar physics. Gaia has brought us detailed information about billions of stars and will keep delivering with the upcoming fourth data release. In its first few years, JWST has revolutionized our understanding of high-redshift galaxies and has provided stunning data sets of the ISM of nearby galaxies. In the coming years this trend is only going to continue at an ever increasing pace, with the recently launched Vera Rubin observatory and upcoming facilities such as the Roman space telescope, SKAO, NewAthena and many more. To keep up with this inflation of ever increasing detail in observational data sets, and provide a timely theoretical basis for their adequate interpretation, theoretical studies are required to overcome various challenges, related to the staggering hierarchy of scales, that one encounters when trying to adequately model the ISM. In general, there are three (complementary) directions in which the work in this thesis can be advanced in:

1. **More complete physics.** In my work I focused on ideal hydrodynamics coupled to self-gravity. I have thereby neglected a number of physical processes that might be dynamically important.
2. **More realistic environments.** In my simulations, I have used an isolated simulated galaxy, which was generated using fairly simplistic prescriptions for Feedback, cooling and star-formation. A more detailed ISM model that better captures the hierarchical structure of the turbulent, multi-phase ISM will allow for a more robust understanding of the complex interplay of SNRs with their environment.
3. **Better tools for comparisons with observations.** Radiative cooling is intimately coupled to the emissivity of gas. Yet, in my current simulations it is currently not possible to self-consistently derive the emissivities of various important gas tracers. Future models might benefit from approaches that allow for self-consistently generated emissivities, and radiative transfer modeling, which would allow direct comparisons with observations.

8.7.1 Towards a Comprehensive Picture of SNR dynamics

SNRs are multi-scale, multi-phase objects, whose dynamics are affected by a number of processes that can act on different scales.

It has been shown that magnetic fields modify the dynamics, and importantly, the *geometry* of SNRs, by providing additional pressure and affecting the growth of instabilities in the shell (Kim & Ostriker, 2015; Gentry et al., 2019). Moreover, they can couple to cosmic rays, which are hypothesized to be accelerated in SNRs, depositing part of the SNRs energy in a slowly cooling non-thermal component (Cristofari et al., 2021; Diesing et al., 2024), which can modify the dynamics and at the very least act as an observational signature.

The dynamics of SNRs are determined by the amount of energy that is radiated away in the unresolved thin layer, between the cold shell and the hot interior. While current three-dimensional simulations are still far away from resolving this interface (Sharma et al., 2014), the cooling across this interface seems to be regulated by the enthalpy flux through this layer, which is well resolved even at fairly coarse resolution (Marin-Gilabert et al., 2025). In this case, however, it is still relevant to consider all the physical processes that might affect the enthalpy flux through this layer. These processes include magnetic fields, non-ideal hydrodynamic effects suchs as thermal conduction (Guo et al., 2025) and viscosity (Marin-Gilabert et al., 2025) and even detailed non-equilibrium (photo-)chemistry (Kim et al., 2023b; Makarenko et al., 2023), which is expected to set the thermodynamic state in the cold shell.

A systematic investigation of how all of these effects affect SN dynamics will provide the foundation of future theoretical studies of SNRs in realistic environments. Importantly, in a realistic environment, all of these processes work in concert to shape the environment that the SNRs expand into, defining what is "realistic" in the first place. While including all of these effects in numerical simulations of SNRs is challenging, models such as the one presented in Section 2 might be useful to explore the vast model space. In order to address these questions, the model would need to be extended from a one-zone model (thin-shell approximation) to a multi-zone model, which covers at least two zones for the cold shell and the hot bubble, where the balance of cooling and enthalpy flux is dictating the mass-, energy- and momentum fluxes between the two zones. In the context of reverse-shock formation such models are already under construction (D. Bulckaen, N. Sartorio, L. Romano, et al. in prep.).

8.7.2 Predictions for Multi-Wavelength Observations of SNRs on All Scales

In observations information is incomplete. All we know about observed astrophysical objects has to be inferred from what little information is contained in the observations. Thus, a robust pipeline from observational data, usually comprising of either photometric data, taken by filters collecting most of the incoming light in specific wavelength windows, spectroscopic data, comprised of the little incoming light at specific wavelengths, or a combination of both, to the physical quantities of interest is required.

On the contrary, in simulations the full information on the physical quantities is available, but it is generally quite difficult to model the actually observable light emission (Matsumoto et al., 2023). With the incoming wealth of observational data, self-consistently modeling the emission and transport of light to an observer such as ourselves is a crucial step towards sustainably making use of the overwhelming amounts of data.

To this end, models that actively model the radiative transfer coupled to the non-equilibrium

photochemistry of SNRs throughout the various stages in their life need to be implemented. Since both radiative transfer and chemistry are strongly dependent on the presence of dust (Romano et al., 2022; Matsumoto et al., 2024), cosmic rays and magnetic fields (Kim et al., 2023b), such models would need to be coupled to the detailed modeling of these processes as well.

8.7.3 Numerical Road-Map for Future Simulations

Eventually a future SISSI-like simulation suite capable of all of these things might emerge. Yet, in order for this to become truly feasible, several algorithmic improvements need to be made, to offset the significant added computational cost that goes hand-in-hand with modeling these processes. Moreover, existing numerical artifacts should be addressed to improve the robustness of the results of future simulations.

One of the weak points of SISSI is the global time-stepping hierarchy in RAMSES, which depends on the highest speed in the simulation box and can drastically slow down the advancement of numerical simulations with deep scale hierarchies. Many modern codes such as AREPO(Springel, 2010; Weinberger et al., 2020), GIZMO (Hopkins, 2015), GADGET-4 (Springel et al., 2021) and OPENGADGET3 (Groth et al., 2023) tend to use local time-stepping approaches that only apply restrictively short time steps where it is urgently needed, significantly reducing the computational cost. There appears to exist a numerically stable implementation in RAMSES that, however, has not yet been shared with the broad community (private comm.).

One of the most widely used numerical solvers in RAMSES is the so-called Harten-Lax-van Leer-Contact (HLLC) Riemann solver (Toro et al., 1994), which is optimized to correctly deal with contact discontinuities. In contrast, the HLLC solver struggles with shocks, introducing the so-called carbuncle instability. Fortunately, a simple fix – the so-called *h-correction* (Stone et al., 2008) – has been suggested, which can resolve this issue for good, essentially by detecting shocks and applying a different solver that does not exhibit this numerical artifact. Unfortunately, in RAMSES this correction has so far only been implemented in two dimensions. It should be relatively straightforward – though likely somewhat tedious – to extend this implementation to three dimensions.

Many aspects of numerical simulations can be accelerated through *efficient* use of GPUs, which generally come at the cost of significant, time-consuming modifications of the algorithms and data-structures used. The GPU-ready next-generation of the RAMSES code, called Mini-RAMSES is expected to be released soon (private comm.). While a speed-up due to GPU capabilities would be a welcome change, it remains to be shown to what extent the next-generation of SISSI can benefit from Mini-RAMSES.

Besides RAMSES there are already existing codes that unify many of these aspects and could in principle be readily used for a next-generation SISSI project. While it might be challenging to replace the flexible AMR capabilities of RAMSES, which lie at the heart of SISSI, in another code base, modern codes such as AREPO (Mayer et al., 2025) and GIZMO (Hopkins et al., 2024) offer well-tested hyper-refinement capabilities that might offer suitable alternatives.

Appendix A

Modelling the Expansion of Supernova Remnants

A.1 Derivation of the Pressure-Gradient Force

Here we show how to derive the expression for the pressure-gradient force Eq. 2.5 following the formalism of Laumbach & Probstein (1969). By following the steps outlined in their paper, the expression for the pressure gradient can be read off from their final results, by noting that they consider an *adiabatic* blastwave, without central forcing, expanding vertically upwards into a stratified atmosphere, neglecting the effects of gravity. Under these assumptions the equation of motion Eq. 2.2 simplifies to

$$\frac{\mathrm{d}}{\mathrm{d}t}\left(Mv_s\right) = \Delta P r_\mathrm{s}^2 \ . \tag{A.1}$$

The starting point of the derivation is the Taylor-expansion of the *Eulerian* radial coordinate r in terms of the *Lagrangian* radial coordinate r_0 at $t = 0$, near the radial location of the shock front r_s to second order

$$r = r_\mathrm{s} + \left.\frac{\partial r}{\partial r_0}\right|_{r_\mathrm{s}} \left(r_0 - r_\mathrm{s}\right) + \frac{1}{2}\left.\frac{\partial^2 r}{\partial r_0^2}\right|_{r_\mathrm{s}} \left(r_0 - r_\mathrm{s}\right)^2 + \ldots \ . \tag{A.2}$$

In order to derive the equation of motion, we make use of the thin-shell approximation, in which $r \to r_\mathrm{s}$ is independent of r_0. In this approximation we can approximate the integral of the Euler-equation for the momentum evolution

$$\frac{\partial^2 r}{\partial t^2} = -\frac{r^2}{\rho r_0^2}\frac{\partial P}{\partial r_0} \ , \tag{A.3}$$

using the value of the acceleration at the shock

$$P\left(0,t\right) - P_\mathrm{s}\left(r_\mathrm{s}\right) = \int_0^{r_\mathrm{s}} \frac{1}{r^2}\frac{\partial^2 r}{\partial t^2}\rho_0 r_0^2 \mathrm{d}r_0 \approx \frac{1}{r_\mathrm{s}^2}\left.\frac{\partial^2 r}{\partial t^2}\right|_{r_\mathrm{s}} M\left(r_\mathrm{s}\right) \ , \tag{A.4}$$

and similarly we can approximate the energy integral using the value of the kinetic energy density at the shock

$$E\left(r_\mathrm{s}\right) = \int_0^{r_\mathrm{s}} \frac{P\left(r\right)}{\gamma - 1} r^2 \mathrm{d}r + \int_0^{r_\mathrm{s}} \frac{1}{2}\left(\frac{\partial r}{\partial t}\right)^2 \rho r_0^2 \mathrm{d}r_0 \approx \frac{P\left(0\right)\, r_\mathrm{s}^3}{3\left(\gamma - 1\right)} + \frac{1}{2} M\left(r_\mathrm{s}\right) \left.\left(\frac{\partial r}{\partial t}\right)^2\right|_{r_\mathrm{s}} \ . \tag{A.5}$$

By combining Eqs. A.4 and A.5 we can eliminate $P(0,t)$, which leaves us with the problem of deriving expressions for the various remaining quantities at the shock r_s.

A.1.1 Derivation of the Acceleration at the Shock

To leading order(s) the first two time-derivatives of Eq: A.2 are

$$\left(\frac{\partial r}{\partial t}\right) = \left(1 - \left.\frac{\partial r}{\partial r_0}\right|_{r_\mathrm{s}}\right)\dot{r}_\mathrm{s} + \left[\frac{\partial}{\partial t}\left(\left.\frac{\partial r}{\partial r_0}\right|_{r_\mathrm{s}}\right) - \left.\frac{\partial^2 r}{\partial r_0^2}\right|_{r_\mathrm{s}}\dot{r}_\mathrm{s}\right](r_0 - r_\mathrm{s}) + \dots\,, \tag{A.6}$$

$$\left(\frac{\partial^2 r}{\partial t^2}\right) = \left(1 - \left.\frac{\partial r}{\partial r_0}\right|_{r_\mathrm{s}}\right)\ddot{r}_\mathrm{s} - 2\,\frac{\partial}{\partial t}\left(\left.\frac{\partial r}{\partial r_0}\right|_{r_\mathrm{s}}\right)\dot{r}_\mathrm{s} + \left.\frac{\partial^2 r}{\partial r_0^2}\right|_{r_\mathrm{s}}\dot{r}_\mathrm{s}^2 + \dots\,, \tag{A.7}$$

where $\dot{r}_\mathrm{s} = v_\mathrm{s}$ is the shock speed.

The Eulerian and Lagrangian radial coordinates are related by the continuity equation

$$\rho_0\, r_0^2 \mathrm{d}r_0 = \rho r^2 \mathrm{d}r\,, \tag{A.8}$$

where $\rho_0(r_0)$ is the unperturbed density profile at r_0 and $\rho(r,t)$ is the density at r and time t. We can use this relation in combination with the Rankine-Hugoniot jump-conditions for strong shocks (e.g. Ostriker & McKee, 1988) to evaluate

$$\left.\frac{\partial r}{\partial r_0}\right|_{r_\mathrm{s}} = \frac{\gamma - 1}{\gamma + 1} = \chi^{-1}, \tag{A.9}$$

which is constant in time and determines the velocity at the shock

$$\left.\frac{\partial r}{\partial t}\right|_{r_\mathrm{s}} = \frac{2}{\gamma + 1} v_\mathrm{s}\,. \tag{A.10}$$

By making use of the momentum equation A.3 and the Rankine-Hugoniot jump-condition for the pressure at the shock

$$P_\mathrm{s} = \frac{2}{\gamma + 1}\rho_0(r_\mathrm{s})\,\dot{r}_\mathrm{s}^2 \tag{A.11}$$

we can evaluate Eq. A.7 at the shock to obtain

$$-\left.\frac{\partial^2 r}{\partial r_0^2}\right|_{r_\mathrm{s}}\dot{r}_\mathrm{s}^2 = \frac{2}{\gamma + 1}\dot{r}_\mathrm{s}^2\left.\left(\frac{1}{P}\frac{\partial P}{\partial r_0}\right)\right|_{r_\mathrm{s}} + \frac{2}{\gamma + 1}\ddot{r}_\mathrm{s}\,. \tag{A.12}$$

The pressure-gradient term can be further evaluated by utilizing the adiabatic condition

$$\frac{P(r_0,t)}{P_\mathrm{s}(r_0)} = \left(\frac{\rho(r_0,t)}{\rho_\mathrm{s}(r_0)}\right)^\gamma\,, \tag{A.13}$$

which yields for the pressure gradient at the shock

$$\left.\left(\frac{1}{P}\frac{\partial P}{\partial r_0}\right)\right|_{r_\mathrm{s}} = \left.\left(\frac{1}{P_\mathrm{s}}\frac{\partial P_\mathrm{s}}{\partial r_0} + \frac{\gamma}{\rho}\frac{\partial \rho}{\partial r_0} - \frac{\gamma}{\rho_0}\frac{\partial \rho_0}{\partial \rho_0}\right)\right|_{r_\mathrm{s}}. \tag{A.14}$$

The first term can be evaluated from Eq. A.11 yielding

$$\left.\left(\frac{1}{P_\mathrm{s}}\frac{\partial P_\mathrm{s}}{\partial r_0}\right)\right|_{r_\mathrm{s}} = \left.\left(\frac{1}{\rho_0}\frac{\partial \rho_0}{\partial r_0}\right)\right|_{r_\mathrm{s}} + \frac{2\ddot{r}_\mathrm{s}}{\dot{r}_\mathrm{s}^2}\,, \tag{A.15}$$

since by the chain-rule

$$\left(\frac{\partial \dot{r}_\mathrm{s}}{\partial r_0}\right)\Big|_{r_\mathrm{s}} = \ddot{r}_\mathrm{s}\left(\frac{\partial t}{\partial r_0}\right)\Big|_{r_\mathrm{s}} = \ddot{r}_\mathrm{s}\,\dot{r}_\mathrm{s}^{-1}\ . \tag{A.16}$$

The second term can be evaluated using the continuity equation A.8 yielding

$$\left(\frac{1}{\rho}\frac{\partial \rho}{\partial r_0}\right)\Big|_{r_\mathrm{s}} = \frac{1}{\rho_0}\frac{\partial \rho_0}{\partial r_0}\Big|_{r_\mathrm{s}} + \frac{4}{\gamma+1}\,r_\mathrm{s}^{-1} - \chi\,\frac{\partial^2 r}{\partial r_0^2}\Big|_{r_\mathrm{s}}\ . \tag{A.17}$$

We thus obtain for the pressure gradient

$$\left(\frac{1}{P}\frac{\partial P}{\partial r_0}\right)\Big|_{r_\mathrm{s}} = \left(\frac{1}{\rho_0}\frac{\partial \rho_0}{\partial r_0}\right)\Big|_{r_\mathrm{s}} + \frac{2\ddot{r}_\mathrm{s}}{\dot{r}_\mathrm{s}^2} + \frac{4\gamma}{\gamma+1}\,r_\mathrm{s}^{-1} - \gamma\,\chi\,\frac{\partial^2 r}{\partial r_0^2}\Big|_{r_\mathrm{s}}\ , \tag{A.18}$$

which we can plug into Eq. A.12 and solve for $\left(\partial^2 r/\partial r_0^2\right)\big|_{r_\mathrm{s}}$ to obtain

$$\frac{\partial^2 r}{\partial r_0^2}\Big|_{r_\mathrm{s}} = -\frac{2\chi^{-1}}{\gamma+1}\,\frac{k_\rho - 3\,r_\mathrm{s}\,\ddot{r}_\mathrm{s}/\dot{r}_\mathrm{s}^2 - 4\gamma/\left(\gamma+1\right)}{r_\mathrm{s}}\ . \tag{A.19}$$

Finally, we can use this to obtain the acceleration at the shock

$$\left(\frac{\partial^2 r}{\partial^2 t}\right)\Big|_{r_\mathrm{s}} = \frac{4\left(2\gamma-1\right)}{\left(\gamma+1\right)^2}\ddot{r}_\mathrm{s} - \frac{2\chi^{-1}}{\gamma+1}\left(k_\rho - \frac{4\gamma}{\left(\gamma+1\right)}\right)\frac{\dot{r}_\mathrm{s}^2}{r_\mathrm{s}}\ . \tag{A.20}$$

A.1.2 Obtaining the Equation of Motion

We have now all the pieces in place to derive the equation of motion. We combine Eqs. A.4 and A.5 to eliminate $P\left(0,t\right)$, plug in Eqs. A.11, A.10 and A.20 and solve for $M\dot{v}_\mathrm{s}$ to obtain

$$M\dot{v}_\mathrm{s} = \frac{\left(\gamma+1\right)^2}{4\left(2\gamma-1\right)}\left[3\left(\gamma-1\right)\frac{E}{r_\mathrm{s}} - \frac{2}{\gamma+1}\rho_0 r_\mathrm{s}^2 v_\mathrm{s}^2 + 2\frac{\gamma-1}{\left(\gamma+1\right)^2}\left(k_\rho - \left(3+\frac{4\gamma}{\gamma+1}\right)\right)\frac{M\,v_\mathrm{s}^2}{r_\mathrm{s}}\right]\ , \tag{A.21}$$

which by adding $\dot{M}v_\mathrm{s} = \rho_0\,r_\mathrm{s}^2\,v_\mathrm{s}^2$ finally yields the equation of motion

$$\frac{\mathrm{d}}{\mathrm{d}t}\left(Mv_\mathrm{s}\right) = \frac{\gamma-1}{2\left(2\gamma-1\right)}\left[\frac{3\left(\gamma+1\right)^2}{2}\frac{E}{r_\mathrm{s}^3} + 3\rho_0 v_\mathrm{s}^2 + \left(k_\rho - \left(3+\frac{4\gamma}{\gamma+1}\right)\right)\frac{M\,v_\mathrm{s}^2}{r_\mathrm{s}^3}\right]r_\mathrm{s}^2\ , \tag{A.22}$$

from which the expression for the pressure gradient Eq. 2.5 can be read off.

While this derivation assumes an adiabatic blastwave in a stationary medium, it might be possible to lift this assumption and derive the pressure-gradient force in more complex cases, such as a radiatively cooling isothermal shock. In this case the compression-ratio at the shock and the shock-pressure would need to be updated to those of an isothermal shock. Moreover, the adiabatic condition would need to be replaced with an appropriate equivalent condition, which might be challenging, and which is mainly the reason why we instead approximate the pressure-gradient force to become negligible once cooling becomes dominant. Future studies that do deal with this complication might be able to incorporate the role of cooling in this derivation and possible recover the pressure-driven snowplow, and justify our assumption of the vanishing pressure-gradient force.

Appendix B

Starburst-Driven Galactic Outflows

Unveiling the Suppressive Role of Cosmic Ray Halos

B.1 Halo and Outflow model

B.1.1 Halo model and CR timescales

In our model, the galaxy halo consists of a thermal gas component and a non-thermal CR component. The gas is treated as an infinite slab in vertical hydrostatic equilibrium, with a density profile given by:

$$\rho\left(z\right) = \rho_{\rm mp}\cosh^{-2}\left(\frac{z}{H_{\rm s}}\right), \tag{B.1}$$

and velocity dispersion $\sigma = 10\,\sigma_1\,{\rm km\ s^{-1}}$, where $\rho_{\rm mp} = \mu\, m_{\rm H}\, n_{\rm H,\ mp}$ is the mid-plane gas density, $\mu = 1.4$ is the mean atomic weight, $n_{\rm H,\ mp} = n_0\,{\rm cm^{-3}}$ is the number density of the gas, and where the scale height of the is given by:

$$H_{\rm s} = \frac{\sigma}{\sqrt{2\pi G\rho_{\rm mp}}} \sim 338\,\sigma_1 n_0^{-0.5}\,{\rm pc} \tag{B.2}$$

(Behrendt et al., 2015). The expected profile of the CR component in the halo is uncertain and depends on the underlying CR transport physics, which remain unsettled. It has been suggested that buoyant bubbles may redistribute CRs in the halo (Recchia et al., 2021). Such bubbles, blown by SN-powered winds in starburst regions of a galaxy (e.g. Herenz et al., 2025), may be associated with outflows when they begin to fragment (e.g., above a cap similar to that seen in M82; Devine & Bally 1999), or could even be attributed to buoyant structures inflated by intensive energetic outbursts akin to the Galactic *Fermi* bubbles (e.g. Su et al., 2010; Zubovas & Nayakshin, 2012; Recchia et al., 2021) analagous to AGN-inflated bubbles in Galaxy clusters (e.g. Yang et al., 2019). Observations of M31 do not yet strongly favor a particular CR distribution profile (Karwin et al., 2019), and detailed physical modeling of the CR halo is beyond the scope of the current work. We therefore adopt a simple spatially uniform CR distribution in the halo, effectively treating it as a CR bath in which an outflow develops. This approach is sufficient to obtain qualitative insights into the effects of a CR halo on outflow development, with more detailed modeling of CR transport mechanisms in galaxy halos left to future work.

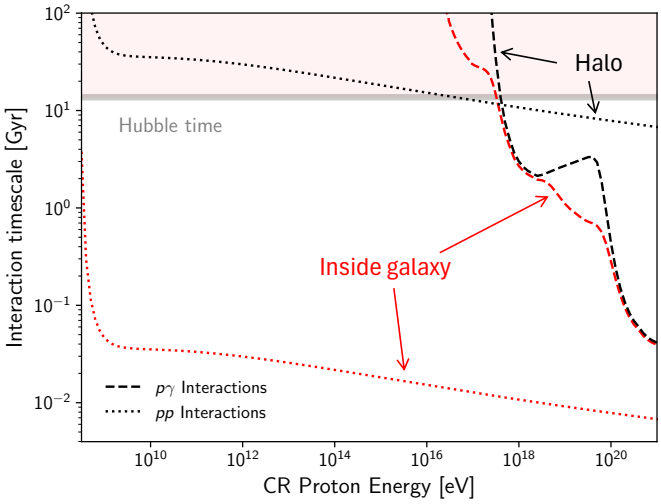

Figure B.1: Characteristic timescales for a CR proton to undergo a hadronic interaction with ambient gas (pp interactions) or radiation (pγ interactions) shown for typical conditions in the galaxy interior (red lines) and halo (black lines). For the galaxy interior, we adopt a gas density of $1\,\mathrm{cm}^{-3}$ and stellar radiation fields consisting of a stellar component with $T = 7100$ K and an energy density of $\sim 0.7\,\mathrm{eV\,cm}^{-3}$, with a dust component at $T = 60$ K and an energy density of $\sim 0.3\,\mathrm{eV\,cm}^{-3}$. For halo conditions, we consider a reduced gas density of $10^{-3}\,\mathrm{cm}^{-3}$, with radiation energy densities scaled down by a factor of 100. pγ losses with cosmological microwave background radiation at $z = 0$ are included for both galaxy interior and halo conditions, with photo-pair and photo-pion interactions occurring at the same rate in both environments. The Hubble timescale is shown in gray. Interaction timescales exceeding this (i.e. within the shaded pink region) practically do not occur. For an overview of these hadronic CR interaction processes and timescale calculations, see Owen et al. (2018).

To achieve a sensible normalization at low altitudes where CR pressure most strongly influences outflow development, the CR content of the halo is set to match the CR energy fraction at the galactic mid-plane. The halo CR pressure can then be expressed as:

$$P_{\mathrm{CR,\,ext}} = \frac{\gamma_{\mathrm{CR}} - 1}{\gamma - 1} f_{\mathrm{CR}} \rho_{\mathrm{mp}} \sigma^2, \tag{B.3}$$

where the thermal gas adiabatic index is $\gamma = 5/3$, and the CR fluid adiabatic index is $\gamma_{\mathrm{CR}} = 4/3$. This configuration creates a layered halo structure, with thermal gas pressure dominating at low altitudes and CR pressure becoming more important at higher altitudes (see the right panel of Fig. 3.1).

The CRs in the galaxy halo are likely primarily hadronic. This is because fast electron cooling in typical galactic conditions limits the electron population. Once deposited in the halo, CR hadrons experience few interaction or energy loss channels, allowing them to survive over Gyr timescales (see Fig. B.1). Adiabatic losses, streaming losses, and diffusive energy gains in micro-turbulence have only modest effects on the overall CR spectrum. Detailed simulations show that these processes rarely impact CR energies significantly in galaxy halos, typically contributing no more than 10 percent level corrections (Chan et al., 2019; Hopkins et al., 2022). We therefore neglect these effects in our model. Without significant cooling or absorption channels, CR hadrons are expected to accumulate in the galaxy halo, forming a fossil record of the host galaxy's CR power generation history.

B.1.2 Outflow model

We consider that an outflow is driven by a continuous injection of energy, momentum, CRs, and thermal gas, forming an expanding super-bubble that launches a galactic wind. This approach allows us to establish a criterion for wind launching and derive an analytical expression for the outflow velocity. To do this, we start from the blastwave equation of motion (Ostriker & McKee, 1988) under the thin-shell and sector approximations (e.g. Laumbach & Probstein, 1969; Koo & McKee, 1990), to derive an analytically tractable equation of motion suitable for modeling CR-driven outflows:

$$M\ddot{z} = \left(\Delta P + \Delta P_{\rm CR} - \rho \dot{z}^2\right) z^2 + M\, g + \frac{\dot{M}_{\rm SB}}{4\pi}\left(v_{\rm ej} - \dot{z}\right) \tag{B.4}$$

Here $z = z\,(t)$ is the shock radius at time t after the onset of shock expansion, $\dot{z}$ and $\ddot{z}$ are the instantaneous expansion velocity and acceleration of a thin shell following the expanding shock, $M = \int \rho z^2 dz$ is the swept-up mass, and ΔP and $\Delta P_{\rm CR}$ are the thermal and non-thermal pressure differences between the shocked and the un-shocked gas, respectively. The gravitational acceleration, g, for a single-component, isothermal slab in vertical hydrostatic equilibrium is given by:

$$g = -2\frac{\sigma^2}{H_{\rm s}}\tanh\left(\frac{z}{H_{\rm s}}\right)\ . \tag{B.5}$$

The speed of the ejecta, $v_{\rm ej}$, is:

$$v_{\rm ej} = \sqrt{2\varepsilon_w\left(1 - f_{\rm CR}\right) E_{\rm SN}/M_{\rm ej}}\ . \tag{B.6}$$

Other terms retain the definitions provided in the main text (see section 3.1).

We set $\Delta P = 0$ to account for the fact that the SBs generally become radiative, and quickly enter a rapidly-cooling wind phase (e.g. Kim & Ostriker, 2015; Oku et al., 2022). While the expansion of such rapidly cooling winds is still formally energy-driven, the coupling between the hot interior and the shell leads to dynamics that are equivalent to those of a momentum-driven wind, but with a slightly boosted momentum injection rate in comparison to that at the source (Lancaster et al., 2024). We account for this boost by means of the energy efficiency factor $\varepsilon_{\rm w}$.

We model the CRs as a non-thermal fluid with an adiabatic index of $\gamma_{\rm CR} = 4/3$, assuming a uniform pressure distribution immediately behind the shock. The CR pressure then evolves as:

$$P_{\rm CR,\ in} = 3\left(\gamma_{\rm CR} - 1\right)\frac{f_{\rm CR}\varepsilon_w\left(\dot{E}_{\rm SB}/4\pi\right)t}{z^3}\ . \tag{B.7}$$

As the outflow reaches a steady state (i.e., over a timescale when the flow reaches its asymptotic limit at high altitudes), the mass it has swept up is given by:

$$\begin{aligned} M_\infty &= \int_0^\infty \rho\left(z\right) z^2 {\rm d}z \\ &= \frac{\pi^2}{12}\rho_{\rm mp} H_{\rm s}^3 \sim 10^6\, \sigma_1^3\, n_0^{-1/2}\, {\rm M}_\odot\ . \end{aligned} \tag{B.8}$$

To analyze the properties of the outflow, we consider steady-state solutions with $\dot{z} \to v_\infty = 100\, v_{\infty,2}\,{\rm km\ s^{-1}}$ in the limit where $z = v_\infty t \gg H_{\rm s}$, and where the mass of the shell is dominated by the swept-up mass, i.e., $\left(\dot{M}_{\rm SB}/4\pi\right)t \ll M_\infty$. In this limit, we can rewrite eq. B.4 as:

$$0 = \Delta P_{\rm CR} z^2 - 2M_\infty\frac{\sigma^2}{H_{\rm s}} + \frac{\dot{M}_{\rm SB}}{4\pi}\left(v_{\rm ej} - v_\infty\right). \tag{B.9}$$

When external CR pressure is absent ($\Delta P_{\rm CR} = P_{\rm CR,\ in}$), this reduces to a quadratic form with a single positive solution:

$$v_\infty = \frac{v_{\rm ej}}{2\sqrt{1-f_{\rm CR}}}\left(\delta + \sqrt{\delta^2 + 2f_{\rm CR}}\right), \tag{B.10}$$

where

$$\delta = \sqrt{1-f_{\rm CR}} - \frac{\mathcal{R}_{\rm c}}{\mathcal{R}_{\rm SN}} \tag{B.11}$$

and

$$\mathcal{R}_{\rm c}^{-1} \sim 0.13\,\varepsilon_{\rm w,\text{-}2}^{1/2}\,E_{51}^{1/2}\,M_{\rm ej,0}^{1/2}\,\sigma_1^{-4}\,{\rm kyr}\ . \tag{B.12}$$

In the absence of CRs, there are no outflow solutions when $\mathcal{R}_{\rm SN} \le \mathcal{R}_{\rm c}$. On the other hand, when CRs are present, outflow solutions are always possible. For weak sources with $\mathcal{R}_{\rm SN} \ll \mathcal{R}_{\rm c}$, the outflow reaches very slow asymptotic speeds:

$$v_\infty^{\rm weak} \to 66\,f_{\rm CR}\varepsilon_{\rm w,\ \text{-}2}\,E_{51}\,\mathcal{R}_{-3}\,\sigma_1^{-4}\,{\rm km\ s^{-1}}\ . \tag{B.13}$$

However, in the strong source limit where $\mathcal{R}_{\rm SN} \gg \mathcal{R}_{\rm c}$, the outflow velocities are much higher, approaching:

$$v_\infty^{\rm strong} \to 10^3\,\varepsilon_{w,-2}^{1/2}\,E_{51}^{1/2}\,M_{\rm ej,\ 0}^{-1/2}\,\frac{\sqrt{1+f_{\rm CR}}+\sqrt{1-f_{\rm CR}}}{2}\,{\rm km\ s^{-1}}\ . \tag{B.14}$$

B.2 Model Limitations and Assumptions

Our model invokes a number of approximations and assumptions. While we consider our results to be qualitatively robust, future developments that relax these assumptions may provide more refined insights. Here, we assess the validity of our assumptions and approximations and discuss their potential impact on our results.

Density Profile and Gravitational Field. The density profile in eq. (B.1) represents an isothermal, single-component atmosphere in vertical hydrostatic equilibrium, providing a reasonably accurate description near the mid-plane. However, the presence of molecular gas and a young stellar disk could create a deeper potential well, leading to a more compact density profile that may affect the early stages of shock breakout. Moreover, explicitly modeling the gravitational potential of different galaxy components (e.g. the bulge, disk and dark-matter halo) could modify flow properties (see Shimoda & Inutsuka, 2022), and this can be affected by the detailed gas distribution throughout the galaxy and inner halo. However, the outflow properties at high altitudes (above $\sim$ 100 kpc) are unlikely to be significantly impacted if the overall gas surface density and wind loading remain unchanged.

Halo Gas Properties. In the halo, the multi-phase CGM contributes a diffuse gas background that exerts additional (ram) pressure, which can counteract outflow expansion (Shin et al., 2021). While the CGM is diffuse, it is expected to follow a shallow density profile that would slow the outflow's expansion once the swept-up CGM mass becomes comparable to M_∞. This occurs at a height of $z_{\rm CGM} \sim 5\,\sigma_1\,n_0^{-1/6}\,n_{\rm CGM,\ \text{-}3}^{-1/3}\,{\rm kpc}$, where $n_{\rm H,\ CGM} = 10^{-3}\,n_{\rm CGM,\ \text{-}3}\,{\rm cm^{-3}}$ is the number density of hydrogen in the CGM.

Ejecta Mass. For the asymptotic steady-state solution, we consider a limit where the outflow has traveled sufficiently far above the disk, yet is not old enough for its mass to be dominated by the ejecta. The timescale for the outflow to become ejecta-dominated is $t_{\rm ED} \sim 4\pi M_\infty/\dot{M}_{\rm SB} \sim 12.6\,\sigma_1^3\,n_0^{-1/2}\,M_{\rm ej,\ 0}^{-1}\,\mathcal{R}_{-3}^{-1}\,{\rm Gyr}$, which is considerably longer than the lifetime of the starburst driving the outflow. We therefore consider our results to be robust against this approximation.

Thin-Shell and Sector Approximation. While the thin-shell approximation is well-suited for radiative blastwaves or those propagating through media with positive density gradients, it becomes increasingly crude in environments with steep negative density gradients. This is because the mass, energy, and momentum distributions behind the shock broaden significantly (see e.g. Laumbach & Probstein, 1969; Koo & McKee, 1990). Despite the steep density gradient considered in this work, our model focuses on a radiative, momentum-driven wind, where the thin-shell approximation is expected to remain reasonably accurate. The sector approximation, on the other hand, is most reliable when the local shock surface remains relatively flat. This approximation can break down if adjacent streamlines begin to diverge significantly, e.g. due to sudden deflections. However, since observed outflows generally exhibit large opening angles, this approximation is likely to have only a negligible impact on our findings.

Treatment of CRs. Our treatment of CRs involves a number of simplifications. While we do not explicitly account for CR cooling or interactions within the flow, this is well justified given the relevant timescales (see Appendix B.1.1). However, future studies with more detailed CR propagation modeling may yield different quantitative results, particularly if a detailed CR transport model within the halo is included. Such models could alter the distribution of halo CRs (Recchia et al., 2021), and reveal the microphysical impacts of CRs on outflows, including re-acceleration processes and interactions with complex magnetic field structures at the outflow–halo interface (see, e.g. Hopkins et al., 2023). Additionally, our study does not consider the spectral evolution of CR particles, which could influence the coupling between CRs and the outflowing wind fluid, potentially modifying their driving efficiency and altering observable CR emission signatures. Future work incorporating these effects could provide a clearer understanding of how CRs shape the development of outflows in CR-rich galaxy halos.

Appendix C

Cloud Formation by Supernova Implosion

C.1 Adaptive Mesh Refinement

In our fiducial simulation suite presented in the main body of the paper we have used AMR to reduce the numerical cost of the simulations. In our prescription we only refine cells, which have been sufficiently enriched by SN ejecta. We thus create a central refinement region that should expand at roughly the same rate as the shock. However, as the ejecta are physically confined behind the contact discontinuity, the refinement region might lag behind the shock and thus one might expect the shock to be slightly less refined than the rarefied gas behind it.

In SNRs the contact discontinuity and the shock are essentially at the same location and thus we expect this lag to be negligible, especially considering the presence of numerical diffusion, which acts to smear out the contact discontinuity.

In order to test whether the use of AMR can qualitatively modify our results in Figure C.1 we compare the results of the models N1_n2_L13 and N1_n2_L13_noAMR. The two models are almost identical, but while in N1_n2_L13 we use our AMR prescription in N1_n2_L13_noAMR we use a static mesh with a grid spacing equal to the finest spacing in N1_n2_L13.

Figure C.1 shows that the two models are essentially identical. Negligibly small differences arise due to small differences in the time when snapshots are written, since they are only written when the entire grid is synchronized.

We thus conclude that the adopted AMR technique does not affect our results in any meaningful way.

C.2 Convergence

In order to test, whether our results are converged, we ran the N1_n2 model at three different resolutions, denoted by N1_n2_L12, N1_n2_L13 and N1_n2_L14. The results are shown in Figure C.2. Shown are the mass, momentum, energy, pressure, volume and ejecta content of the different gas components as a function of time.

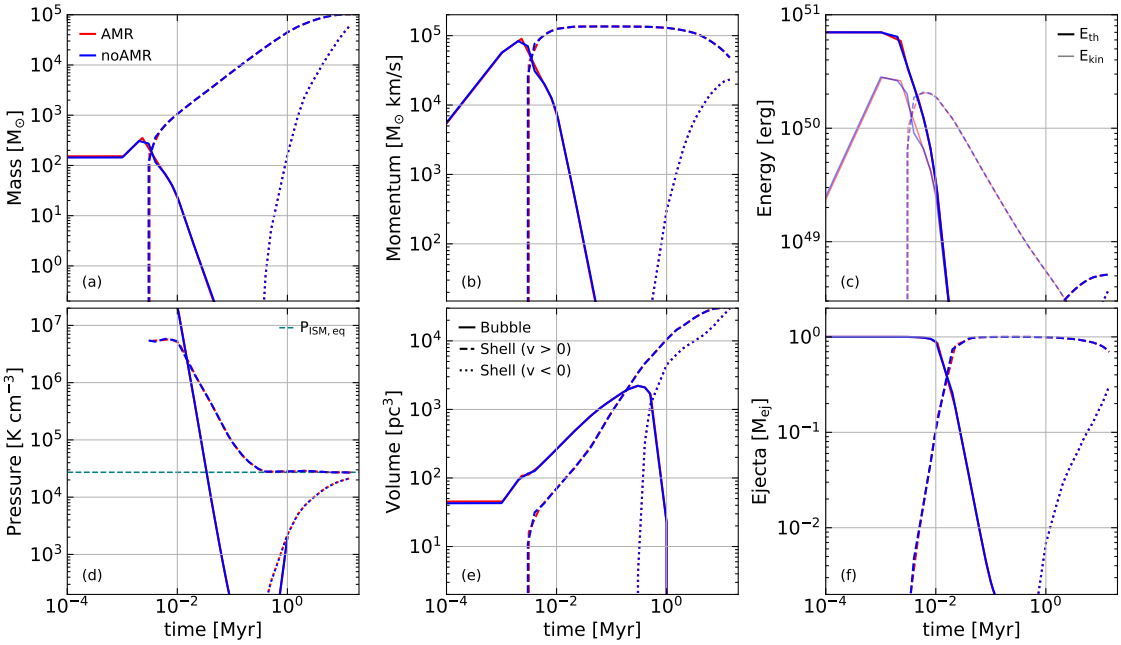

Figure C.1: Similar to Figure 4.5 for model N1_n2_L13 with and without AMR. Solid, dashed and dotted lines correspond to the hot bubble, outflowing and inflowing shell, respectively. In panel (c) the thermal and kinetic energy are plotted with an opacity alpha of 1 and 0.5, respectively.

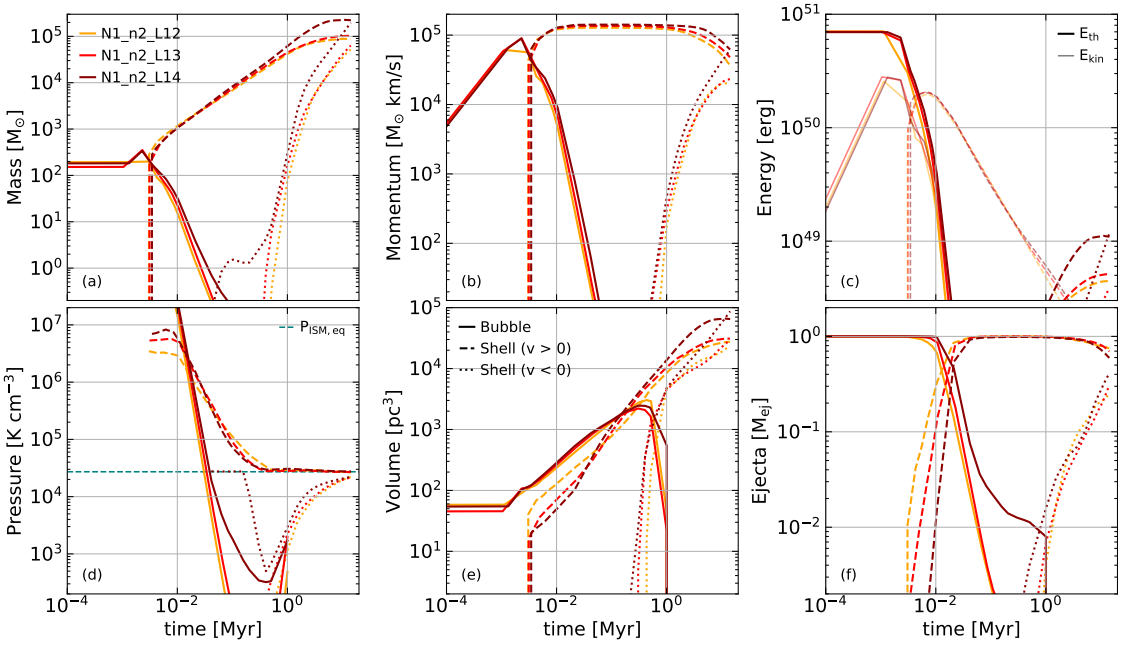

Figure C.2: Similar to Figure 4.5 for models with different resolution. Solid, dashed and dotted lines correspond to the hot bubble, outflowing and inflowing shell, respectively. In panel (c) the thermal and kinetic energy are plotted with an opacity alpha of 1 and 0.5, respectively.

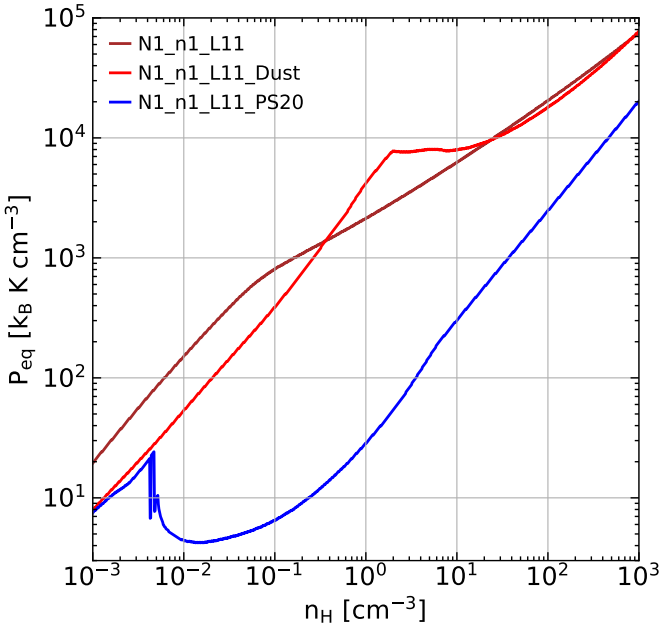

Figure C.3: Equilibrium pressure as a function of density for different cooling models. The brown curve corresponds to the default RAMSES cooling, and the red and blue curves correspond to different models taken from Ploeckinger & Schaye (2020).

Before shell formation, there are only minor differences between the models, which seem to stem from slightly different snapshot times and the analysis procedure. There is a slight dip in the mass, momentum and energy of the hot phase, in the lowest resolution run, which likely might have arisen from the SNR selection criterion (Figure 4.1).

The shell formation timescale, as well as the properties of the SNR at shell formation appear converged in line with the convergence criteria by Kim & Ostriker (2015).

Slight differences appear after shell formation. The pressure of the cold phase, during the PDS increases with resolution. Since the temperature of the shell during this phase is roughly fixed to about 10^4 K, the pressure is determined by the density of the shell, which depends on the width of the shell. In all runs, the shell during the PDS is resolved with only few resolution elements and thus indeed is not converged, as already noted by Sharma et al. (2014) who estimate that the width of the shell should be $\sim 0.001\,R_{\rm sf} \sim 10^{-3} - 10^{-2}$ pc. Despite the different PDS shell pressure, the PDS ends at a similar time in all runs and the shell pressure approaches a very similar evolution during the MCS and following phases.

In the lower resolution runs more of the ejecta tend to be incorporated in the shell right after shell formation. However, these differences are negligible by $t = 0.1$ Myr.

During the MCS, prior to implosion, there is already a small non-growing fraction of backflowing cold gas in the highest resolution run. This component is in pressure equilibrium with the ISM suggesting that it arises from small blisters in the shell's outer edge, which form, when the shell fragments due to thin shell shell instabilities which are unresolved in the lower resolution runs.

The implosion is launched at roughly the same time after $\sim 300 - 500$ Myr and forms a central cloud ($V_{\rm hot} \to 0$) after 1 Myr in all runs, indicating that these timescales are converged.

The mass, momentum, thermal energy and volume of the cold components diverge at late times.

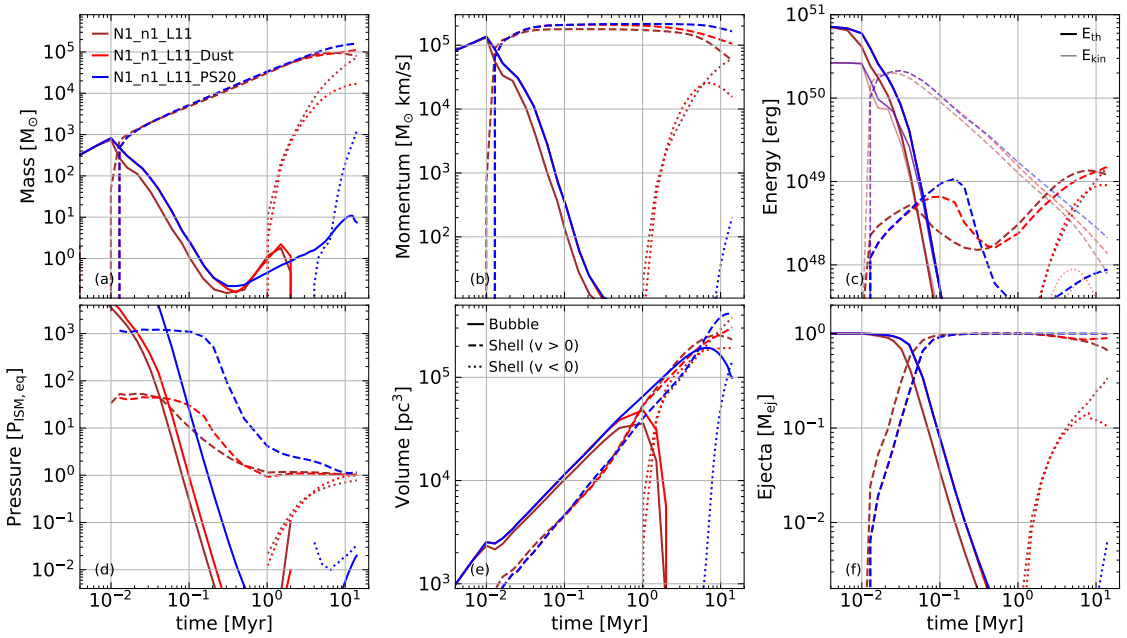

Figure C.4: Rescaled version of Figure 4.5 for models with different cooling functions. Solid, dashed and dotted lines correspond to the hot bubble, outflowing and inflowing shell, respectively. In panel (c) the thermal and kinetic energy are plotted with an opacity alpha of 1 and 0.5, respectively.

Despite this non-convergence all SNRs exhibit the same qualitative features, and thus it does not affect our conclusions in any meaningful way.

C.3 Cooling Models

In order to investigate the role of the cooling function, we have rerun the model N1_n1_L11 with two different cooling models taken from Ploeckinger & Schaye (2020) integrated using an exact integration scheme (Townsend, 2009; Zhu et al., 2017). For details of the implementation we refer the reader to Behrendt et al. (in prep.). The cooling functions in the models N1_n1_L11_Dust (Dust) and N1_n1_L11_PS20 (PS20) correspond to their models UVB_dust1_CR0_G0_shield0 and UVB_dust1_CR1_G1_shield1, respectively. The models' cooling-equilibrium curves in the $P - n_{\mathrm{H}}$-plane are shown in Figure C.3.

Dust differs from the Ramses cooling model in that the equilibrium curve has a pronounced kink at around $n_{\mathrm{H}} \sim 1\,\mathrm{cm}^{-3}$, while PS20 has a steep drop in pressure at around $n_{\mathrm{H}} \sim 0.01\,\mathrm{cm}^{-3}$ above which the pressure is 2-3 orders of magnitude below the pressure in the Ramses model.

In Figure C.4 we show a comparison of the results for the different models. As expected the SNR evolution before shell formation is not affected by the cooling. The length of the PDS phase and the momentum boost during this phase are slightly increased for the Dust and PS20 models.

Despite these differences, the timescales for implosion and cloud formation hardly differ between the Ramses and Dust models. On the contrary, for the PS20 model, since the equilibrium ISM pressure is several orders of magnitude lower, implosion is delayed by $\gtrsim 3\,\mathrm{Myr}$ and does not lead to cloud formation within the simulated time.

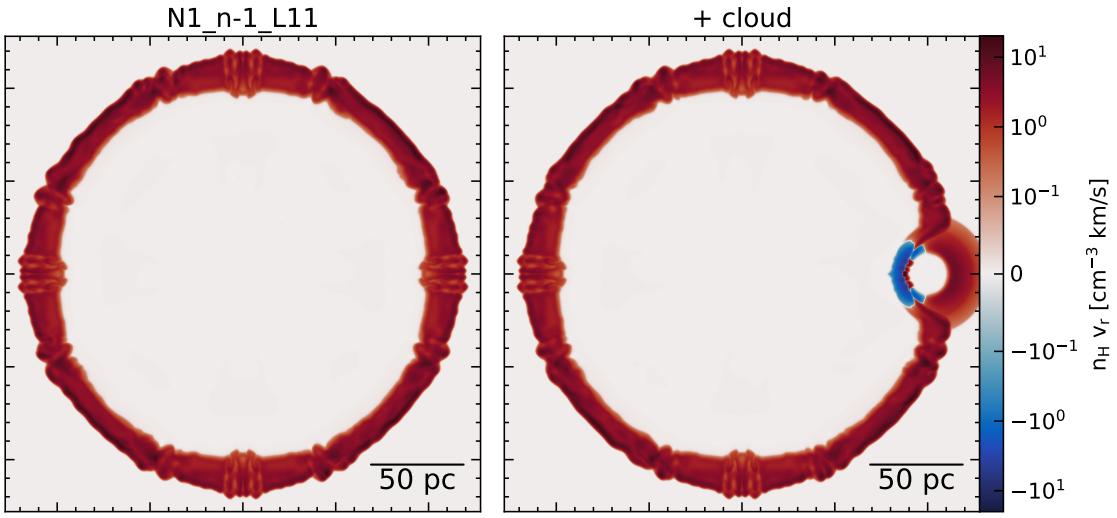

Figure C.5: Slices through the XY-plane of the radial mass flux 1.5 Myr after the explosion for models with and without a cold, dense cloud placed near the explosion center.

These results indicate that it is indeed the ISM pressure, which controls the implosion, since all other quantities that might have an effect do not differ very much between the runs.

C.4 Locally Triggered Implosions

In order to investigate, whether or not the implosion can be triggered by local pressure enhancements, we have rerun the model N1_n-1_L11 for 1.5 Myr with a cold ($T \sim 800\,\mathrm{K}$), dense ($n_\mathrm{H} \sim 10\,\mathrm{cm}^{-3}$) cloud of Radius $R_{cl} = 15\,\mathrm{pc}$ centered at a distance of $d_{cl} = 100\,\mathrm{pc}$ from the explosion center. The pressure in the cloud is about an order of magnitude higher than that of the ambient medium.

As shown in Figure 4.7, N1_n-1_L11 does not implode until $t = 1.75 \pm 0.25\,\mathrm{Myr}$ and thus there should be no *global* implosion within the simulated time. However, if the implosion is indeed a local effect, the increased pressure within the cloud, should trigger a *local* implosion shortly after impact.

In Figure C.5 we show slices of the radial mass flux, 1.5 Myr years after the explosion for the runs with and without a cloud. In the run without a cloud there is no implosion, while in the run with the cloud, there is a significant backflowing component behind the shock coming from the direction of the cloud. This confirms that the implosion can indeed be triggered *locally*.

We note, that the cloud is slowly expanding due to the pressure gradient relative to the ambient medium, leading to a radially inflowing component downstream of the shock. This flow is unrelated to the implosion, which is necessarily upstream.

Appendix D

SISSI: Supernovae in a stratified, shearing interstellar medium

I. The geometry of supernova remnants

D.1 The ISM of the SISSI galaxy

The SNRs of the SISSI simulations expand into a complex environment which differs between different regions of the ISM. In order to help interpreting the role of the ISM, here we describe the properties of this environment.

Figure D.1 shows the $T - n_{\mathrm{H}}$ phase diagram of the gas in the SISSI galaxy at $t = 0$. In the ISM most of the gas is concentrated in two distinct gas phases: Warm neutral gas at $T \sim 7 \times 10^3\,\mathrm{K}$ for densities in the range $\sim 10^{-2} - 10^2\,\mathrm{cm}^{-3}$, and colder gas at a constant pressure of $P \sim 10^4\,k_{\mathrm{B}}\,\mathrm{K\,cm}^{-3}$ for denser gas above $n_{\mathrm{H}} \sim 1\,\mathrm{cm}^{-3}$. For gas above $n_{\mathrm{H}} \sim 1\,\mathrm{cm}^{-3}$ the warm phase is unstable and cools after $\sim 1\,\mathrm{Myr}$.

Cold ($T \lesssim 10^2\,\mathrm{K}$) and dense ($n_{\mathrm{H}} \gtrsim 10^2\,\mathrm{cm}^{-3}$) gas is star-forming and thus steadily being consumed.

The galactic ISM is surrounded by a hot, diffuse circumgalactic medium (CGM), corresponding to a roughly adiabatic phase with $T_{\mathrm{CGM}} \sim 10^7 \left(n_{\mathrm{H}} / \left(10^{-3}\,\mathrm{cm}^{-3}\right)\right)^{\gamma-1}$, with a maximum density of $\sim 10^{-3}\,\mathrm{cm}^{-3}$ at a temperature of $\sim 10^7\,\mathrm{K}$, in pressure balance with the cold ISM.

Of course, locally the ISM properties may not adhere to this simple picture. In Fig. D.2 we show the initial properties of the local ISM at the various explosion sites. All quantities are derived from density, and vertical velocity profiles averaged over ISM patches of side lengths $\ell = 0.2, 0.5, 1, 1.5\,\mathrm{and}\,2\,\mathrm{kpc}$ parallel to the galactic plane centered around the explosion site. The error bars indicate how much a quantity varies with scale.

We define the vertical scale height as half the distance between the $\sim 12\,\%$ and the $\sim 88\,\%$ mass percentiles of the density profile, roughly matching the definition of a $\mathrm{sech}^2\left(z/z_{\mathrm{scale}}\right)$-profile, as would be appropriate for a single-component, isothermal disk. While the simulated galaxy, is neither consisting of only a single component, nor is it isothermal, our definition still yields a reasonable definition for an effective gas scale-height. Correspondingly, we define the midplane

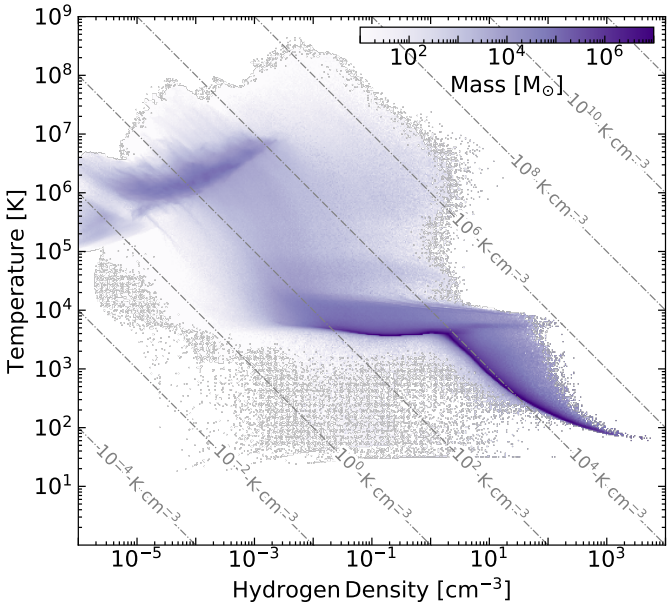

Figure D.1: Temperature-density phase-diagram of the global ISM. The galactic ISM features a stable phase at $P/k_\mathrm{B} \sim 10^4\,\mathrm{K\ cm^{-3}}$ for $n_\mathrm{H} \sim 1 - 100\,\mathrm{cm^{-3}}$, and an unstable phase at $T \lesssim 10^4\,\mathrm{K}$, which becomes stable below $n_\mathrm{H} \sim 1\,\mathrm{cm^{-3}}$.

density as

$$n_{\mathrm{H,\ mp}} = \frac{1}{2\tanh(1)\, z_\mathrm{scale}} \int_{z_0 - z_\mathrm{scale}}^{z_0 + z_\mathrm{scale}} n_\mathrm{H}(z)\,\mathrm{d}z\ , \tag{D.1}$$

where z_0 is the midplane, lying right in between the $\sim 12\,\%$ and the $\sim 88\,\%$ mass percentiles of the density profile.

The velocity dispersion is defined as the average of the three components of the velocity dispersion vector, i.e. $\sigma^2 = \left(\sum_{i\in\{x,y,z\}} \sigma_i^2\right)/3$, within all vertical bins within the midplane, i.e. within $z_0 \pm z_\mathrm{scale}$.

We find a diverse range of midplane densities spanning over two orders of magnitude. The densities roughly follow the radial trend of the initial conditions, albeit with considerable scatter and a steepening towards $R_\mathrm{gal} = 2\,\mathrm{kpc}$. We thus expect SNRs at larger galactic radii to grow bigger, with more variation between regions.

The velocity dispersion is roughly constant throughout the sample of regions with a typical value of $\sigma \sim 10\,\mathrm{km\ s^{-1}}$, though with larger spatial variations in some regions. SNRs should therefore merge with the ISM at around the same time in all regions.

The measured scale heights indicate that, while the overall trend follows the expected scaling from dynamical equilibrium considerations in a single-component disk, it is more compact due to the dominant gravitational potential of the stellar disk. SNRs will start to be affected by vertical stratification once their size grows similar to this scale height, indicating that these effects might become important earlier for SNRs in higher-density regions.

In some regions we find that the mean vertical velocity is increasing (decreasing) linearly as a function of height with a midplane vertical velocity gradient on the order of σ/z_scale. These motions appear to be strongest around $n_{\mathrm{H,\ mp}} \sim 1\mathrm{cm^{-3}}$, indicating that gas at this density can be thermally unstable and is driven towards lower (higher) densities ($\partial_z v_z > 0\,(<0)$). We interpret these

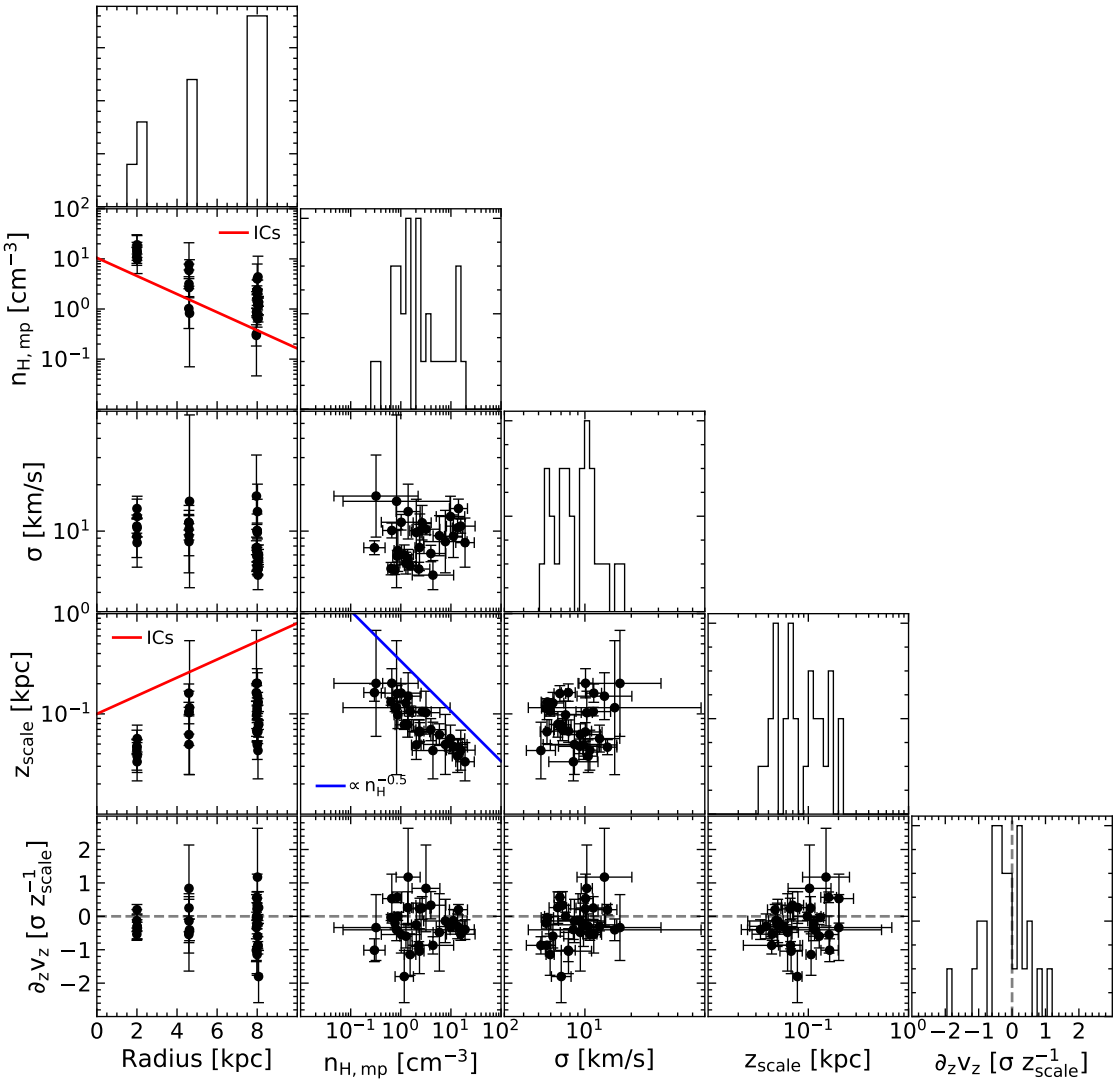

Figure D.2: Corner plot showing the distribution of ISM properties (Galactocentric radius R, midplane density $n_{\mathrm{H,\,mid}}$, velocity dispersion σ, vertical scale height z_{scale} and vertical velocity gradient $\partial_z v_z$) at the SNR locations averaged over various length scales. We average over quadratic apertures with side lengths $L = 0.2$, 0.5, 1.0, 1.5 and 2.0 kpc. As expected the mean of $n_{\mathrm{H,\,mid}}$ decreases with R, with large scatter at $R > 2$ kpc. Compared to the ICs, the mean density profile has steepened. The velocity dispersion is roughly constant $\sigma \sim 10$ km/s throughout the disk with considerable scatter. The disk scale height follows the scaling behavior predicted by vertical hydrostatic equilibrium of the gas $z_{\mathrm{scale}} \propto \sigma / n_{\mathrm{H}}^{0.5}$, but with a slightly lower normalization, likely due to the presence of stars. The vertical velocity gradient on average is zero with increasing scatter towards larger R. The maximum values reveal a preferred scale of $|\partial_z v_z| \sim \sigma / z_{\mathrm{scale}} \sim t_{\mathrm{ff}}^{-1}$ indicating that these expansion and contraction motions correspond to gravitational breathing modes of the disk. The velocity gradients peak around $n_{\mathrm{H,\,mid}} \sim 1\,\mathrm{cm}^{-3}$, i.e. the breathing of the disk coincides with the presence of multi-phase gas (see fig:D.1).

motions as disk *breathing*-modes around the dynamical equilibrium, with an expected period of about a free-fall timescale, much longer than the dynamical timescale of an expanding SNR. Thus we expect the velocity gradients to be frozen-in during the lifetime of an SNR. SNRs expanding into a positive velocity gradient will grow faster as they sweep-up co-expanding material, while SNRs expanding into a collapsing region will be slowed down.

D.2 Analytic theory of SNR evolution in a uniform medium

In this section we briefly review the analytic theory for the dynamics of radiative SNRs and SBs (see e.g. Kim & Ostriker, 2015; Oku et al., 2022; Romano et al., 2024a). We consider the case of spherical expansion driven by point-explosions with explosion energy $E_{\rm SN} = 10^{51}\,E_{51}\,{\rm erg}$ into a uniform medium with hydrogen number density $n_{\rm H} = n_0\,{\rm cm}^{-3}$, solar metallicity and pressure $P = \mu\,n_{\rm H}\,\sigma^2$, where $\mu = 1.4$ is the mean atomic weight and $\sigma = 10\,\sigma_1\,{\rm km\ s}^{-1}$ is the sound speed, which in a supersonically turbulent medium such as the ISM, may be replaced with the turbulent velocity dispersion.

Since here we are mostly interested in the dynamics of old radiative SNRs we skip the dynamics of the initial ejecta dominated expansion and start directly with that of adiabatic expansion; the so-called Sedov-Taylor (ST) phase (Sedov, 1959). The internal structure of the Sedov-Taylor blastwave is described by a similarity solution with similarity parameter $\xi = r/\left(E_{\rm SN}t^3/\rho\right)^{1/5}$, with $\xi_0 \approx 1.15167$ at the position of shock radius. During the ST phase, the radially outward momentum increases as a function of time and is given by (Kim & Ostriker, 2015)

$$p_{\rm ST} = 2.21\times10^4\,E_{51}^{4/5}\,n_0^{1/5}\,t_3^{3/5}\,{\rm M}_\odot\,{\rm km\ s}^{-1}\ , \tag{D.2}$$

where $t = t_3\,{\rm kyr} = t_6\,{\rm Myr}$.

The ST phase ends, once radiative cooling becomes dominant and a thin shell forms right behind the shock front, after (Kim & Ostriker, 2015)

$$t_{\rm sf} \sim 44\,E_{51}^{0.22}\,n_0^{-0.55}\,{\rm kyr}\ , \tag{D.3}$$

at which point the SNR has a size of

$$R_{\rm sf} = 22.6\,E_{51}^{0.29}\,n_0^{-0.42}\,{\rm pc}\ , \tag{D.4}$$

and a momentum of

$$p_{\rm sf} = 2.17\times10^5\,E_{51}^{0.93}\,n_0^{-0.13}\,{\rm M}_\odot\,{\rm km\ s}^{-1}\ . \tag{D.5}$$

Right after shell formation, the interior of the SNR is still hot and at a higher pressure than the shell, which has a temperature of about $T_{\rm shell} \sim 10^4\,{\rm K}$ and is highly compressed relative to the ambient medium $\chi \sim 10$. During this so-called pressure-driven snowplow (PDS) stage, the SNR expands $R \propto t^{2/7}$, leading to a slight enhancement of the radial momentum $\propto t^{1/7}$. The PDS ends when the pressure in the bubble becomes comparable to the pressure in the shell (Romano et al., 2024a) after

$$t_{\rm PDS} \sim 0.15\,E_{51}^{0.27}\,n_0^{-0.44}\,{\rm Myr}\ , \tag{D.6}$$

corresponding to a size of

$$R_{\rm PDS} \sim 32.1\,E_{51}^{0.3}\,n_0^{-0.39}\,{\rm pc}\ . \tag{D.7}$$

Depending on the details of radiative cooling and incorporation of mass from the bubble into the shell, the radially outward momentum of the SNR is boosted by up to about $\sim 50\,\%$ during the PDS.

Once the pressure in the interior of the bubble has dropped, the SNR expands solely due to its inertia $R \propto t^{1/4}$. During this so-called momentum-conserving snowplow (MCS) phase, the pressure of the shell is proportional to the shock velocity $P_{\rm shell} \propto t^{-3/2}$. During this stage, the back of the shell is unstable and a reflected shockwave or implosion is driven into the interior of the SNR once the pressure of the shell becomes comparable to that of the ambient medium (Romano et al., 2024a) after

$$t_{\rm launch} \sim 0.5\, E_{51}^{0.27}\, n_0^{-0.44}\, \sigma_1^{-4/3}\, {\rm Myr}\ , \tag{D.8}$$

at which point the SNR has a size of

$$R_{\rm launch} \sim 43.6\, E_{51}^{0.3}\, n_0^{-0.39}\, \sigma_1^{-1/3}\, {\rm pc}\ . \tag{D.9}$$

These expressions differ from those derived by Romano et al. (2024a), due to the differences in our model for the ambient pressure.

There are various different models for the case of an SB, driven by subsequent SN explosions (e.g. El-Badry et al., 2019; Oku et al., 2022). The basic assumption in these models is that, if the age of the SB is greater than the average time between SN explosions $t \gg \Delta t_{\rm SN} = \Delta t_6\, {\rm Myr}$, the expansion can be approximately described by that of a wind with a constant mechanical luminosity $L = E_{\rm SN}/\Delta t_{\rm SN} = 10^{45}\, L_{45}\, {\rm erg\ yr^{-1}}$. The dynamics of a radiative SB depend on the efficiency of energy dissipiation, e.g. due to radiative cooling, facilitated by thermal conduction and turbulent mixing of the hot interior and the cold shell. When energy injection dominates over dissipation, the expansion can be described by that of an energy-driven wind (Weaver et al., 1977; El-Badry et al., 2019). In contrast, if cooling losses dominate, the expansion is effectively momentum-driven (Lancaster et al., 2021; Oku et al., 2022; Lancaster et al., 2024).

In the model N1x10, $\Delta t_{\rm SN} = 1\, {\rm Myr} \gg t_{\rm cool}$, corresponding to the momentum-driven regime. The size of a momentum-driven SB is given by Eq. 26 of Oku et al. (2022)

$$R = 40\, t_6^{1/2}\, L_{45}^{0.23}\, n_0^{-0.28}\, {\rm pc}\ . \tag{D.10}$$

D.3 Shearing-sphere model

In order to model the deformation by shear, here we derive the simplest possible model: starting from $t = 0$, a sphere of radius r_0, centered in the galactic midplane at a galactocentric radius R_0, is subjected to differential rotation with a constant rotation speed $V_{\rm rot}$, corresponding to an angular frequency of $\Omega\,(R) = V_{\rm rot}/R$. Correspondingly, the orbital timescale is $t_{\rm orb}\,(R) = 2\pi\,\Omega^{-1}\,(R)$.

We parameterize the surface of the sphere using the polar angles θ and φ at $t = 0$

$$\mathbf{\Phi}_t\,(\theta, \phi; r_0) = \begin{pmatrix} R\cos\,(\phi_0 + \Omega t) \\ R\sin\,(\phi_0 + \Omega t) \\ r_0\cos\,(\theta) \end{pmatrix}\ , \tag{D.11}$$

where

$$R^2 = R_0^2 + 2R_0 r_0 \cos\,(\varphi)\, \sin\,(\theta) + r_0^2 \sin^2\,(\theta) \tag{D.12}$$

is the galactocentric radius of the point on the surface of the sphere and the initial azimuthal angle ϕ_0 is defined by

$$R\cos\,(\phi_0) \;=\; R_0 + r_0 \sin\,(\theta)\, \cos\,(\varphi) \tag{D.13}$$

$$R\sin\,(\phi_0) \;=\; r_0 \sin\,(\theta)\, \sin\,(\varphi)\ . \tag{D.14}$$

Due to the differential rotation, parts of the sphere that are at a larger galactocentric radius lag behind and the parts that are at a smaller R advance ahead, leading to deformation. It can be shown that in spite of the deformation, the volume remains constant.

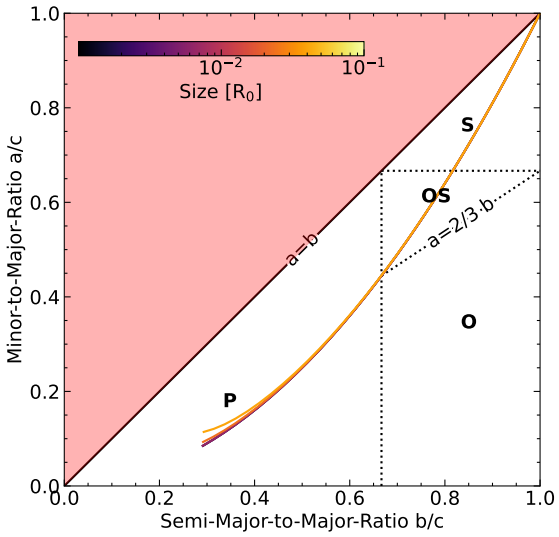

Figure D.3: Same as Fig. 6.10 for the shearing sphere model for spheres with different sizes, evolved for $0.5\,t_{\rm orb}\,(R_0 - r_9)$. The phase-space trajectories of the spheres with different sizes are almost identical.

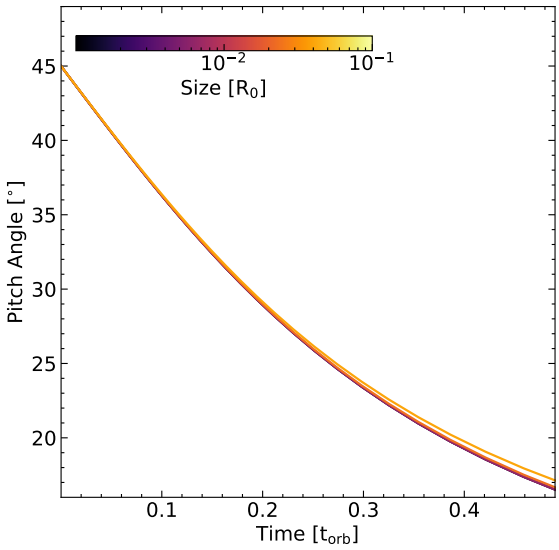

Figure D.4: Time evolution of the pitch angle of the major axis of the shearing sphere for spheres with different sizes. The pitch angle starts off near 45 ° and decays over time. Larger spheres tend to have slightly larger pitch angles.

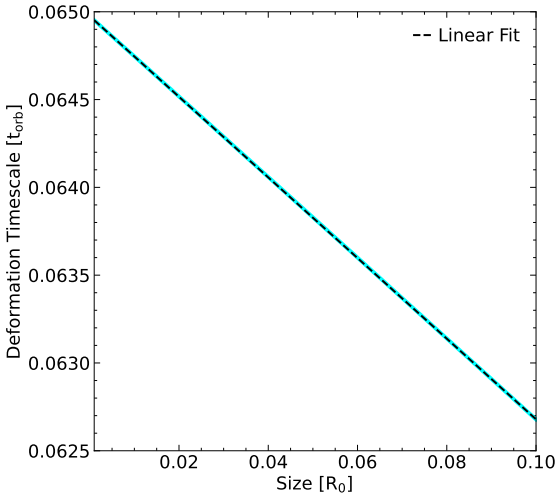

Figure D.5: Deformation timescale as a function of size. Spheres are deformed greatly after ~ 6.5 per cent of $t_{\rm orb}\left(\bar{R}\right)$, where $\bar{R} = pR_0 + (1-p)\left(R_0 - r_0\right)$ is a characteristic radius lying between $R_0 - r_0$ and R_0. Our linear fit yields $p \sim 0.65$.

We measure the geometry as defined, in Sec. 6.2.3, i.e. by computing the shape tensor

$$S_{ij} = V^{-1} \int_V \left(\left\| \Delta \mathbf{\Phi}_t \right\|^2 \delta_{ij} - \Delta\Phi_{t,i} \Delta\Phi_{t,j} \right) \mathrm{d}V \ , \tag{D.15}$$

where $\Delta\mathbf{\Phi}_t = \mathbf{\Phi}_t\left(\theta, \phi; r\right) - \mathbf{\Phi}_c\left(t\right)$ is the coordinate vector of a point within the shearing ball, relative to the volume-weighted center

$$\mathbf{\Phi}_{\rm c}\left(t\right) = V^{-1} \int_V \mathbf{\Phi}_t\left(\theta, \phi; r\right) \mathrm{d}V \ . \tag{D.16}$$

Since the polar points are always co-rotating with the center, the semi-major axis $\hat{e}_{\text{semi-major}} = \hat{e}_z$ and $b = r_0$. The major axis evolves from $\alpha_{\text{major},\,0} \sim 45^\circ$ towards $\alpha_{\text{major},\,\infty} \sim 0^\circ$, and necessarily $\alpha_{\text{minor}} = \alpha_{\text{major}} + 90^\circ$.

For the sake of a better intuition of the model, in Figs. D.3 and D.4 we show the shape phase-space trajectories as well as the time evolution of the pitch angle for various shearing spheres with different r_0/R_0. We show the time evolution over half an orbit. The trajectories in shape phase-space differ only marginally between different sized spheres for $r_0 \lesssim 0.1\,R_0$. However, at later times larger spheres tend to have slightly larger pitch angles and minor-to-major axis ratios.

In Fig. D.5 we show the dependence of the deformation timescale on the size of the sphere for $r_0 < 0.1\,R_0$. We find a weak linear dependence on the size, which is approximately fit by

$$t_{\rm deform} \approx 0.065\, t_{\rm orb}\left(\bar{R}\right) \ , \tag{D.17}$$

where $\bar{R} = pR_0 + (1-p)\left(R_0 - r_0\right)$ is a characteristic radius lying between $R_0 - r_0$ and R_0. Our linear fit yields $p \sim 0.65$.

We do not show any results for $r_0 > 0.1\,R_0$ due to the large difference in orbital timescales, which leads to rapid deformation and even winding of the part of the sphere with $R \ll R_0$, while the rest has hardly moved.

Appendix E

SISSI: Supernovae in a stratified, shearing interstellar medium

II. Star formation near the Sun is quenched by expansion of the Local Bubble

E.1 Evaluation of analysis methods

E.1.1 Modified smoothing Kernel

O'Neill et al. (2024) use a Gaussian smoothing-kernel W to obtain smooth density profiles before applying their peak-finding algorithm. This procedure is not manifestly mass-conserving and might lead to numerical artifacts that can bias the results.

In order to account for this potential bias, we use an explicitly mass-conserving approach, by introducing weights that account for the non-uniformity of the volume elements $\mathrm{d}V = r^2\,\mathrm{d}r\,\mathrm{d}\Omega$. In particular, the condition that the mass is identical between the unsmoothed and smoothed profiles can be written as

$$M = \sum_i \mathrm{d}V_i \rho_i = \sum_{i,j} \mathrm{d}V_i W_{ij} \rho_j \ , \tag{E.1}$$

where the smoothed density

$$\bar{\rho}_i = \sum_j W_{ij} \rho_j \ . \tag{E.2}$$

Condition E.1, leads to the normalization condition for the smoothing matrix W

$$\mathrm{d}V_j = \sum_i \mathrm{d}V_i W_{ij} \ . \tag{E.3}$$

We find that with these modifications a smoothing length of $\sigma_{\mathrm{smth}} = 9\,\mathrm{pc}$, slightly above the value used by O'Neill et al. (2024) yields robust results. However, we find that unless one uses the smoothed density profile for integrals – which like O'Neill et al. (2024), we do not – the differences due to the mass-conserving Gaussian kernel are only minor.

E.1.2 The role of the boundary treatment

The choice of the boundary conditions can qualitatively affect the results, by introducing spurious peaks or erasing physical peaks near the boundary.

While O'Neill et al. (2024) do not explicitly mention how they treat boundaries, the shape of the profiles displayed in their Fig. 1, suggests that they might have used SCIPY's "gaussian_filter" function, which by default uses reflective boundaries.

The simplest way to deal with the boundaries is not to deal with them at all. In particular, consider the smoothing matrix W and assume that it is properly normalized, i.e.

$$\sum_i w_i W_{ij} = w_j \ , \tag{E.4}$$

where w_i are some weights (e.g. volume, a constant, etc.), then weights of the points near the boundary are systematically boosted. This results in smoothed data that will systematically lie below (above) the original data values, if they exhibit a negative (positive) gradient near the boundary. On the other hand, if proper normalization is omitted, points near the boundaries lose weight and the smoothed profile is always systematically lower than the data.

A similar way to deal with boundaries are so-called reflective boundary conditions, where the values of the data as well as their positions are mirrored beyond the boundary, i.e. $x_{-i} = x_0 - (x_i - x_0)$ and $y_{-i} = y_i$. This method increases the weight of points near the boundary, but in a more controlled way.

Another common method is to set the data outside of the boundary region to a constant value, e.g. the value of the data at the boundary. This leads to a slight over- (under-) estimation near the boundary, in the case of a positive (negative) slope in the original data.

Finally, linear extrapolation of the data beyond the boundary promises to capture steep gradients near the boundaries well. In particular, here we consider a linear extrapolation centered around the boundary point, i.e.

$$y_{-i} = y_0 + \frac{y_i - y_0}{x_i - x_0} \left(x_{-i} - x_0\right) \ . \tag{E.5}$$

Since all of these methods are linear, they can be directly incorporated into the smoothing kernel matrix W, which can be precomputed.

In Fig. E.1 we show how these various methods compare for two directions, exhibiting some of the features where differences between the methods are likely to arise, i.e. a peak near the boundary, and a steep negative gradient.

In the case of the peak near the boundary it is critical, that the smoother does not remove the peak. However, we find that this is the case for reflective boundary conditions. In the other cases with extrapolation, a shallow peak remains, indicating that in certain cases the peak might still disappear. Only in the case without extrapolation, we recover a strong peak.

On the other hand, in the case of a steep negative gradient, it is important that no spurious peaks emerge, a condition that is not satisfied for the smoother without extrapolation alone.

In summary, reflective boundary conditions as well as no extrapolation are not well suited for the task at hand, while linear extrapolation and constant boundaries appear to capture the most important features. Due to the slightly better performance at capturing peaks near the boundary, we opt for linear extrapolation.

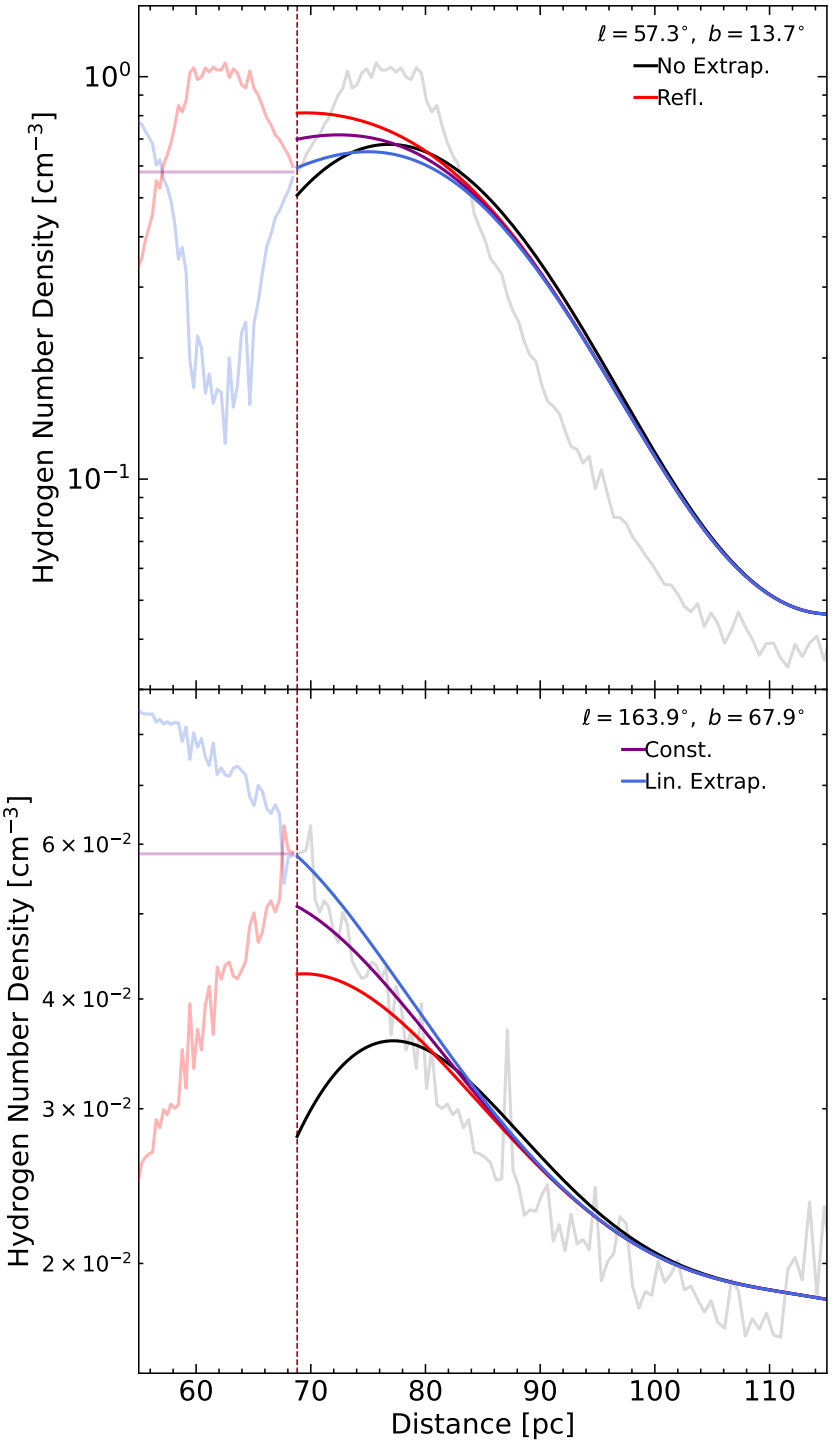

Figure E.1: Smoothed density profiles using different boundary treatments for two characteristic lines-of-sight. The boundary is indicated by the dashed vertical line. The original data is shown as a gray line, and the extrapolations beyond the boundary are shown at decreased opacity. The top panel shows a line-of-sight with a peak near the inner boundary, while the bottom panel shows a line of sight with a steep decline near the boundary. With reflective boundary conditions, the peak is missed entirely, while simple normalization adds a spurious peak even in the case of the steep decline.

Table E.1: Comparison of LB properties derived using different methods.

Property	This work	Repr.	O'Neill+ (2024)	Unit
Inner Edge	151^{+177}_{-71}	151^{+179}_{-69}	150^{+172}_{-70}	pc
Peak Distance	172^{+191}_{-80}	169^{+192}_{-77}	170^{+192}_{-79}	pc
Outer Edge	194^{+206}_{-89}	190^{+201}_{-89}	191^{+204}_{-90}	pc
Shell Thickness	38^{+87}_{-24}	34^{+80}_{-22}	35^{+88}_{-22}	pc
Shell Mass	6.5	5.8	6.0 ± 0.7	$10^5\,M_\odot$

E.1.3 Comparison to previous work

In order to ensure that our results are robust, we try to reproduce the shell properties reported by O'Neill et al. (2024) using the method described in their paper as well as the method described in Sec. 7.1, both applied to the sample mean 3D dust map.

In particular, we sample the dust map between 69 and 1244 pc at uniform 1 pc intervals and smooth it with a Gaussian kernel with a smoothing length of $\sigma_{\mathrm{smth}} = 7\,\mathrm{pc}$ with reflective boundary conditions.

Peak finding and the location of the inner and outer peak boundaries are done identically between the two methods.

In Tab. E.1 we compare the thus obtained results. For the distances to the peak (boundaries) and the width of the shell we show the median, including $\pm 2\sigma$ uncertainties, corresponding to the 2.28^{th} and 97.72^{th} percentiles, while for the shell mass, i.e. the mass between the inner and outer edge of the shell, we simply show the value obtained from the analysis of the sample mean 3D dust map.

While we could not reproduce the results of O'Neill et al. (2024) exactly, our results are reasonably close and small differences are likely due to minor details omitted in their description of their analysis.

E.1.4 Momentum estimate

In order to assess the accuracy of the momentum estimate in Eq. 7.1, we compute such geometrical momentum estimates for the SISSI sample of simulated SNRs at different points in time and compare them to the true momentum obtained from the velocity field. The result of this comparison is shown in Fig. E.2, which shows that the geometrical momentum estimate is slightly biased towards greater values, by a factor of ~ 2.

E.1.5 Number of SN explosions

We assess the accuracy of the SN count estimate in Eq. 5.14, using our sample of simulated SBs, by comparing the thus estimated SN count with the actual number of injected SNe.

The result of the comparison is shown in Fig. E.3 which shows that for moderate densities comparable to that of the LB, the estimate is fairly accurate, while for higher and lower densities it increasingly overestimates the number of SNe as time passes.

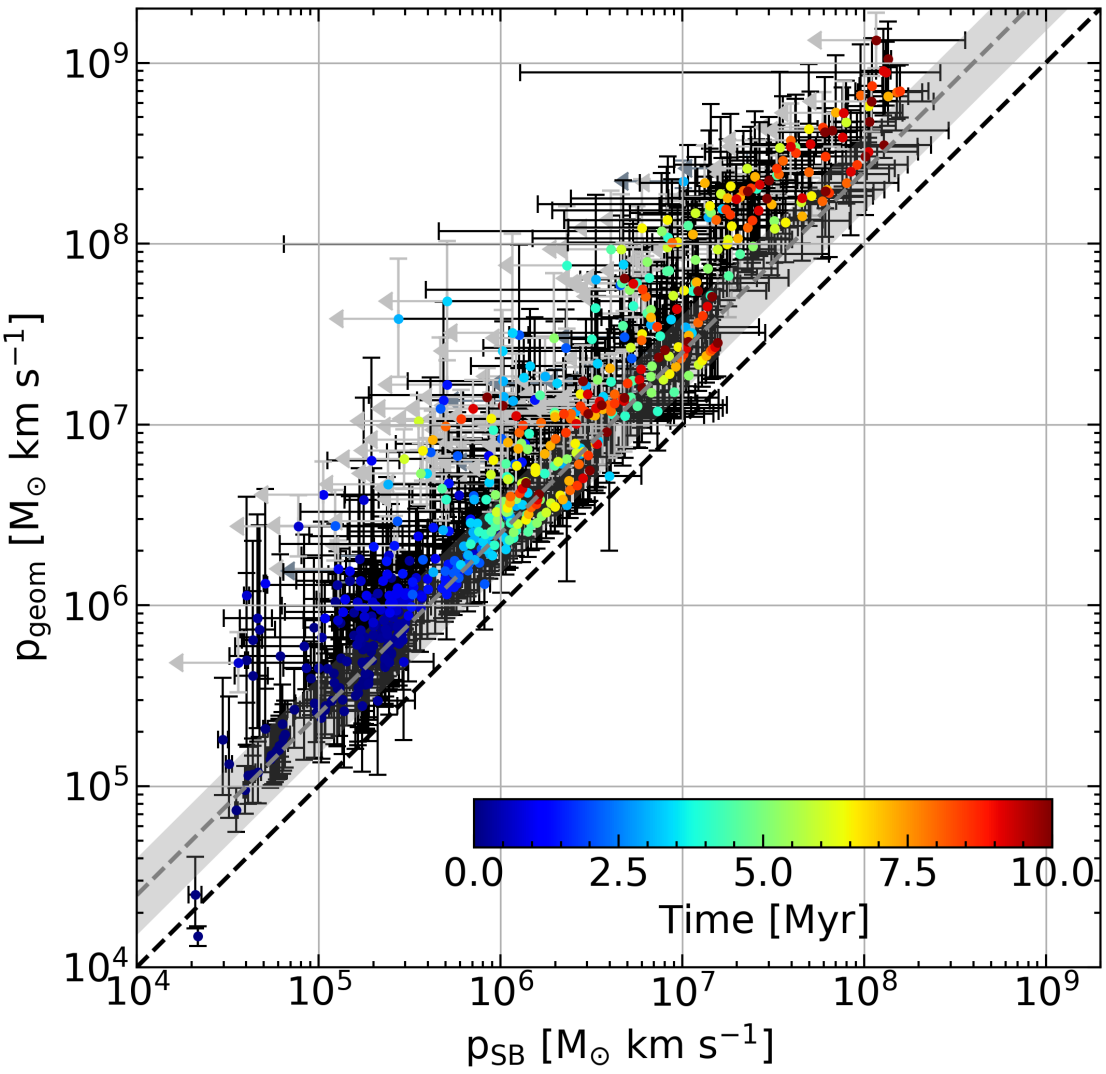

Figure E.2: Comparison of the geometric momentum estimate Eq. 7.1 to the true momentum for the simulated sample of SBs from the SISSI simulation at different points in time, as indicated by the color scheme. Error bars correspond to uncertainties due to different ways of defining the center (geometric center vs. center of mass) of the SBs and their volume (threshold value for passive-scalar tracer-variable). Points with gray arrows exhibit negative radial momenta (net-inflows) for some of the definitions. The geometrical momentum estimate is slightly biased towards larger values, by a factor of ~ 2.

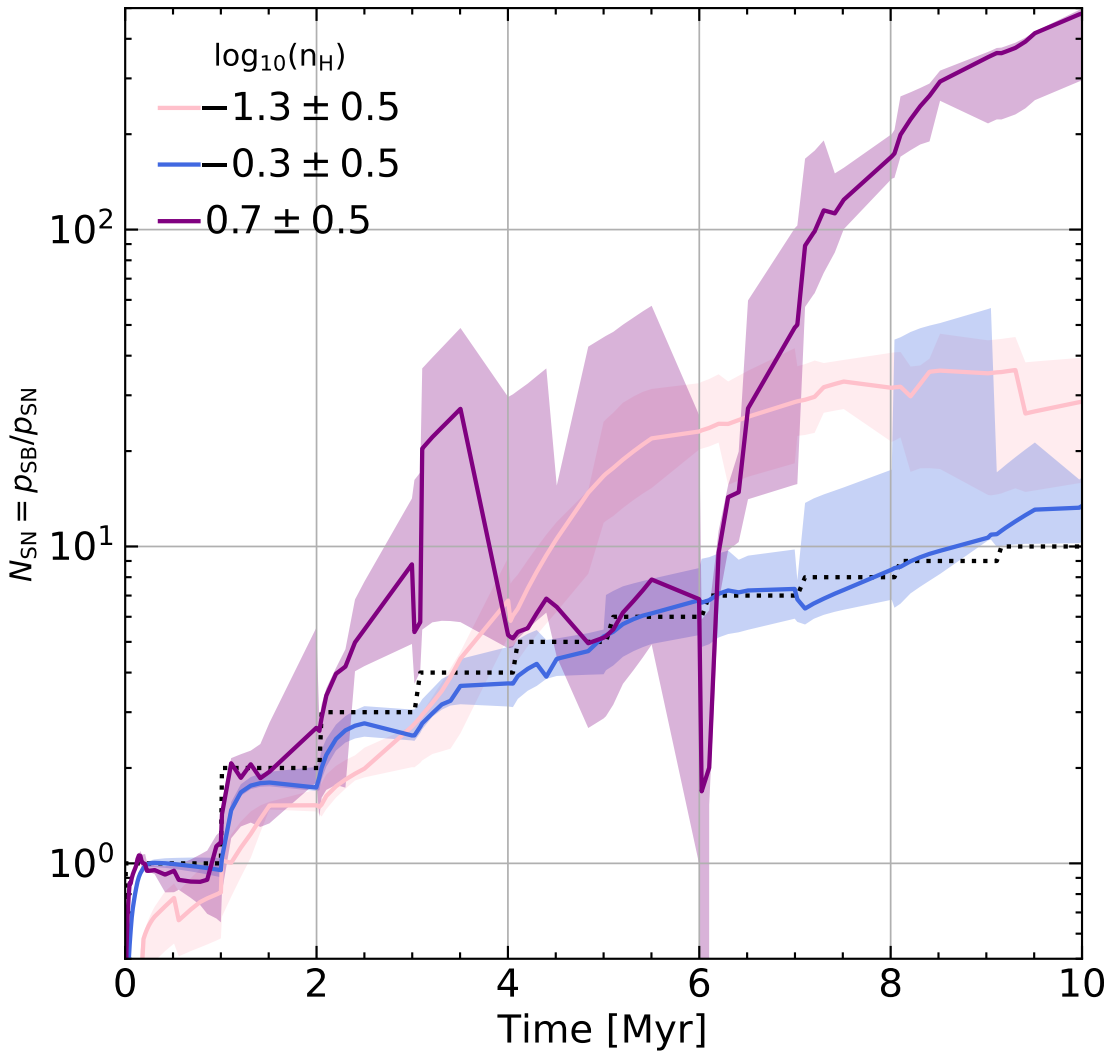

Figure E.3: Time-evolution of the SN count estimate Eq. 5.14 for the simulated sample of SBs in different density ranges. The true SN count is shown as a black dashed line. At extremely high and low ambient densities the estimate appears to overestimate the number of SNe, while for moderate densities, around the density of the LB, the estimate is quite accurate, within about $\lesssim 50\%$.

We argue that this overestimate might be driven by mergers of the simulated, controlled SBs with preexisting SBs in their environment, for which we have no handle to accurately count the number of SNe that they would contribute. At low densities, SBs grow much larger and are thus more likely to merge with other large SBs, while at high densities, the star-formation rate is elevated, leading to a more active environment, with a high density of SNRs.

E.1.6 Shape Tensor

Romano et al. (2025a) define the shape tensor as

$$S_{ij} = V_{\mathrm{SNR}}^{-1} \int_{\mathrm{SNR}} \left(\|\mathbf{x}\|^2 \, \delta_{ij} - x_i x_j \right) \mathrm{d}^3\mathbf{x} \ . \tag{E.6}$$

By assuming an approximately ellipsoidal shape, the three ellipsoidal radii, are defined by

$$r_i = \sqrt{2.5 \left(\mathrm{tr}\,(S) - 2S_i \right)} \ , \tag{E.7}$$

where S_i are the eigenvalues of S_{ij} and $\mathrm{tr}\,(S)$ is the trace. The smallest, intermediate and largest eigenvalues correspond the minor a, semi-major b and major c axis, respectively. The effective size of an SNR is the geometric mean of the three eigenvalues

$$r_{\mathrm{eff}} = (abc)^{1/3} \ . \tag{E.8}$$

To determine the alignment of the LB within the Galaxy, we measure the pitch angle α and polar direction $\cos(\theta)$ for both the major and minor axes. The pitch angle is defined relative to the direction of Galactic rotation, with $\alpha = 90°$ and $\alpha = -90°$ corresponding to the Galactic center and anti-center, respectively. The magnitude of the polar direction is 0 (1) for directions parallel (perpendicular) to the Galactic plane.

E.2 Models for radiative blastwaves in uniform media

We distinguish between blastwave models driven by a single explosion at $t = 0$ and blastwaves that are driven by continuous energy- and momentum-injection.

The dynamics of a radiative blastwave driven by a single explosion are determined the conservation of the radial momentum that was acquired before the onset of radiative cooling. This phase is also known as the *momentum-conserving snowplow* phase (e.g. Oku et al., 2022). The shock radius of the momentum-conserving snowplow as a function of expansion time t is given by (e.g. Oku et al., 2022)

$$R_{\mathrm{MCS}} = \left(\frac{3 N_{\mathrm{SN}} \, \hat{p}_{\mathrm{SN}} \, t}{\pi \, \rho_{\mathrm{ISM}}} \right)^{1/4} \ , \tag{E.9}$$

where N_{SN} is the number of SNe exploding at $t = 0$, $\hat{p}_{\mathrm{SN}}$ is the momentum injected per SN, given by Eq. 7.2 and ρ_{ISM} is the ambient density.

The dynamics of continuously driven blastwaves are more uncertain and seem to depend on the detailed balance of cooling and energy injection (El-Badry et al., 2019; Oku et al., 2022; Lancaster et al., 2024). If the cooling is relatively gentle and a large fraction of the injected energy can reach the radiative shell, the dynamics of the blastwave match those of an *energy-driven wind* with a scaled down energy injection rate (El-Badry et al., 2019), i.e.

$$R_{\mathrm{EDW}} = \xi_{\mathrm{EDW}} \left(\frac{(1-\theta) \ E_{\mathrm{SN}} \, t^3}{\Delta t_{\mathrm{SN}} \, \rho_{\mathrm{ISM}}} \right)^{1/5} \ , \tag{E.10}$$

where $\xi_W \sim 0.88$ is determined by considering the internal structure of the blastwave, $E_{\rm SN} = 10^{51}\,{\rm erg}$ is the total injected per SN, $(1-\theta) \sim 0.3$ (Zucker et al., 2022) is a reduction factor, accounting for the effect of radiative cooling and $\Delta t_{\rm SN}$ is the average time between SN explosions. On the other hand, if cooling is sufficiently rapid each SN contributes the same momentum $\hat{p}_{\rm SN}$ and the dynamics are determined by the conservation of the momentum, which is imparted onto the radiative shell at a constant rate (Oku et al., 2022; Lancaster et al., 2024)

$$R_{\rm MDW} = \left(\frac{3 \hat{p}_{\rm SN}\, t^2}{2\pi\, \Delta t_{\rm SN}\, \rho_{\rm ISM}} \right)^{1/4} , \tag{E.11}$$

which may be compared to Eq. E.9 upon substituting $N_{\rm SN}(t) = t \,/\, \Delta t_{\rm SN}$. This model is often referred to as *momentum-driven* or *rapidly-cooling wind* (Lancaster et al., 2024).

E.3 Passage of the solar system

Fossil records of sedimentary ^{60}Fe and ^{244}Pu on earth suggest an enrichment with SN ejecta over the past 4 Myr (Wallner et al., 2021). If this enrichment was due to the SNe powering the LB, the solar system must have entered the LB shortly before the enrichment started (Breitschwerdt et al., 2016; Ertel et al., 2023). Making use of this insight, Zucker et al. (2022) estimate that the solar system has entered the LB $\sim 5\,$Myr ago.

For a given expansion model for the LB's shell, we estimate when the solar system entered the LB, by comparing the trace-back distance of the solar system from the center of the LB to the radius of the expanding shell. We adopt the same magnitude of $v_\odot \sim 20\,{\rm km\ s^{-1}}$ for the speed of the solar system as Zucker et al. (2022) and assume that it moves radially, with a present-day distance from the center of $d_\odot(t_{\rm age}) = 0$.

Under these assumptions, the distance of the solar system from the center of the LB is

$$d_\odot \sim v_\odot\,(t_{\rm age} - t)\ . \tag{E.12}$$

In Fig. E.4 we show the passage of the solar system through the LB's shell. For values of $t_{\rm age} \gtrsim 4\,$Myr, the solar system would have crossed the LB's shell during the first $\lesssim 1\,$Myr of its expansion. Incorporation of sediments into earth's crust over the past $\sim 4\,$Myr could have commenced shortly after the passage (Ertel et al., 2023; Ertel & Fields, 2024) and is therefore in agreement with the value $t_{\rm age} \gtrsim 4\,$Myr obtained above.

E.4 Recent star formation and SNe in the solar neighborhood

Swiggum et al. (2024) have used the star cluster catalogue of (Hunt & Reffert, 2023) to group the clusters in the solar neighborhood into three distinct families of star clusters that likely share a common origin. One of these cluster families, named αPer, after its prominent member Alpha Persei can be both spatially and temporally associated with the LB.

Previous analyses of the origin of the LB usually focused on the role of Sco-Cen in driving its expansion (Maíz-Apellániz, 2001; Breitschwerdt et al., 2016; Zucker et al., 2022). While the findings of Swiggum et al. (2024) agree with these studies if only the SNe in Sco-Cen are considered, the potential contribution from other members of αPer remains unclear. Swiggum et al. (2024) report the SFH in αPer which suggests the existence of a peak in the star-formation activity

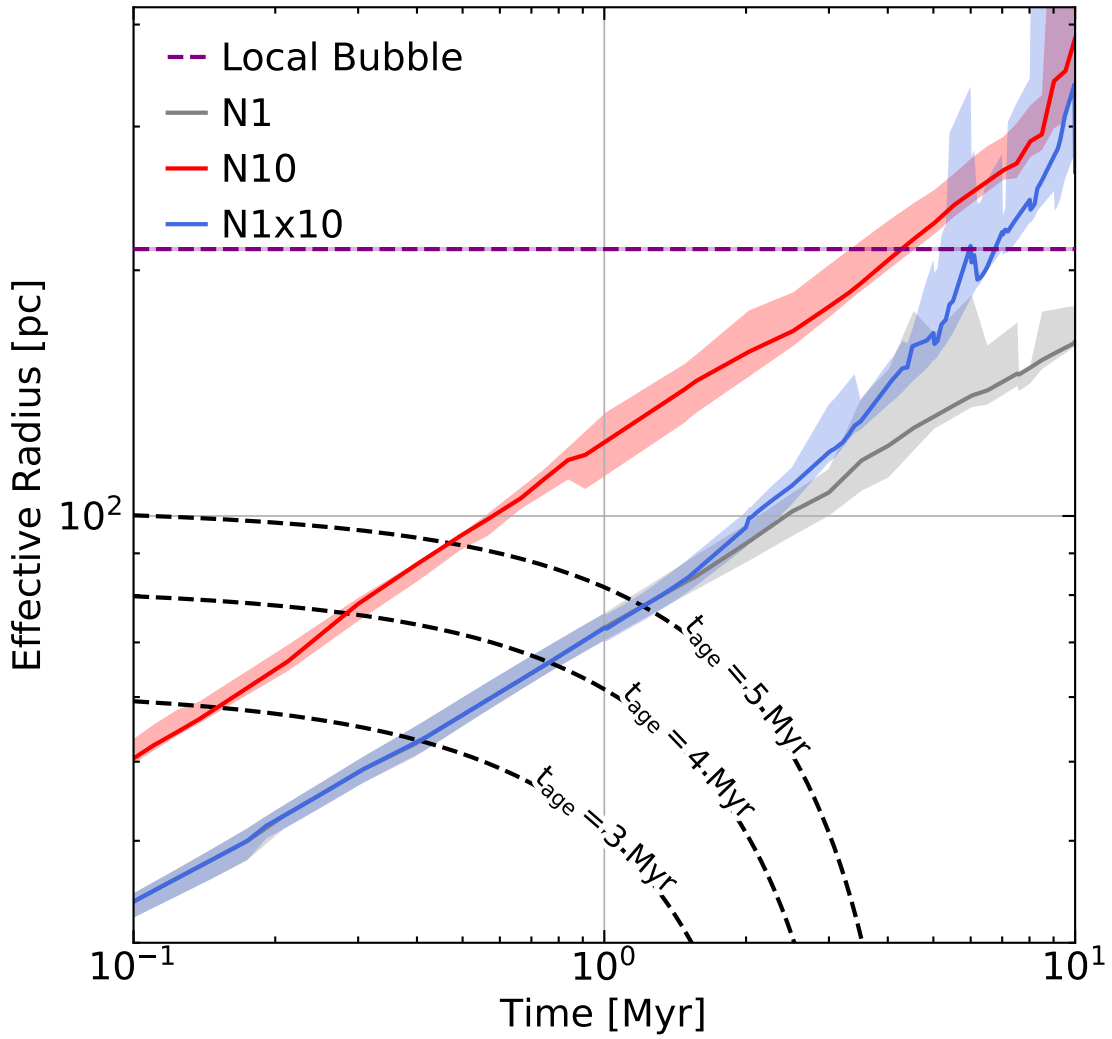

Figure E.4: Crossing of the expanding LB's shell and the solar system. Gray, red, blue and purple lines are the same as in Fig. 7.1. Black dashed lines correspond to the distance of the solar system from the center of the LB (Eq. E.12) for different ages of the LB. The solar system passes earlier through the LB's shell for more powerful explosions, but even for a single SN explosion it would have crossed the shell within the first ~ 1 Myr of its expansion.

associated with young clusters in Sco-Cen $\sim 10\,\mathrm{Myr}$ ago, which might be linked to a more recent burst in SN activity than previous studies considered. Unfortunately, the low time resolution of the reported SFH does not allow to draw any further conclusions.

In order to investigate the role of this recent increase in star-formation, we use the data products of Swiggum et al. (2024) to compute the recent SFH at higher temporal resolution and use it to estimate the SN-rate history for αPer. To this end, we use the 16%, 50% and 84% quantiles of the cluster ages, masses and the number of SNe that exploded since their formation for all clusters associated with αPer.

The SFH is the mass-weighted sum of the age distributions of each cluster, convolved with a window function $W(t;\Delta t)$:

$$\mathrm{SFH}(t) = \int_{-\infty}^{\infty} W(t - t_{\mathrm{age}};\Delta t) \sum_{i\in\mathrm{family}} m_i\,\mathcal{P}_i(t_{\mathrm{age}})\,\mathrm{d}t_{\mathrm{age}}\ . \tag{E.13}$$

Here m_i is the mass of each cluster, which we sample from its posterior distribution.

We can reproduce the SFH reported by Swiggum et al. (2024) if we use a top-hat filter with $\Delta t = 12.5\,\mathrm{Myr}$ as the window function, use the median cluster mass for m_i and use delta-peaks, peaked at the median age for the age distributions of the clusters. We note however, that this treatment does not necessarily capture the sizeable uncertainties in the cluster ages and masses, encoded in their 16% and 84% quantiles.

To account for the uncertainty in the age and simultaneously push the time resolution of the SFH to the limit, we reconstruct plausible age distributions from the available data and set $W = \delta(t - t_{\mathrm{age}})$, i.e. we take the SFH as the mass-weighted sum of the age distributions of the clusters. We account for the uncertainty in the mass by sampling from the posterior distribution, leaving us with a number of sample SFHs.

We estimate the SN-rate history, by assuming that the SN rate of each cluster remains at an approximately constant value between the onset of SN explosions t_{delay} after the clusters formation and the life-time t_{active} of the least massive stars undergoing type-II SN explosions (Leitherer et al., 1999; Kim et al., 2017) and is zero otherwise, i.e.

$$\mathcal{R}_{\mathrm{SN},\,i}(t) = \frac{N_{\mathrm{SN},\,i}}{\min(t_{\mathrm{age},\,i}, t_{\mathrm{active}}) - t_{\mathrm{delay}}}\,\mathbf{1}_{(t_{\mathrm{delay}},\,t_{\mathrm{active}})}(t_{\mathrm{age},\,i} - t)\ , \tag{E.14}$$

where $\mathbf{1}_X(x)$ is the indicator function, which evaluates to unity if $x \in X$ and zero otherwise and $N_{\mathrm{SN},\,i}$ is the number of SNe that exploded since the formation of the cluster. We sample both $N_{\mathrm{SN},\,i}$ and $t_{\mathrm{age},\,i}$ from their respective posterior distributions.

E.4.1 Probability Distributions

Given only a number of quantiles $x_0 \le ... \le x_i \le ... \le x_n$ corresponding to percentiles $0 = p_0 < ... < p_i < ... < p_n = 1$ and a prior probability density function (pdf) $q(x)$, the most plausible posterior pdf is a locally reweighted version of the prior, where the weights are chosen such that the cumulative probabilities match those of the quantile constraints, i.e. (Jaynes, 1957)

$$\mathcal{P}\left(x\,\middle|\,q, (x_i)_{i=0,\ldots,n}, (p_i)_{i=0,\ldots,n}\right) = q(x)\sum_{i=1}^{n} w_i\,\mathbf{1}_{(x_{i-1},\,x_i)}(x)\ , \tag{E.15}$$

where the weights

$$w_i = \frac{p_i - p_{i-1}}{\mathbb{P}(x_{i-1} < x < x_i|q)}\ . \tag{E.16}$$

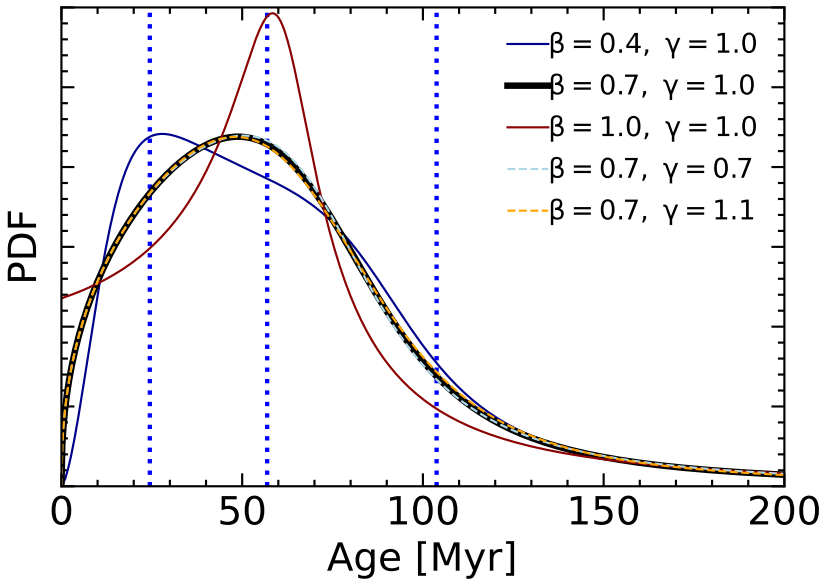

Figure E.5: Reconstructed posterior age-pdf for the cluster ADS_16795 for various values of β and γ. Dotted, blue lines correspond to the 16%, 50% and 84% quantiles. For smaller values of β the mode of the distribution is closest to the 16% quantile, while for $\beta \sim 1$ it is closer to the median. For $\beta \geq 1$ the pdf approaches a constant non-zero value for $x \to 0$. While the choice of γ has little influence on the shape of the pdf, for $\gamma \gtrsim 1.1$ the pdf is not longer positive-definite. The pdf corresponding to our fiducial choice of parameters is depicted as a solid, black line.

With most smooth priors, the posterior distribution will exhibit large jumps, a feature that might be undesirable for our reconstruction of the SFH.

Generating smooth pdfs from quantile constraints is a common data-science application to which a number of creative approaches exist. One particularly simple and flexible method that makes inverse-sampling trivial are so-called *quantile-parametrized distributions* (Keelin & Powley, 2011).

The method uses a parameterization of the the quantile function that is linear in the quantile data constraints, using a number of arbitrary basis functions. The corresponding pdf can then be simply derived using the inverse function rule of calculus, since the quantile function is the inverse of the cumulative distribution function. However, care needs to be taken to ensure that the resulting pdf is positive definite.

We adopt this method to reconstruct the mass- and age posterior-pdfs using the following parameterization

$$x\left(p\right) = \frac{p^{\beta}}{\left(1-p\right)^{\gamma}} \left(a_1 + a_2\, p + a_3 \sin\left(\pi\, p\right)\right) \ , \tag{E.17}$$

where $\beta > 0$, $\gamma > 0$, $p \in [0, 1]$ is the cumulative probability, and a_i are the parameters determined by the quantile constraints $x\left(p_i\right) = x_i$. For $\beta < 1$, the pdf tends towards zero for $y \to 0$, while for $\beta > 1$ it tends toward a constant value > 0. We adopt $\gamma = 1$ and $\beta = 0.7$ for which we confirm that all pdfs are positive definite. In Fig. E.5 we show how the pdf depends on the values of β and γ for one of the clusters in αPer.

Since the number of SNe is limited to positive integers we do not need to worry about smoothness. However, there are other complications. The data provided by Swiggum et al. (2024) correspond to the quantiles of the marginal distribution. Yet, it is clear that the number of SNe has to correlated

with the age of the cluster, at the very least, because it can only be non-zero for clusters older than $t_{\rm delay}$.

To account for this correlation, we set the probability of $N_{\rm SN} > 0$ SNe to zero for $t_{\rm age} < t_{\rm delay}$, but otherwise keep the pdf for $N_{\rm SN} > 0$ unchanged with respect to the marginal distribution. The marginal and joint probabilities of $N_{\rm SN} = 0$ SNe are then linked by the condition

$$\mathcal{P}\left(N_{\rm SN}=0\right) = p_0 + \left(1-p_0\right)\,\mathcal{P}\left(N_{\rm SN}=0\,|t_{\rm age} > t_{\rm delay}\right)\ , \tag{E.18}$$

where $p_0 = \mathbb{P}\left(t_{\rm age} < t_{\rm delay}\right)$.

To define a sensible marginal pdf for the number of SNe, we assume a constant prior for $N_{\rm SN} < N_{\rm SN,\,84\%}$, an exponential tail for $N_{\rm SN} > N_{\rm SN,\,84\%}$ and we set

$$\mathcal{P}\left(N_{\rm SN}=0\right) = \max\left(p_0, \max_{\{i\,|\,Q_i=0\}} p_i, \min_{\{i\,|\,Q_i>0\}} \frac{p_i - p_{i-1}}{1+Q_i}\right)\ , \tag{E.19}$$

where Q_i are the quantiles of the marginal distribution. The joint pdf of $t_{\rm age}$ and $\rm N_{SN}$ is then fully specified by applying Eqs. E.15 and E.18.

E.4.2 SFH and SN-rate in αPer

For each cluster in αPer we draw a million samples of the cluster mass, age and number of SNe from their respective pdfs and use them to derive a million realizations of the SFH (Eq. E.13) and the SN-rates (Eq. E.14). For each realization, we sum up the SN-rates of the clusters to obtain the SN-rate history of αPer. We also derive the average time between SNe, by taking the reciprocal.

In Fig. E.6 we show the 16%, 50% and 84% quantile histories, obtained by drawing computing the quantiles at each point in time. We mark the onset of the expansion of the LB according to our model and that of Zucker et al. (2022) as well as the SN rates, required by the respective models.

We find that there is a broad peak in the SFH $\sim 4-10\,$Myr ago, which according to Swiggum et al. (2024) is associated with the formation of Upper Scorpius, Corona Australis, ρ Ophiuchus, which are all part of Sco-Cen, and various other clusters in Taurus. The SFH in the region coincident with the LB is quite low $\lesssim 100\,\mathrm{M_\odot\,Myr^{-1}}$ before the onset of the peak $\sim 10\,$Myr. Moreover, the range of ages for the LB found by our analysis above, coincides with the downturn in the peak of star-formation activity, which is consistent with a scenario where the birth of the LB, powered by the delayed feedback from first stars formed in the peak, is quenching any further star-formation in the region, which would be in stark contrast to the positive-feedback scenario proposed by Zucker et al. (2022).

This can be compared with the SN rate, which has been steadily increasing from $\sim 1\,$SN / Myr 20 Myr ago to $\lesssim 10\,$SNe / Myr at the present day. These values grow increasingly larger than the value of $\Delta t_{\rm SN}^{-1} \sim 1\,\mathrm{Myr^{-1}}$ required by the model of Zucker et al. (2022), while they are well within the range of values required by our analysis above.

To verify, whether this SN activity is actually spatially associated with the LB, in Fig. E.7 we show the trajectories of the clusters in αPer in the vicinity of the LB, colored by their instantaneous SN Rate, over the past 5, $5-10$, $10-15$, and $15-20$ Myr. Trajectories are calculated using the galactic dynamics package GALPY (Bovy, 2015), following the parameter choices outlined in Swiggum et al. (2024). We find that the majority of the clusters has been co-spatial with the current extent of the LB over the past few Myr, with just over 10 of the 66 cluster members being too distant to have contributed.

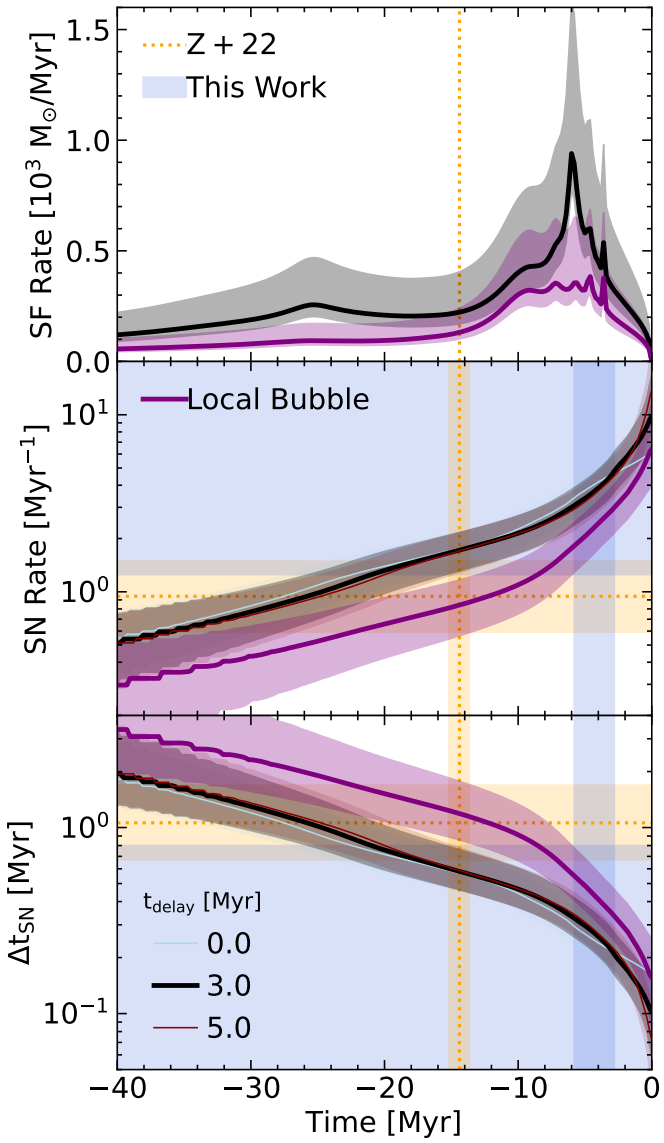

Figure E.6: Top panel: Star-formation History of αPer over the past 40 Myr. The SFR is peaked around 8 Myr ago. The peak is associated with recent star formation in Sco-Cen Swiggum et al. (2024). However, the dominant peak corresponds to the formation of the $\sim 1000\,M_\odot$ cluster Theia 38, at a distance of $\sim 500\,$pc from the solar system. Middle and bottom panel: SN rate and average time between SNe in αPer over the past 40 Myr for different values of $t_{\rm delay}$. The SN rate continuously grows (the time between SNe shortens) as the stellar mass of the αPer is built up, with a sharp increase in SN activity in the last few Myr, associated with the peak in the SFR, 8 Myr ago. The steepness of the increase slightly depends on the choice of $t_{\rm delay}$, with a more gradual increase for $t_{\rm delay} = 0$ and a steeper increase for $0 < t_{\rm delay} < 8\,$Myr. The SFH, SN Rate and average time between SNe of the clusters spatially associated with the LB are shown in purple, where we assume a fiducial value of $t_{\rm delay} = 3\,$Myr. Also shown as shaded regions are the age of the LB as well as the average time between SNe found by Zucker et al. (2022) (orange) and this work (blue).

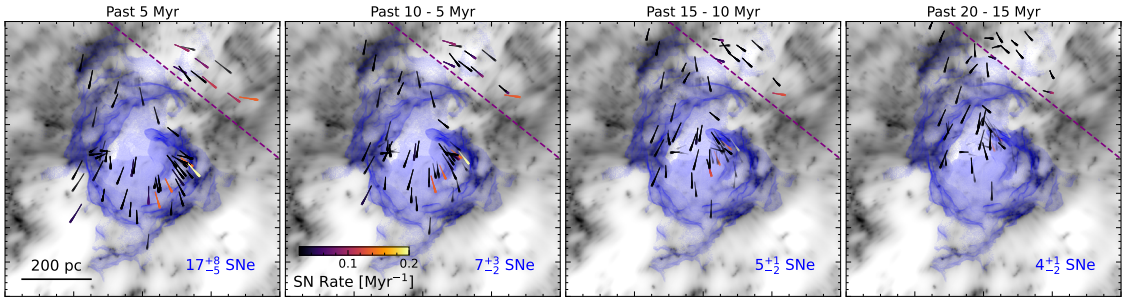

Figure E.7: Trajectories of the member clusters of αPer in the local standard of rest, within the vicinity of the LB, from left to right, over the past 5, $5-10$, $10-15$ and $15-20$ Myr. Trajectories are plotted as lines of increasing width, where increasingly wider lines correspond to later times. Trajectories are colored based on the clusters' instantaneous SN Rate and the opacity is set to the instantaneous probability that the cluster is between $t_{\rm delay}$ and $t_{\rm active}$ after its formation, i.e. is potentially contributing SNe at a given time. While it is unlikely that a particular cluster colored black has contributed a SN, due to the large stochasticity in low mass clusters, the numerous black clusters might still collectively contribute a significant number of SNe. The projected gas density as well as a projection of the LB's shell at the present time are also shown to provide context. We also show the number of SNe contributed within each time frame by the clusters, that are co-spatial with the current extent of the LB, using the purple dashed line to decide whether a cluster belongs to the LB or not. With the exception of about 10 clusters in the top right (a few outside the frame) the majority of the clusters has been co-spatial with the current extent of the LB (in projection) for the past few Myr and therefore could have contributed SNe. The number of SNe contributed by nearby clusters in the past 5 Myr is consistent with our estimate in Tab. 7.2.

In order to separate out the contributions from these distant clusters, we perform a simple spatial cut, indicated by the purple-dashed line in Fig. E.7. The SN Rate of the remaining clusters is shown as a purple line in Fig. E.6, which shows that the SN Rate of the clusters co-spatial with the LB is still consistent with our findings, highlighted in Tab. 7.2.

In Fig. E.7 we also show the number of SNe contributed by the clusters associated with the LB during each time frame. Even though there were on average 9 SNe in the time window from 10-20 Myr ago, the fact that most of the contributing clusters have low SN rates suggests, that these SNe merged with the ISM in isolation before they could have combined to form a coherent SB. On the other hand, the more frequent SNe in the past 10 Myr might be more clustered, especially towards the Sco-Cen region, where 4-5 exceptionally active clusters reside. These clustered SNe likely overlapped, forming the coherent LB that suppressed further star formation in the local ISM and reached a large enough size to be coherently powered by most subsequent SNe in the solar neighborhood.

Bibliography

Alsulami, R., Einecke, S., Rowell, G., et al. 2024, PASA, 41, e098

Anderson, M. C. & Rudnick, L. 1995, ApJ, 441, 307

Araya, M. 2024, A&A, 691, A225

Arenou, F., Grenon, M., & Gomez, A. 1992, A&A, 258, 104

Arias, M., Vink, J., de Gasperin, F., et al. 2018, A&A, 612, A110

Arias, M., Zhou, P., Chiotellis, A., et al. 2024, A&A, 684, A178

Armillotta, L., Ostriker, E. C., Kim, C.-G., & Jiang, Y.-F. 2024, ApJ, 964, 99

Bakış, H., Aktekin, E., Bakış, V., Sano, H., & Sezer, A. 2025, MNRAS, 537, 2412

Bamba, A., Agarwal, M., Vink, J., et al. 2025, PASJ

Barcos-Muñoz, L., Aalto, S., Thompson, T. A., et al. 2018, ApJ, 853, L28

Behrendt, M. 2023a, Mera

Behrendt, M. 2023b, Mera

Behrendt, M., Burkert, A., & Schartmann, M. 2015, MNRAS, 448, 1007

Bezanson, J., Edelman, A., Karpinski, S., & Shah, V. B. 2017, SIAM Review, 59, 65

Bialy, S., Zucker, C., Goodman, A., et al. 2021, ApJ, 919, L5

Bianchi, S. & Schneider, R. 2007, MNRAS, 378, 973

Bieri, R., Naab, T., Geen, S., et al. 2023, MNRAS, 523, 6336

Birnstiel, T. 2024, ARA&A, 62, 157

Bisnovatyi-Kogan, G. S. & Silich, S. A. 1995, Reviews of Modern Physics, 67, 661

Bland-Hawthorn, J. & Gerhard, O. 2016, ARA&A, 54, 529

Blondin, J. M., Wright, E. B., Borkowski, K. J., & Reynolds, S. P. 1998, ApJ, 500, 342

Blondin, S. 2024, arXiv e-prints, arXiv:2411.09740

Bolatto, A. D., Levy, R. C., Tarantino, E., et al. 2024, ApJ, 967, 63

Bolatto, A. D., Warren, S. R., Leroy, A. K., et al. 2013, Nature, 499, 450

Bovy, J. 2015, ApJS, 216, 29

Bradshaw, E. J., Almaini, O., Hartley, W. G., et al. 2013, MNRAS, 433, 194

Breitschwerdt, D. & de Avillez, M. A. 2006, A&A, 452, L1

Breitschwerdt, D., Feige, J., Schulreich, M. M., et al. 2016, Nature, 532, 73

Breitschwerdt, D., Freyberg, M. J., & Egger, R. 2000, A&A, 361, 303

Burkert, A. & Lin, D. N. C. 2000, ApJ, 537, 270

Butsky, I. S. & Quinn, T. R. 2018, ApJ, 868, 108

Caldwell, N., Raymond, J. C., Long, K. S., & Lee, M. G. 2025, ApJ, 983, 150

Carr, C., Bryan, G. L., Fielding, D. B., Pandya, V., & Somerville, R. S. 2023, ApJ, 949, 21

Cazzoli, S., Arribas, S., Maiolino, R., & Colina, L. 2016, A&A, 590, A125

Chabrier, G. 2003, PASP, 115, 763

Chan, T. K., Kereš, D., Gurvich, A. B., et al. 2022, MNRAS, 517, 597

Chan, T. K., Kereš, D., Hopkins, P. F., et al. 2019, MNRAS, 488, 3716

Chevalier, R. A. 1974, ApJ, 188, 501

Chevalier, R. A. & Clegg, A. W. 1985, Nature, 317, 44

Chevance, M., Kruijssen, J. M. D., Hygate, A. P. S., et al. 2020, MNRAS, 493, 2872

Chi, Y.-H., Huang, J., Zhou, P., et al. 2024, ApJ, 975, L28

Cicone, C., Maiolino, R., & Marconi, A. 2016, A&A, 588, A41

Cioffi, D. F., McKee, C. F., & Bertschinger, E. 1988, ApJ, 334, 252

Cox, D. P. 2005, ARA&A, 43, 337

Cox, D. P. & Anderson, P. R. 1982, ApJ, 253, 268

Cox, D. P. & Reynolds, R. J. 1987, ARA&A, 25, 303

Cox, D. P. & Smith, B. W. 1974, ApJ, 189, L105

Cristofari, P., Blasi, P., & Amato, E. 2020, Astroparticle Physics, 123, 102492

Cristofari, P., Blasi, P., & Caprioli, D. 2021, A&A, 650, A62

Cristofari, P., Tatischeff, V., & Chabot, M. 2025, A&A, 693, A145

de Avillez, M. A. & Breitschwerdt, D. 2004, A&A, 425, 899

de Avillez, M. A. & Breitschwerdt, D. 2005, A&A, 436, 585

de Avillez, M. A. & Mac Low, M.-M. 2002, ApJ, 581, 1047

De Looze, I., Milisavljevic, D., Temim, T., et al. 2024, ApJ, 976, L4

Dekel, A., Sarkar, K. C., Birnboim, Y., Mandelker, N., & Li, Z. 2023, MNRAS, 523, 3201

Deng, Y., Zhang, Z.-Y., Zhou, P., et al. 2023, MNRAS, 518, 2320

Devine, D. & Bally, J. 1999, ApJ, 510, 197

Diesing, R., Guo, M., Kim, C.-G., Stone, J., & Caprioli, D. 2024, ApJ, 974, 201

Diesing, R. & Gupta, S. 2025, ApJ, 980, 167

Do, T., Kerzendorf, W., Winsor, N., et al. 2015, ApJ, 809, 143

Dobbs, C. L., Bending, T. J. R., Pettitt, A. R., & Bate, M. R. 2022, MNRAS, 509, 954

Draine, B. T. 2011, Physics of the Interstellar and Intergalactic Medium (Princeton University Press)

Duffell, P. C., Polin, A., & Mandal, S. 2024, arXiv e-prints, arXiv:2403.13641

Dwarkadas, V. V., Dauphas, N., Meyer, B., Boyajian, P., & Bojazi, M. 2017, ApJ, 851, 147

Edenhofer, G., Zucker, C., Frank, P., et al. 2024, A&A, 685, A82

El-Badry, K., Ostriker, E. C., Kim, C.-G., Quataert, E., & Weisz, D. R. 2019, MNRAS, 490, 1961

Ellison, D. C., Drury, L. O., & Meyer, J.-P. 1997, ApJ, 487, 197

Elmegreen, B. G. 1998, in Astronomical Society of the Pacific Conference Series, Vol. 148, Origins, ed. C. E. Woodward, J. M. Shull, & J. Thronson, Harley A., 150

Elmegreen, B. G. 2011, in EAS Publications Series, Vol. 51, EAS Publications Series, ed. C. Charbonnel & T. Montmerle, 45–58

Elmegreen, B. G. & Lada, C. J. 1977, ApJ, 214, 725

Epstein, R. I. 1980, MNRAS, 193, 723

Ercolano, B. & Clarke, C. J. 2010, MNRAS, 402, 2735

Ertel, A. F. & Fields, B. D. 2024, ApJ, 972, 179

Ertel, A. F., Fry, B. J., Fields, B. D., & Ellis, J. 2023, ApJ, 947, 58

Farias, J. P., Offner, S. S. R., Grudić, M. Y., Guszejnov, D., & Rosen, A. L. 2024, MNRAS, 527, 6732

Faucher-Giguère, C.-A., Quataert, E., & Hopkins, P. F. 2013, MNRAS, 433, 1970

Federrath, C. 2013, MNRAS, 436, 1245

Ferrara, A., Scannapieco, E., & Bergeron, J. 2005, ApJ, 634, L37

Fesen, R. A., Milisavljevic, D., Patnaude, D., et al. 2025, ApJS, 278, 17

Fesen, R. A., Schaefer, B. E., & Patchick, D. 2023, ApJ, 945, L4

Fichtner, Y. A., Mackey, J., Grassitelli, L., Romano-Díaz, E., & Porciani, C. 2024, A&A, 690, A72

Fielding, D., Quataert, E., & Martizzi, D. 2018, MNRAS, 481, 3325

Fielding, D., Quataert, E., Martizzi, D., & Faucher-Giguère, C.-A. 2017, MNRAS, 470, L39

Fielding, D. B. & Bryan, G. L. 2022, ApJ, 924, 82

Fierlinger, K. M., Burkert, A., Ntormousi, E., et al. 2016, MNRAS, 456, 710

Filipović, M. D., Lazarević, S., Araya, M., et al. 2024, PASA, 41, e112

Filipović, M. D., Smeaton, Z. J., Kothes, R., et al. 2025, PASA, 42, e104

Finkelstein, S. L., Bagley, M. B., Ferguson, H. C., et al. 2023, ApJ, 946, L13

Forbes, J. C., Alves, J., & Lin, D. N. C. 2021, Nature Astronomy, 5, 1009

Freundlich, J. 2024, Fundamental Plasma Physics, 11, 100059

Gaczkowski, B., Preibisch, T., Stanke, T., et al. 2015, A&A, 584, A36

Gaczkowski, B., Roccatagliata, V., Flaischlen, S., et al. 2017, A&A, 608, A102

Gaffet, B. 1978, ApJ, 225, 442

Gaffet, B. 1983, ApJ, 273, 267

Gaia Collaboration, Vallenari, A., Brown, A. G. A., et al. 2023, A&A, 674, A1

Gao, B. A., Zucker, C., Sridharan, T. K., et al. 2025, ApJ, 987, 73

Gatto, A., Walch, S., Naab, T., et al. 2017, MNRAS, 466, 1903

Gent, F. A., Mac Low, M. M., Käpylä, M. J., Sarson, G. R., & Hollins, J. F. 2020, Geophysical and Astrophysical Fluid Dynamics, 114, 77

Gent, F. A., Mac Low, M.-M., & Korpi-Lagg, M. J. 2024, ApJ, 961, 7

Gent, F. A., Mac Low, M.-M., Korpi-Lagg, M. J., & Singh, N. K. 2023, ApJ, 943, 176

Gentry, E. S., Krumholz, M. R., Dekel, A., & Madau, P. 2017, MNRAS, 465, 2471

Gentry, E. S., Krumholz, M. R., Madau, P., & Lupi, A. 2019, MNRAS, 483, 3647

Genzel, R., Jolly, J. B., Liu, D., et al. 2023, ApJ, 957, 48

Genzel, R., Newman, S., Jones, T., et al. 2011, ApJ, 733, 101

Girichidis, P., Naab, T., Walch, S., et al. 2016, ApJ, 816, L19

Girichidis, P., Werhahn, M., Pfrommer, C., Pakmor, R., & Springel, V. 2024, MNRAS, 527, 10897

Glasstone, S. & Dolan, P. J. 1977, The Effects of Nuclear Weapons (United States Department of Defense and Energy Research and Development Administration)

Górski, K. M., Hivon, E., Banday, A. J., et al. 2005, ApJ, 622, 759

Goswami, S., Vilchez, J. M., Pérez-Díaz, B., et al. 2024, A&A, 685, A81

Green, D. A. 2019, Journal of Astrophysics and Astronomy, 40, 36

Green, D. A. 2025, Journal of Astrophysics and Astronomy, 46, 14

Grefenstette, B. W., Fryer, C. L., Harrison, F. A., et al. 2017, ApJ, 834, 19

Groth, F., Steinwandel, U. P., Valentini, M., & Dolag, K. 2023, MNRAS, 526, 616

Groth, F., Valentini, M., Steinwandel, U. P., Vallés-Pérez, D., & Dolag, K. 2025, A&A, 693, A263

Grudić, M. Y., Guszejnov, D., Offner, S. S. R., et al. 2022, MNRAS, 512, 216

Grudic, M. Y., Offner, S. S. R., Guszejnov, D., Faucher-Giguère, C.-A., & Hopkins, P. F. 2023, The Open Journal of Astrophysics, 6, 48

Guo, M., Kim, C.-G., & Stone, J. M. 2025, ApJ, 990, 49

Haid, S., Walch, S., Naab, T., et al. 2016, MNRAS, 460, 2962

Heckman, T. M., Alexandroff, R. M., Borthakur, S., Overzier, R., & Leitherer, C. 2015, ApJ, 809, 147

Heiles, C. 1998, ApJ, 498, 689

Henderson, A. 2007, ParaView Guide, A Parallel Visualization Application (Kitware Inc.)

Herenz, E. C., Kusakabe, H., & Maulick, S. 2025, PASJ, 77, L63

Herrington, N. P., Dobbs, C. L., & Bending, T. J. R. 2023, MNRAS, 521, 5712

Hewitt, J. W. & Yusef-Zadeh, F. 2009, ApJ, 694, L16

Heyer, M., Di Teodoro, E., Loinard, L., et al. 2025, A&A, 695, A60

Hollenbach, D. & Salpeter, E. E. 1971, ApJ, 163, 155

Hopkins, P. F. 2015, MNRAS, 450, 53

Hopkins, P. F., Butsky, I. S., Ji, S., & Kereš, D. 2023, MNRAS, 522, 2936

Hopkins, P. F., Butsky, I. S., Panopoulou, G. V., et al. 2022, MNRAS, 516, 3470

Hopkins, P. F., Grudic, M. Y., Su, K.-Y., et al. 2024, The Open Journal of Astrophysics, 7, 18

Hopkins, P. F., Quataert, E., Ponnada, S. B., & Silich, E. 2025, The Open Journal of Astrophysics, 8, 78

Horie, S., Okamoto, T., & Habe, A. 2024, MNRAS, 527, 10077

Hunt, E. L. & Reffert, S. 2023, A&A, 673, A114

Hunter, J. D. 2007, Computing in Science & Engineering, 9, 90

Hunter, Jr., J. H., Sandford, II, M. T., Whitaker, R. W., & Klein, R. I. 1986, ApJ, 305, 309

Ibrahim, D. & Kobayashi, C. 2024, MNRAS, 527, 3276

Irwin, J., Beck, R., Cook, T., et al. 2024, Galaxies, 12, 22

Jacob, S., Pakmor, R., Simpson, C. M., Springel, V., & Pfrommer, C. 2018, MNRAS, 475, 570

Janka, H.-T. 2025, Annual Review of Nuclear and Particle Science, 75, 425

Jaynes, E. T. 1957, Physical Review, 106, 620

Jeans, J. H. 1902, Philosophical Transactions of the Royal Society of London Series A, 199, 1

Ji, S., Chan, T. K., Hummels, C. B., et al. 2020, MNRAS, 496, 4221

Jiménez, S., Silich, S., Mayya, Y. D., & Zaragoza-Cardiel, J. 2024, ApJ, 960, 81

Jing, W., West, J. L., Sun, X., et al. 2025, ApJ, 980, 162

Jones, T. J., Dowell, C. D., Lopez Rodriguez, E., et al. 2019, ApJ, 870, L9

Karwin, C. M., Murgia, S., Campbell, S., & Moskalenko, I. V. 2019, ApJ, 880, 95

Katsuragawa, M., Lee, S.-H., Odaka, H., et al. 2022, ApJ, 938, 23

Katz, N. 1992, ApJ, 391, 502

Keelin, T. W. & Powley, B. W. 2011, Decision Analysis, 8, 206

Kennicutt, Robert C., J. 1989, ApJ, 344, 685

Khabibullin, I. I., Churazov, E. M., Bykov, A. M., Chugai, N. N., & Sunyaev, R. A. 2023, MNRAS, 521, 5536

Kim, C.-G., Kim, J.-G., Gong, M., & Ostriker, E. C. 2023a, ApJ, 946, 3

Kim, C.-G. & Ostriker, E. C. 2015, ApJ, 802, 99

Kim, C.-G. & Ostriker, E. C. 2017, ApJ, 846, 133

Kim, C.-G. & Ostriker, E. C. 2018, ApJ, 853, 173

Kim, C.-G., Ostriker, E. C., & Raileanu, R. 2017, ApJ, 834, 25

Kim, J.-G., Gong, M., Kim, C.-G., & Ostriker, E. C. 2023b, ApJS, 264, 10

Kirchschlager, F., Sartorio, N. S., De Looze, I., et al. 2024, MNRAS, 528, 5364

Kjellgren, K., Girichidis, P., Göller, J., et al. 2025, A&A, 700, A124

Klessen, R. S. & Glover, S. C. O. 2016, Saas-Fee Advanced Course, 43, 85

Kobashi, R., Lee, S.-H., Tanaka, T., & Maeda, K. 2024, ApJ, 961, 32

Kobulnicky, H. A. 1999, in Wolf-Rayet Phenomena in Massive Stars and Starburst Galaxies, ed. K. A. van der Hucht, G. Koenigsberger, & P. R. J. Eenens, Vol. 193, 670

Kompaneets, A. S. 1960, Soviet Physics Doklady, 5, 46

Koo, B.-C., Kim, C.-G., Park, S., & Ostriker, E. C. 2020, ApJ, 905, 35

Koo, B.-C. & McKee, C. F. 1990, ApJ, 354, 513

Kozasa, T., Hasegawa, H., & Nomoto, K. 1989, ApJ, 344, 325

Krause, M. G. H., Burkert, A., Diehl, R., et al. 2018, A&A, 619, A120

Kretschmer, K., Diehl, R., Krause, M., et al. 2013, A&A, 559, A99

Krieger, N., Bolatto, A. D., Walter, F., et al. 2019, ApJ, 881, 43

Kroupa, P. & Jerabkova, T. 2021, arXiv e-prints, arXiv:2112.10788

Krumholz, M. R. & Burkhart, B. 2016, MNRAS, 458, 1671

Krumholz, M. R., Burkhart, B., Forbes, J. C., & Crocker, R. M. 2018, MNRAS, 477, 2716

Lada, C. J., Lombardi, M., Roman-Zuniga, C., Forbrich, J., & Alves, J. F. 2013, ApJ, 778, 133

Lallement, R., Babusiaux, C., Vergely, J. L., et al. 2019, A&A, 625, A135

Lancaster, L., Ostriker, E. C., Kim, C.-G., Kim, J.-G., & Bryan, G. L. 2024, ApJ, 970, 18

Lancaster, L., Ostriker, E. C., Kim, J.-G., & Kim, C.-G. 2021, ApJ, 914, 90

Lau, C. S. C. & Bonnell, I. A. 2025, MNRAS, 540, 1124

Laumbach, D. D. & Probstein, R. F. 1969, Journal of Fluid Mechanics, 35, 53

Lee, E. J., Miville-Deschênes, M.-A., & Murray, N. W. 2016, ApJ, 833, 229

Lehnert, M. D., Heckman, T. M., & Weaver, K. A. 1999, ApJ, 523, 575

Leike, R. H., Glatzle, M., & Enßlin, T. A. 2020, A&A, 639, A138

Leitherer, C., Schaerer, D., Goldader, J. D., et al. 1999, ApJS, 123, 3

Leroy, A. K., Walter, F., Martini, P., et al. 2015, ApJ, 814, 83

Li, G.-X., Zhou, J.-X., & Chen, B.-Q. 2022, MNRAS, 516, L35

Li, J., Kreckel, K., Sarbadhicary, S., et al. 2024, A&A, 690, A161

Li, Y., Giacinti, G., & Liu, S. 2025, ApJ, 990, 9

Linsky, J. L. & Redfield, S. 2021, ApJ, 920, 75

Lopez, S., Lopez, L. A., Thompson, T. A., Leroy, A. K., & Bolatto, A. D. 2025, ApJ, 989, 100

Lopez-Rodriguez, E., Guerra, J. A., Asgari-Targhi, M., & Schmelz, J. T. 2021, ApJ, 914, 24

Mac Low, M.-M. & Klessen, R. S. 2004, Reviews of Modern Physics, 76, 125

Maiolino, R., Nagao, T., Grazian, A., et al. 2008, A&A, 488, 463

Maíz-Apellániz, J. 2001, ApJ, 560, L83

Makarenko, E. I., Walch, S., Clarke, S. D., et al. 2023, MNRAS, 523, 1421

Marasco, A., Belfiore, F., Cresci, G., et al. 2023, A&A, 670, A92

Marin-Gilabert, T., Gronke, M., & Oh, S. P. 2025, arXiv e-prints, arXiv:2504.15345

Mathis, J. S., Rumpl, W., & Nordsieck, K. H. 1977, ApJ, 217, 425

Matsumoto, K., Camps, P., Baes, M., et al. 2023, A&A, 678, A175

Matsumoto, K., Hirashita, H., Nagamine, K., et al. 2024, A&A, 689, A79

Matsuura, M., Dwek, E., Meixner, M., et al. 2011, Science, 333, 1258

Mayer, A. C., Naab, T., Caselli, P., et al. 2025, MNRAS, 543, 3321

Mayker Chen, N., Leroy, A. K., Lopez, L. A., et al. 2023, ApJ, 944, 110

McCallum, L., Wood, K., Benjamin, R., Krishnarao, D., & McLeod, A. F. 2025, MNRAS, 541, 2324

McComas, D. J., Bzowski, M., Fuselier, S. A., et al. 2015, ApJS, 220, 22

McKee, C. F. & Ostriker, E. C. 2007, ARA&A, 45, 565

McKee, C. F. & Ostriker, J. P. 1977, ApJ, 218, 148

McKee, C. F., Parravano, A., & Hollenbach, D. J. 2015, ApJ, 814, 13

McQuinn, K. B. W., van Zee, L., & Skillman, E. D. 2019, ApJ, 886, 74

Meyer, D. M. A., Pohl, M., Petrov, M., & Egberts, K. 2023, MNRAS, 521, 5354

Micelotta, E. R., Jones, A. P., & Tielens, A. G. G. M. 2010, A&A, 510, A37

Milisavljevic, D., Temim, T., De Looze, I., et al. 2024, ApJ, 965, L27

Miret-Roig, N., Galli, P. A. B., Olivares, J., et al. 2022, A&A, 667, A163

Mitchell, A. M. W. 2024, A&A, 684, A66

Miville-Deschênes, M.-A., Murray, N., & Lee, E. J. 2017, ApJ, 834, 57

Modak, S., Quataert, E., Jiang, Y.-F., & Thompson, T. A. 2023, MNRAS, 524, 6374

Moellenhoff, C. 1976, A&A, 50, 105

Mora-Partiarroyo, S. C., Krause, M., Basu, A., et al. 2019, A&A, 632, A10

Mulcahy, D. D., Horneffer, A., Beck, R., et al. 2018, A&A, 615, A98

Muratov, A. L., Kereš, D., Faucher-Giguère, C.-A., et al. 2015, MNRAS, 454, 2691

NASA, E. & the Hubble Heritage Team (STScI/AURA). 2006, The magnificent starburst galaxy Messier 82, `https://esahubble.org/images/heic0604a/`, accessed: 2025-06-30

Nianias, J., Lim, J., & Yeung, M. 2024, ApJ, 963, 19

Nieuwmunster, N., Nandakumar, G., Spitoni, E., et al. 2023, A&A, 671, A94

Nonhebel, M., Barnes, A. T., Immer, K., et al. 2024, A&A, 691, A70

Nozawa, T., Kozasa, T., Habe, A., et al. 2007, ApJ, 666, 955

Ntormousi, E., Burkert, A., Fierlinger, K., & Heitsch, F. 2011, ApJ, 731, 13

Ohlin, L., Renaud, F., & Agertz, O. 2019, MNRAS, 485, 3887

Okada, Y., Ohshiro, Y., Suzuki, S., et al. 2025, ApJ, 982, 190

Oku, Y., Tomida, K., Nagamine, K., Shimizu, I., & Cen, R. 2022, ApJS, 262, 9

O'Neill, T. J., Zucker, C., Goodman, A. A., & Edenhofer, G. 2024, ApJ, 973, 136

Orlando, S., Janka, H. T., Wongwathanarat, A., et al. 2025, A&A, 696, A108

Orr, M. E., Fielding, D. B., Hayward, C. C., & Burkhart, B. 2022, ApJ, 932, 88

Ostriker, E. C. & Kim, C.-G. 2022, ApJ, 936, 137

Ostriker, J. 1964, ApJ, 140, 1056

Ostriker, J. P. & McKee, C. F. 1988, Reviews of Modern Physics, 60, 1

Owen, E. R., Jacobsen, I. B., Wu, K., & Surajbali, P. 2018, MNRAS, 481, 666

Owen, E. R., Jin, X., Wu, K., & Chan, S. 2019, MNRAS, 484, 1645

Owen, E. R., Wu, K., Inoue, Y., Yang, H. Y. K., & Mitchell, A. M. W. 2023, Galaxies, 11, 86

Palouš, J., Ehlerová, S., Wünsch, R., & Morris, M. R. 2020, A&A, 644, A72

Parker, R. J., Lichtenberg, T., Patel, M., Polius, C. K. M., & Ridsdill-Smith, M. 2023, MNRAS, 521, 4838

Paylı, G., Bakış, H., Aktekin, E., Sano, H., & Sezer, A. 2024, MNRAS, 527, 11685

Pelgrims, V., Ferrière, K., Boulanger, F., Lallement, R., & Montier, L. 2020, A&A, 636, A17

Ploeckinger, S. & Schaye, J. 2020, MNRAS, 497, 4857

Posch, L., Miret-Roig, N., Alves, J., et al. 2023, A&A, 679, L10

Pshirkov, M. S. & Nizamov, B. A. 2024, arXiv e-prints, arXiv:2410.02066

Quataert, E. & Hopkins, P. F. 2025, The Open Journal of Astrophysics, 8, 66

Rathjen, T.-E., Naab, T., Girichidis, P., et al. 2021, MNRAS, 504, 1039

Rathjen, T.-E., Walch, S., Naab, T., et al. 2025, MNRAS, 540, 1462

Ratzenböck, S., Großschedl, J. E., Alves, J., et al. 2023, A&A, 678, A71

Reach, W. T., Tram, L. N., DeWitt, C., et al. 2024, ApJ, 977, 149

Recchia, S., Gabici, S., Aharonian, F. A., & Niro, V. 2021, ApJ, 914, 135

Reed, J. E., Hester, J. J., Fabian, A. C., & Winkler, P. F. 1995, ApJ, 440, 706

Reynolds, S. P. & Borkowski, K. J. 2024, ApJ, 962, 179

Rho, J., Park, S. H., Arendt, R., et al. 2024, ApJ, 969, L9

Richie, H. M. & Schneider, E. E. 2026, ApJ, 996, 17

Richie, H. M., Schneider, E. E., Abruzzo, M. W., & Torrey, P. 2024, ApJ, 974, 81

Ritchey, A. M. 2023, ApJ, 959, 29

Rix, H.-W., Chandra, V., Zasowski, G., et al. 2024, ApJ, 975, 293

Romano, L. E. C., Behrendt, M., & Burkert, A. 2024a, ApJ, 965, 168

Romano, L. E. C., Behrendt, M., & Burkert, A. 2025a, A&A, 702, A12

Romano, L. E. C. & Burkert, A. 2025, arXiv e-prints, arXiv:2509.04221

Romano, L. E. C., Burkert, A., & Behrendt, M. 2024b, ApJ, 971, L44

Romano, L. E. C., Nagamine, K., & Hirashita, H. 2022, MNRAS, 514, 1461

Romano, L. E. C., Owen, E. R., & Nagamine, K. 2025b, A&A, 701, L5

Romano, M., Nanni, A., Donevski, D., et al. 2023, A&A, 677, A44

Rosen, A. & Bregman, J. N. 1995, ApJ, 440, 634

Rosen, A. L., Offner, S. S. R., Sadavoy, S. I., et al. 2020, Space Sci. Rev., 216, 62

Ruszkowski, M. & Pfrommer, C. 2023, A&A Rev., 31, 4

Saha, L., Ergin, T., Majumdar, P., Bozkurt, M., & Ercan, E. N. 2014, A&A, 563, A88

Saintonge, A. & Catinella, B. 2022, ARA&A, 60, 319

Saitoh, T. R. 2017, AJ, 153, 85

Sakashita, S. & Morita, K. 1977, Ap&SS, 50, 133

Sánchez-Cruces, M. & Rosado, M. 2023, MNRAS, 524, 4907

Schinnerer, E. & Leroy, A. K. 2024, ARA&A, 62, 369

Schmidt, N. & Arcand, K. 2024, CASSIOPEIA A RESOURCES, `https://universe-of-learning.org/informal-educators/science-resources/cassiopeia-a-resources`, accessed: 2025-06-30

Sedov, L. I. 1959, Similarity and Dimensional Methods in Mechanics (New York: Academic)

Sextl, E., Kudritzki, R.-P., Burkert, A., et al. 2024, ApJ, 960, 83

Sharma, P., Roy, A., Nath, B. B., & Shchekinov, Y. 2014, MNRAS, 443, 3463

Shen, Y.-Z., Chen, Y., Zhang, X., et al. 2025, MNRAS, 537, 464

Shetty, R. & Ostriker, E. C. 2012, ApJ, 754, 2

Shimizu, I., Todoroki, K., Yajima, H., & Nagamine, K. 2019, MNRAS, 484, 2632

Shimoda, J. & Inutsuka, S.-i. 2022, ApJ, 926, 8

Shin, E.-J., Kim, J.-H., & Oh, B. K. 2021, ApJ, 917, 12

Slavin, J. D. & Cox, D. P. 1992, ApJ, 392, 131

Smith, M. C., Fielding, D. B., Bryan, G. L., et al. 2024, MNRAS, 527, 1216

Snowden, S. L., Freyberg, M. J., Kuntz, K. D., & Sanders, W. T. 2000, ApJS, 128, 171

Sofue, Y. 2024, PASJ, 76, 773

Springel, V. 2010, MNRAS, 401, 791

Springel, V. & Hernquist, L. 2003, MNRAS, 339, 289

Springel, V., Pakmor, R., Zier, O., & Reinecke, M. 2021, MNRAS, 506, 2871

Steinwandel, U. P., Kim, C.-G., Bryan, G. L., et al. 2024, ApJ, 960, 100

Stone, J. M., Gardiner, T. A., Teuben, P., Hawley, J. F., & Simon, J. B. 2008, ApJS, 178, 137

Straka, W. C. 1974, ApJ, 190, 59

Su, M., Slatyer, T. R., & Finkbeiner, D. P. 2010, ApJ, 724, 1044

Sugahara, Y., Ouchi, M., Harikane, Y., et al. 2019, ApJ, 886, 29

Suzuki, S., Sonoda, H., Sakai, Y., et al. 2025, PASJ

Swiggum, C., Alves, J., Benjamin, R., et al. 2024, Nature, 631, 49

Tacconi, L. J., Genzel, R., & Sternberg, A. 2020, ARA&A, 58, 157

Taylor, E., Maltby, D., Almaini, O., et al. 2024, MNRAS, 535, 1684

Taylor, G. 1950, Proceedings of the Royal Society of London Series A, 201, 159

Tenorio-Tagle, G., Bodenheimer, P., Franco, J., & Rozyczka, M. 1990, MNRAS, 244, 563

Tenorio-Tagle, G. & Palous, J. 1987, A&A, 186, 287

Teyssier, R. 2002, A&A, 385, 337

Thompson, T. A. & Heckman, T. M. 2024, ARA&A, 62, 529

Thompson, T. A., Quataert, E., Zhang, D., & Weinberg, D. H. 2016, MNRAS, 455, 1830

Thornton, K., Gaudlitz, M., Janka, H. T., & Steinmetz, M. 1998, ApJ, 500, 95

Tibaldo, L., Digel, S. W., Casandjian, J. M., et al. 2015, ApJ, 807, 161

Tomasi, M. & Li, Z. 2021, Healpix.jl: Julia-only port of the HEALPix library

Toomre, A. 1964, ApJ, 139, 1217

Toro, E. F., Spruce, M., & Speares, W. 1994, Shock Waves, 4, 25

Townsend, R. H. D. 2009, ApJS, 181, 391

Toyouchi, D., Yajima, H., Ferrara, A., & Nagamine, K. 2025, MNRAS, 541, 3606

Truelove, J. K. & McKee, C. F. 1999, ApJS, 120, 299

Tsuru, T. G., Ozawa, M., Hyodo, Y., et al. 2007, PASJ, 59, 269

Tu, T.-y., Chen, Y., Zhou, P., Safi-Harb, S., & Liu, Q.-C. 2024, ApJ, 966, 178

Urey, H. C. 1955, Proceedings of the National Academy of Science, 41, 127

Vasiliev, E. O., Drozdov, S. A., Nath, B. B., Dettmar, R.-J., & Shchekinov, Y. A. 2023, MNRAS, 520, 2655

Veilleux, S., Cecil, G., & Bland-Hawthorn, J. 2005, ARA&A, 43, 769

Velázquez, P. F., Meyer, D. M. A., Chiotellis, A., et al. 2023, MNRAS, 519, 5358

Verma, A., Sharma, S., Mallick, K. K., et al. 2023, ApJ, 953, 145

Vink, J., Agarwal, M., Slane, P., et al. 2024, ApJ, 964, L11

Vishniac, E. T. 1983, ApJ, 274, 152

Vishniac, E. T. 1994, ApJ, 428, 186

Walch, S., Girichidis, P., Naab, T., et al. 2015, MNRAS, 454, 238

Walch, S. & Naab, T. 2015, MNRAS, 451, 2757

Wallner, A., Feige, J., Kinoshita, N., et al. 2016, Nature, 532, 69

Wallner, A., Froehlich, M. B., Hotchkis, M. A. C., et al. 2021, Science, 372, 742

Walter, F., Bolatto, A. D., Leroy, A. K., et al. 2017, ApJ, 835, 265

Watkins, E. J., Barnes, A. T., Henny, K., et al. 2023, ApJ, 944, L24

Weaver, R., McCray, R., Castor, J., Shapiro, P., & Moore, R. 1977, ApJ, 218, 377

Weinberger, R., Springel, V., & Pakmor, R. 2020, ApJS, 248, 32

Williams, J. P. & McKee, C. F. 1997, ApJ, 476, 166

Winkler, P. F., Long, K. S., & Blair, W. P. 2023, ApJ, 959, 62

Wolfire, M. G., McKee, C. F., Hollenbach, D., & Tielens, A. G. G. M. 2003, ApJ, 587, 278

Woltjer, L. 1972, ARA&A, 10, 129

Xie, Y.-H., Li, G.-X., & Chen, B.-Q. 2024, ApJ, 975, 39

Xu, X., Heckman, T., Henry, A., et al. 2022, ApJ, 933, 222

Xu, X., Heckman, T., Henry, A., et al. 2023a, ApJ, 948, 28

Xu, X., Heckman, T., Yoshida, M., Henry, A., & Ohyama, Y. 2023b, ApJ, 956, 142

Yang, H. Y. K., Gaspari, M., & Marlow, C. 2019, ApJ, 871, 6

Yeung, M. C. H., Ponti, G., Freyberg, M. J., et al. 2024, A&A, 690, A399

Yu, B. P. B., Owen, E. R., Wu, K., & Ferreras, I. 2020, MNRAS, 492, 3179

Zangrandi, F., Jurk, K., Sasaki, M., et al. 2024, A&A, 692, A237

Zhang, D. 2018, Galaxies, 6, 114

Zhang, S., Tian, W., Zhang, M., Zhu, H., & Cui, X. 2023, ApJ, 942, 94

Zhou, X., Su, Y., Yang, J., et al. 2023, ApJS, 268, 61

Zhu, Q., Smith, B., & Hernquist, L. 2017, MNRAS, 470, 1017

Zhukovska, S., Gail, H. P., & Trieloff, M. 2008, A&A, 479, 453

Zubovas, K. & Nayakshin, S. 2012, MNRAS, 424, 666

Zucker, C., Goodman, A. A., Alves, J., et al. 2022, Nature, 601, 334

Acknowledgements

This thesis marks the end of a long and challenging journey, one that would not have been possible without the support, guidance, and encouragement of many people to whom I am deeply grateful.

First and foremost, I would like to thank my wife, Courtney, for her unwavering support, patience, and encouragement throughout this entire process. Her presence has been a constant source of strength and motivation.

I am also profoundly grateful to my parents Wolfgang and Cornelia, who raised me into who I am today, and whose upbringing always encouraged me to stay curious and critically question the status-quo.

I also thank my brother and sister Samuel and Olivia, who were my first friends and who continuously supported me over the years, in my academic pursuit and beyond. Their belief in me has always been a quiet but steady foundation.

I would like to thank my PI, Prof. Andreas Burkert, for giving me the opportunity to pursue this work and for his guidance throughout the course of my PhD. I am particularly indebted to Manuel, my supervisor, whose expertise with RAMSES was instrumental in helping me get started with my numerical work and data analysis. His thoughtful feedback, scientific insight, and patient advice have been invaluable at every stage.

I would like to acknowledge the members of my thesis committee—Eric, Volker, my mentor Rhea, and, of course, my PI and supervisor – for their time, valuable feedback, and interest in my work.

Thanks also go to my office mates, Valentin and Hans-Christian –and later Ming-Yu – for creating a friendly and collaborative working environment. On this note, I would also like to thank Benedict, the Bachelor student, who I co-supervised during the first year of my PhD, for providing me the opportunity to learn hands-on how to work with people who are less experienced and actively provide guidance.

I am fortunate to have worked alongside many supportive colleagues in the CAST group at the USM for their scientific input, discussions, and collegiality.

I also wish to thank the staff at ORIGINS, particularly Alice and Ina, for their help and organizational support with my duties as PhD representative, the ORIGINS cluster for trusting me with this role and my fellow PhD students in the cluster whose enthusiastic participation in the activities that we organized made all of our efforts so rewarding. It has been fulfilling to know that some of the activities we organized made a positive difference. On this note, I would especially like to express my gratitude towards my fellow PhD representatives, Asmaa and Luise, for being such a dependable and motivated team to work with throughout.

Outside the scientific sphere, I am grateful to those who lead initiatives that made Garching such

a fulfilling work environment and provided an additional sense of belonging. In particular, I thank Marta and Jorge for leading the ESO choir, and the IMPRS PhD representatives Catarina and Soumya for organizing a number of mindfulness and relaxation activities such as the bi-annual yoga classes or the weekly meditation.

I am grateful to the efforts of the editors and anonymous reviewers whose comments helped improve the quality of my publications.

I am thankful to the members of the German public, whose continued support for basic scientific research made this work possible and who funded my research throughout by proxy of the Deutsche Forschungsgemeinschaft (DFG, German Research Foundation) under Germany's Excellence Strategy – EXC 2094 – 390783311.

Last but not least, I am grateful to anyone I may have inadvertently forgotten to mention here – please know that your help has been appreciated as well.